

HYDROPHOBIC FLUOROPOLYMER NANO-COATINGS:
STUDY OF ANTI-REFLECTIVE AND ANTI-SOILING
PROPERTIES AND APPLICATIONS

by

ILLYA NAYSHEVSKY

A dissertation submitted to the Graduate Faculty in Chemistry in partial fulfilment of the
requirements for the degree of Doctor of Philosophy, The City University of New York

2020

© 2020

ILLYA NAYSHEVSKY

All Rights Reserved

Approval Page

Hydrophobic Fluoropolymer Nano-Coatings:

Study of Anti-Reflective and Anti-Soiling Properties and Applications

by

Illya Nayshevsky

This manuscript has been read and accepted for the Graduate Faculty in Chemistry
in satisfaction of the dissertation requirement for the degree of Doctor of Philosophy.

Date Alan M. Lyons

Chair of Examining Committee

Date Brian R. Gibney

Executive Officer

Supervisory Committee:

Professor Alan M. Lyons

Professor Alexander Greer

Professor Chwen-Yang Shew

THE CITY UNIVERSITY OF NEW YORK

Abstract

Hydrophobic Fluoropolymer Nano-Coatings:

Study of Anti-Reflective and Anti-Soiling Properties and Applications

by

Illya Nayshevsky

Advisor: Alan M. Lyons

Anti-reflective, anti-soiling and self-cleaning coatings are currently of interest for photovoltaic (PV) cover glass applications due to their potential to increase the amount of light transmitted through the glass and improve efficiency by reducing the number of contaminants bound to the surface of the glass (soiling). Naturally occurring dew is known to exacerbate soiling via cementation of dust on the glass surface. To address these challenges, fluorinated ethylene-propylene (FEP) polymer coatings were formed on solar cover glass using a lamination-peeling technique. This process forms a thin (<100 nm thick) polymer coating on the glass with a nano-texture that can be controlled by modifying the lamination-peeling process conditions.

Anti-reflective properties of the nano-coating were achieved by using a low refractive index polymer. Moreover, the morphology of the coating creates a refractive index gradient further reducing the effective refractive index. The anti-soiling and self-cleaning properties were achieved due to the surface's low chemical reactivity and stable hydrophobicity. Self-cleaning performance was increased by forming a hybrid surface where hydrophilic domains, formed by selectively removing the hydrophobic polymer to expose the underlying hydrophilic glass substrate, accelerated condensation of atmospheric water vapor. Characterization of the coating morphology was performed by atomic force microscopy (AFM), and scanning electron microscopy (SEM). X-

ray photoelectron spectroscopy (XPS) was used to analyze the chemical bonding between the fluoropolymer coating and the underlying soda-lime glass.

The anti-soiling and self-cleaning properties of the coatings were evaluated using laboratory soiling tests in the presence of condensed water. These tests were designed and built to mimic natural soiling conditions, with a focus on soiling in the presence of simulated dew. Automation of experimental equipment and self-cleaning analytical methods was done by implementing microcontrollers and computer vision assisted algorithms respectively. Laboratory soiling and cleaning experiments conducted on fluoropolymer coated PV grade cover glass revealed a novel “dust herding” anti-soiling mechanism along with improved self-cleaning abilities. Hybrid hydrophobic-hydrophilic surfaces enhanced the self-cleaning effect in the presence of various soil types.

Nanotextured fluoropolymer coatings were also fabricated on aluminum substrates. These surfaces exhibited stable coalescence-induced drop jumping under atmospheric pressure, which proved stable for 1000 hours at elevated temperature and humidity conditions (saturated vapor 50 K above the surface temperature). Jumping rates and stabilities were correlated with surface morphology. This phenomenon may prove useful for self-cleaning surfaces, as well as enhanced heat transfer for applications in electronic packaging and thermal power plant production of electricity.

Acknowledgements

Firstly, I would like to express my sincere gratitude to my advisor Prof. Alan M. Lyons for the continuous support of my Ph.D. study and related research, for his patience, motivation, and immense knowledge. His guidance helped me in all the time of research and writing of this thesis. I could not have imagined having a better advisor and mentor for my Ph.D. study.

Besides my advisor, I would like to thank the rest of my thesis committee: Prof. Alexander Greer and Prof. Chwen-Yang Shew for their insightful comments and encouragement, but also for the hard question which incited me to widen my research from various perspectives.

My sincere thanks also goes to Dr. QianFeng Xu, who has given me the opportunity to learn many valuable laboratory techniques and has provided exceptional guidance in all of my work. Without his precious support it would not be possible for me to conduct this research.

I thank my fellow graduate and undergraduate lab mates in for the stimulating discussions, and all of their assistance throughout the years. I would also like to thank Dr. Michael Bucaro, at the CSI Advanced Imaging Facility for enlightening me in the field of microscopy.

I thank my friends in the CUNY Advanced Science Research Center. In particular, I am grateful to Dr. Tai-De Li, at the ASRC Surface Science Suite for teaching me the use of XPS and AFM instruments.

Last but not the least, I would like to thank my wife, Dr. Ilona Stoyko, my mother and her life partner, Valeriya Nayshevska and Rocco Trotta, my grandmother, Lioudmila Nuccio, and my good friend, Alexander Miller, J.D., for supporting me spiritually throughout writing this thesis and in my life in general.

Table of Contents

<i>Abstract</i>	<i>iv</i>
<i>Acknowledgements</i>	<i>vi</i>
<i>Table of Contents</i>	<i>vii</i>
<i>List of Figures</i>	<i>x</i>
<i>List of Tables</i>	<i>xviii</i>
<i>List of Abbreviations</i>	<i>xviii</i>
<i>List of Equations</i>	<i>xix</i>
<i>List of Schemes</i>	<i>xix</i>
<i>Chapter 1. Introduction</i>	<i>1</i>
1.1 Properties and Applications of Hydrophobic coatings	1
1.1.1 Anti-reflective coatings.....	1
1.1.2 Anti-soiling and Self-cleaning Coatings.....	5
1.1.3 Hybrid Hydrophobic-Hydrophilic Surfaces.....	11
1.2 Objectives of Thesis and Scope of Work	15
<i>Chapter 2. Design and Development of Fluoropolymer Coatings, Accelerated Testing Apparatus and Analytical Methods</i>	<i>16</i>
2.1 Fabrication and Characterization of Fluoropolymer Hydrophobic Coatings	16
2.1.1 Textured Nano-coating Fabrication via Lamination-Peeling Method	16
2.1.2 Hybrid Hydrophobic-Hydrophilic Surface Fabrication	18
2.2 Dust Deposition Apparatus	30
2.3 Simulated Dew Condensation Chamber	34
2.4 Optical Microscopy Analysis of Soiling on Surfaces	36
2.5 Automated Self-Cleaning Detection Methods via Computer Vision Analysis of Condensation Derived Water Droplets	40
2.6 Determination of Dust Particle Size Observed in Nature	44
<i>Chapter 3. Fluoropolymer Coatings for Solar Cover Glass: Anti-Soiling Mechanisms in the Presence of Dew</i>	<i>47</i>
3.1 Introduction	47
3.2 Material and Methods	51
3.2.1 Materials	51
3.2.2 Measurements	51
3.2.3 Dust Deposition Apparatus	53

3.2.4	Pulsed Deposition Apparatus (PDA)	54
3.2.5	Cloud Deposition Apparatus (CDA).....	55
3.2.6	Cleaning Process	56
3.3	Results and Discussion.....	57
3.3.1	Samples and Wetting Properties	57
3.3.2	UV-Vis Spectra: % Light Transmittance	58
3.3.3	Atomic Force Microscopy	59
3.3.4	Condensation Mechanisms	60
3.3.5	Soiling Rates and Soiling Mechanisms	62
3.3.6	No-Touch Cleaning on Coated Surfaces.....	71
3.4	Conclusions	73
3.5	Appendix.....	76
<i>Chapter 4. Hydrophobic-Hydrophilic Surfaces Exhibiting Dropwise Condensation for Anti-Soiling Applications</i>		90
4.1	Introduction.....	90
4.2	Methods.....	92
4.2.1	Sample Fabrication	92
4.2.2	Condensation Chamber.....	94
4.2.3.	Experimental Methods	95
4.3	Results	96
4.3.1	Bare Glass vs. Hydrophobic Glass.....	96
4.3.2	Water Collection Rates on Hybrid Hydrophobic-Hydrophilic Surfaces	97
4.3.3	Water Collection: Staggered vs. Square Arrays of Hydrophilic Rings	98
4.3.4	Water Collection: Number of Rows of Hydrophilic Features	100
4.3.5	Water Collection: Distance Between Features	100
4.3.6	Water Collection: Feature Diameter	101
4.3.7	Roll-off location and critical droplet diameter.....	102
4.4	Discussion.....	103
4.5	Conclusions	105
<i>Chapter 5. Self-Cleaning Hybrid Hydrophobic-Hydrophilic Surfaces: Durability and Effect of Artificial Soilant Particle Type</i>		107
5.1	Introduction.....	107
5.2	Methods.....	109
5.2.1	Material Fabrication.....	109
5.2.2	Experimental Methods	110
5.2.3	Analytical Methods and Automation Controls.	113
5.3	Results	114
5.3.1	Optical and Wetting Properties	114
5.3.2	Artificial Weathering	115
5.3.3	Anti-Soiling Properties	116
5.3.4	Self-Cleaning Properties	118

5.4 Conclusion	123
<i>Chapter 6. Approximating Partial Wetting Regions on Rough Hydrophobic Surfaces Using Atomic Force Microscopy Derived Topography</i>	125
6.1 Introduction.....	125
6.2 Methods.....	128
6.3 Results and Discussion.....	132
6.4 Conclusion	133
<i>Chapter 7. Stable Jumping Dropwise Condensation under Large Subcooling Conditions....</i>	134
7.1 Introduction.....	134
7.2 Methods.....	136
7.2.1 Surface Fabrication	136
7.2.2 Surface Characterization	137
7.2.3 Condensation Chamber	138
7.2.4 Experimental Conditions	140
7.2.5 Video and Image Processing.....	142
7.3 Results and Discussion.....	142
7.4 Conclusion	148
7.5 Addendum	150
<i>Chapter 8. Characterizing the Chemical Bonding of a Fluoropolymer Coating on Soda-Lime Glass via XPS Depth Profiling of the Polymer-Glass Interface.....</i>	151
8.1 Introduction.....	151
8.1.1 ARC and Anti-Soiling Coatings	152
8.1.2 Soda-Lime Glass Surface De-alkalization	153
8.2 Methods.....	154
8.2.1 Sample Fabrication	154
8.2.2 X-ray Photoelectron Spectroscopy	155
8.3 Results and Discussion.....	157
8.3.1 Determination of interface location	157
8.3.2 Depth Profiling.....	158
8.3.3 C 1s Spectra Analysis	160
8.3.4 O 1s Spectra Analysis	162
8.3.5 F 1s and Na 1s Spectra Analysis.....	164
8.3.6 Fluorine-Sodium Bonding Chemistry	166
8.3.7 Si 2p Spectra Analysis	166
8.3.8 Polymer-Glass Bonding Interface.....	168
8.4 Conclusion	172
<i>Chapter 9. Conclusion</i>	173
<i>Bibliography</i>	177

List of Figures

Figure 1.1	Schematic of single film AR coating.....	2
Figure 1.2	Schematic of Inhomogeneous AR coatings compared to Regular Glass (a), with Layered surface (b) and Rough Surface (b) models.....	4
Figure 1.3	Schematic of wetting on smooth surface (a) and rough surfaces, with water drops in Wenzel state (b) and Cassie state (c).....	5
Figure 1.4	Schematic of wetting condensation on rough surfaces; initial nucleation of water drops and transition to Cassie or Wenzel state.....	6
Figure 1.5	Schematic of drop mobility on surfaces, comparing high CAH and low CAH.....	7
Figure 1.6	Schematic of a rough hydrophobic surface composed of fluoropolymer coating on glass substrate.....	9
Figure 1.7	Schematic of condensation on hydrophilic and hydrophobic surfaces.....	11
Figure 1.8	Radius of water drops growing on Hydrophobic and Hydrophilic surface.....	12
Figure 1.9	Schematic representation of Oswald Ripening with initial drop and film nucleation (a), initial condensation rates (b), and steady state condensation rate with Oswald Ripening effect observed (c).....	13
Figure 1.10	Schematic of nucleation, drop growth and slide-off on hybrid hydrophobic- hydrophilic surface.....	14
Figure. 2.1	Application of nano-textured fluoropolymer coating on the surface of a glass or metal substrate.....	17
Figure 2.2	Schematic of hybrid surface fabrication using selective chemical vapor deposition of FEP.....	18
Figure 2.3	Schematic of water condensation on hybrid surface.....	19

Figure 2.4	Photographs of hybrid surfaces taken at T0:00hr-T3:00hrs, of surfaces with hydrophilic features of 1mm, 2mm, and 3mm.....	22
Figure 2.5	Schematic of hybrid hydrophobic-hydrophilic surface produced by mechanically removing the polymer coating	23
Figure 2.6	Schematic of hybrid hydrophobic-hydrophilic surface produced by mechanically removing the polymer coating using an abrasive liquid and a 3D printed PLA mask as a guide.....	25
Figure 2.7	a) Computer engraved image of hybrid surface with hydrophilic channels, where hydrophobic surface is black and hydrophilic channels are white, .(b) plot of the time has taken for the first drop to slide-off from the hybrid channels, and (c) time is has taken for the entire row of drops to slide-off from the array of hybrid channels.....	26
Figure 2.8	Cleaning efficacy of uniform hydrophobic surface (red), hybrid surfaces with hydrophilic rings (gray), and hydrophilic channels (green).....	28
Figure 2.9	a) Schematic of the Pulsed Dust Apparatus (PDA); b) Schematic of the Cloud Deposition Apparatus (CDA).....	32
Figure 2.10	Percent Transmittance at 550nm as a function of dust application cycle for Bare glass soiled via CDA method for 5 sec. (red), 10 sec. (empty), 20 sec. (green) and 60 sec. (blue).....	33
Figure 2.11	Cross-sectional schematic of the condensation chamber including the thermoelectric cooler system, water collection scheme and humidification system (not to scale).....	34

Figure 2.12	Flowchart of PySurfaceArea algorithm, which calculates the amount of dust covering the surface area of a soiled glass sample, using optical microscopy data.....	37
Figure 2.13	Screenshot of PySurfaceArea user interface (UI).....	38
Figure 2.14	Schematic showing the methodology of the drop detection algorithm.....	41
Figure 2.15	Computer vision image of the analytical surface with pink mask highlighting the paths cleaned by water drops (a), and computer vision image of the calculation, with local maxima of image(b), with water drops still pinning to the surface in blue, local maxima of image with water drops already slid-off and the difference between the local maxima in green.....	42
Figure 2.16	Soil particle distribution around the world, with median dust particle size reported in literature = 16 μm (red dotted line).....	45
Figure 3.1	a) Schematic of the Pulsed Dust Apparatus (PDA); b) Schematic of the Cloud Deposition Apparatus (CDA).....	55
Figure 3.2	Schematic of no-touch cleaning system used to assess effectiveness of anti-soiling coatings.....	57
Figure 3.3	Initial optical transmittance (% τ) of test samples: Phobic, Philic, SH and Bare glass surfaces	58
Figure 3.4	AFM images of a) Bare glass (CA: 10°); b) Hydrophilic-1 (CA: 63°); c) Hydrophobic-1 (CA: 106°), and d) SH (CA: 149°).....	60
Figure 3.5	Transmittance (%) at 550nm and Surface Area Coverage by Dust (%) as a function of dust application cycles for solar glass with different coatings.....	63

Figure 3.6	Sequence of enhanced optical microscope images during evaporation of condensate drops on soiled Hydrophobic-1 surface on surface heated to 50°C	66
Figure 3.7	Cartoon illustrating the dust herding mechanism observed on the hydrophobic surface.....	67
Figure 3.8	Water drop (2.0 μ L) placed on glass substrates after soiling without condensate (CDA) on a,c) Bare glass, and b,d) hydrophobic coated glass.....	70
Figure 3.9	Optical microscope images after dust deposition onto dry surfaces a,c,d) Bare glass and b,d,f) hydrophobic coated glass with CA of 110°; after exposure to a condensing environment for 2 minutes.....	72
Figure 3.10	Soiling rate using CDA (cloud deposition apparatus) measured by a decrease in % τ at $\lambda=550\text{nm}$ as a function of dust exposure time (open-door time).	76
Figure 3.11	Initial Direct Light Percent Transmittance(% τ).....	77
Figure 3.12	Atomic Force Microscopy (AFM) Images of Test Surfaces	78
Figure 3.13	Microscopy Images of Condensed Water on Test Surfaces	79
Figure 3.14	Soiling plots of all individual samples: Percent Transmittance at 550 nm.....	81
Figure 3.15	Soiling plots of all individual samples: Percent Surface Area Covered by Dust... <td>82</td>	82
Figure 3.16	Large Area View of Hydrophobic Coated Glass After One Dew-Dust-Dry Cycle	83
Figure 3.17	Effect of Soiling Sequence: Dust Deposited on Condensate vs Condensation onto a Dust- coated Surface.....	84
Figure 3.18	No-Touch Cleaning after Dry Soiling	86

Figure 3.19	Photographs of Bare Glass and Hydrophobic Surfaces after soiling (before controlled cleaning) and after controlled cleaning.....	88
Figure 4.1	Schematic of hybrid hydrophobic–hydrophilic surface preparation.....	92
Figure 4.2	Top-down photographs (computer enhanced) of coated glass surfaces showing the geometric arrangement of hydrophilic circle features.....	93
Figure 4.3	Cross-sectional schematic of the condensation chamber.....	94
Figure 4.4	Timeline of condensation on hydrophobic(control) and hybrid hydrophobic–hydrophilic surface.....	97
Figure 4.5	Water collection rates as function of a) number of rows of 2.0 mm diameter hydrophilic ring features and b) diameter of two rows of hydrophilic features....	101
Figure 4.6	Computational analysis of water drop diameter and location of the drop initiating the roll-off event for a) Hydrophobic Control and b) Hybrid Surface with 3 rows of 2 mm diameter rings spaced 4 mm apart.....	103
Figure 5.1	Drawing of a hybrid surface showing a) top and b) cross-sectional views.....	110
Figure 5.2	Schematic of artificial soiling chamber.....	111
Figure 5.3	Schematic of artificial dew cleaning chamber.....	112
Figure 5.4	Properties of control and coated Phobic substrates subjected to 2000 h of accelerated indoor weathering: a) change in solar weighted direct transmittance; b) change in CA.....	115
Figure 5.5	Change in % τ at 550 nm as a function of soilant type and surface coating for Bare Glass, Phobic and Hybrid coatings after three dew-dust-bake soil deposition cycles.....	116

Figure 5.6	Optical microscopy images of Bare Glass, Phobic and Hybrid surfaces after 3 dew-dust-bake cycles and after simulated dew cleaning at 45° tilt angle.....	119
Figure 5.7	Restoration of original % τ as a function of simulated dew cleaning tilt angle on Bare Glass, hydrophobic (Phobic) and Hybrid coatings after three dew-deposit-bake soil deposition cycles utilizing all test dust types.....	120
Figure 5.8	Optical microscopy images of Bare Glass, soiled with a) Arizona Test Dust, b) Calcium Carbonate and c) Portland cement followed by condensation cleaning step at 45°, 85°, and 25° tilt angles respectively.....	120
Figure 5.9	Optical photographs of water condensing on a soiled Hybrid surface in the condensation chamber at 45° tilt angle and using Arizona Test Dust.....	122
Figure 6.1	Schematic of surface wetting on a rough surfaces and transition to the Wenzel and Cassie states on rough surface.....	126
Figure 6.2	Schematic of a water drop residing on rough surface in Cassie state. The water drop is supported on the peaks of the large scale features.....	127
Figure 6.3	Steps in the AFM image processing, leading to the calculation of Delaunay plot.....	129
Figure 6.4	Schematic of water drop residing on the peaks of large scale features, with meniscus distance approximated by a disc fitted to the large features peaks, and the distance between the features.....	130
Figure 6.5	Schematic illustrating the approximated water drop meniscus on a surface that is computer to have a high binary probability of getting wetted, and a low binary probability of getting wetted (transmission to Wenzel state).....	131

Figure 6.6	Binary wetting probability surface maps of hydrophilic and hydrophobic surfaces	132
Figure 7.1	The sketch of condensation chamber and chiller stage set-up.....	140
Figure 7.2	Still frames from experimental video, showing examples of jumping (a) and sweeping (b) events.....	144
Figure 7.3	Jumping dropwise condensation performance of Surface R ₁₇₀ , R ₁₇₉ and SM ₁₈₀ at different ΔT. a, Typical optical images of the condensation on R ₁₇₀ , R ₁₇₉ and SM ₁₈₀ at different ΔT after 15-20 min of condensation.....	144
Figure 7.4	(a) The average diameter of the condensed water droplets. (b) The percentage of coalescence events resulting in droplet jumping over 2 min for R ₁₇₀ , R ₁₇₉ and SM ₁₈₀ at different ΔT after 20 min of condensation.....	145
Figure 7.5	AFM image of surface nano-fibril, with areas of measurement of Young's modulus.....	147
Figure 8.1	Determination of location of the polymer glass interface via XPS depth profile analysis of oxygen to silicon atomic concentration ratio (O/Si).....	158
Figure 8.2	XPS depth profile of bare (uncoated) glass, etching 107 nm deep.....	159
Figure 8.3	XPS depth profile of FEP polymer-coated glass, etching 24 nm deep into the SiO ₂ glass.....	160
Figure 8.4	High resolution XPS spectra of carbon atom at depth intervals: surface (a), 2.6 nm of interface (b), 3.6 nm of interface (c), and 4.5 nm of interface (c).....	161
Figure 8.5	High-resolution XPS spectra of oxygen atom at depth intervals of: 2.6 nm of interface (a), 3.6 nm of interface (b), and 4.5 nm of interface (c).....	163

Figure 8.6	High resolution XPS spectra of fluorine atom at following depth intervals: the surface (a), 2.6 nm of interface (b), 3.6 nm of interface (c), and 4.5 nm of interface (c).....	165
Figure 8.7	High-resolution Si (2p) spectra obtained within the bulk glass layer and at various depth of the polymer-interface layer.....	167
Figure 8.8	XPS depth profile of F atomic ration deconvoluted to covalent fluorine bonding (F-C and F-Si) and ionic fluorine bonding (F-Na).....	168
Figure 8.9	Si2p peak location derived from the depth profile, eV, plotted as a function of SiO ₂ etch depth within the interface.....	168
Figure 8.10	Depth profile of O (1s) (dotted line), non-bridging oxygen (blue triangles), and bridging oxygen (red circles) spectra, taken within the polymer-glass interface..	170

List of Tables

Table 2.1	Effect Of Surface Chemistry And Structure On Condensation Water Collection.....	20
Table 3.1	Sample Wetting Properties	61
Table 3.2	Surface Roughness and Condensation Characteristics of Surfaces	61
Table 3.3	Optical Transmittance Changes after Soiling on Condensate and Subsequent Cleaning	64
Table 3.4	Surface Coverage Analysis after Soiling on Condensate	64
Table 3.5	Contact Angle Hysteresis and Sliding Angles of the Test Substrates	89
Table 4.1	Effect of Surface Chemistry and Structure on Condensation Water Collection...	99
Table 4.2	Water Drop Diameter at Roll-Off.....	102
Table 5.1	Soilant Type, Composition, Solubility, and Change in Optical Performance....	117
Table 7.1	Surface fabrication conditions.....	137
Table 7.2.	Experimental environmental parameters and the calculated subcooling temperature for superhydrophobic surfaces exhibiting drop jumping properties.....	150

List of Abbreviations

- AH : absolute humidity
CA : contact angle
CAH : contact angle hysteresis
DP : dew-point
OD : outer diameter
FEP: fluorinated ethylene propylene
 θ_{adv} : advancing contact angle
 θ_{rec} : receding contact angle
PV: photovoltaic
RH : relative humidity
RI: refractive index
 T_g : glass transition temperature
 T_m : melting temperature
 γ^{lv} = liquid/surface free energy
 γ^{sl} = solid/liquid interfacial free energy
 γ^{sv} = solid/surface free energy

List of Equations

Equation 1.1	Reflections on quarter-wavelength thick anti-reflective coating.....	3
Equation 1.2	Young's equation.....	5
Equation 1.3	Kelvin Effect.....	12
Equation 2.1	Cleaning Efficacy.....	27
Equation 3.1	Decrease in Soiling Rate.....	63
Equation 7.1	The intrinsic wettability of the surface dependency on nucleation	135
Equation 7.2	The relationship between nucleation radius r_c and ΔT	135
Equation 7.3	Relative Humidity from Dry/Wet Bulb.....	141
Equation 7.4	Drop Volume Calculation from Still Images of Dew Drops on Superhydrophobic Surface.....	142

List of Schemes

Scheme 2.1	Molecular structure of Fluorinated Ethylene Propylene (FEP).....	16
------------	--	----

Chapter 1. Introduction

1.1 Properties and Applications of Hydrophobic Coatings

1.1.1 Anti-Reflective Coatings

1.1.1.1 Introduction to Anti-Reflectivity

Reflections occur at sharp or abrupt interfaces with discontinuous refractive indices (RI) between two materials. RI refers to the speed of light in a material versus that in a vacuum or air, thus RI in a vacuum/air = 0. Materials with a low RI value will thus decrease the magnitude of discontinuities, effectively lowering the reflectance of light from the surface of such materials. Anti-reflective (AR) surfaces occur in nature via the production of composite materials with mixtures of different low-RI materials and/or air. AR surfaces containing air in the composite material form porous surfaces which contain a material with a relatively high RI. Thus, porosity lowers the average RI, rendering a material anti-reflective.

J.A. Dobrowolski [1], [2] has broadly classified surfaces as either homogeneous or inhomogeneous. Homogenous coatings contain a material with a single RI value or layers of materials with various distinct RIs. Inhomogeneous coatings contain only a single or many materials that produce an RI gradient, or porous materials in which air is a component.

The AR properties of homogenous coatings become apparent when normal-incidence reflection is minimized (Fig. 1.1), which can be achieved by limiting the thickness of the coating to $\lambda/4$, where λ is the wavelength of monochromatic light:

$$n = \sqrt{(n_s \times n_0)}$$

where n_s is the refractive index of the substrate.

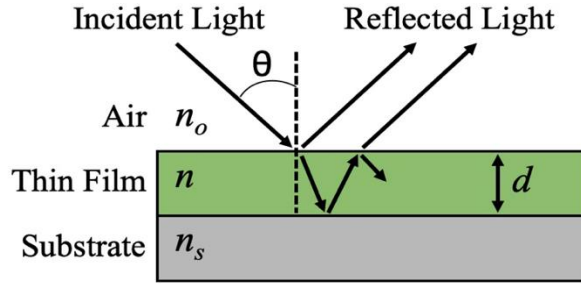


Fig 1.1 Schematic of a single-film AR coating

Another way to attain AR properties is the use of multilayer coatings in which materials with various RI's are incrementally stacked from an Air/Thin-Film interface to a Thin-Film/Substrate interface. In theory, homogenous AR coatings can be obtained using a single-layer dielectric film with a low refractive index (n) in which n_s is larger than n . The thin film creates a double interface at which two reflected waves can be canceled by destructive interference. In a perfect scenario, the combination of the magnitude of transmitted and refracted waves will always equal the magnitude of the incident wave.

The vector method [3] can be utilized to model a monochromatic wave through a homogenous film utilizing a characteristic matrix to approximate anti-reflection the of an ideal AR film, where B and C are components of electric and magnetic fields, θ is the angle of incident light, d is the thickness of the homogenous dielectric coating, and $\partial = (2\pi n d \cos \theta)/\lambda$ is the film phase thickness:

$$\begin{bmatrix} B \\ C \end{bmatrix} \begin{bmatrix} \cos \partial & \frac{i}{n} \sin \partial \\ i n \sin \partial & \cos \partial \end{bmatrix} = \begin{bmatrix} 1 \\ n_s \end{bmatrix}$$

When the sum of the vectors is 0, the refractive index and film thickness will produce AR properties. The reflectance at an interface is defined as:

$$R = |(n_0 - Y)/(n_0 + Y)|^2$$

where n_0 is the refractive index of air, and $Y = C/B$. If the incident wave is monochromatic and of the same amplitude, the AR properties will be evident when the interferences from the Air/Thin Film and Thin-Film/Substrate interfaces effectively cancel each other out.

Two additional components are required for ideal AR properties: the thickness of the dielectric thin film must be an odd number of quarter wavelengths, and the reflected wavelengths must be 180° out-of-phase. With normal incident light, the characteristic matrix would result in reflectively according to the equation:

$$R = \left| \frac{n_0 n_s - n^2}{n_0 n_s + n^2} \right| \text{ and } Y = \frac{n^2}{n_s}$$

For coatings with multilayered dielectric thin-film coatings (n_1 and n_2), each being a quarter-wavelength thick, the reflectance would thus be (**Equation 1.1**):

$$R = \left| \frac{n_2^2 n_0 - n_s n_1^2}{n_2^2 n_0 + n_s n_1^2} \right|$$

Taking the polarization of light into account, RI (n) will be replaced by (η) as per Fresnel matrix calculations, where η_s and η_p are the polarizations of light:

$$\eta_s = Y \cos \theta \text{ and } \eta_p = Y (\cos \theta)^{-1}$$

1.1.1.2 Anti-Reflective Coatings

In practice, the fabrication of single-layer AR coatings is limited by the availability of materials with low RI values. The RI of common commercial glass is 1.5, which means that the thin-film coatings must have an RI value of ≈ 1.25 . Although such materials do exist, e.g., MgF_2 , CaF_2 , and

SiO_2 ($n = 1.39, 1.44, 1.46$, respectively), they are relatively rare, thus other AR coating fabrication methods are required to obtain functional AR coatings.

Inhomogeneous coatings have been developed to address the lack of low-RI materials (Fig. 1.2 b,c). Layered surface coatings produce a refractive gradient by incrementally placing layers of thin-film coatings with stepwise RI values (Fig. 1.2 b). Single-layer inhomogeneous coatings can also be achieved by producing a coating with a single layer in which the RI varies throughout the thickness, from an RI similar to air to an RI similar to that of the substrate. One can also utilize single materials with an RI lower than n_s along with air to produce a refractive gradient by varying the fraction of air in the coating from 0 at the Air/Coating interface to 1 at the Coating/Substrate interface (Fig. 1.2 b). Thus, a refractive gradient is created by physically manipulating the material to include air as a coating component.

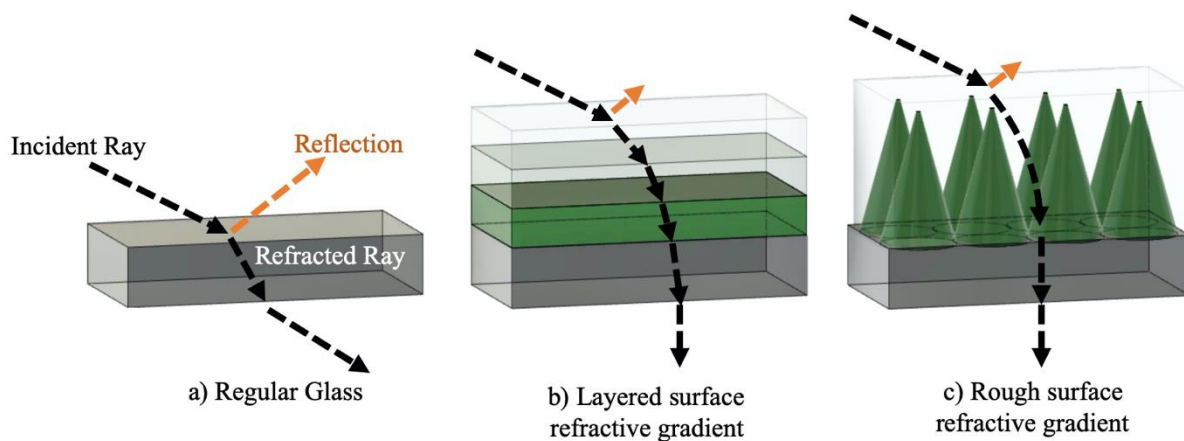


Fig 1.2 Schematic of inhomogeneous AR coatings compared with regular glass (a), with layered surface (b) and rough surface (b) models.

1.1.2 Anti-soiling and Self-Cleaning Coatings

1.1.2.1 Introduction to Surface Wetting

The wettability of a surface can be characterized as either hydrophobic or hydrophilic.

Hydrophobic surfaces repel water, while hydrophilic surfaces are wet by water. A surface's hydrophobicity and hydrophilicity can be controlled via manipulating its surface roughness (morphology) and surface chemistry.

The interaction with between a surface and a liquid and air can be described by Young's equation (**Equation 1.2**):

$$\gamma^{sv} = \gamma^{sl} + \gamma^{lv} \cos\theta$$

where γ^{sl} is the solid/liquid interfacial free energy, γ^{sv} is the solid/surface free energy, γ^{lv} is the liquid/surface free energy, and $\cos\theta$ is the contact angle of a liquid droplet (Fig. 1.3 a).

Wetting on a rough surface can proceed in 2 states: Wenzel and Cassie (Fig. 1.3 b,c). In the Wenzel state, a liquid wets into the grooves of the structure, potentially pinning the liquid drop on the surface. In the Cassie state, the liquid is suspended on the tips of asperities, which lowers the contact area between liquid and surface, as well as the length of the contact line (sum of lengths of all contact lines), which allows the drop to more easily move over the surface.

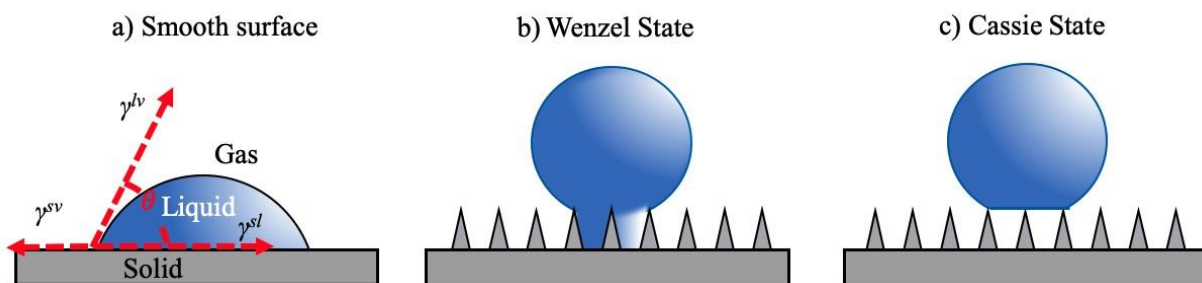


Fig 1.3 Schematic of wetting on a smooth surface (a) and rough surfaces, with water drops in the Wenzel state (b) and Cassie state (c).

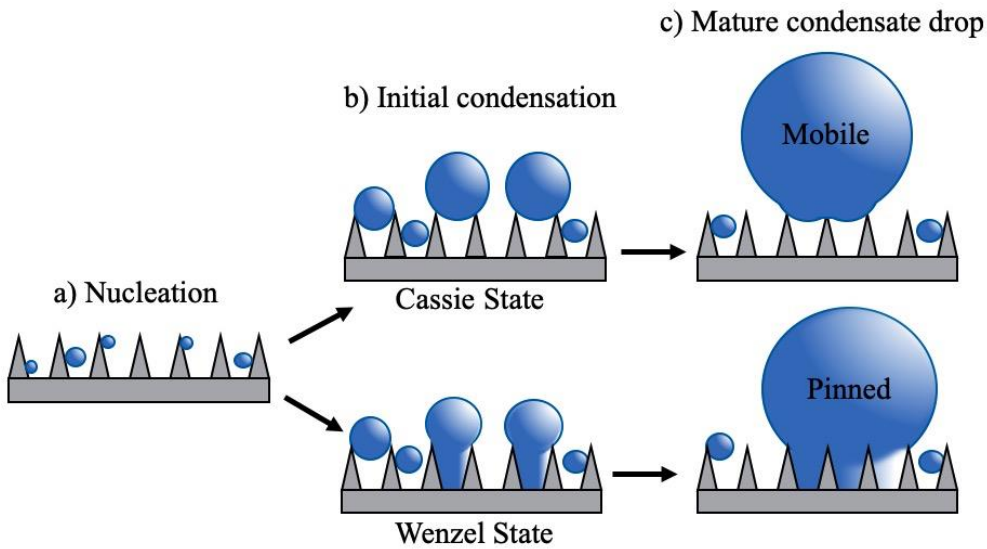


Fig 1.4 Schematic of wetting condensation on rough surfaces; initial nucleation of water drops (a), transition to Cassie or Wenzel state (b), which results in a mobile or pinned drop (c).

When water condenses on rough surfaces, water drops form at random locations on features of the rough surface during initial nucleation (Fig. 1.4 a). As the water drops increase in size, they can transition to the Cassie state due to being pushed out of the valleys on the rough surface because the surface tension of water exerts a force large enough to push the water drop up. They can also transition to the Wenzel state by wetting the underlying surface and become pinned (Fig. 1.4 b,c). The drop can transition to the Wenzel state due to the inherent hydrophilicity of the underlying exposed substrate. Drops in the Wenzel state will remain pinned, requiring a greater force to break the liquid-surface interactions.

The mobility of water droplets on surfaces can be characterized by measuring the contact angle hysteresis (CAH), which is the measurement of the difference between the advancing (θ_a) and receding (θ_r) angles of a water drop. On a level surface, assuming uniform surface chemistry, the CAH will be 0, and both the advancing and receding contact angles will be the same. If the surface is tilted at an angle (θ_t), the difference between the forces pinning the drop to the surface and the

force of gravity acting on the mass of the drop will change the drop's shape. The forces pinning the drop to the surface will therefore increase the receding contact angle in an effort to prevent the drop from moving. The force of gravity acting on the mass of the drop will decrease the advancing angle as the mass of the drop will overhang the interface at the triple contact line (TLC). The shape of the drop depends on: 1) the size of the drop, given the surface tension energy of the particular liquid and the drop's surface area; 2) the ratio of the magnitude of pinning force to the gravitational force acting on the drop. The magnitude of the pinning force depends on the TLC of the drop and the wettability of the surface, which is defined by its surface roughness and chemistry. On hydrophilic surfaces, the force of gravity acting on the mass of the liquid drop is therefore balanced by the force pinning the drop to the substrate surface (Fig. 1.5 a). As the hydrophobicity of the surface increases, the magnitude of the forces responsible for pinning the drop to the surface decrease, which decreases the difference between the advancing and receding contact angles. Thus, the contact angle hysteresis is decreased (Fig. 1.5 b), making CAH measurements on a goniometer a valuable analytical tool to evaluate the mobility of a liquid drop on surfaces.

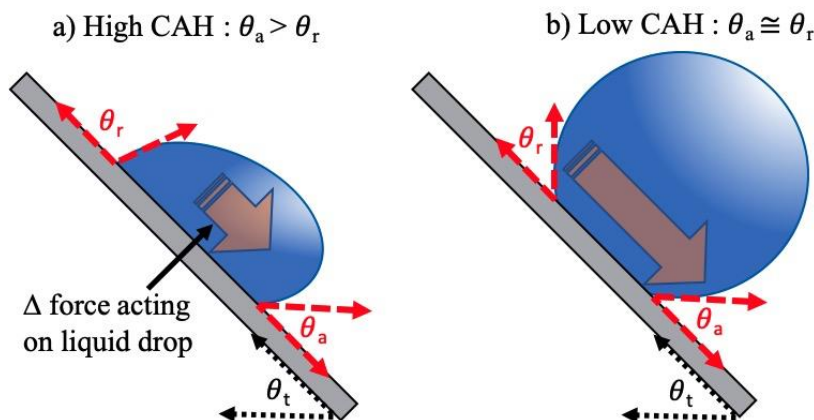


Fig 1.5 Schematic of drop mobility on surfaces, comparing high CAH and low CAH.

1.1.2.2 Anti-soiling and Self-cleaning Principles

Dust deposition on the surface of solar cover glass can cause significant loss of electrical output from photovoltaic (PV) panels, and anti-soiling and self-cleaning coatings have been developed to reduce the rate of dust deposition and improve the cleaning effectiveness of glass. The two primary types of transparent, anti-soiling and self-cleaning surface coatings that have been reported in the literature are hydrophobic [4]–[11] and hydrophilic [11]–[14] coatings.

Dust particles can react in the presence of liquid water by several mechanisms, including adhesion of dust particles through capillary aging [15]–[17] and chemical bonding of the particles to the glass surface, also known as cementation [12], [18], [19]. Heat from solar insolation evaporates dew and accelerates the formation of chemical bonds, and a greater mechanical force is required to remove dust when dew is present [20]. The presence of liquid water on PV cover glass is observed in form of dew in many regions of the world, including the Middle East and North Africa (MENA) [15], [21]. It is caused by the radiative cooling of the PV cover glass surface below the dew point at night.

On hydrophilic surfaces, water condenses in a film [22] and wets the glass. The water film can then carry away dust particles as the water layer flows downward to the bottom of the glass. Applying a hydrophilic coating in an outdoor environment poses an issue because the surface will become contaminated with proteins, surfactants, and salts, which render the surface less hydrophilic. This transforms the condensation on the surface from a film to drops, diminishing the ability of the water to carry dust particles because the dust particles get trapped in isolated water puddles. To overcome contamination issues, TiO₂ coatings were developed [16], [23], [24] that can photochemically oxidize absorbed organic compounds, allowing the surface to remain hydrophilic for longer periods of time [25], [26]. The application of such coatings in self-cleaning

glass systems is challenging because TiO_2 coatings have a high index of refraction and absorption of light below ~ 400 nm. This leads to increased reflections compared with bare glass and lower light absorption in the high-energy region of the electromagnetic spectrum, thus diminishing the performance of the PV panel that the glass covers. TiO_2 coatings are only able to photooxidize organic contaminants [27], and not inorganic soil particles (e.g. salt, silicates, oxides, etc.) which are the major contributor to the soiling of PV glass, rendering TiO_2 coatings even less favorable.

Hydrophobic coatings are composed of a low-surface-energy material that is chemically inert, which lowers the probability of chemical reactions occurring between soil and the surface of the glass. This lowers the adhesion of dust to the surface and allows the surface to remain relatively dust-free, rendering the surface anti-soiling. Increasing the surface roughness further reduces the contact between the soil and surface by lowering the contact area, which improves the anti-soiling effect (Fig. 1.6). A higher surface energy limits the water-surface interactions resulting from the presence of water droplets on the surface, allowing the surface to retain high contact angles (CAs), which provides a medium for other anti-soiling mechanisms (as described in Chapter 3).

If a coating structure is relatively defect-free and has a rough morphology to support water droplets in the Cassie-Baxter state, the CAH will be low (Fig. 1.5), which will allow the droplets

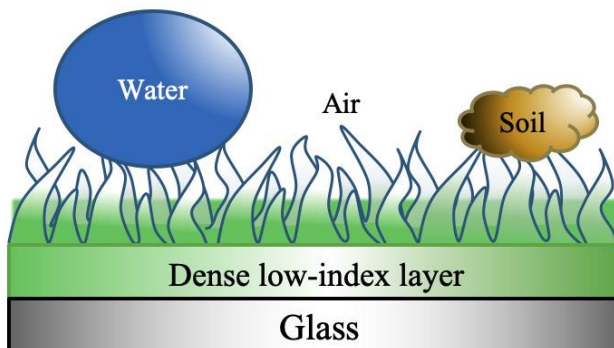


Fig 1.6 Schematic of a rough hydrophobic surface composed of a fluoropolymer coating on glass substrate.

to slide off the surface at low tilt angles [28]. As the droplets slide off, they remove weakly-adhered dust from the surface via a self-cleaning mechanism.

Although some anti-soiling coatings have been reported, e.g., Enki CleanARC® [11], [29], [30], DSM's anti-soiling coating [31], [32], and 3M's anti-soiling liquid coating [33], their mechanisms of action have not been well characterized. Several challenges in the further development of anti-soiling and self-cleaning coatings include their reliability and cost. A fluoropolymer coating was thus chosen for this research project due to its chemical inertness, high inherent contact angle, and a history of reliability testing of fluoropolymers. Fluorinated ethylene propylene (FEP) is a fluoropolymer copolymer of hexafluoropropylene and tetrafluoroethylene with a contact angle of 108°[34], CAH of 13.4° [35], and γ^s of 17.9 mJ/m², making it ideal for fabricating anti-soiling and self-cleaning surface coatings.

1.1.3 Hybrid Hydrophobic-Hydrophilic Surfaces

Biomimetic surfaces such as hybrid hydrophobic-hydrophilic surfaces have been investigated for use in water collection. An example of a biomimetic-inspired hybrid coating is the Namib Desert beetle, which utilizes a hybrid hydrophobic-hydrophilic surface (a hydrophobic coating with hydrophilic spots) on the back of its body to harvest water for consumption [36]. The water preferentially condenses on the hydrophilic spots with drops nucleating and growing to a critical mass required for drops to break the TLC and slide down to the hydrophobic portion of the coating, and into the beetles mouth [36]. The Namib Desert beetle was used as the model for a surface composed of a hydrophobic fluoropolymer coating containing hydrophilic spots with various shapes, sizes, and geometric configurations.

Both hydrophilic and hydrophobic surfaces have positive and negative attributes (Fig. 1.7). One benefit of a hydrophobic surface coating is that it increases the water drop nucleation rate and thus the initial condensation rate. A higher number of water drop nucleation sites on hydrophilic spots will allow more water to condense on the surface compared with fewer potential nucleation sites on a hydrophobic surface [37]. The downside of hydrophilic coatings is that the water condenses in a film-wise manner, with the water film spreads on the surface of the substrate.

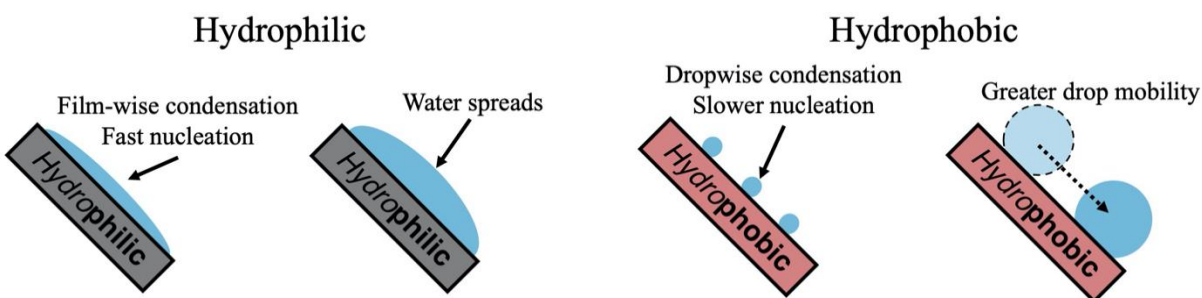


Fig 1.7 Schematic illustration of condensation on hydrophilic and hydrophobic surfaces.

The benefit of hydrophobic coatings arises from the lower surface energy compared with hydrophilic surfaces, causing them to exhibit lower chemical and physical reactivity. This, in turn, increases the drop mobility by lowering the length of TLC contact lines, which is evident by a decrease in CAH ($\theta_{adv} - \theta_{rec}$). The roughness of the coating can also decrease the contact area between contaminant particulates, thus decreasing the physical and chemical bonding between the surface and the particles. The downside of hydrophobic surfaces is that the initial nucleation rate is very low due to the poor interaction between the water molecules and the surface, which lowers the probability of drop nucleation.

Due to the fast, initial nucleation rate of the water droplets on hydrophilic regions, the water drops will grow slightly faster than those on hydrophobic surfaces, until the thermally insulating effects of the water layer decreases the condensation rate. Thereafter, the faster condensation rate of drops on hydrophilic regions could be due to the Kelvin effect and Ostwald ripening.

Due to the Kelvin effect, the radius of larger drops would increase faster than that of smaller drops, as approximated by the Kelvin equation (Equation 1.3), where P is the vapor pressure over a curved surface, P_0 is the vapor pressure over a flat surface, V_m is the molar volume of a liquid, R is the universal gas constant, T is the absolute temperature, γ is the surface tension, and r is the radius of a water drop [38] (Fig. 1.8).

(Equation 1.3) Kelvin Effect

$$\ln\left(\frac{P}{P_0}\right) = \frac{V_m}{RT} \frac{2\gamma}{r}$$

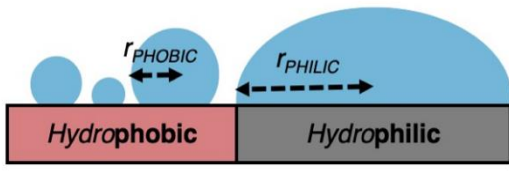


Fig 1.8 Growth of the radius of a water droplet on hydrophobic and hydrophilic surfaces.

The steady-state growth of a larger droplet on the hydrophilic part of a hybrid surface, but similar to the hydrophobic part of a hybrid surface, can be sustained by Ostwald ripening. The

vapor near the large water drop (with a larger condensation rate) is consumed, resulting in more rapid growth of larger water droplets and a smaller growth for the vapor-deprived smaller droplets with a low rate of condensation (Fig. 1.9).

The resulting effect of the rapid growth of water droplets in local areas can be improved by increasing the tilt angle of the surface, which would allow gravity to act on the mass of the water drops. This would decrease the critical mass necessary in order for the water droplet to slide off the surface. The application mechanism of this surface in water harnessing and self-cleaning surfaces is outlined in Chapters 2-5. The water layer would initially nucleate on the hydrophilic

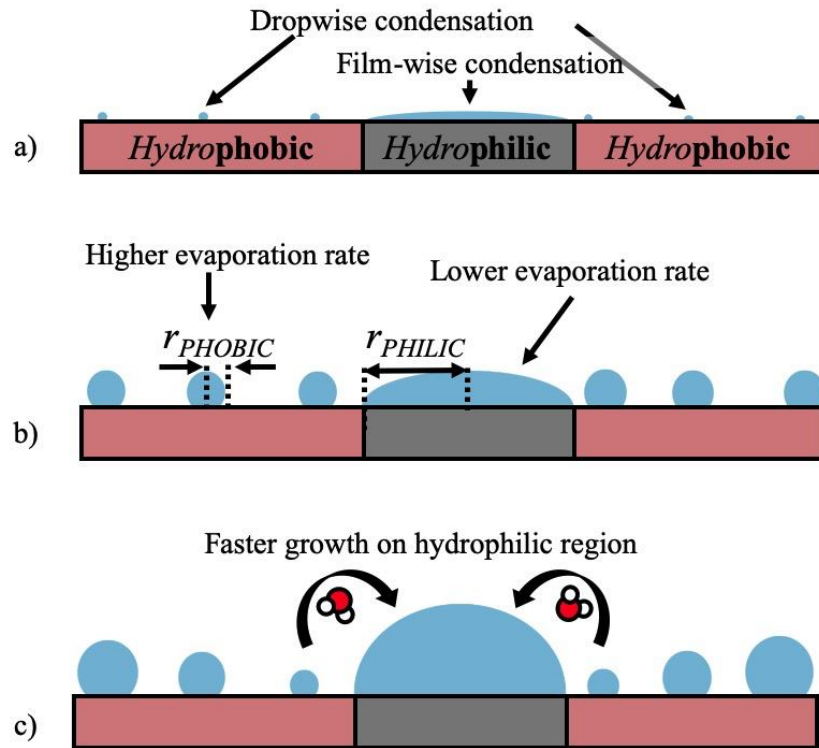


Fig 1.9 Schematic representation of Ostwald Ripening with initial drop and film nucleation (a), initial condensation rates (b), and steady-state condensation rate with Ostwald ripening (c).

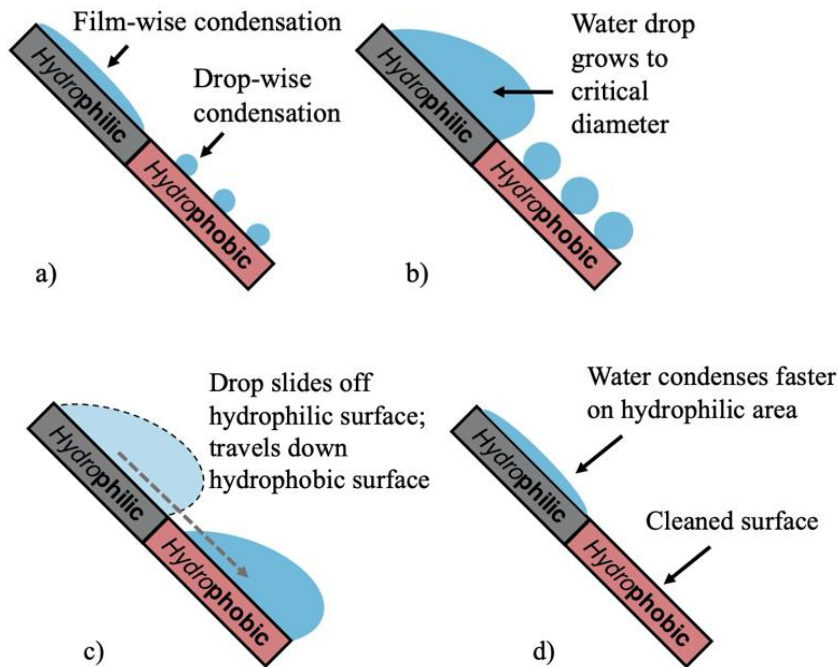


Fig 1.10 Schematic of nucleation, drop growth and slide-off on a hybrid hydrophobic-hydrophilic surface.

part of the surface, and the water droplets would initially nucleate on the hydrophobic part of the surface (Fig. 1.10. a). The water drop will grow larger on the hydrophilic part of the glass (Fig. 1.10. b), and it will slide off (Fig. 1.10. c) and consume all water drops below it on the hydrophobic surface, thus cleaning the surface.

The hydrophobic region of the hybrid surface was prepared via the platen lamination method (as described in 1.2.1), in which the hydrophilic part of the hybrid surface was prepared in 4 distinct steps: selective chemical vapor deposition, mechanical removal coating via automated diamond drill-bit, the application of anatase TiO₂ particles through a mask, and the mechanical removal of coatings via abrasive liquids through a mask.

1.2 Objectives of Thesis and Scope of Work

The objective of this thesis is to advance the fabrication methods of hydrophobic fluoropolymer nano-coatings on glass surfaces, develop methods for accelerated testing of polymer coatings for PV anti-reflective and anti-soiling coating applications, and determine the bonding mechanism of the polymer coating to PV-grade soda-lime glass substrates.

During the course of this work, multiple laboratory soiling and cleaning apparatuses were constructed and used to characterize anti-soiling and self-cleaning properties, with novel anti-soiling, “dust herding” mechanisms discovered in the process. Furthermore, hybrid hydrophobic-hydrophilic nano-coatings were developed and tested, with a novel application of dew harnessing for self-cleaning. To assist with analytical work and expedite data acquisition, algorithmic methods of microscopy imagery and video footage were developed and optimized.

Lastly, the polymer-substrate interface was characterized via X-ray photoelectron spectroscopic depth profiling, and the bonding mechanism of the polymer coating was identified.

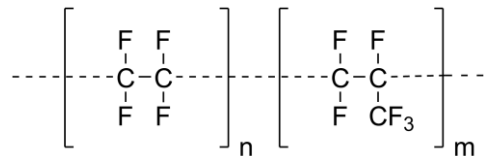
Chapter 2. Design and Development of Fluoropolymer Coatings, Accelerated Testing Apparatus and Analytical Methods

2.1 Fabrication and Characterization of Fluoropolymer Hydrophobic Coatings

2.1.1 Textured Nano-coating Fabrication via Lamination-Peeling Method

The fabrication of fluoropolymer coatings on metal and glass substrates was conducted via a platen lamination process. [39] First, the substrate was prepared cutting it into a particular shape, and then cleaning it with Alconox® (sodium linear alkyl aryl sulfonate, alcohol sulfate, phosphates, carbonates perfluoropolymer) in order to remove organic and inorganic contaminants from the substrate surface (Fig. 2.1 a).

Scheme 2.1. Fluorinated ethylene propylene (FEP)



Fluorinated ethylene propylene (FEP) (Scheme 1), has been used to create nano-textured coatings on substrates. FEP has a T_m of 260 °C and T_g of 80 °C [40]. A sheet of bulk fluoropolymer (Teflon® FEP film purchased from American Durafilm) was placed on top of the glass or aluminum substrate and then placed in a lamination press and pre-heated to 304 °C. The platens were closed to ensure contact with and heat the polymer layer, but without an applied force ≈ 0 kPa. (Fig. 2.1 b) The polymer was heated above its melting point to increase its contact area with the substrate, as the melt wet the substrate surface. Once the polymer was melted, the platens were closed by applying a pressure of 10 kPa. The substrate, along with the attached bulk

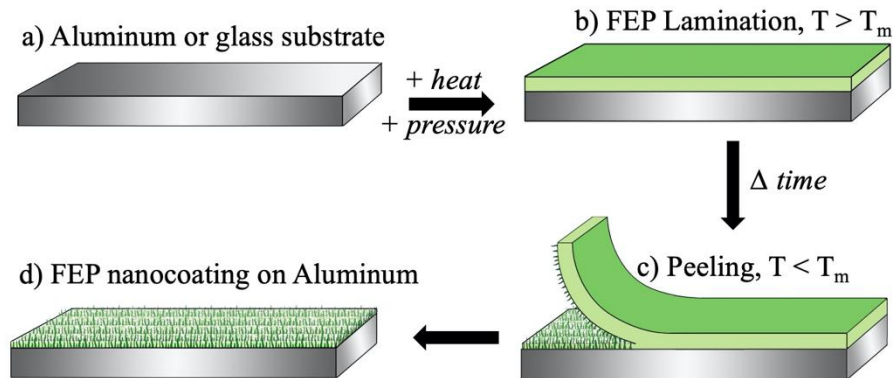


Fig. 2.1 Application of nano-textured fluoropolymer coating on the surface of a glass or metal substrate.

polymer, was annealed at 175 °C for 20 minutes. Afterward, the bulk polymer was peeled away (Fig. 2.1 c) to reveal the nano-textured fluoropolymer layer on the substrate surface (Fig. 2.1 d). The fluoropolymer peeled at the interface of the adhesively bonded and cohesively bonded polymer, and cohesive failure occurred between the T_g and T_m of the polymer. The polymer was thereafter allowed to cool to 175 °C, which was between the polymer's T_g and T_m , and then peeled by hand at room temperature. As the bulk polymer was peeled from the substrate surface, the cohesive forces in the polymer stretched it at the peeling interface of the adhesively and cohesively bonded polymer. The stretching force produced fluoropolymer nanofibrils between the two sides of the interface. As room-temperature air passed between the nano-fibrils, they were cooled below the T_g of the polymer, causing the nano-fibrils to break, creating a long, fibrous texture at the substrate surface.

2.1.2 Hybrid Hydrophobic-Hydrophilic Surface Fabrication

2.1.2.1 Selective Chemical Vapor Deposition of Polymer Using K_2CO_3 Mask

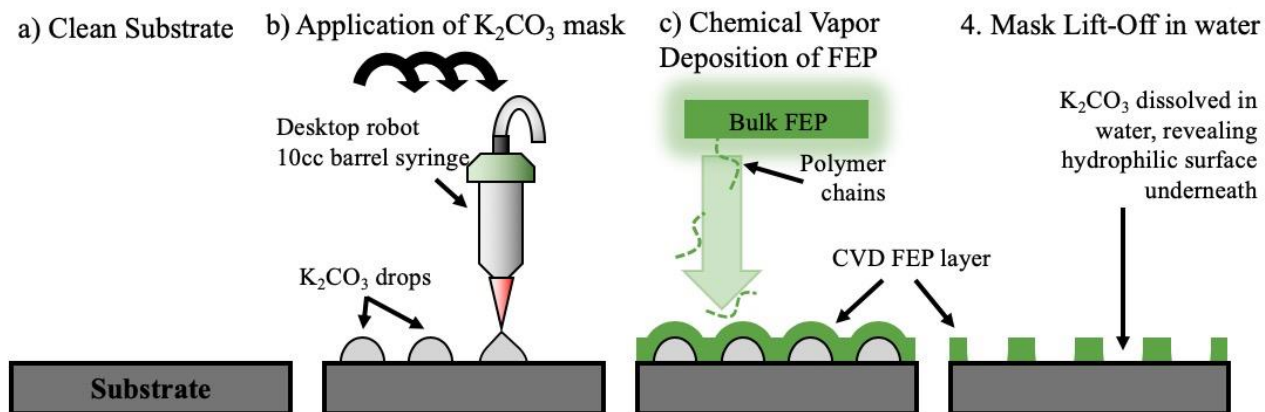


Fig. 2.2 Schematic of hybrid surface fabrication using selective chemical vapor deposition of FEP, where the clean substrate (a) was used for the automated application of a K_2CO_3 mask in the form of drops (b), followed by chemical vapor deposition of FEP (c), and dissolution of the mask, revealing the hydrophilic surface underneath.

A hybrid surface was prepared for the evaluation of observation and controlled condensation on hybrid surfaces. The selective chemical deposition of the polymer was accomplished by applying a mask consisting of drops of potassium carbonate (K_2CO_3) solution deposited on the glass substrates via an automated drop dispenser, whereby the FEP coating was applied on top of the mask. The mask was therefore dissolved in water, revealing the underlying hydrophilic substrate, surrounded by the hydrophilic polymer coating (Fig 2.2).

A Janome® JR 2200N mini desktop robot (Janome Sewing Machine Co., Ltd) was equipped with a pneumatically-activated liquid dispenser. The dispenser was composed of a Fishnar® 10cc (cm^3) barrel syringe with a 27 ga (0.008" diameter) tapered dispense tips (Nordson®). The desktop robot triggered an air pump at pre-programmed and controlled intervals to dispense liquid onto the substrate surface. The volume of the dispensed liquid was controlled by an EFD® Performus V pressure controller, with air delivered by a generic 1100 kPa air pump. The desktop robot was

controlled using JR C-Points Version 9.03 (Janome Sewing Machine Co., Ltd) by executing user-programmed instructions.

A 10cc barrel syringe was filled with a 0.81 M (saturated) solution of K_2CO_3 and attached to the Janome® mini desk robot. Glass substrates (Pilkington® OptiWhite) were cut into 3" x 3" coupons. Substrates were cleaned with an Alconox solution and placed on the printing bed (Fig. 2.2 a) of the mini desk robot. The bed was then leveled using a Precision Bullseye Level (Rieker Inc.) An instruction set was then programmed into the JR C-Points software. The diameter of the dispensed drops of the K_2CO_3 solution was then fixed by modulating the pressure and time using the EFD® Performus V pressure controller. The diameter of the liquid drop was calculated by an optical micrometer (Keyence). The mini desk robot then proceeded to dispense drops of saturated K_2CO_3 solution with precise diameters and in precise locations on the surface of the substrate (Fig. 2.2 b).

The K_2CO_3 solution was then dehydrated at 60 °C, and a mask of crystalline K_2CO_3 remained with a diameter controlled by the TLC of the droplets. Afterward, the chemical vapor deposition

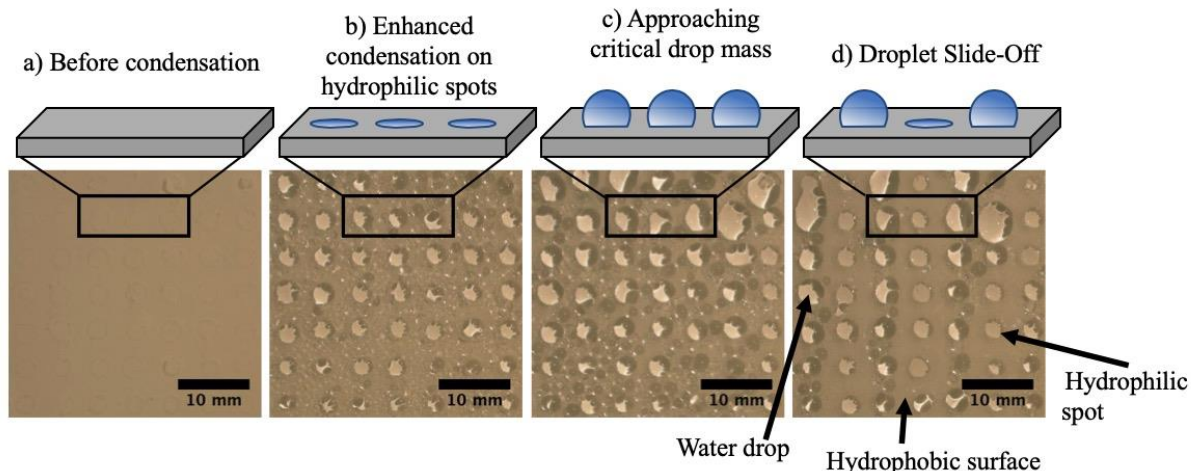


Fig. 2.3 Schematic illustration of water condensation on the hybrid surface; surface before condensation (a), after nucleation/initial condensation (b), approaching critical mass drop of water droplets on hydrophilic spots (c), and after the first set of water drops slide-off (d).

of the FEP polymer was conducted by placing the substrate in an oven at 275 °C with the mask facing downward. Bulk FEP polymer was then placed 3 cm under the substrate. At temperatures above the T_m of the polymer and in the presence of oxygen, the FEP at the surface of the bulk sample will oxidize, and polymer chains will fracture. The air currents will thus carry the fractured FEP polymer chains upward and re-deposit them on the substrate-mask complex above (Fig. 2.2 c). CVD proceeded for 1 hour.

After chemical deposition, samples were placed in DI water for 2-5 hours to allow the K_2CO_3 mask to dissolve, removing the layer of FEP that was deposited on top, and thus revealing the hydrophilic substrate underneath the FEP coating. This created a hybrid surface of hydrophilic features with precise diameters located on a hydrophobic surface (Fig. 2.2 d).

Six types of surfaces were used: Bare Glass (negative control), Hydrophobic (positive control), and three (3) hydrophobic-hydrophilic hybrid surfaces as described in Table 2.1. Water contact angle measurements were obtained on a ráme-hart 250-F1 goniometer with a 5 μ l drop of water. Condensation experiments were conducted by reducing the temperature of the Al cooling plate to 10°C. The temperature of the air inside the chamber was 25.6°C (\pm 0.1°C), and the relative humidity inside the chamber was 85.2% (\pm 0.9%).

Table 2.1
Effect Of Surface Chemistry And Structure On Condensation Water Collection

Hydrophilic Feature Diameter	Water Contact Angle [°]	Number of Hydrophilic spots [n]	Hydrophilic Spot Dimeter [mm]	Distance Between Hydrophilic Spots [mm]	Area Ratio Hydrophobic-Hydrophilic [%]	Water Collection Rate [mg/mm ² min] ·10 ⁻⁶
0.9 mm	104.8 \pm 0.2	256	0.9 \pm 0.4	1.7 \pm 0.1	6.2	2.6
1.9 mm	103.5 \pm 0.2	121	1.9 \pm 0.2	1.9 \pm 0.2	12.9	1.8
2.8 mm	97.3 \pm 0.3	81	2.8 \pm 1.2	2.1 \pm 0.9	17.3	1.2
Hydrophobic	103.8 \pm 0.2	NA	NA	NA	0	1.7
Bare Glass	19.1 \pm 0.2	NA	NA	NA	100	0.68

The controlled condensation of water on the surface was experimentally tested utilizing a simulated dew condensation chamber (the construction of which is discussed in Chapter 2, Section 2). Images of the surface were recorded with a Nikon Coolpix P2 camera at 1 minute time increments. The size of hydrophilic features was determined from optical images. The diameter of the condensate water droplets at roll off were calculated with a python script designed to control the experiment. The condensation proceeded with a RH of 90%, an ambient temperature of \approx 25 °C, and a surface temperature of 10 °C, with a DP of 23.2 °C. Controlled condensation was observed on the test surfaces, with visible condensation on hydrophilic features preceding the condensation on hydrophobic surfaces (Fig. 2.3 b). Since the drop growth on the hydrophilic channels was observed to occur faster than the hydrophobic part of the surface, the water drops on the hydrophilic features grew faster (Fig. 2.3 c) and slid off the surface faster (Fig. 2.3 d). As a water drop slid down from its point of origin, it effectively captured and removed all water drops below it, effectively freeing the surface from a thick insulating liquid layer and restarting the drop growth, which then proceeded at a much faster rate than condensation on the hydrophobic surface. The effective result of such a surface allowed water drops to be grown selectively on the hydrophilic regions.

Results from the condensation experiments, summarized in Table 1, demonstrate an inverse correlation between water collection rates and hydrophilic spot diameter. The surface with the smallest diameter hydrophilic spots (0.9 mm) exhibited the highest water collection efficiency, which was 220% greater than the surface with 2.8 ± 1.2 mm diameter hydrophilic spots and over 380% greater than the bare glass control. This hybrid surface also shows enhanced condensation efficiency compared to a uniform hydrophobic surface with no hydrophilic regions. The increased water collection rate is attributed to the smaller hydrophobic-hydrophilic contact line, which

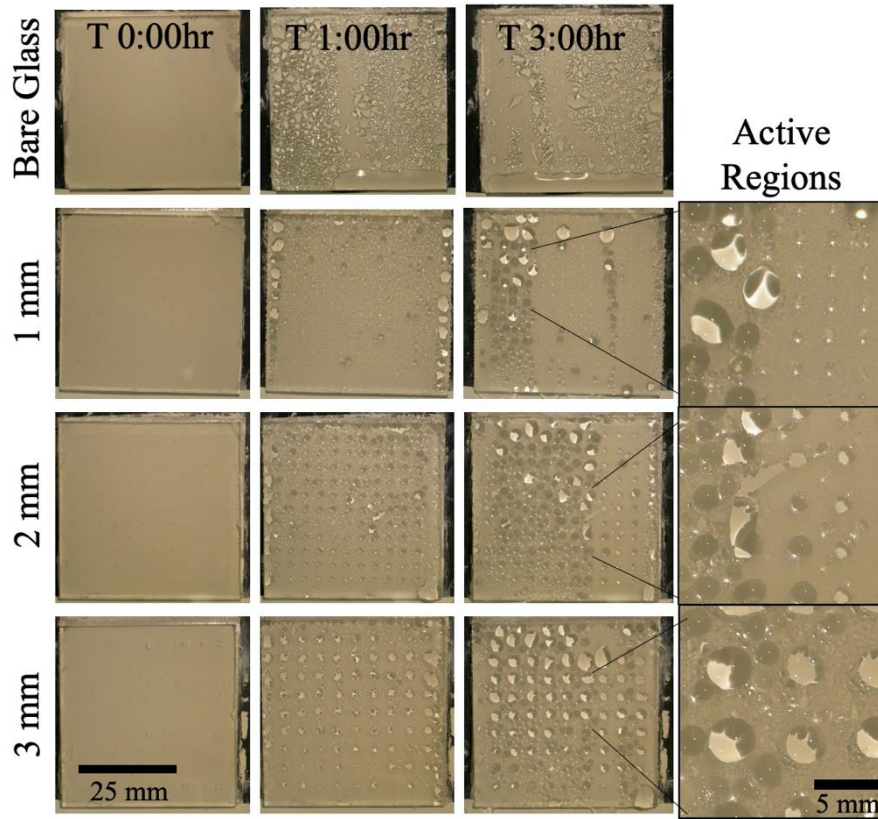


Fig. 2.4 Photographs of hybrid surfaces taken at 0:00 hr. – 3:00 hr., of surfaces with hydrophilic features of 1 mm, 2 mm, and 3 mm, to provide a visual comparison with the drop diameters of condensed water on the surface as a function of hydrophilic feature size.

allows water drops of smaller mass to be removed by gravity from the surface. The hydrophilic surface exhibits the lowest water collection rate as expected based on prior work [8] because water is strongly bound to the entire surface area. The higher water roll-off rate, which we observed on the hybrid surface under simulated dew conditions, is expected to result in enhanced self-cleaning properties under soiling conditions. Results from laboratory soiling experiments using Arizona test dust, will be reported in the final paper and presented at the conference.

Condensation trials were conducted to determine the water drop diameter of the condensate. Experiments showed that the drop diameter was successfully controlled by modifying the diameter of the K_2CO_3 droplets and thus the diameter of the mask. and the results confirmed the condensate drop diameter on the mask diameter (Fig. 2.4).

2.1.2.2 Mechanical Removal of Coating via Automated Diamond-bit Drilling

In order to produce hydrophilic features on hydrophobic surfaces that are more precise and geometrically reproducible, a method to mechanically remove the polymer coating was introduced.

Glass substrates (Pilkington® OptiWhite) were cut to 3" x 3" coupons and washed using Alconox® solution. An FEP coating was laminated onto the substrate surface as described in Chapter 1.2.1 (Fig. 2.5 a). An electric drill was mounted on the Janome® JR 2200N mini desktop robot (Janome Sewing Machine Co., Ltd). A set of diamond drill bits (Rio Grande®) with outer diameters (OD) of 1.0, 2.0, and 3.0 mm were used. The drill bits were aligned with the $x = 0$, $y = 0$,

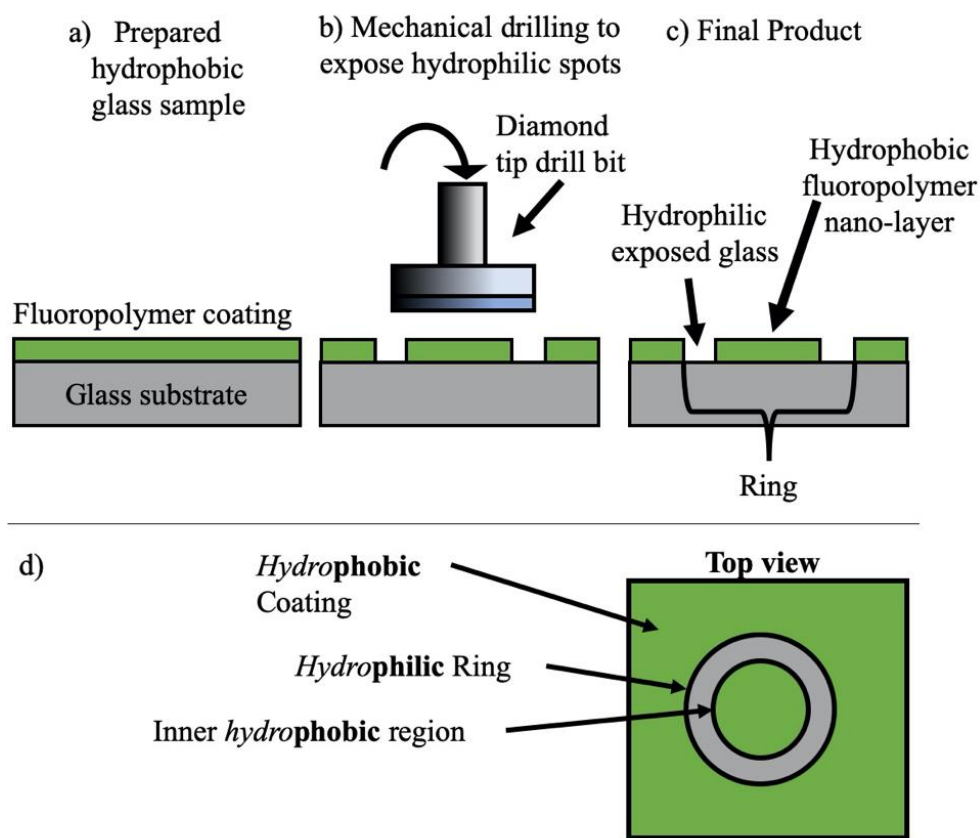


Fig. 2.5 Schematic of hybrid hydrophobic-hydrophilic surface produced by mechanically removing the polymer coating (b), leaving exposed ring-shaped hydrophilic glass (c) with a precise diameter (d).

and $z=0$ coordinates of the Jenome® bed, using an optical micrometer (Keyence). The drill depth was then calibrated by adjusting the Z-axis parameters in the instructions sent to a Janome® controller using JR C-Points software. The drill depth was set to $\approx 200 \mu\text{m}$. Hydrophilic rings were drilled in various geometric configurations as programmed via instructions set using JR C-Points software (Fig. 2.5 b-d).

Preliminary tests of the surfaces revealed that the position of the hydrophilic features could be in either a square or staggered confirmation, with rows spanning from 1 row to n rows spanning the length of the glass coupon, and with rows beginning at the top, bottom, or the sides of the glass coupon. The surfaces with n rows or hydrophilic features located on the right, left, or on the bottom of the glass only, yielded non-uniform condensation and drop growth on the surface in which a part of the surface yielded a higher condensation rate, while other parts performed poorly. Thus, it failed to maximize the surface area to improve the water condensation rate and potentially lowered the water collection rate or cleaning effectiveness. Placing n rows of hydrophilic features at the top of the surface allowed to maximize the potential water condensation rate. This occurred because when the water drops slide off the hydrophilic features at the top of the surface, they collect the water drops beneath the hydrophilic features and effectively remove them from the surface (as described in Chapter 2.1.2). The evaluation of hybrid hydrophobic-hydrophilic surfaces with ring-shaped hydrophobic features is described in Chapter 4.

2.1.2.3 Mechanical Removal of Polymer via Abrasive Solution Using a 3D-printed Plastic Mask

Expanding the hydrophilic part of the hybrid surface was considered as a means to improve the water collection rate (as reported in Chapter 4). In order to maximize the hydrophilic area, the surfaces were prepared via the selective removal of FEP on the surface of the glass substrate using a plastic stencil as a guide and an abrasive liquid.

The plastic mask was 3D printed using 1.75 mm poly-lactic acid filament (PLA) with a print width of 0.35 mm and a print height of 0.2 mm, which were respectively the width and height of the molten filament that was deposited on the print bed. The printer bed was heated to 60 °C (T_g of PLA), while the extruder was heated to 210 °C (above the T_m of 190 °C).

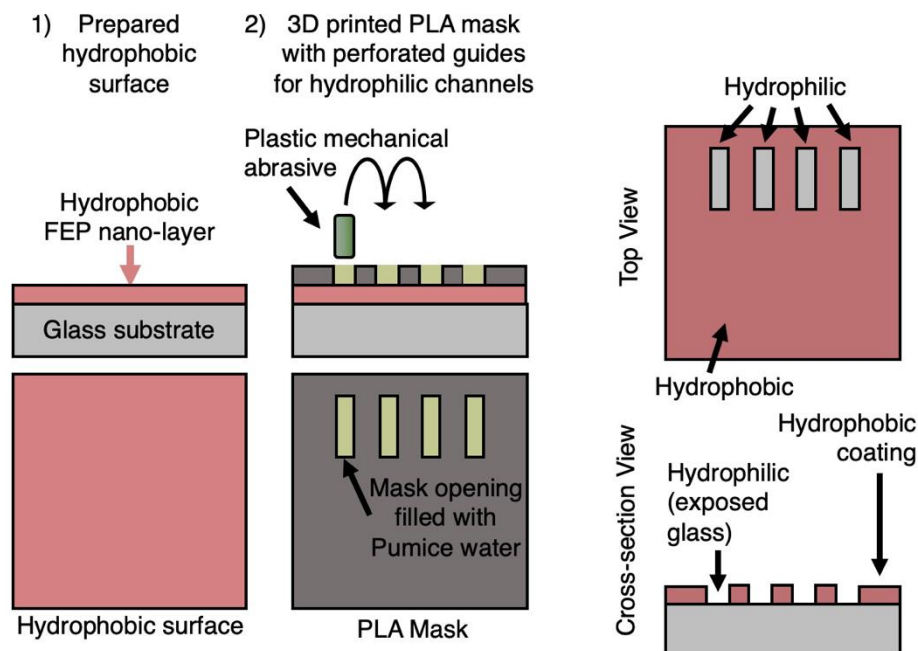


Fig. 2.6. Schematic of hybrid hydrophobic-hydrophilic surface produced by mechanically removing the polymer coating using an abrasive liquid and a 3D-printed PLA mask as a guide.

Similar to the fabrication of hybrid surfaces with circular hydrophilic features, the hydrophobic coated glass substrates were prepared by applying a <1 μm thick, fluorinated ethylene propylene (FEP) coating onto the cleaned glass using a lamination-peeling process [39]. A Teflon® FEP film (American Durafilm) was laminated to the glass substrate at ≥ 275 °C for ≥ 5 minutes and then allowed to cool below the resin melting point (260 °C). Excess polymer was peeled from the surface, leaving a nanometer-thick coating of FEP strongly adhered to the glass (Fig. 2.1). Furthermore, pumice powder (~5 % by weight) dispersed in water was rubbed against the coating using a plastic rod (0.5 mm diameter) guided by rectangular openings in a 3-D printed mask (Fig 2.6). The resulting sample contained a hydrophobic surface with an array of hydrophilic rectangular features localized to the top of the glass sample (Fig. 2.7a).

The width of the hydrophilic channels was optimized to allow condensed water droplets to slide off from the surface of the glass fastest, and the time for the first drop to slide off (Fig. 2.7b) and

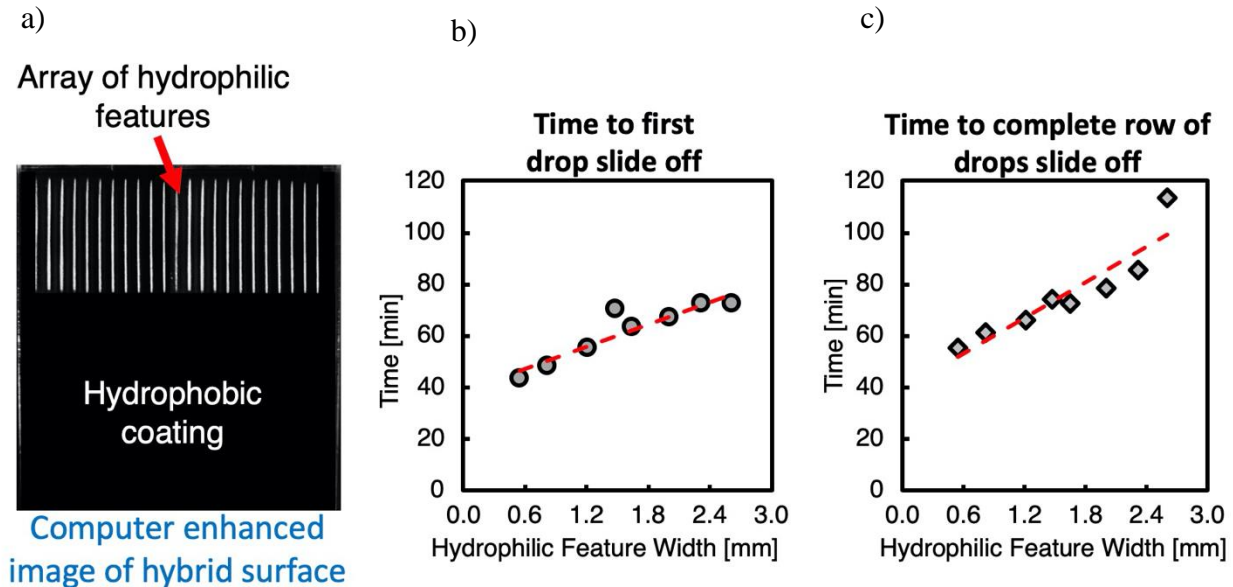


Fig. 2.7. a) Computer-enhanced image of a hybrid surface with hydrophilic channels, where the hydrophobic surface is black and the hydrophilic channels are white, (b) plot of the time taken for the first drop to slide off from the hybrid channels, and (c) the time taken for the entire row of drops to slide off from the array of hybrid channels.

time needed for the entire row of drops to slide off from the array of hydrophilic features were recorded (Fig. 2.7 c). The experimental results show a direct correlation between the time necessary for the drop to slide off and the width of the hydrophilic channel. The size of the PLA mask was limited by the 3D printer resolution, which limited the study to 0.6 mm hydrophilic channels. This channel size showed the best performance, with 42 minutes necessary for the first drop to slide off and 56 minutes needed for the row of drops to depart the array of hydrophilic features. A control experiment with ~0.1 mm hydrophilic channels produced by scribing the surface of the coated glass with a diamond scribe showed poor results. The first drop slid off at the 61-minute mark, and the first row of drops slid off at the 72-minute mark, indicating a reversal in performance enhancement by narrowing the hydrophilic features. This can be explained by the extremely high water surface tension within a narrow line of water residing on the narrow, which constricted the hydrophilic channels. This, in turn, would restrict the mobility of the water layer on the hydrophilic channel, preventing it from producing a water drop at the bottom of the channel. Also, the condensation rate on a narrow hydrophilic channel could be greatly impeded. It is also understood that a hydrophilic channel must be narrow enough to allow the water drop that forms on the bottom of the channel to break away from the water layer housed on the channel above the drop.

Initial results comparing the cleaning efficacy of uniform hydrophobic glass, a hybrid surface with hydrophilic rings, and a hybrid surface with hydrophilic channels showed that the hydrophilic channels were superior to uniform hydrophobic (Phobic) or hybrid rings (Rings) (Fig. 2.8). The cleaning efficacy of uniform hydrophobic glass (Phobic) was $4.2 \text{ mm}/(\text{hour} \cdot \text{mm}^2)$, for the hybrid ring surface, $4.9 \text{ mm}/(\text{hour} \cdot \text{mm}^2)$, and for the hybrid channels, $8.7 \text{ mm}/(\text{hour} \cdot \text{mm}^2)$.

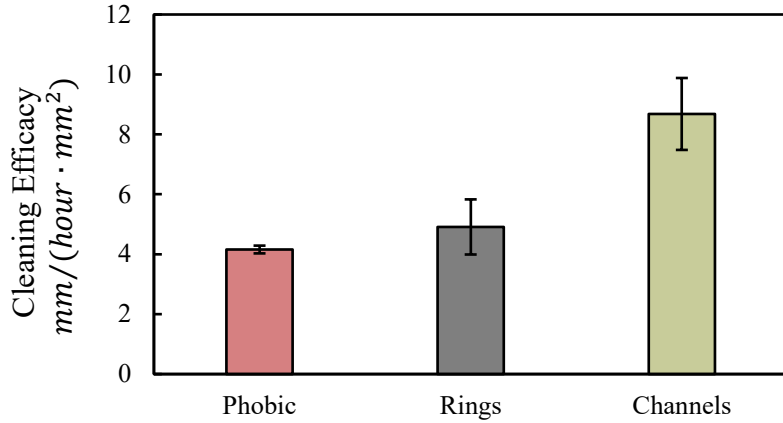


Fig. 2.8. Cleaning efficacy of uniform hydrophobic surface (red), hybrid surfaces with hydrophilic rings (gray), and hydrophilic channels (green).

Water collection efficacy can be used to measure how well a surface is cleaned via dew-derived drops by measuring the area cleaned by the drops as a function of time (**Equation 2.1**):

$$\text{Cleaning Efficacy} = \frac{\text{total width of cleaned paths } (\sum_{r=1}^n w_n), \text{ mm}}{(\text{time, hour}) (\text{active area, mm}^2)}$$

Where total width of cleaned paths is measured by the self-cleaning detection mechanism (Section 2.5) and the width of paths cleaned by drops are summed and normalized to the active area of the surface and time. The active area of the surface is the area occupied by the hydrophilic channel array on the glass surface. Since the area on the PV glass is valuable, in the sense that any obstructions on the glass surface may lower the amount of light transmitted through glass, it is important to consider the area that the hydrophilic features will occupy on the PV glass. Also, normalization to time is important because the goal of surface optimization is to enable water drop removal from the hydrophilic features in the shortest time since there is a limited amount of time that dew can form on glass in natural settings.

The optimal dimensions of the channels were determined to be 0.6 mm x 20 mm with a 1.7 mm pitch based on a parametric study [41]. As reported in Chapter 5, a single row of 23 channels, each measuring 20 ± 0.3 mm tall, 0.6 ± 0.1 mm wide, and spaced 1.1 ± 0.1 mm apart was found to be optimal and was positioned along the top edge of the hybrid substrates.

2.2 Dust Deposition Apparatus

Soiling of the solar panels in the field is a process that can last from days to many months between the cleaning cycles. Field testing the various anti-soiling technologies in field is a very long and impractical process, thus the need for an accelerated testing process has been expressed. Various methods have been developed, with the most popular methods being: the DIN EN 1096-5 by Photovoltaik Institut [42], Soiling test by Sandia National Laboratory [43] , and Fraunhofer ISE [44]. These methods provide either for humidity control, temperature control and/or wind speed control but in all instances, not all 3 controls are provided. These tests provide for a good experimental control of the test environment, but a test environment replicating dust deposition with dew mediated cementation needed to be produced.

Two apparatuses were built to apply a uniform layer of dust onto the glass test surfaces: a pulsed deposition apparatus (PDA) and a cloud deposition apparatus (CDA). The PDA was designed to replicate the quantity of dust that is deposited in Arizona over the course of one average week [45] during each deposition cycle, which corresponds to a decrease in % τ of ~1% per application. The PDA uses compressed nitrogen along with an electrical fan to uniformly distribute the dust within the air tunnel before it reaches the substrate below. In cases in which water is not condensed on the glass surface, air flowing from the fan across the glass reduces the amount of dust deposited on the surface. To overcome this limitation, a CDA process was designed to deposit the test dust on dry surfaces, as opposed to wet surfaces. The CDA dust deposition method allowed dust to settle from a cloud of suspended particles without interference from flowing air. The CDA method deposited dust at a higher rate than the PDA, decreasing the % τ by ~5.6% per application.

For both apparatuses, the dust was deposited uniformly over two 50 mm x 50 mm glass samples at the same time. Dust was applied to coated and uncoated samples simultaneously, and their relative positions were alternated to prevent potential systematic dust application errors. Both apparatuses were housed in Plexiglas enclosures to minimize external air currents that enabled the relative humidity to be controlled at 70% \pm 4% using a BONECO Travel Cool Mist Ultrasonic Humidifier 7146 with an Auber Instruments temperature humidity controller (model TH210).

2.2.1 Pulsed Deposition Apparatus (PDA)

The PDA is illustrated schematically in Fig. 2.9a. Prior to dust deposition, the humidity in the chamber (not shown) was stabilized, and two glass samples were placed side-by-side on the aluminum substrate holder (heat sink): one test sample with a polymer nano-coating and one uncoated glass control. The aluminum substrate holder was cooled to 10 °C using a recirculating chiller to allow condensation on the substrates, simulating dew. After 2 mins of water condensation, 20 mg of Arizona test dust (pre-loaded onto a wire-mesh holder) was launched into the wind tunnel using a pulse of dry N₂ gas (20 psi, 1 min) applied from under the support mesh to project the dust upwards into the wind tunnel. The dust encountered a downward stream of air from the overhead 9 cm diameter fan which generated an airflow velocity of 1.2 m/s. The turbulent air stream helped uniformly disperse the dust while directing it downwards towards the glass samples. The tunnel was made from scribed and folded polyethylene with a 10 cm x 10 cm upper opening, tapering down to a 5 cm x 10 cm exit over a length of 20 cm. The exit was positioned 10 mm above the glass surfaces. Samples were removed 1 minute after the N₂ pulse and placed in a pre-heated 65 °C forced air convection oven for 30 minutes to thoroughly dry the samples. Optical microscopy and UV-Vis spectra of the dried samples were recorded before replacing them on the

cold plate and starting the next soiling cycle. This soiling cycle was repeated a total of 5 times, and the total elapsed time for the five cycles, including measurements, was approximately 4 hours.

2.2.2 Cloud Deposition Apparatus (CDA)

The CDA soiling apparatus shown in Fig. 2.9b was used for soiling tests on dry surfaces without condensation, as well as on dry surfaces followed by condensation. To generate the dust suspension, 150 g of Arizona test dust was placed into a Hamilton Beach personal single-serve blender equipped with a 700 mL plastic blender jar. The top of the blender jar was connected via a flexible, corrugated, aluminum duct (8 cm o.d. and 60 cm long) to an aluminum connector (9 cm o.d. and 23 cm long). This connector included a 45° bend and a mechanically-actuated door positioned 2.5 cm above the exposed glass surfaces placed on the substrate holder and maintained

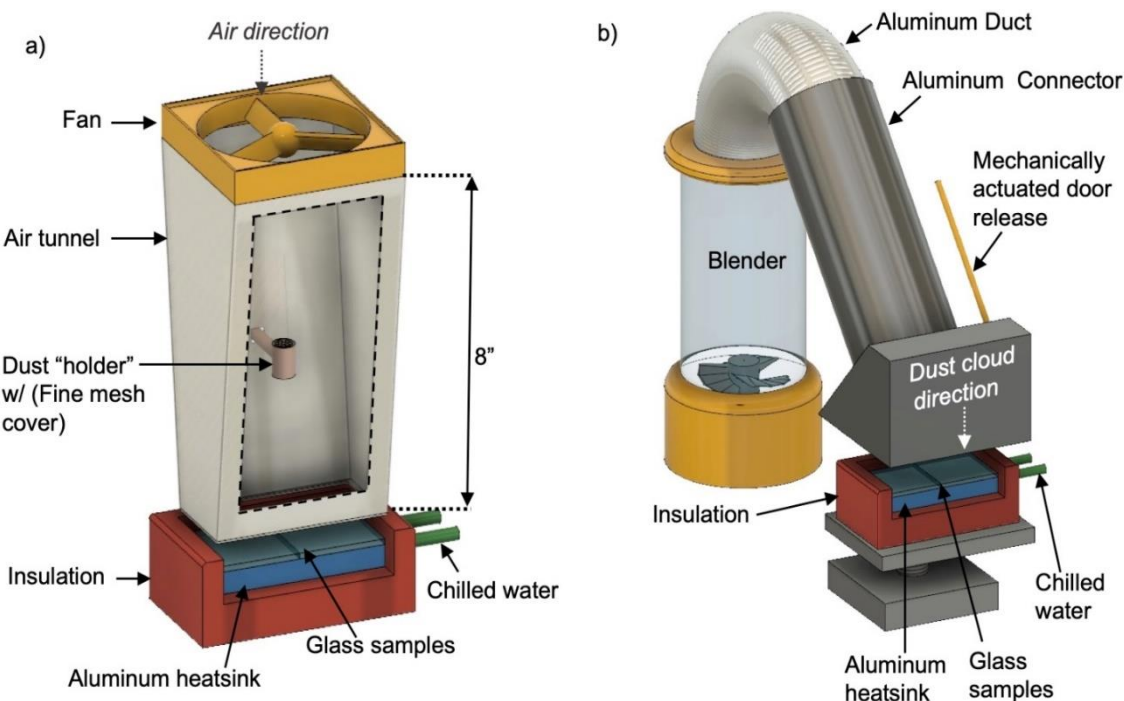


Fig. 2.9 a) Schematic of the pulsed dust apparatus (PDA); b) Schematic of the cloud deposition apparatus (CDA).

at room temperature to prevent condensation. After placing a pair of samples, the blender was energized to disperse the dust, creating a dust “cloud” throughout the blender jar and aluminum duct. After 20 seconds, the blender was turned off, and the door (measuring 10 mm x 10 mm) was opened for 10 seconds to allow the dust cloud to deposit onto the glass substrates. A plot of dust coverage (as measured by a decrease in $\% \tau$) as a function of exposure time is shown in Fig. 2.10. After deposition, selected samples were exposed to condensation by cooling the heatsink to 10 °C for 2 minutes. All samples were baked (65 °C for 30 minutes) and characterized by optical transmittance measurements and microscopy images. The soiled samples were placed in the UV-Vis spectrophotometer, ensuring that the glass was perpendicular to the beam without touching the front face of the soiled surface. The dusting, drying, and analysis sequence was repeated for a total of 3 dust cycles before cleaning. The total elapsed time for the three cycles was approximately 2.5 hours.

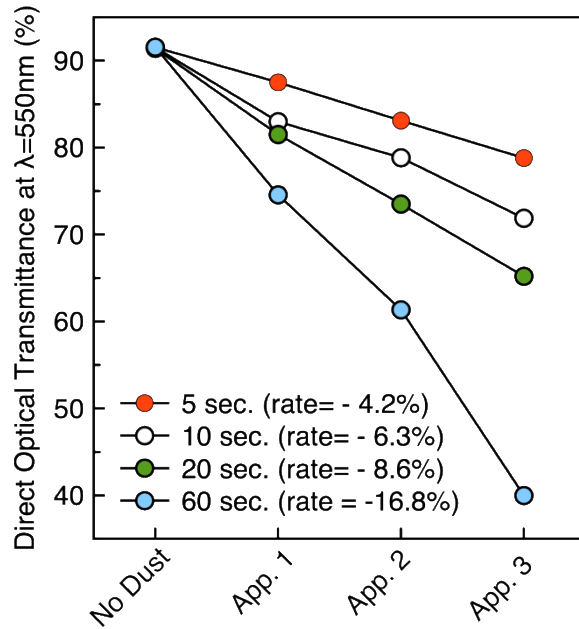


Fig. 2.10. Percent transmittance at 550 nm as a function of dust application cycle for bare glass soiled via the CDA method for 5 s (red), 10 s (empty), 20 s (green), and 60 s (blue).

2.3 Simulated Dew Condensation Chamber

Condensation experiments were conducted in a Delrin/Acrylic chamber, specifically built for experiments to simulate dew condensation on surfaces and self-cleaning properties (Fig. 2.11). Hybrid-coated glass samples were mounted on an aluminum plate measuring 5.0 cm x 5.0 cm x 0.75 cm. A digital thermometer integrated circuit (IC) housed within a 6.0 mm o.d. stainless-steel sheath (Maxim Integrated DS18B20) was mounted inside the aluminum heat-spreader. This heat-spreader was mounted onto a 60 W Peltier thermoelectric cooler (TEC) (Laqiya TEC1-12706). An aluminum heatsink and a CPU fan were mounted under the TEC to remove heat from the hot side of the TEC. The heatsink/fan, TEC, and aluminum heat-spreader were secured to the Delrin back-plate with springs. Thermal grease was used at all interfaces to enhance the thermal conductivity

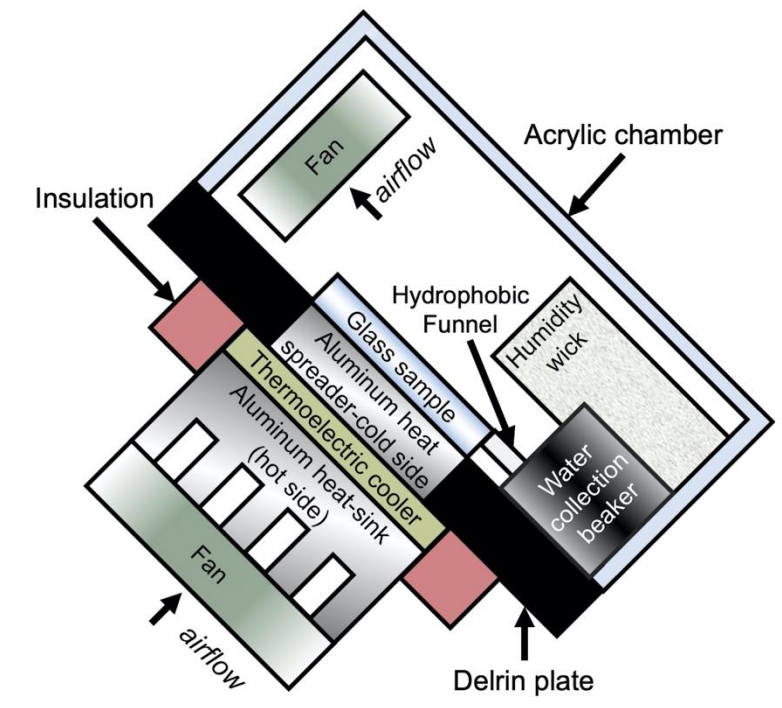


Fig. 2.11. Cross-sectional schematic of the condensation chamber, including the thermoelectric cooler system, water collection scheme, and humidification system (not to scale).

(Wakefield Solutions, Inc., Type 126 Non-Silicone Thermal Joint Compound). The temperature of the TEC was controlled using a digital thermometer IC located in the heat-spreader, and a 10 A 12VDC relay (Songle SRD-05VDC-SL-C) connected to a Raspberry Pi 3 microcontroller running a Python script.

The entire substrate-TEC assembly was mounted onto the base of the environmental chamber, which was constructed from a 25.4 cm x 25.4 cm x 0.25 cm Delrin plate, with a machined opening of 5.0 cm x 5.0 cm in the center. The Delrin plate was mounted at a 45° angle, and an acrylic enclosure (LWH: 18 cm x 18 cm x 10 cm) with a silicone gasket was used to isolate the system. The atmosphere inside the enclosure was saturated with water vapor using a wick cut from a Honeywell HC22P Humidifier Pad which was partially immersed in a beaker of deionized water. A low-velocity fan (Thermaltake Mobile Fan II) was mounted to the top of the chamber

The relative humidity was measured with a dry bulb/wet bulb method using two digital thermometer ICs, housed in 6 mm diameter stainless steel sheaths that were connected to the microcontroller. Water condensate was collected with a home-made superhydrophobic water collection channel and a 50 mL 3D printed plastic beaker that was tared before use.

2.4 Optical Microscopy Analysis of Soiling on Surfaces

In order to properly analyze the amount of soiling on the glass substrates, an optical microscopy analytics method was designed that used optical image manipulation using an algorithm written in Python. The algorithm is available in the folder titled PySurfaceArea in a Github repository: <https://github.com/illyanayshevsky/pyCondrop>.

The software utilized OpenCV computer vision libraries to identify areas on the surface of the glass covered by dust. Previous reports of such analytical methods in the literature [46] rely on lighting effects and manual thresholding, thus a new method with automatic background thresholding was developed. The algorithm used optical microscopy images as inputs and the outputs were floating point values of an area covered by dust.

The logic of the algorithm is outlined in the flowchart in Fig. 2.12, while the user interface (UI) is shown in Figure 2.13. The user of the algorithm begins by selecting a single standard image, which is an image of a surface type that best matches the surface to be analyzed (bare glass or hydrophobic), that has no dust on its surface. The standard image is used to automatically calibrate the lighting effects used during the acquisition of the optical microscopy image. The lighting effects are calibrated by calculating the average pixel intensity of the standard image, which is later used in background subtraction in order to identify the baseline pixel intensity of the surface to be analyzed. Afterward, the user loads the analytical image and the image of the surface to be analyzed. The analytical image is converted to grayscale (`cv2.imread(image, 0)`) using OpenCV library. Baseline subtraction is then performed by subtracting the average pixel intensity previously calculated from the standard image (using numpy arrays) from the analytical image, setting the pixels with no dust to a value of 0. Afterward, the process of calculating a mask that overlays the area not covered by dust begins. First, a Gaussian blur is applied to the image

(cv2.GaussianBlur(*image*)), followed by splitting the image into an arbitrary number of sub-images. Each of the sub-images then undergoes binary thresholding (cv2.threshold(*image*)), using pre-set, previously calibrated threshold parameters. The images were then recombined into a single image. The method of splitting images into sub-images prior to applying the binary threshold allows the algorithm to eliminate errors caused by variations in lighting throughout a single image. The binary image now symbolizes the area on the surface of the sample that is not covered by dust. After the images are recombined, a mask is calculated from the binary image, which is then applied

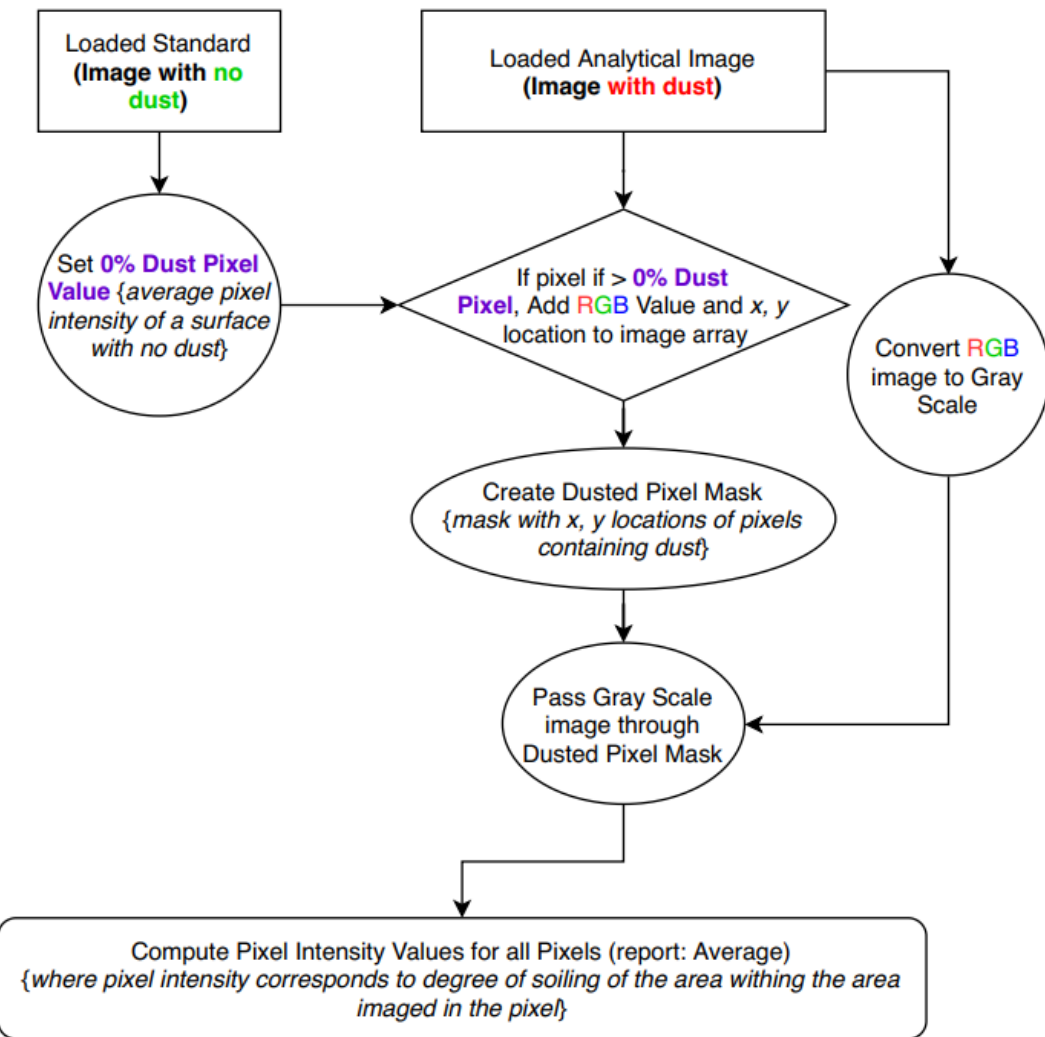


Fig. 2.12. Flowchart of the PySurfaceArea algorithm, which calculates the amount of dust covering the surface of a soiled glass sample using optical microscopy data.

to the original, unedited image. The mask is applied to the image using the `bitwise_and` OpenCV method (`cv2.bitwise_and(image, image, mask = mask)`). The pixels in the original image that do not correspond to the locations of pixels in the mask, i.e., the soiled pixels showing dust on the surface of the glass, are then used to calculate the pixel intensity. The pixel intensity of the soiled pixels is normalized to 100% utilizing the range bound by the values of the background calculated in the standard image and the value of the brightest pixel within the analytical image. Thus, the dimmest soiled pixel will receive a soiling value of 1%, and the brightest soiled pixel will get a soiling value of 100%. This, in turn, is used to calculate the degree of soiling within a single pixel, and the algorithm iterates through all the soiled pixels in this manner. The values of the soiled pixels are summed and divided by the total number of pixels in the analyzed image, therefore returning a single value which represents the average dust coverage of a glass surface.

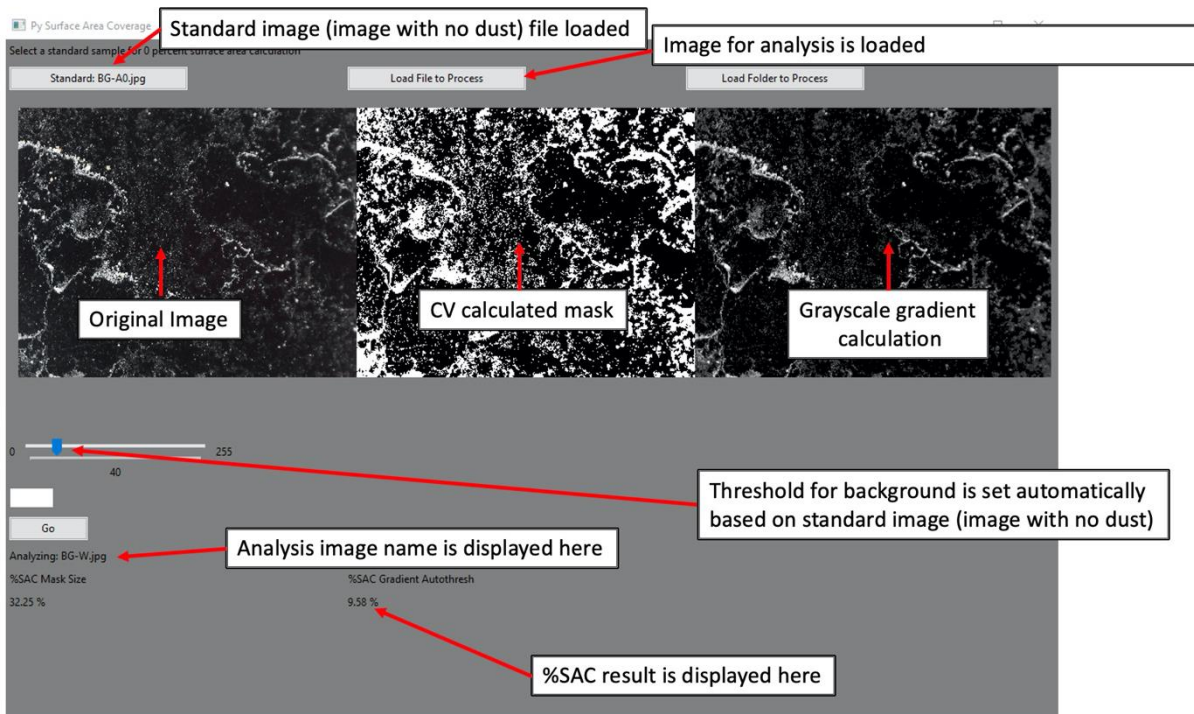


Fig. 2.13. Screenshot of PySurfaceArea user interface (UI).

The method is unique in the sense that instead of using a binary calculation for pixel soiling (soiled or not soiled), it uses a pixel intensity value and thus captures the degree of soiling within one pixel and eliminates inaccurate manual thresholding. The method also eliminates the issue of measuring soiling by sub-pixel particles and semi-transparent films on the surface of the glass, which may be difficult to capture by manually thresholding the entire image.

2.5 Automated Self-Cleaning Detection Methods via Computer Vision Analysis of Condensation Derived Water Droplets

The challenge with conducting long experiments, i.e., those >1 hr. in length, where observation is required to collect data is the human error, which will in effect corrupt the experimental data. In order to eliminate human error while manually counting the number of drops, recording the time at which a water drop slid off, or measuring the diameter of water drops over multi-hour periods, an algorithm was developed. The algorithm took video footage of the experiment and calculated the time and location that the water drop slid off from the surface of the test substrate. The algorithm can also trace the path of the drop as it slides off, capturing the area and location of the area cleaned by the sliding water drop.

The algorithm was developed in Python 2.7 utilizing OpenCV, Numpy, and Pandas libraries. Although algorithms that detect water drops have already been reported in the literature [47], the analysis of large water drops with non-diffuse lighting has proved challenging. The challenges that differentiate the experiments conducted in the condensation chamber from the work conducted by Afik, 2015 are: 1) the circles were much less uniform in appearance - we had dark/grey/light droplets; 2) some droplets, especially grey ones, have a light ring at their edges; 3) some droplets have double or even triple edges (with a darker inner ring); 4) all droplets have interior light reflections; 5) more often than not, light refraction occurs inside and/or outside the droplets; 6) the droplets have shadows which sometimes look like proper droplets themselves; 7) the droplets are not always circular and are sometimes oval, or even look like rounded rectangles; 8) the background is not uniform; 9) the overall image appears noisier. All of these issues make it impossible to use the traditional Hough Circle method of droplet detection.

To address the above issues, an approach was used which refrained from detecting circles, and instead detected the paths left by drops as they slid off the surface (Fig. 2.14). This method allowed the drop location to be calculated by calculating the origin of the drop path, the drop diameter by calculating the width of the top portion of the drop path, and the cleaning area calculated from the area of the drop path. The algorithm was further equipped to disregard any changes on the surface

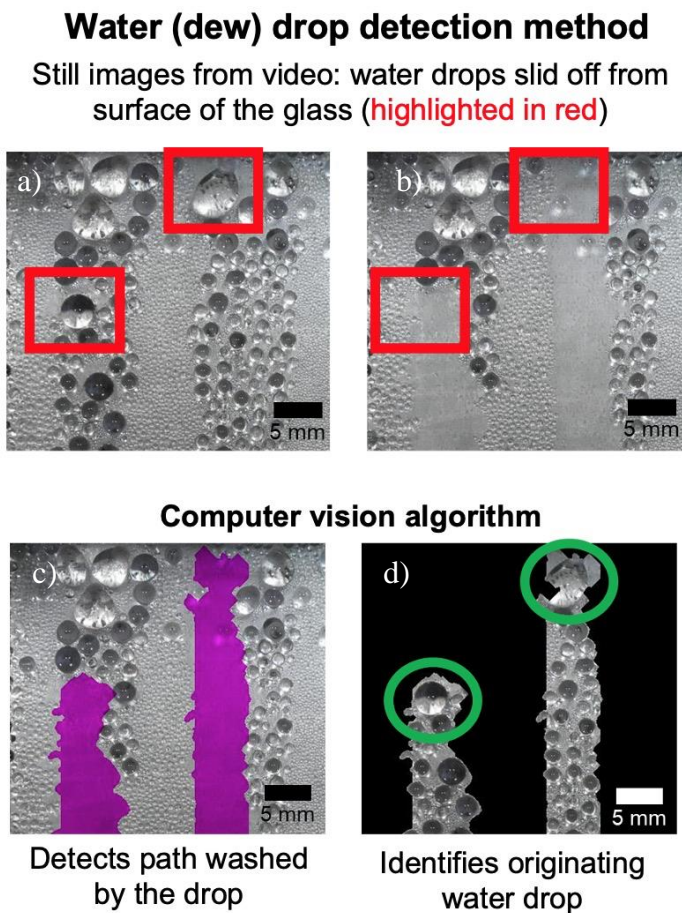


Fig. 2.14. Schematic showing the methodology of the drop detection algorithm, where a) shows the frame in which the water droplet that is about to slide off from the surface is highlighted in red; b) shows the same area, but the water droplet has already slid off from the surface of the glass, taking with it all the water drops below it. The red circle outlines the area where the water drop was before it slid off. The mask created by the algorithm showing the path that the water drop has traveled is shown in c), and the inverse mask overlaid on top of frame is shown in (a), confirming that the water drop that has slid off was in fact located at the top of the mask path, enclosed by green circle.

due to the water drops growing, merging, or sliding short distances, and it only detected water drops that slid and completely departed from the view of the camera.

The algorithm functions used to identify differences in the two frames were adjected in time by merging various combinations of ridge detection methods, gradients, and/or anisotropic diffusion, which is a kind of smoothing process that preserves edges more than other smoothing methods. The resulting mask clearly outlines the path that a slid-off drop has traveled since the sliding drop always removes all drops below it as it travels downward (Fig. 2.14 c). This is achieved by calculating the local maxima of the image with respect to the x-axis. The local maxima was calculated from the image with a water drop still pinned to the surface of the glass (Fig. 2.15 b),

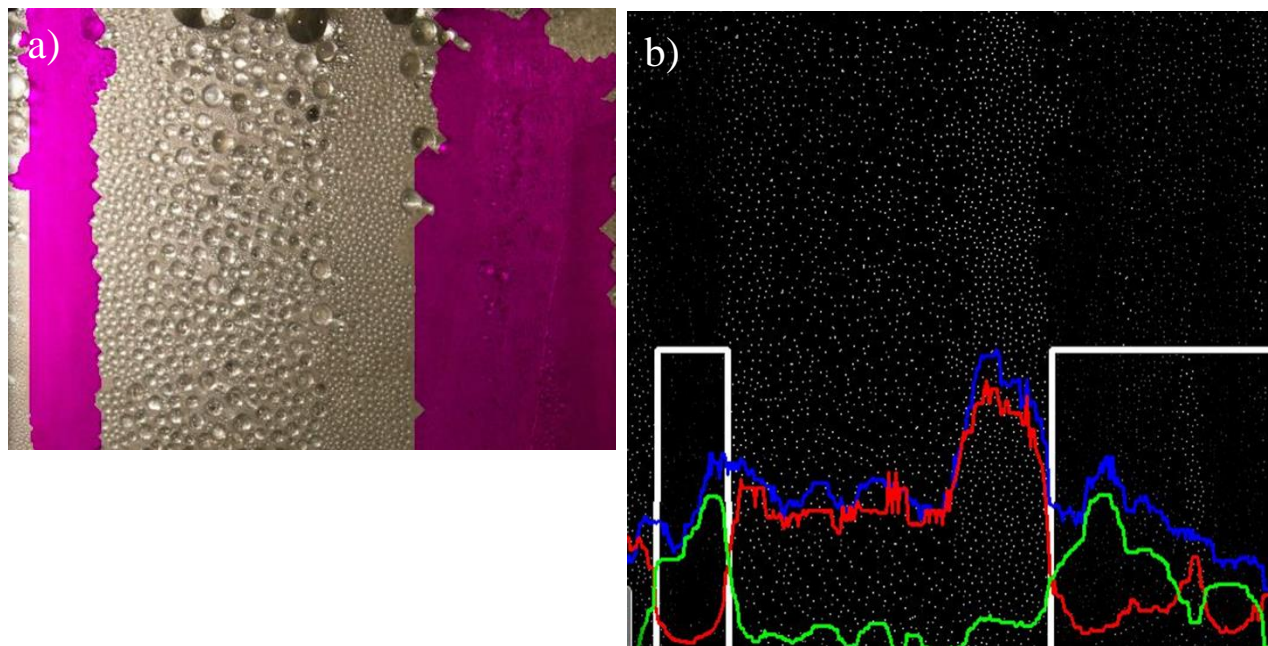


Fig. 2.15. Computer visualization image of the analytical surface with a pink mask highlighting the paths cleaned by water drops (a), and computer visualization image of the calculation, with local maxima of image (b) with water drops still pinned to the surface in blue, the local maxima of the image with water drops already slid-off in red, and the difference between the local maxima in green. The areas highlighted in white were determined by the computer algorithm to contain the paths cleaned by the drops, with the width of the white boxes representing the original drop width.

and the local maxima was calculated from the image in which the water drop had already slid off from the surface of the glass (Fig. 2.15 b), followed by calculating the difference between the maxima. The x-axis locations on the image, which correspond to the peaks in the local maxima, were determined to correspond to the x-axis location of the water drops. The same calculation was performed on the y-axis, and then the values were intercalated to produce the mask overlaying the sliding drop path in 2 dimensions. The code for the algorithm is available in the PyDrop folder of the Github repository: <https://github.com/illyanayshevsky/pyCondrop>.

2.6 Determination of Dust Particle Size Observed in Nature

Soiling of PV cover glass degrades solar panel efficiency by shading and scattering light. Frequent cleaning is required to maintain electrical output and minimize overall LCOE. However, cleaning can scratch the glass surface or abrade away anti-reflective and anti-soiling coatings. Larger particles have been shown to increase the rate of abrasion of the underlying surface. When developing standardized abrasion tests, selecting appropriately sized particles is one factor that can help ensure that the laboratory test will faithfully replicate field-observed degradation mechanisms. The purpose of this review is to determine the mean particle diameter of soil found on solar panels as well as assess regional differences of observed soil diameters.

A systematic review of the literature using the Web of Science search engine revealed 58 articles (Bibliography Addendum 1, [1]-[58]) that characterized particulates found on solar panels and solar panel test sites at 74 locations around the world. Diameters of soil particles reported in these articles are plotted and compared to standard Arizona Test Dust grades available from Powder Tech Inc. (PTI). The analysis has been summarized and shown in Fig. 2.16 [48]. An interactive map of soil particle dimensions as a function of geographic location has been published online (www.bit.ly/soiling), which reports: particle diameter, geographical location, chemical composition and characterization method.

The inclusion criteria for the literature search was:

- 1) Dust accumulation on live solar panels
- 2) Dust accumulation on solar panel test cites
- 3) Dust particle size on solar panels
- 4) Dust particle size on solar panel test cites

While the exclusion criteria was :

1) Articles describing dust as aerosols

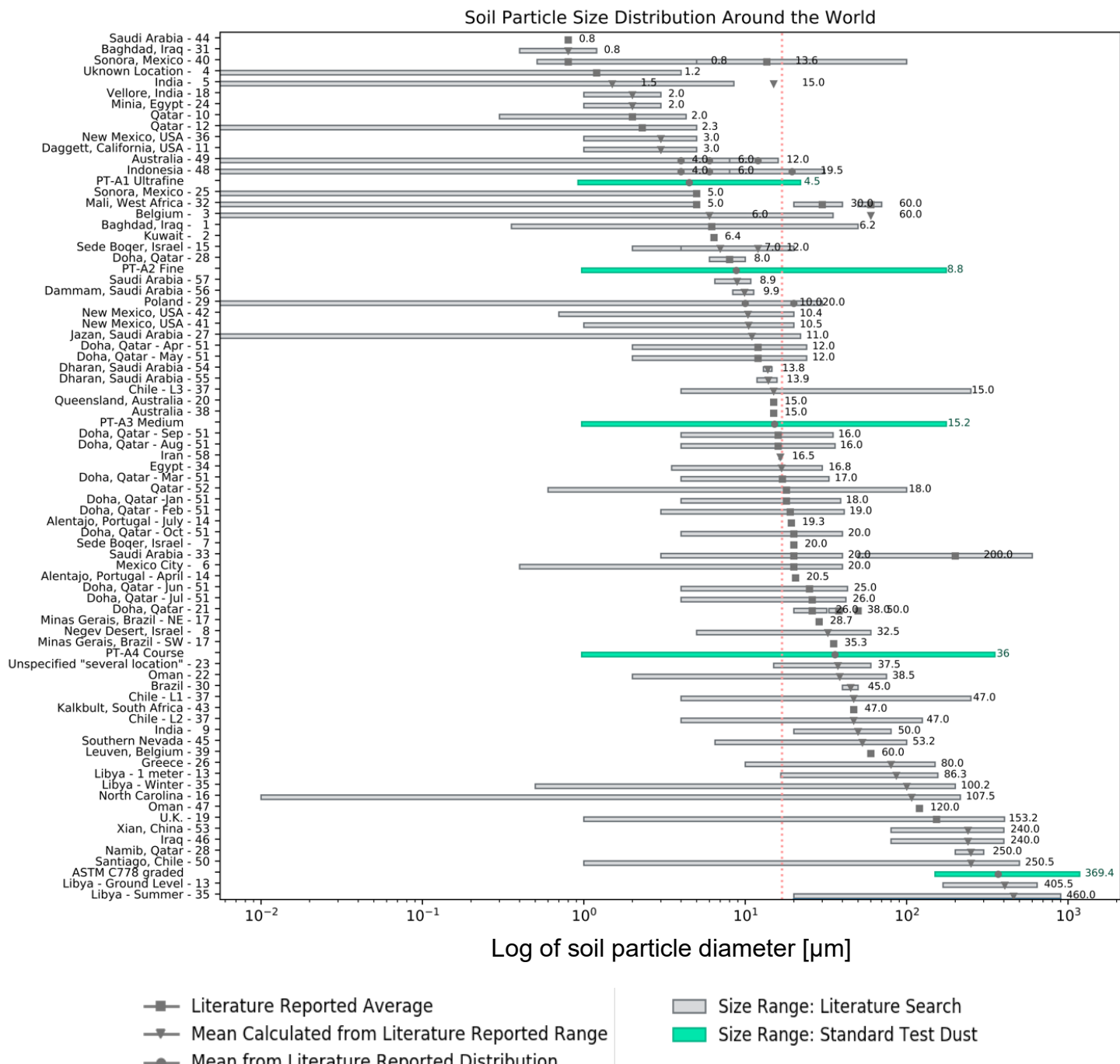


Fig. 2.16 Soil particle distribution around the world, with median dust particle size reported in literature = $16 \mu\text{m}$ (red dotted line).

A broad size range observed of the particles reported in the literature was observed: 0.8 μm to 1000 μm , with 11 sources reporting particles reaching >100 μm . This study reveals that the median diameter of the dust particles reported in nature was 16 μm . Comparing the median particle size reported in literature to the median particle size of Arizona Test Dust A2, 8.8 μm , and Arizona Test Dust A3, 15.2 μm the two sizes are comparative. Both Arizona Test Dust A2 and A3 possess particle size distribution range of 1.0 μm -176 μm , which covers 86% of literature sourced mean particle sizes and 70% of literature sourced particle size distributions. This indicates that Arizona Test Dust A2 and A3 possess particle size distribution comparative to that found in the literature and therefore are good candidates for use in laboratory soiling and abrasion studies of PV grade cover glass.

The outcome of this study has also lead to : IEC 62788-8-2 Abrasion Test Standard Committee recommending A3 medium Test Dust for all laboratory abrasion tests of PV grade cover glass.[49]

Chapter 3. Fluoropolymer Coatings for Solar Cover Glass: Anti-Soiling Mechanisms in the Presence of Dew

I. Nayshevsky, Q. Xu, G. Barahman, and A. M. Lyons, “Fluoropolymer Coatings for Solar Cover Glass : Anti-Soiling Mechanisms in the Presence of Dew,” *Sol. Energy Mater. Sol. Cells*, vol. In Press, 2019

3.1 Introduction

Soiling of solar cover glass can cause a significant loss of electrical output from PV panels. Dew condensed on the surface exacerbates soiling rates and promotes reactions between dust and glass leading to stronger adhesive forces that make cleaning more expensive. To reduce soiling rates and lower cleaning costs, anti-soiling coatings are being developed. Although the interactions between dust particles and uncoated low-iron glass surfaces are known, the mechanisms by which anti-soiling coatings reduce soiling rates are less well understood.

In this paper we report on the effect of wetting properties on both the soiling rate as well as the cleaning efficiency of polymer coated solar cover glass substrates in the presence of condensed water in a controlled environment. Coatings were fabricated with water contact angles (CAs) ranging from 149° to 51° and compared to bare glass. Arizona Test Dust was applied onto substrates on which water condensate (i.e. artificial dew) had formed. The surfaces were baked to enable cementation to occur. Such dew-dust-dry cycles were repeated to simulate naturally occurring, cumulative soiling processes. Changes in dust accumulation rates were assessed as a function of coating properties. Hydrophobic coated glass exhibited 42% lower soiling rates compared to hydrophilic glass. A dust “herding” mechanism was identified to account for these reduced soiling rates, by which dust is concentrated into discrete piles during the lateral shrinkage of droplets on low-energy surfaces. These hydrophobic surfaces were also easier to clean with >99% of the original direct transmittance restored using only water.

The reliability of solar photovoltaic (PV) modules depends on the protective solar cover glass to provide both mechanical rigidity as well as an environmental barrier against water, dust, and other contaminants. However, the solar cover glass contributes to two sources of loss: reflections and soiling. Reflections at the air-glass interface occur because of the abrupt change in refractive index between air ($n=1$) and glass ($n=1.52$). In this way, ~ 4% of incident light is reflected at normal incidence, with greater percentages of reflection observed at steeper angles. Soiling can reduce electrical output by a much greater amount. In most North American and European locations, 4% to 7% of light is lost per year due to dust deposited on the surface that scatters light and shadows the underlying solar cells [12], [17], [45], [50]–[54]. In other locations and seasons, annual soiling losses are reported to reach as high as 70% [12], [17], [53], [55]–[57]. Severity of soiling is reported to be greatest when dew is present [12], [15], [17]–[19], [53]. Dust particles can react in the presence of liquid water, by several mechanisms including adhesion of dust particles through capillary aging [15]–[17] and chemical bonding of the particles to glass surface, also known as cementation [12], [18], [19]. Heating from solar insolation evaporates the dew and accelerates chemical bond formation. As a result of these mechanisms, a greater mechanical force is required to remove dust when dew is present [20], which increases cleaning costs. Some of the cleaning methods currently used, including: manual brush cleaning; robotic brush cleaning; and water cleaning [12], [55], are expensive [58] and may abrade the glass leading to additional transmission losses [12]. A novel anti-soiling and self-cleaning technique, electrodynamic screens [59], poses essentially no abrasion risk to the panels, although it is more expensive to implement.

Dew formation occurs in many arid climates such as Arizona, USA [45], [54], as well as the Middle East, and North Africa (MENA)[15], [21], and is caused by a drop in the temperature of a solid surface below the dew point during the night when radiative cooling is most prevalent.

Because these arid regions experience both higher soiling rates as well as higher water costs, the cleaning costs alone can reach as high as \$2.67 / kW-year [58]. As a result, the operations and maintenance (O&M) component of the LCOE in regions experiencing high soiling rates will be greater than the 2018 value of \$14 / kW-year for utility-scale solar in the U.S.A. [60]. Thus, anti-soiling coatings for solar cover glass are needed to lower O&M costs by reducing the accumulation of dust (i.e. anti-soiling properties) and/or reducing the adhesion of dust to the glass surface.

The two primary types of transparent, anti-soiling coatings that have been reported in the literature are hydrophobic [4]–[11] and hydrophilic [11]–[14]. Hydrophilic coatings rely on water to fully wet the glass and carry away dust particles as water is wicked down-slope to the bottom of the panel. Because clean bare glass readily becomes contaminated from absorbed chemicals (e.g. proteins, salts, surfactants) it can become progressively less hydrophilic (i.e. more hydrophobic) over time, losing its ability to wick water. To overcome this change in wettability, TiO₂ coatings have been developed [16], [23], [24] that can photochemically oxidize absorbed organics to maintain a high degree of hydrophilicity [25], [26]. However, such coatings, have a high index of refraction leading to increased reflections compared to bare glass, and absorb radiation below ~400 nm, thus lowering overall PV efficiency. The impact of TiO₂ on cementation processes has not been reported. Moreover, TiO₂ coatings are only able to photooxidize organic contaminants [27]; these coatings cannot oxidize or degrade the inorganic soil particles (e.g. salt, silicates, oxides, etc.) typically found on solar panels.

Hydrophobic coatings are composed of a chemically inert, low surface energy material and so prevent chemical reactions from occurring between soil and the glass surface. Moreover, dew does not spread out (wet) a hydrophobic surface to form a liquid film; instead water condensate will form discrete droplets with relatively high contact angles (CAs). With certain nanostructures, the

difference between advancing and receding CA (CA hysteresis or CAH) is small allowing the droplets to slide off the low-energy surface at low tilt angles [28]. These sliding droplets can then carry-away absorbed dust, resulting in a cleaned surface. Such hydrophobic coatings would enable the surface to be cleaned using less water and time and potentially avoid mechanical abrasion.

There are numerous challenges to developing a commercially viable anti-soiling coating including: cost, durability and anti-soiling effectiveness. Although several anti-reflective coatings currently exist on the market, practical anti-soiling coatings are still under development. Coatings that have been reported include: Enki CleanARC® [11], [29], [30], DSM's anti-soiling coating [31], [32], and 3M's anti-soiling liquid coating [33]. However, the mechanism(s) by which these coatings reduce dust accumulation rates as well as mitigate adhesion strength of soil to glass in the presence of dew, have not been reported.

In this paper, we describe the anti-reflective and anti-soiling properties of a novel nano-textured fluoropolymer coating for solar cover glass. The coating process results in a thin ($\sim 0.5 \mu\text{m}$) layer of the fluoropolymer strongly bonded to low-iron glass. A series of coated low-iron glass samples were prepared with CA values of 149° , 106° , 87° , 63° and 51° by modifying coating process variables. The effect of coating wetting properties on both soil accumulation rates and cleaning efficacy was studied by direct optical transmittance measurements and optical image processing. Test rigs were constructed to apply a uniform layer of Arizona Test Dust onto the coated surfaces, with and without the presence of simulated dew, mimicking natural dust accumulation processes and rates. Samples were baked after dust deposition to simulate natural cementation processes. Dew-dust-dry cycles were repeated before evaluating cleaning efficacy using a controlled drop dispenser. Anti-soiling and no-touch water cleaning behaviors are reported as a function of coating CA.

3.2 Material and Methods

3.2.1 Materials

Low-iron glass substrates, 3 mm thick, (Pilkington OptiWhite) were cut into 100 x 100 mm squares, washed with Alconox powder, rinsed in deionized water and dried before use. Fluoropolymer coatings were applied to the cleaned glass surface via a platen lamination process [39], [61]. In brief, Teflon® FEP film purchased from American Durafilm was laminated to the glass substrate at ≥ 275 °C for ≥ 5 minutes and allowed to cool below the melt point of the resin (260 °C). Excess polymer was peeled from the surface leaving a nano-coating of FEP strongly adhered to the glass. Lamination process conditions, as well as peeling temperatures, speeds and angles were modified to produce coatings that exhibited specific wetting properties. Each 100 mm x 100 mm coupon was cut into four samples measuring 50 mm x 50 mm, which were used for: soiling tests (2 samples), wetting properties characterization (1 sample), and AFM analysis (1 sample). Standard Arizona Test Dust (A2 Fine Grade ISO 12103-1) was purchased from Powder Technology Inc. The dust was dried at 65 °C and stored in a desiccator before use.

3.2.2 Measurements

Direct optical transmittance spectra were recorded using a PerkinElmer Lambda 650 UV-Vis spectrophotometer in the range from 350 nm to 850 nm with a scan resolution of 3 nm. Care was taken to mount the samples to ensure reproducible direct transmittance measurements at normal incidence. Spectra from 8 clean, uncoated low-iron glass substrates were recorded and averaged to serve as a baseline. Spectra of fluoropolymer coated samples were similarly averaged and compared to the uncoated baseline to calculate the average % τ gain for each sample set. Error bars

indicate one standard deviation. We used direct transmittance measurements at a single wavelength (550 nm), as opposed to a Representative Solar Weighted Transmittance (RSWT) [49], [62] for several reasons. Micheli et. al. [63] demonstrated that the % τ of soiled samples measured at 550 nm correlates well (R^2 value > 98%) with the soiling ratio (SR), as defined by IEC 61724-1 [64]. The 550 nm wavelength is especially well-correlated to SR because wavelengths < 600 nm are more sensitive to scattering by soil particles [65], [66] and semiconductor absorbing materials generate the most energy at wavelengths >500 nm [63]. We have observed an excellent correlation between RSWT values and % τ at 550 nm for several samples. Moreover, direct transmittance measurements at a single wavelength are rapid and economical, allowing multiple measurements to be obtained on each sample after each soiling cycle.

Water contact angle values were measured with a 5 μL droplet of deionized (DI) water using a contact angle goniometer (model 250-F1, ramé-hart Instrument Co.)

Optical microscopy was performed with a Nikon SMZ1500 stereo-zoom microscope equipped with a ring illuminator and Lumenera INFINITY 2-1C USB 3.0 microscope camera. Samples were placed on a black plastic background, with water introduced between glass and black plastic, to minimize reflections. The percent of the surface area coated with dust was determined from these microscopy images. Images were recorded from five specific regions of each surface (four corners and the center) after each step of the dusting process (i.e. before dusting, after each dust/bake cycle and after cleaning) The camera resolution was set to 1342 by 1040 pixels, resulting in a field of view of 7.87 mm x 5.88 mm. The coverage area of dust particles was quantified by summing the grey-scale pixel values in the optical micrographs. Values were converted from a scale of 0 to 255 to a scale of 0% to 100% and normalized to the brightest and darkest pixel in the image. Differences between clean and soiled samples were averaged to calculate the reflection

gain after dust deposition. A python program [67] was written to automate the optical micrograph analysis and standardize the quantification method. Videos of individual droplets interacting with dust were acquired using the Nikon stereomicroscope and camera used above at 30 fps with resolution of 1342 by 1040 pixels, using either condensed water or individual 2 μL drops of water.

Atomic force microscopy (AFM) images were obtained on Bruker MultiMode 8 AFM, utilizing ScanAsys-Air probe in Peak Force ScanAsyst mode. The images obtained were 256 x 256 pixels with a view area of 5 μm x 5 μm . RMS roughness of the sample was calculated via Gwyddion 2.51.

3.2.3 Dust Deposition Apparatus

As described in Section 2.2, two apparatus were built to apply a uniform layer of dust onto glass test surfaces: Pulsed Deposition Apparatus (PDA) and Cloud Deposition Apparatus (CDA). The PDA is designed to replicate the quantity of dust that is deposited in Arizona over the course of one average week [45] in each deposition cycle, which corresponds to a decrease in % τ of ~1% per application. The PDA uses compressed nitrogen along with an electrical fan to distribute the dust uniformly within the air tunnel before it reaches the substrate below. In those cases where water is not condensed on the glass surface, air flowing from the fan across the glass reduces the amount of dust deposited on the surface. To overcome this limitation, a CDA process was designed to deposit the test dust on dry surfaces, as opposed to wet surfaces. CDA dust deposition method allowed the dust to settle from a cloud of suspended particles, without interference from flowing air. The CDA method deposited dust at a higher rate than the PDA, decreasing the % τ by ~5.6% per application.

For both apparatuses, the dust was deposited uniformly over two 50 mm x 50 mm glass samples at the same time. Dust was applied to coated and uncoated samples simultaneously; their relative positions were alternated to avoid the potential for systematic dust application error. Both apparatuses were housed within Plexiglas enclosures to minimize external air currents and enable relative humidity to be controlled at $70\% \pm 4\%$ using a BONECO Travel Cool Mist Ultrasonic Humidifier 7146, with an Auber Instruments temperature humidity controller (model TH210).

3.2.4 Pulsed Deposition Apparatus (PDA)

As described in Section 2.2, the PDA is illustrated schematically in Fig. 3.1a. Prior to dust deposition, the humidity in the chamber (not shown) was stabilized and two glass samples were placed side-by-side on the aluminum substrate holder (heat sink); one test sample with a polymer nano-coating and one uncoated glass control. The aluminum substrate holder was cooled to 10 °C using a recirculating chiller to enable condensation to occur on the substrates, simulating dew. After 2 mins of water condensation, 20 mg of Arizona Test Dust (pre-loaded onto a wire-mesh holder) was launched into the wind tunnel using a pulse of dry N₂ gas (20 psi, 1 min) applied from under the support mesh to project the dust upwards into the wind tunnel. The dust encounters a downward stream of air from the overhead 9 cm diameter fan, which generates an air flow velocity of 1.2 m/s. The turbulent air stream helps to disperse the dust uniformly while directing it downwards towards the glass samples. The tunnel is made from scribed and folded polyethylene with a 10 cm x 10 cm upper opening, tapering down to a 5 cm x 10 cm exit over a 20 cm length. The exit is positioned 10 mm above the glass surfaces. Samples were removed 1 minute after the N₂ pulse and placed in a pre-heated 65 °C forced air convection oven for 30 minutes to thoroughly dry the samples. Optical microscopy and UV-vis spectra were recorded on the dried samples before

replacing them onto the cold plate and starting the next soiling cycle. This soiling cycle was repeated for a total of 5 times; the total elapsed time for the five cycles, including measurements, was approximately 4 hours.

3.2.5 Cloud Deposition Apparatus (CDA)

As described in Section 2.2, the CDA soiling apparatus, shown in Fig. 3.1b, was used for soiling tests on dry surfaces without condensation as well as on dry surfaces followed by condensation. To generate the dust suspension, 150 g of Arizona Test Dust was placed into a Hamilton Beach Personal Single Serve Blender equipped with a 700 mL plastic blender jar. The top of the blender jar was connected via a flexible, corrugated, aluminum duct (8 cm o.d. and 60 cm long) to an aluminum connector (9 cm o.d. and 23 cm long). This connector includes a 45° bend and a

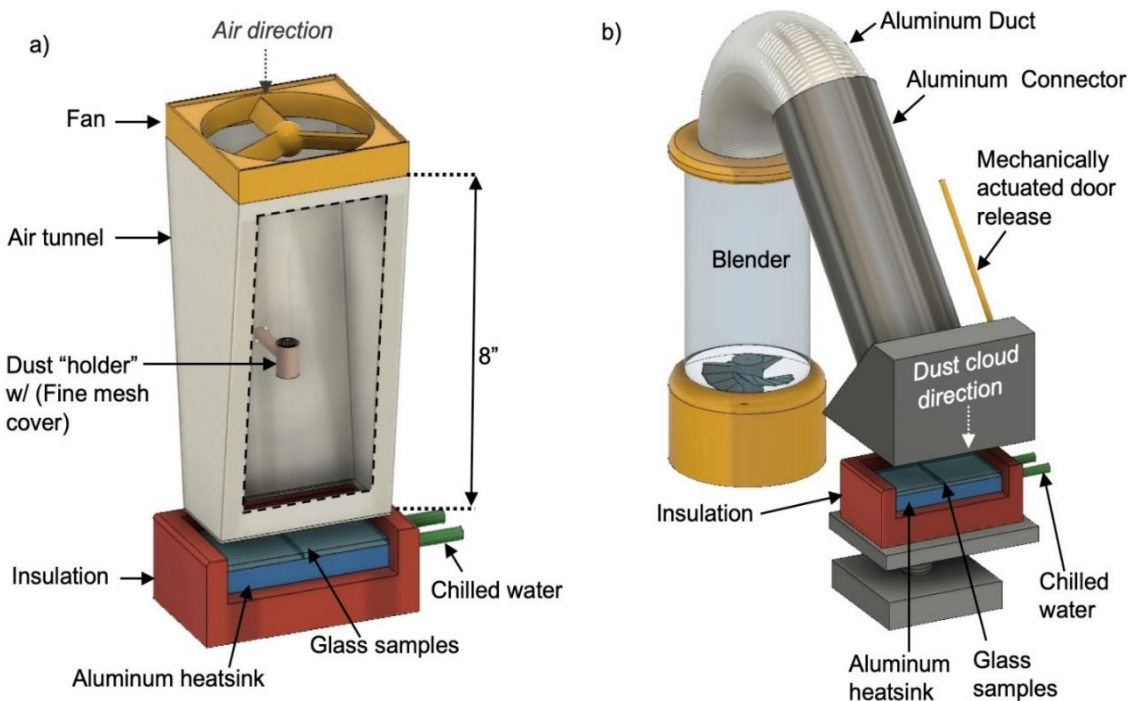


Fig. 3.1 a) Schematic of the Pulsed Dust Apparatus (PDA); b) Schematic of the Cloud Deposition Apparatus (CDA)

mechanically actuated door positioned 2.5 cm above the exposed glass surfaces placed on the substrate holder maintained at room temperature to prevent condensation from occurring. After placing a pair of samples, the blender was energized to disperse the dust creating a dust “cloud” throughout the blender jar and aluminum duct. After 20 seconds, the blender was turned off and the door (measuring 10 mm x 10 mm) was opened for 10 seconds allowing the dust cloud to deposit onto the glass substrates. A plot of dust coverage (as measured by a decrease in % τ) as a function of exposure time is shown in Appendix Fig. 3.10. After deposition, selected samples were exposed to condensation by cooling the heatsink to 10 °C for 2 minutes. All samples were baked (65 °C for 30 minutes) and characterized by optical transmittance measurements and microscopy images. The soiled samples were placed in the spectrophotometer ensuring the glass was perpendicular to the beam without touching the front face of the soiled surface. The dusting, drying, analysis sequence was repeated for a total of 3 dust cycles, before cleaning. The total elapsed time for the three cycles was approximately 2.5 hours.

3.2.6 Cleaning Process

To assess the anti-soiling properties of the coated surfaces, a no-touch cleaning system was built as shown schematically in Fig. 3.2. The system was designed to quantify the amount of test dust removed from the surface without the use of brushes. The apparatus also enables capturing and quantifying the amount of water that slides off the surface. Test samples coated with dust were placed on a substrate holder and tilted at an angle of 33°, simulating the tilt angle in Arizona installations. The holder was translated at a velocity of 50 mm/min under a 17-gauge syringe needle connected to a KD Scientific KDS Legato 210 syringe pump. Translation of the platform was performed via an electric motor. Water droplets were dispensed from the syringe tip at a rate

of 3.0 mL/min (3.0 mL total volume). The distance between the syringe tip and the surface was 10 mm. Water that ran off the dusted samples was collected using a superhydrophobic funnel and measured using an electronic balance.

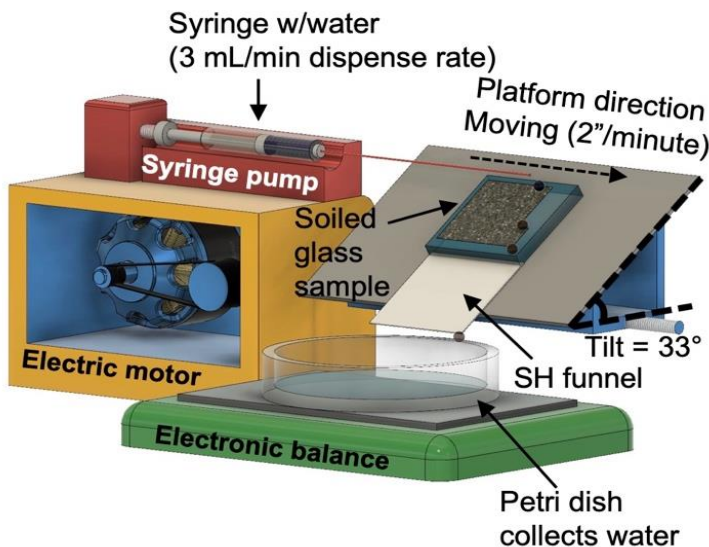


Fig. 3.2 Schematic of no-touch cleaning system used to assess effectiveness of anti-soiling coatings.

3.3 Results and Discussion

3.3.1 Samples and Wetting Properties

FEP coated glass coupons were prepared with surface wetting properties, ranging from hydrophilic (CA of $51.2^\circ \pm 0.2^\circ$) to superhydrophobic (CA of $148.7^\circ \pm 0.3^\circ$). The sample designation and water contact angle (CA) values of the five types of coated surfaces, as well as uncoated glass controls, are shown in Table 1. Because the properties of the two hydrophilic (Philic) coated samples and the two hydrophobic (Phobic) coated samples are so similar, the results presented in this manuscript will show averages for these pairs of hydrophilic and pairs of hydrophobic coatings for clarity; data for all surfaces is reported in the Supplementary Materials

section. The samples were grouped into four types with the following CA value ranges: uncoated glass (Bare): $<10^\circ$; hydrophilic (Philic): 51° - 63° ; hydrophobic (Phobic): 87° - 106° ; and superhydrophobic (SH): 149° . Surface sliding angle, advancing contact angle, receding contact angle, and contact angle hysteresis for each of the surfaces is shown in Appendix Table 3.5.

3.3.2 UV-Vis Spectra: % Light Transmittance

The UV-vis spectra of coated surface types are shown in Fig. 3.3. For clarity, all spectra from the two hydrophilic surfaces are combined into one plot (Philic, blue curve); similarly, all spectra from the two hydrophobic surfaces are combined into a single plot (Phobic, red curve). Spectra for each individual coating type, and details concerning the number of samples and scans averaged together, are presented in Appendix Fig. 3.11. The anti-reflective properties of the fluoropolymer coated glass are clearly evident in these spectra (Fig. 3.3). The anti-reflective (AR) gain (difference between coated and Bare glass) is approximately constant over the entire visible

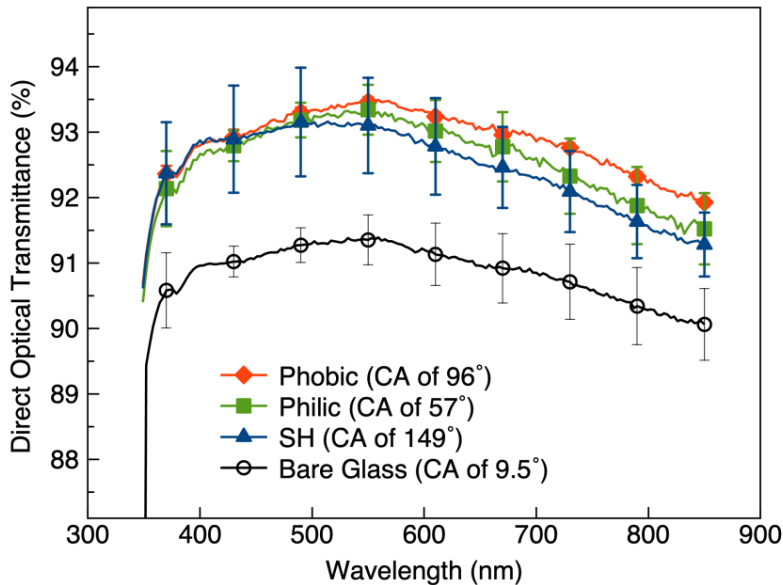


Fig. 3.3 Initial optical transmittance ($\% \tau$) of test samples: Phobic (CA = 96°) red, Philic (CA = 57°) green, SH (CA = 149°) blue and Bare glass (CA = 9.5°) black open circles.

spectrum, with the highest AR gain at 550 nm. The $\% \tau$ increase at 550 was $2.0 \pm 0.5\%$ for Philic samples, $2.2 \pm 0.2\%$ for Phobic samples, and $1.8 \pm 0.7\%$ for SH samples. Error bars indicate the standard deviation in transmittance values obtained.

The UV-vis transmittance measurements are recorded in direct transmission mode and so no forward scattering is included in the measurement. Forward scattering, which would further increase overall transmittance (and thus represent a further decrease in reflection from the coating), is not detected by this instrumental method.

3.3.3 Atomic Force Microscopy

Atomic force microscopy images of representative Bare, Hydrophilic-1 Hydrophobic-1 and SH surfaces are shown in Fig. 3.4; images of all samples are shown in Appendix Figure 3.12. RMS surface roughness values are summarized in Table 3.2. The Bare surface (Fig. 3.4a) is the smoothest with occasional circular features ~20 nm in height and average root mean square (RMS) roughness of 2 nm. The Hydrophilic-1 surface (Fig. 3.4b) exhibits a higher degree of roughness (average RMS = 11) with features up to ~ 80 nm in height. Hydrophobic-1 surface (Fig. 3.4c) exhibits less roughness (average RMS = 7 nm); with features up 70 nm. For the SH surface, the presence of high aspect ratio FEP fibers account for the high contact angles and Cassie-Baxter wetting state (Fig. 3.4d). The fibers are oriented parallel to the surface with the tips protruding upwards as high as 310 nm. Fiber diameters range from 50 nm to 200 nm and the average RMS roughness of this SH surface is 31 nm.

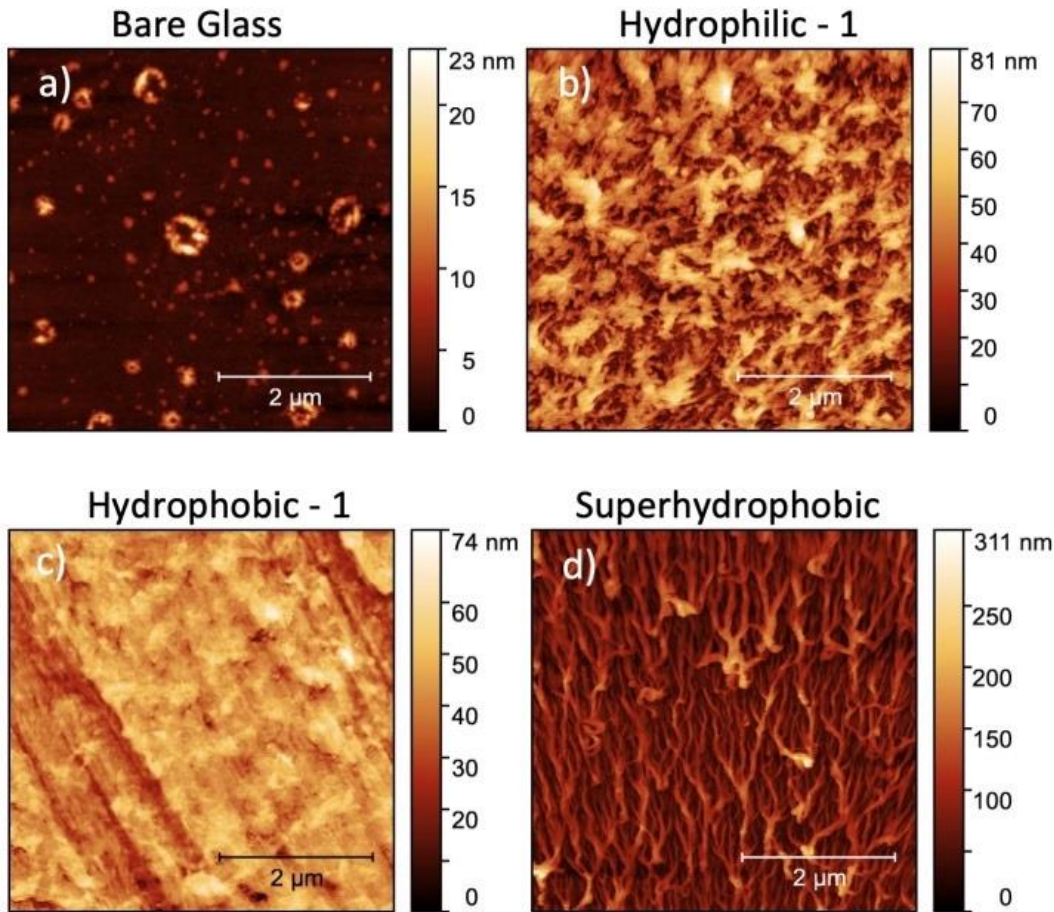


Fig. 3.4 AFM images of a) Bare glass (CA: 10°); b) Hydrophilic-1 (CA: 63°); c) Hydrophobic-1 (CA: 106°), and d) SH (CA: 149°).

3.3.4 Condensation Mechanisms

Condensation of water occurs by one of two well-known mechanisms, which depend upon the wetting properties of the surface; filmwise condensation occurs on hydrophilic surfaces, whereas dropwise condensation is observed on hydrophobic surfaces [22]. Consistent with these mechanisms and the CA values of the surfaces we studied, water condenses in a filmwise manner on unoiled Bare and Philic surfaces, but in a dropwise manner on Phobic and SH surfaces as shown for selected surfaces in Appendix Figure 3.13 and summarized in Table 3.2. The

condensation time was limited to prevent a contiguous liquid water film from forming on the surfaces.

The shape of the liquid water droplets that form on the surface is defined by the solid-liquid-vapor triple contact line (TCL), which is the intersection of solid, liquid and vapor phases found along the perimeter of a liquid droplet on a surface. [68], [69]. On a hydrophilic surface, the liquid-solid interactions are relatively strong compared to liquid-liquid interactions, which results in low CA values. For Bare and Philic surfaces, the TCL is irregularly shaped, indicating that liquid water

Table 3.1 Sample wetting properties

Surface Type	Sample Group	Sample Count [n]	Surface Designation	Contact Angle	Average Contact Angle
Uncoated Glass	Bare	8	Bare glass	$9.5^\circ \pm 1.2^\circ$	10°
Hydrophilic	Philic	2	Hydrophilic - 1	$62.8^\circ \pm 0.1^\circ$	57°
		2	Hydrophilic - 2	$51.2^\circ \pm 0.2^\circ$	
Hydrophobic	Phobic	2	Hydrophobic - 1	$105.6^\circ \pm 0.1^\circ$	96°
		1	Hydrophobic - 2	$87.3^\circ \pm 0.1^\circ$	
Superhydrophobic	SH	2	Superhydrophobic - 1	$148.7^\circ \pm 0.3^\circ$	149°

Table 3.2 Surface Roughness and Condensation Characteristics of Surfaces

Sample Name	Surface Type	Contact Angle	RMS Roughness (nm)	Condensation Type	Condensate Droplet Diameter (μm)
Bare glass	Bare	10°	2	Filmwise	1,100
Hydrophilic-1	Philic	63°	11	Filmwise	170
Hydrophilic-2		51°	6	Filmwise	
Hydrophobic-1	Phobic	106°	7	Dropwise	50
Hydrophobic-2		87°	7	Dropwise	
Superhydrophobic	SH	149°	31	Dropwise	40

becomes strongly pinned to the surface where solid-liquid interactions are the strongest. For Phobic and SH surfaces, the TCL is circular, which is the minimum contact line length theoretically possible. The circular TCL demonstrates that the solid-liquid interactions are relatively weak compared to liquid-liquid interactions. As a result, the droplet is mobile compared to liquid on a hydrophilic surface because the TCL can be more easily displaced. Owing to this mobility of the TCL, the diameter of a droplet on a hydrophobic surface contracts during evaporation, reducing the TCL length while maintaining a constant liquid-solid CA.

3.3.5 Soiling Rates and Soiling Mechanisms

3.3.5.1 Soiling on Condensate: Dust Deposition

This soiling deposition process was designed to simulate natural soiling on PV panels observed in the southwestern United States. An average soiling rate of 1.1% per week was reported in Arizona test sites during the winter months [45]. This soiling rate coincides with times when morning dew is also frequently observed. To simulate these conditions, dust deposition was conducted on coated glass samples on which water was allowed to condense for 2 minutes prior to soiling as described in section 3.4 above. Arizona Test Dust was deposited using the PDA.

Plots of soiling as a function of coating type and dust application cycle are shown in Fig. 3.5; soiling rates for uncoated and coated surfaces are summarized in Table 3.3. For Bare glass, the $\% \tau$ decreases linearly with each successive dust application cycle (Fig. 3.5a). The average rate of $\% \tau$ loss for Bare glass was 1.1% per dust application cycle, and the total decrease in $\% \tau$ is $5.7 \pm 1.8\%$ after five dew-dust- dry cycles. Philic coated surfaces exhibited essentially the same soiling rate as Bare glass, 1.3% per dust application cycle and total decrease in $\% \tau$ of $5.9 \pm 1.2\%$ after 5 dew-dust-bake cycles. In contrast, the $\% \tau$ decrease was 0.7% per dust application cycle for both Phobic

and SH surfaces whereas the combined average for Bare and Philic surfaces was 1.2% per cycle. Transmittance data for all surface coatings is shown in Fig. 3.14. The Phobic and SH coated surfaces exhibited 42% lower soiling rates than the average of bare glass and Philic surfaces as measured by the decrease in % τ per cycle (Table 3.3, column 3) and calculated using the formula:

(Equation 3.1) Decrease in Soiling Rate

$$\% \text{ Decrease in soiling rate} = \frac{|\%T \text{ loss}_{\text{Hydrophobic}} - \%T \text{ loss}_{\text{Hydrophilic}}|}{\%T \text{ loss}_{\text{Hydrophilic}}} \times 100\%$$

Optical micrograph image analysis was also used to calculate the soiling rates on Bare and coated glass substrates, with results plotted in Fig. 3.5b and summarized in Table 3.4. On Bare and Philic coated glass, soiling proceeds in a linear fashion, at a rate of 1.2% per application, with a total surface coverage after 5 dust cycles of 6%. Phobic and SH coated again exhibit lower soiling

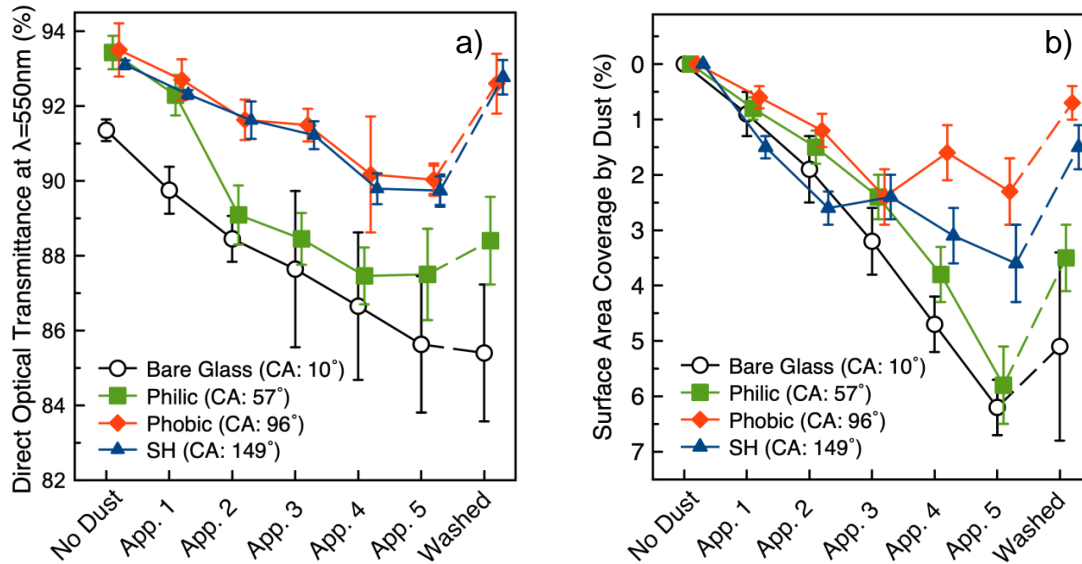


Fig. 3.5 a) Transmittance (%) at 550nm as a function of dust application cycles for solar glass with different coatings: Bare glass (black circles); Philic (green squares); Phobic (red rhombus); and SH (blue triangle); b) Surface Area Coverage (%) as a function of dust application cycles for solar glass with different coatings Bare glass (black circles); Philic (green squares); Phobic (red rhombus); and SH (blue triangle).

rates of $0.5 \pm 0.7\%$ and $0.7 \pm 0.6\%$ with average surface area coverages of $2.3 \pm 0.3\%$ and $3.6 \pm 0.3\%$, respectively. Percent of surface area covered by dust for all surfaces is shown in Fig. 3.15.

Comparing results in Fig. 3.5 and Tables 3.3 and 3.4 demonstrates that dust surface coverage measured by microscopy image analysis correlates well with $\%t$ measurements. These methods are complementary; direct transmittance quantifies the amount of light lost due to scattering whereas the image analysis method provides insight into the distribution of dust particles on the surface and thus the anti-soiling mechanism. Moreover, the microscopy techniques are easier to implement in the field [70].

Table 3.3 Optical Transmittance Changes after Soiling on Condensate and Subsequent Cleaning

Surface Type	Average Transmittance Decrease per Soiling Cycle ($\%t$)	Transmittance Decrease after 5 Soiling Cycles ($\%t$)	Transmittance Recovered after Cleaning ($\%t$)	Percent Transmittance Recovered after Cleaning (%)
Bare	1.1	5.7 ± 1.8	-0.2 ± 1.8	-4 ± 32
Philic	1.3	5.9 ± 1.2	$+0.9 \pm 1.2$	15 ± 20
Phobic	0.7	3.5 ± 0.6	$+2.6 \pm 0.4$	75 ± 18
SH	0.7	3.4 ± 0.8	$+3.0 \pm 0.4$	90 ± 13

Table 3.4 Surface Area Coverage by Dust Changes after Soiling on Condensate and Subsequent Cleaning

Surface Type	Surface Area Coverage Increase per Soiling Step (%)	Surface Area Increase after 5 Soiling Cycles (%)	Surface Area Coverage after Cleaning (%)
Bare	1.2 ± 0.3	6.2 ± 0.2	5.1 ± 1.7
Philic	1.2 ± 0.6	5.8 ± 0.3	3.5 ± 0.5
Phobic	0.5 ± 0.7	2.3 ± 0.3	0.7 ± 0.3
SH	0.7 ± 0.6	3.6 ± 0.3	1.5 ± 0.4

3.3.5.2 Anti-Soiling Mechanism on SH and Phobic Coated Glass

Two mechanisms were observed to reduce the soiling rates on Phobic and SH coatings compared to Philic and Bare glass substrates: dropwise condensation and droplet mobility during evaporation. The surface energy of the coating determines how water condenses onto surfaces: filmwise condensation occurs on Bare and Philic glass surfaces whereas dropwise condensation occurs on Phobic and SH surfaces [71], [72]. The diameter of water droplets condensed on soiled hydrophobic surfaces ranged from 35 μm to 590 μm with a mean diameter of $180 \mu\text{m} \pm 150 \mu\text{m}$ (Fig. 3.6a).

In the presence of condensate, Arizona Test Dust was observed to more readily adhere to wetted regions compared to dry regions of the surface, which is consistent with the hydrophilic nature of the silica-containing dust. Thus, on a hydrophilic surface that undergoes filmwise condensation, the dust is spread over the large, wetted regions (mm's in diameter), whereas on hydrophobic surfaces that undergo dropwise condensation, the dust becomes concentrated in the small, 40-200 μm diameter condensate droplets.

The mobility of liquid water on surfaces during evaporation of the condensate determines the mechanism by which dust is ultimately deposited on the surfaces. On a hydrophilic surface, liquid water films are pinned along the perimeter due to the strong attractive forces between water and glass, resulting in constant contact line evaporation [73]. As this liquid evaporates, the thickness of the liquid decreases while the TCL (i.e. the solid-liquid-vapor perimeter) remains pinned. During evaporation of water on soiled glass surfaces, convection within the liquid disperses dust agglomerates throughout the liquid. After the liquid evaporates, dust is distributed across the entire area initially occupied by water as shown schematically in Fig. 3.7.

In contrast, evaporation on a soiled hydrophobic surface proceeds by a different mechanism because condensed water forms as small droplets that are highly mobile as shown schematically in Fig. 3.7. As evaporation proceeds, the contact angle remains constant [73], and the TCL of these droplets shrink in order to maintain this constant receding CA, reducing the diameter of the droplets. Eventually, when the droplet becomes sufficiently small ($91 \mu\text{m} \pm 72 \mu\text{m}$) the TCL becomes pinned to the surface and evaporation proceeds by vertical shrinkage of the drop height. Dust particles remain dispersed in the liquid water and so stay within the droplet during evaporation. As the droplet contact area with the surface decreases, dust particles are concentrated or “herded”, keeping them within the ever-shrinking TCL. As a result, concentrated piles of dust

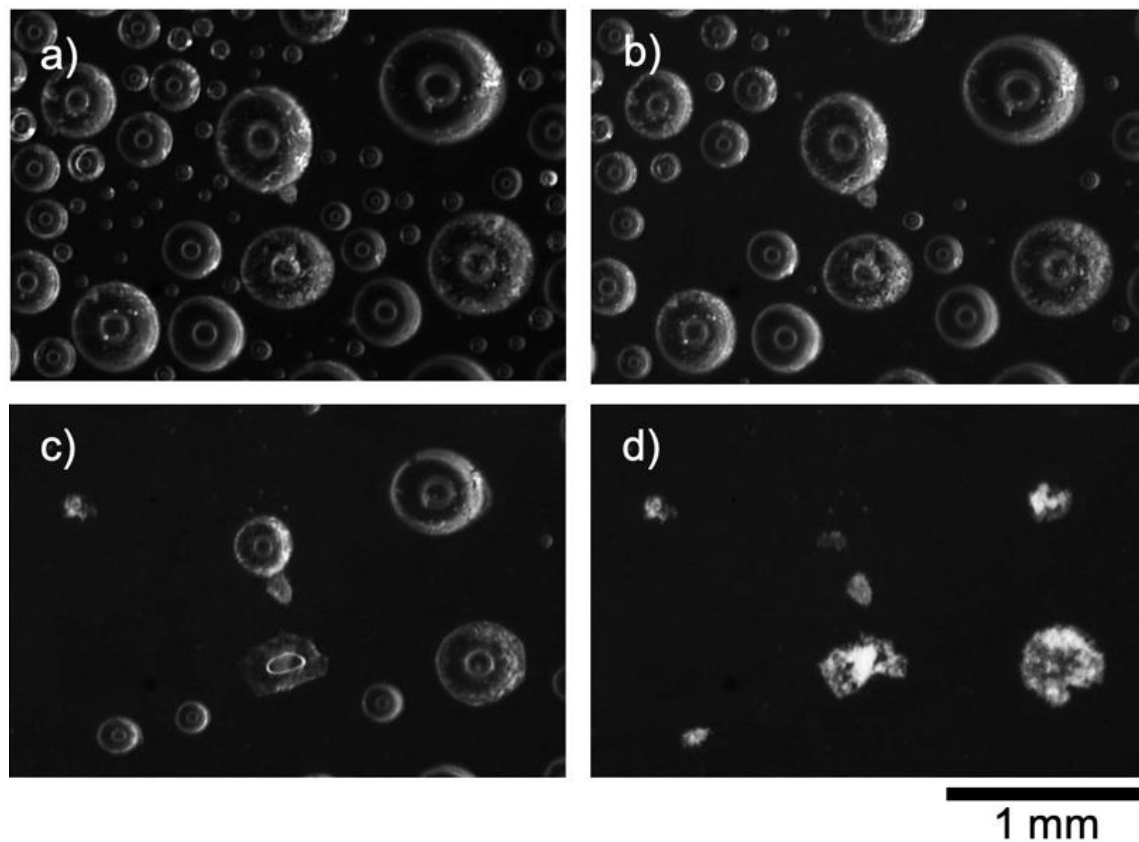


Fig. 3.6 Sequence of enhanced optical microscope images during evaporation of condensate drops on soiled Hydrophobic-1 surface on surface heated to 50°C : a) Before evaporation, b) after 60 seconds, c) after 100 seconds, d) after total evaporation. Note piles of herded dust after evaporation.

are formed, and the region previously covered by liquid is cleaned, as shown in Fig 3.6 and a larger area in Fig 3.16. Note, the smallest droplets evaporate most rapidly.

To better observe the dust herding mechanism, a larger droplet of water ($2 \mu\text{L}$) was placed on dusted Bare glass and Hydrophobic-1 surfaces using a micro-pipet and evaporation was observed under the stereomicroscope. Evaporation of a drop on Bare glass highlights the pinning of the TCL and dispersion of dust within the liquid by evaporation induced convection (Figs. 3.8 a & c). On the Hydrophobic-1 surface, the $2 \mu\text{L}$ droplet forms a CA of 110° as observed in Fig. 3.8b. During evaporation, movement of dust particles along with the droplet is clearly visible as the TCL contracts. Thus, the dust particles are herded into a small pile leaving the majority of the surface clean (Fig. 3.8 d).

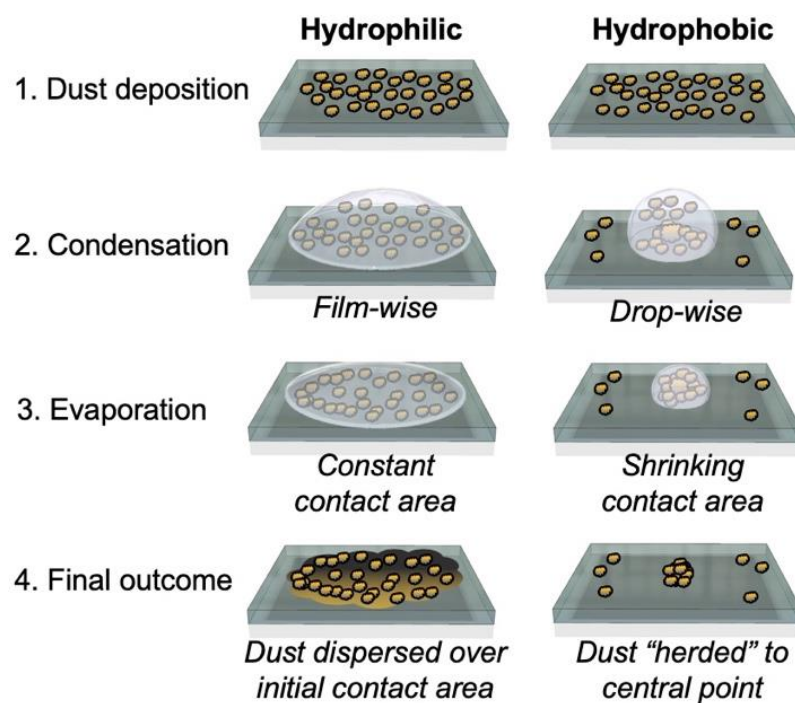


Fig. 3.7 Cartoon illustrating the dust herding mechanism observed on the hydrophobic surface.

Assessing the results from the AFM images, condensation observations and soiling rate measurements, we conclude that the water contact angle of a surface is the primary material property responsible for the anti-soiling mechanism observed in the presence of condensed water reported in this paper. Several types of dust-surface forces have been shown to contribute to soiling mechanisms as a function of environmental conditions. For example, rough surfaces can reduce soil adhesion in dry environments by limiting particle-surface contact area thereby reducing the Van der Waals interactions [17], [20], [74]. In humid environments, capillary forces have been shown to predominate over Van der Waals forces [15], [16], [20]. Increasing the relative humidity of the test environment up to 70% leads to increased particle-surface adhesion forces on hydrophilic surfaces; the magnitude of this effect increased with decreasing roughness [20]. Thus, humidity is more significant on smoother surfaces where the meniscus covers a relatively large fraction of the surfaces. However, in a condensing environment where liquid water is present (e.g. dew), the particle-surface adhesive strength depends upon the relative strength of the chemical interactions at three different interfaces: soil particles with the surface, soil particles with the surrounding water; and liquid water with the solid surface. It has been shown that silica soil particles develop strong chemical bonds to glass upon evaporation of liquid water droplets through cementation and related reactions [15], [19]. The strong interactions between water and glass surfaces are well known; this results in water drops being pinned to hydrophilic surfaces. Roughness would not play a major role on a hydrophilic surface because there is sufficient water to fill any nano-scale or micro-scale features that might be present. In contrast, a surface coated with a hydrophobic polymer is chemically unreactive towards most dust particulates so adhesion forces between these two materials would be lower than on uncoated glass; yet adhesion forces between oxide dust particles and water remain strong. Moreover, adhesion forces between liquid

water and the hydrophobic surface coating are lower than on glass. The magnitude of this difference is reflected in the contact angle of water on the surface; a higher contact angle indicates weaker liquid-surface interactions. Because of these weaker water-surface forces, as well as the strong particle-water interactions, the water droplet is easily displaced and the hydrophilic soilant particles will move along with the movement of the droplet. Thus, mobility of liquid water droplets governs soiling behavior in the presence of condensate and the contact angle can be used as a parameter to predict anti-soiling behavior.

3.3.5.3 Soiling on a Dry Surface Followed by Condensation

The dust herding mechanism is effective even when dust is first deposited on a dry surface that is subsequently exposed to condensation. As shown in Fig. 3.9, dust deposits uniformly over both Bare glass and Hydrophobic-1 coated surfaces. The CDA apparatus was used to deposit sufficient dust that 13% of the area was covered, as measured by image analysis. During exposure to a humid environment under the stereomicroscope, water condensed in a filmwise manner on the dust-coated Bare Glass surface (Fig. 3.9c). A close examination of this image shows that the dust becomes re-suspended and partially de-agglomerates in the liquid water. After drying, the dust becomes redistributed with regions that appear lightly coated with de-agglomerated dust whereas other regions are more heavily coated as shown in Fig. 3.9e. Although the surface visually appears different from the original appearance (Fig. 3.9a), there is no net change in dust surface area coverage as measured by image analysis.

On the Hydrophobic-1 surface, ~30 μm diameter droplets formed during condensation of water on the dusted surface under the microscope (Fig. 3.9d). Upon drying, the dust became concentrated (Fig. 3.9f) showing the characteristic dot pattern that was observed when dust was deposited onto a surface on which water had previously been allowed to condense. The impact of the hydrophobic

coating is significant. Exposure to condensation after dust deposition reduced the percentage of the surface obstructed by dust, as measured by image analysis, from 15.3% to 11.1%. No dust was removed; however, the mobility of condensed water droplets herded the dust into discrete piles that reduce overall scattering losses and thus imparts anti-soiling properties.

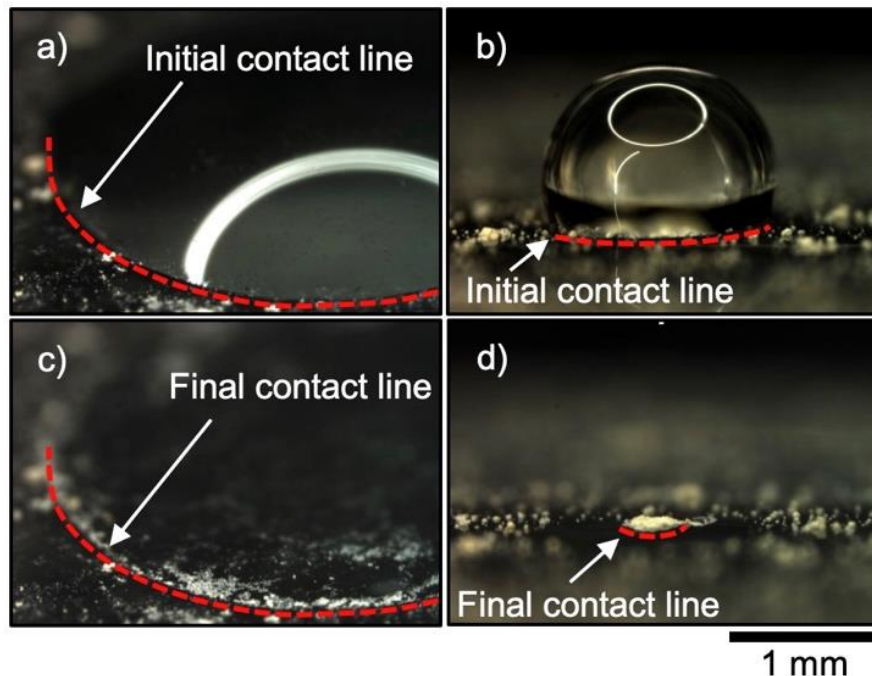


Fig. 3.8 Water drop ($2.0 \mu\text{L}$) placed on glass substrates after soiling without condensate (CDA) on a) Bare glass, and b) hydrophobic coated glass; surfaces after evaporation of the water drop on c) Bare glass and d) hydrophobic coated glass. Red dashed line indicates location of initial and final TCL.

Similarly, the loss of optical transmission through the sample is not affected by the sequence of dew and dust application. Applying dust first onto a dry glass surface vs. condensing water prior to dust deposition results in essentially the same rates of $\% \tau$ decrease for both Bare glass ($4.1 \pm 1.3\%$ vs. $3.9 \pm 1.7\%$) and hydrophobic glass ($1.9 \pm 0.7\%$ vs. $2.1 \pm 0.9\%$) respectively as shown in Appendix Fig. 3.17. Control experiments where surfaces were not exposed to a condensing

environment exhibited no difference in soiling properties regardless of coating type. For Bare glass and SH coated surfaces in the absence of condensed water, the same soiling rate of 6.1% per dust application cycle using the CDA apparatus was observed as shown in Fig. 3.18.

3.3.6 No-Touch Cleaning on Coated Surfaces

For hydrophilic samples, dispensing 3.0 mL of water on the tilted surfaces (no-touch cleaning) has a relatively small impact on the optical transmittance as shown in Fig. 3.5. Bare glass shows essentially no change in $\% \tau$ after cleaning; the $\% \tau$ decreases by $0.2 \pm 1.8\%$. The Philic coated glass surfaces clean more effectively than Bare glass, but recover only $0.9 \pm 1.2\%$ of the original $\% \tau$ value. In contrast, no-touch cleaning nearly completely restores the transparency of the Phobic and SH coated glass surfaces; 99.6% of the original $\% \tau$ is restored as shown in Fig. 3.5a and Table 3.3. Image analysis of dust on coated and bare surfaces demonstrates the same trends as the direct transmittance results shown in Fig. 3.5 and Tables 3.3 and 3.4. Photos of a soiled (after 5 dew-dust-dry cycles) and cleaned Bare and Phobic glass are shown in Fig. 3.19.

Poor cleaning effectiveness observed on Bare and Philic-coated glass occurs because the dispensed water strongly wets the underlying glass (see Fig. 3.19c). Dispensed water droplets wet the Philic glass surface as soon as the liquid contacts the dusted surface. The initial droplets become pinned to the surface and do not flow downslope. Subsequently dispensed water droplets add to this pinned droplet until the mass becomes sufficiently large that it overcomes the TCL force and begins to flow down the surface. As it flows, it creates a feature in the dust coating similar to an erosion gully. Additional cleaning water will follow this same path until the lateral translation of the sample under the syringe is sufficiently large that a new gully forms. This process leaves the surface partially cleaned, with some areas unaffected by the cleaning water. Because

of this wetting mechanism, mechanical brushing would be needed to clean dust from the entire hydrophilic surface, especially when limited water is available. The large variance in direct transmittance measurements arise from this inhomogeneous dust-removal process.

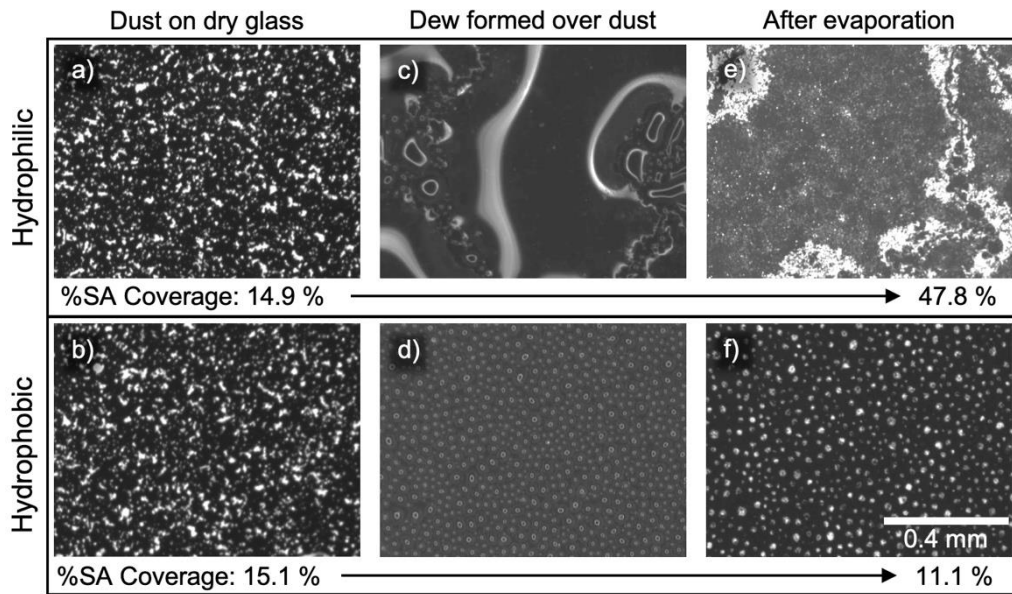


Fig. 3.9. Optical microscope images after dust deposition onto dry surfaces a) Bare glass and b) hydrophobic coated glass with CA of 110° ; after exposure to a condensing environment for 2 minutes for c) Bare glass and d) hydrophobic glass; and after evaporation of condensate droplets e) Bare glass and f) hydrophobic coated glass; where %SA = % Surface Area.

In contrast, on Phobic and SH coated glass, droplets released from the syringe tip immediately travel downslope, imbibing dust particles along the. Unlike on hydrophilic substrates, the droplets do not wet the glass or spread along the surface. Because of the weak interactions between water and coating, the droplet path is straight as it proceeds downslope. This enables the entire surface to be cleaned as the glass is translated under the dispenser. The facility with which dust particles transfer from the coated surface to the droplet demonstrate how the wetting forces between dust and water are stronger than those that might develop between dust and Phobic and SH coatings, even after 5 dew-drying cycles.

Droplets on the SH surface exhibit higher CA values and so contact a smaller portion of the surface. Thus, each drop cleans a relatively narrow swath of the surface. Because of the limited contact area between liquid and surface, the droplets tend to bounce off the surface. These two effects combine such that small areas of the SH surface escape contact with water and so remain soiled. This type of partial cleaning is a function of drop volume, drop frequency and translation rate. However, under the same no-touch washing conditions, the hydrophobic surface is completely cleaned, because each droplet contacts a larger area of the surface due to the lower contact angle. Moreover, droplets do not jump and so no region of the surface is left un-washed. Thus, hydrophobic coatings may be preferable over superhydrophobic coatings in certain conditions, such as light rain.

The lack of wetting of the hydrophobic substrates was corroborated by the amount of water collected after washing. For the Bare glass surface, only $85 \pm 21\%$ of the water was retrieved after washing, which means that an average of 15% of the water was retained on the glass and/or absorbed into the dust. In comparison, more than $98 \pm 1\%$ of the water was recovered from the hydrophobic coated surface. This collected water could be filtered and reused for additional cleaning cycles, or other applications, such as agriculture.

3.4 Conclusions

The presence of dew increases the rates of soil accumulation and must be considered when examining anti-soiling effects. To gain insight into the mechanisms by which coatings reduce the impact of soiling, a series of fluoropolymer coatings were prepared on low-iron soda-lime glass substrates where the surface wetting properties were systematically varied. Coatings were prepared by laminating a high molecular weight fluorinated ethylene-propylene (FEP) polymer to

clean glass surfaces followed by peeling away excess polymer. By controlling process parameters, coating wetting properties ranging from superhydrophobic to hydrophilic (CA values from 149° to 51°) were prepared. The effects of these wetting properties on both soiling behavior in controlled environments, as well as no-touch cleaning properties, were studied.

Philic coated glass, like the Bare glass controls, exhibited no significant anti-soiling behavior. In contrast, Phobic and SH coatings imparted significant anti-soiling properties in the presence of simulated dew. Soiling rates decreased from 1.3% to 0.7% per dust application cycle for Philic and Phobic/SH coatings respectively. Similar reduced soiling rates were observed for both Phobic and SH coatings, regardless of the sequence in which dust and simulated dew were deposited on the surface. The chemical composition of soil particles was shown to affect soiling mechanisms, such that compounds that partially dissolve or react with water (i.e. CaCO₃ and Portland cement) soil at a higher rate than compounds that are insoluble (i.e. Arizona Test Dust) or include highly soluble NaCl (Aramco Dust)[75].The hygroscopic nature of dust particles may also affect water condensation and soiling rates; such compounds are the focus of our current research.

Two mechanisms were observed to account for this anti-soiling behavior on hydrophobic surfaces: condensation mode and droplet mobility. On hydrophilic substrates, filmwise condensation occurs such that the surface of the glass is covered by pools of thin water films. In contrast, dropwise condensation occurs on a hydrophobic coating such that the surface is covered by an array of liquid water droplets with an average diameter of 40-200 µm. The second mechanism, droplet mobility, relates to the fate of condensed water during evaporation (i.e. drying). On hydrophilic surfaces (Philic and Bare glass), the relatively strong liquid-solid interactions pin the TCL, resulting in vertical shrinkage of the water regions, which promotes dispersal of the dust over the entire wetted surface. In contrast, the high droplet mobility on

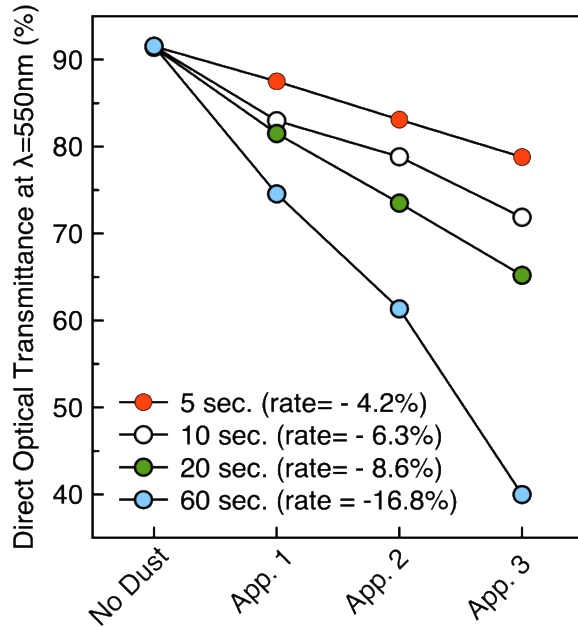
hydrophobic surfaces (Phobic and SH) enables droplets to shrink horizontally during evaporation. As the droplet diameters decrease, dust within the evaporating droplets is “herded” along with the decreasing TCL perimeter. As a result, the dust becomes concentrated into isolated piles, leaving the surrounding surface clean. Phobic coated surfaces on which dust was deposited before exposure to condensation (CDA method) exhibited the same anti-soiling mechanisms as when dust was deposited on a surface covered with condensed water droplets (PDA method).

The wetting properties of the coatings not only affect the anti-soiling properties of the solar cover glass surface, but they also affect the ease with which the surfaces can be cleaned. The relatively high surface energy of hydrophilic surfaces causes droplets to interact strongly with and spread out over the surface. As a result, the water is absorbed along the interface, keeping the dust on the surface and facilitating chemical reactions between dissolved components from the dust and the glass. The low surface energy of the Phobic and SH fluoropolymer coatings allows water droplets to slide straight down the surface because they interact weakly with the surface. In this way, dust along the path is imbibed into the droplet and carried off the surface.

This work provides evidence that hydrophobic coatings impart both anti-reflective and anti-soiling properties to solar cover glass, which can be especially useful in arid regions where natural dew frequently occurs. Moreover, the low surface energy of the coatings facilitates cleaning. Recent work has demonstrated that FEP coating on glass exhibit transparency and contact angles after 2000 hours of artificial UV weathering tests [75]. Thus, hydrophobic FEP coatings offer the potential to both reduce energy losses from reflections and soiling, as well as reduce operation and maintenance costs associated with cleaning, and so lower the overall LCOE of solar PV energy.

3.5 Appendix

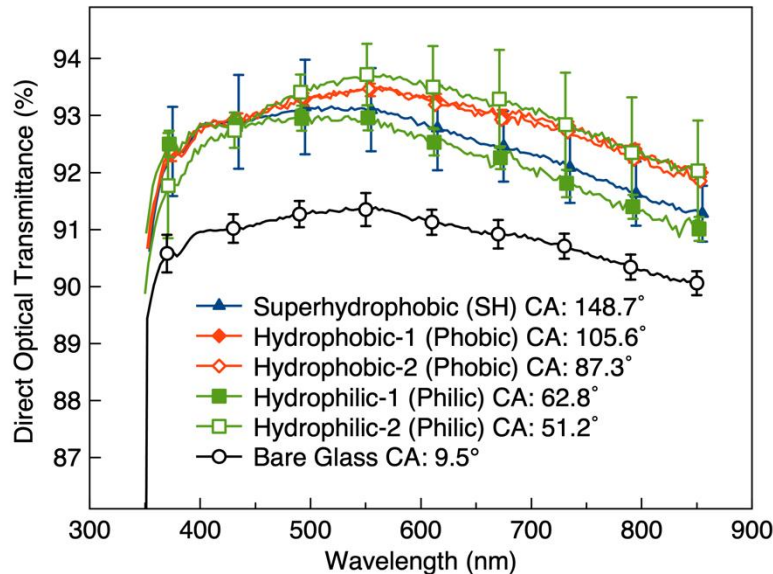
Fig. 3.10 Soiling rate using CDA (cloud deposition apparatus) measured by a decrease in $\% \tau$ at $\lambda=550\text{nm}$ as a function of dust exposure time (open-door time).



Percent Transmittance at 550nm as a function of dust application cycle for Bare glass soiled via CDA method for 5 sec. (red), 10 sec. (empty), 20 sec. (green) and 60 sec. (blue)

Dust deposition on the surface of Bare glass was measured in the Cloud dust apparatus (CDA) as a function of exposure time (i.e. the time that the door between the Aluminum Connector (Fig. 3.2b) and the sample was held open). When the door is open the dust suspension (cloud) that accumulated in the duct and connector can settle on the glass sample under the force of gravity. An open-door time of 10 seconds was selected for the experiments using the CDA method in order to control the quantity of dust deposited while insuring reproducible dust deposits.

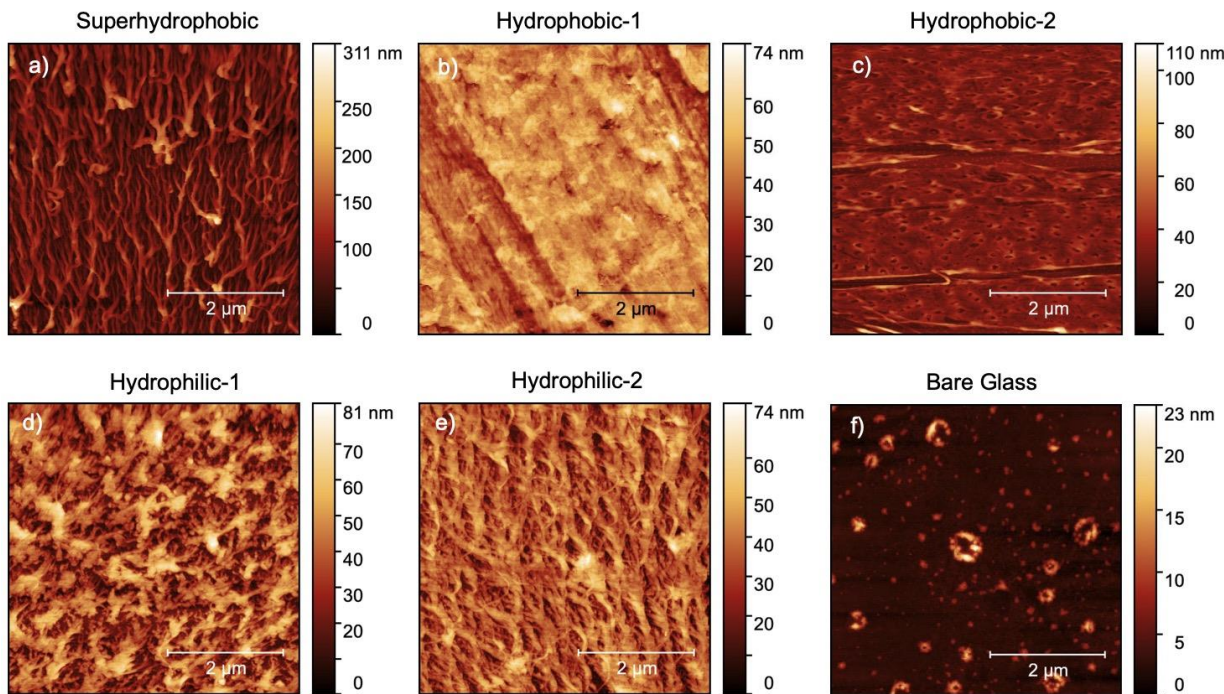
Fig. 3.11 Initial Direct Light Percent Transmittance (% τ)



Direct light percent transmittance for all types of coated and bare low-iron solar glass measured from 350nm – 850nm. Each plot is an average of multiple scans recorded from one or more samples as detailed below.

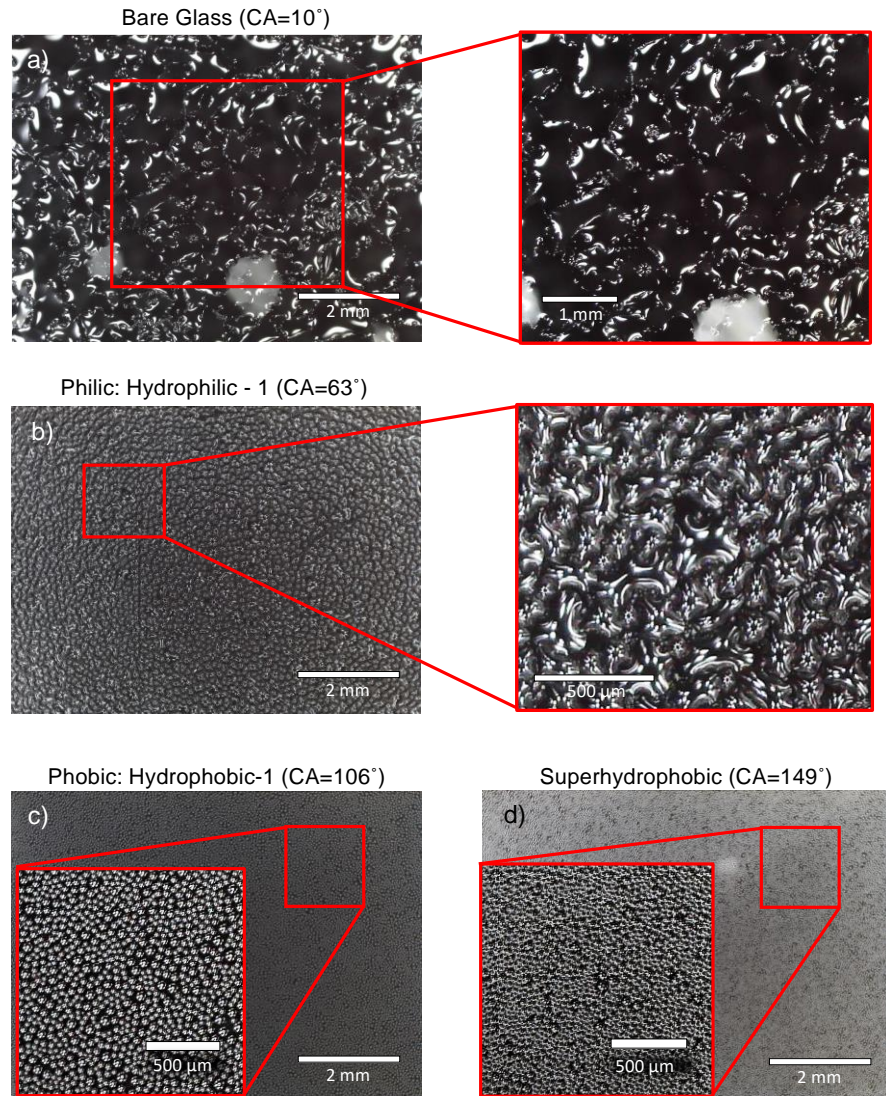
Initial direct optical transmittance measurements were obtained for all uncoated and coated glass surfaces. The measurements were obtained in the range of 350nm to 850nm. The surfaces used in the experiments were: Superhydrophobic (2 samples), Hydrophobic-1 (2 samples), Hydrophobic-2 (1 sample), Hydrophilic-1 (2 samples), and Hydrophilic-2 (2 samples). Each sample was measured three times, with each measurement taken in a different location within a 2 cm radius of the center of the sample. Figure 3.11 shows the average of 6 scans taken per sample (with exception of Hydrophobic-2: 3 scans); the error bars span 1 standard deviation from the mean.

Fig. 3.12 Atomic Force Microscopy (AFM) Images of Test Surfaces



Atomic force microscopy (AFM) images of all coated surfaces and bare glass control. Root mean square (RMS) roughness was calculated for all of the surfaces to be: a) Superhydrophobic = 31 nm, b) Hydrophobic-1 = 7 nm, c) Hydrophobic-2 = 7 nm, d) Hydrophilic-1 = 11 nm, e) Hydrophilic-2 = 6 nm, and f) Bare glass control = 2 nm.

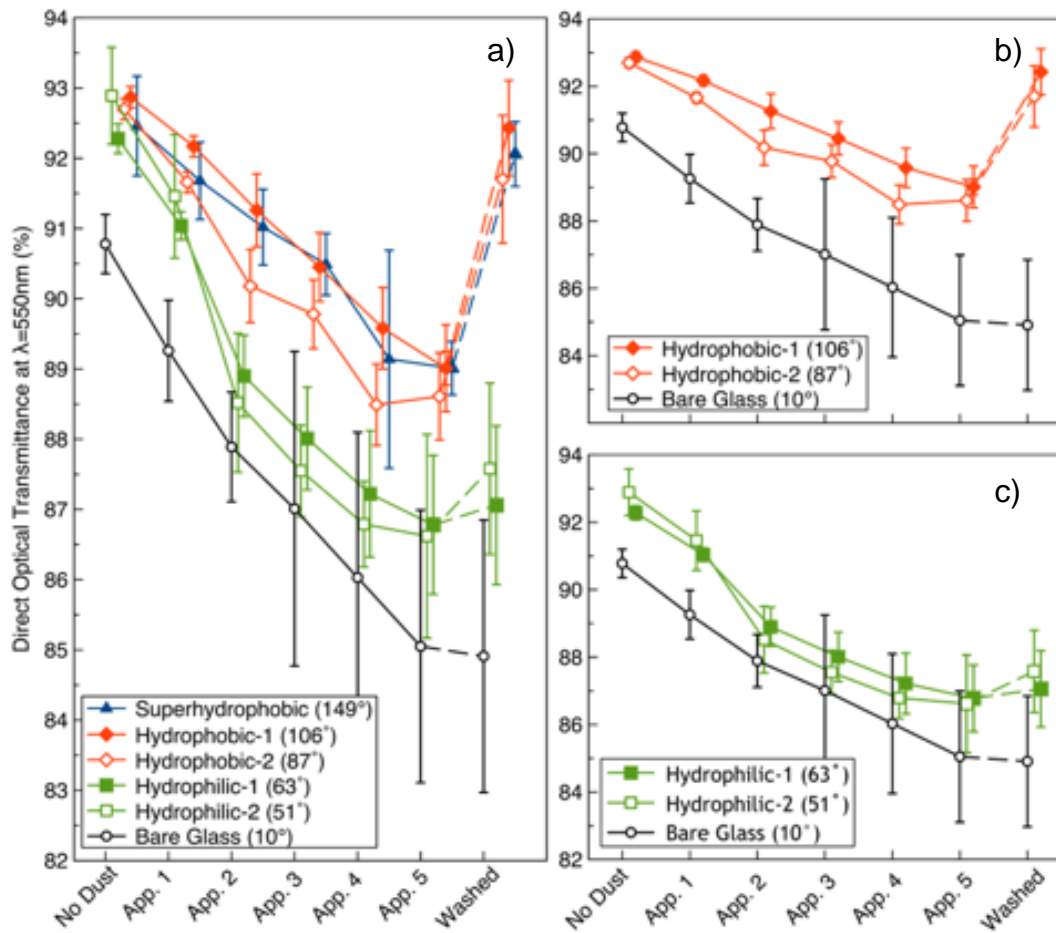
Fig. 3.13 Microscopy Images of Condensed Water on Test Surfaces



Water condensate (dew) layer type (filmwise vs. dropwise) and dew layer/droplet geometry were evaluated on coated and bare glass control surfaces. The surfaces were cooled to 10 °C in an environment with relative humidity (RH) ~70%. The water was allowed to condense on the surface for 2 minutes. No dust (artificial soilant) was applied to the surface. Bare glass control (a) surfaces have shown to condense dew in filmwise manner, with observable water “puddles” extending up to 4 x 4 mm, with largest water puddles being 6-7 mm² in area. Hydrophilic-1 surface (b) was selected for water layer analysis, with filmwise condensation forming water puddles of 500 x 500

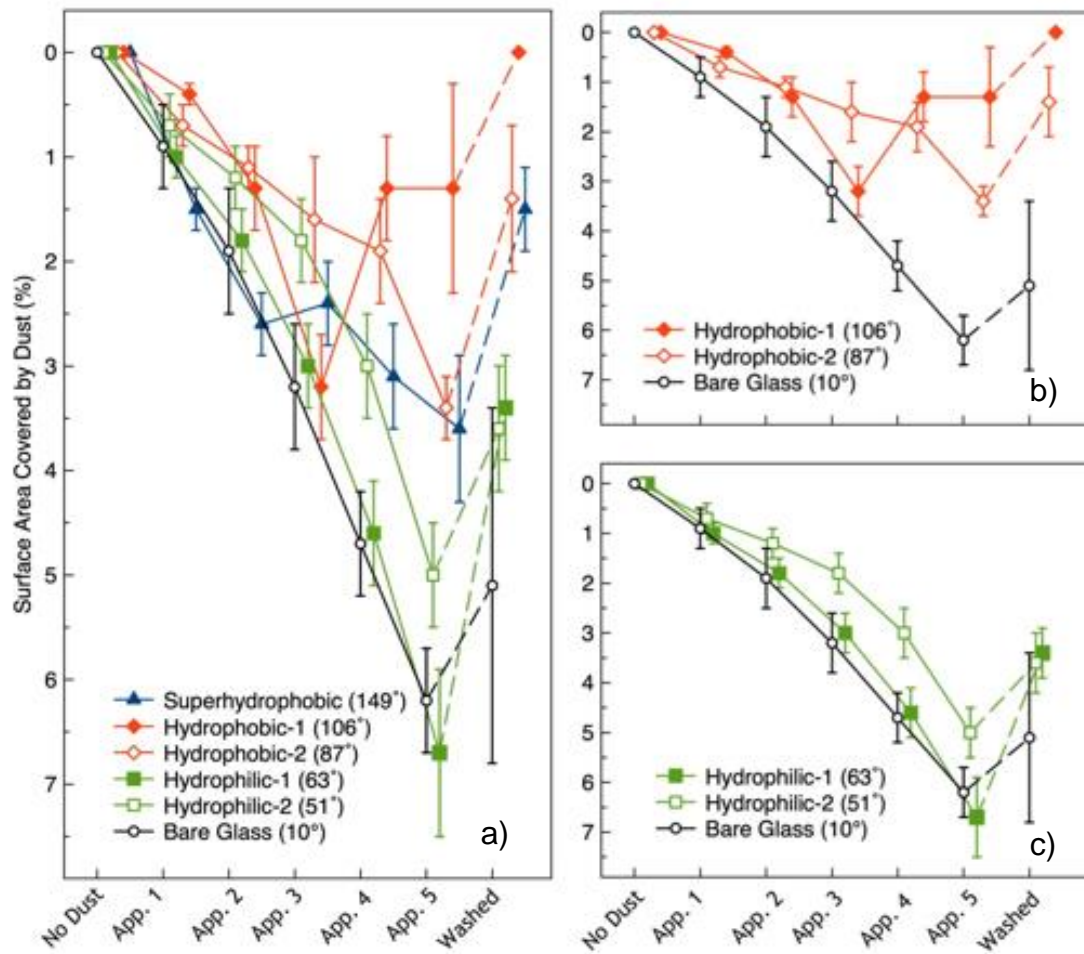
μm , and occupying areas of up to $6 \times 10^{-2} \text{ mm}^2$. Hydrophobic-1 surface has shown to condense water in dropwise manner, with water drops of $\sim 80\mu\text{m}$ in diameter. Superhydrophobic surface was observed to condense water in dropwise manner as well, with water drops being $\sim 70 \mu\text{m}$ in diameter.

Fig. 3.14. Soiling plots of all individual samples: Percent Transmittance at 550 nm



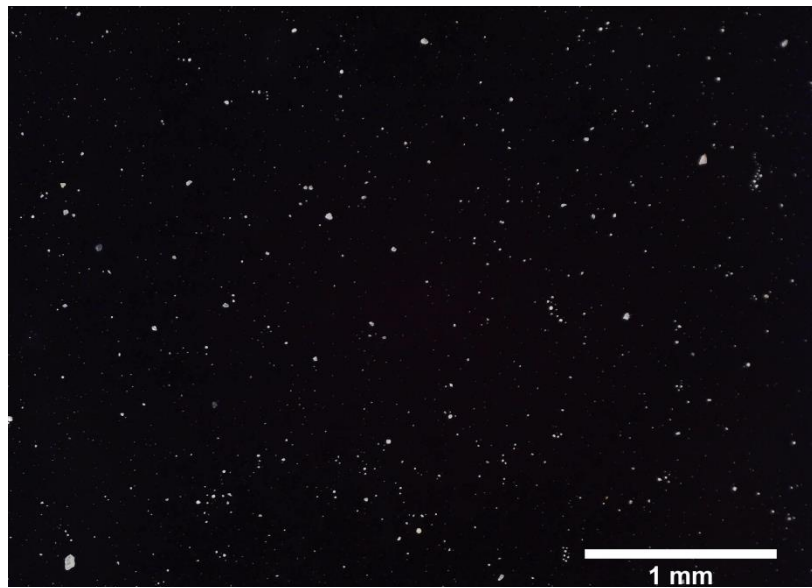
Direct light percent transmittance measured at 550 nm plotted as a function of the number of soiling cycles and one cleaning cycle for coated surfaces and bare glass controls (a); all five coated surfaces plotted on the same graph (b); plots of the two types of hydrophobic coatings compared to bare glass where these two plots of Hydrophobic-1 and Hydrophobic-2 were averaged together to form the plot labeled Phobic in Figure 3.5a; plots of the two types of hydrophilic coatings compared to bare glass where these two plots of Hydrophilic-1 and Hydrophilic-2 were averaged together to form the plot labeled Philic in Figure 3.5a.

Fig. 3.15. Soiling plots of all individual samples: Percent Surface Area Covered by Dust



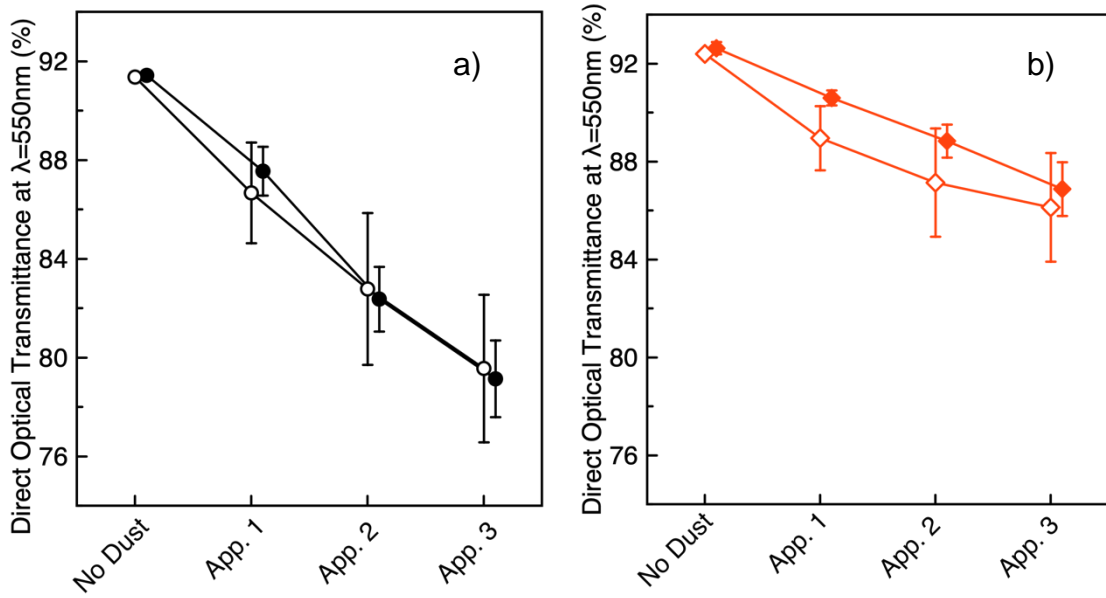
Percent surface area covered by dust plotted as a function of the number of soiling cycles and one cleaning cycle for coated surfaces and bare glass controls (a); all five coated surfaces plotted on the same graph (b); plots of the two types of hydrophobic coatings compared to bare glass where these two plots of Hydrophobic-1 and Hydrophobic-2 were averaged together to form the plot labeled Phobic in Figure 3.5b; plots of the two types of hydrophilic coatings compared to bare glass where these two plots of Hydrophilic-1 and Hydrophilic-2 were averaged together to form the plot labeled Philic in Figure 3.5b.

Fig. 3.16. Large Area View of Hydrophobic Coated Glass After One Dew-Dust-Dry Cycle



Optical microscope image of a hydrophobic coated glass surface after one dew-dust-dry cycle illustrating the effect of the dust-herding mechanism creating isolated piles of dust, leaving the majority of the surface clean.

Fig. 3.17. Effect of Soiling Sequence: Dust Deposited on Condensate vs Condensation onto a Dust-coated Surface.



Percent transmittance at 550nm as a function of dust application cycle for bare glass under SAC method (open circles) and SBC method (filled circles)

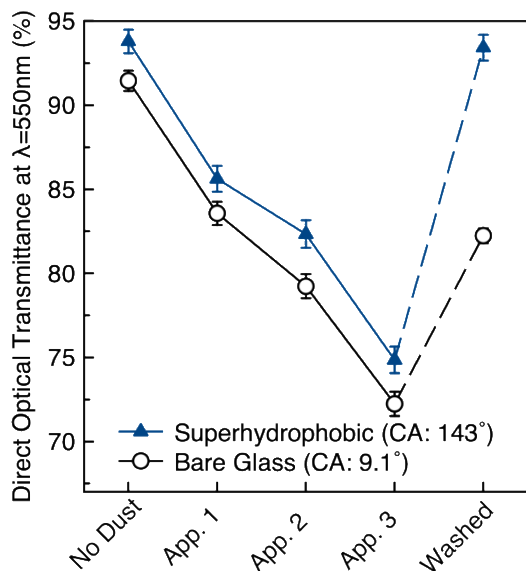
Percent transmittance at 550nm as a function of dust application cycles for Hydrophobic-1 coated glass under SAC method (filled red) and SBC method (open red)

In order to identify how soiling rates are affected by the sequence of dust and condensate applications, two different sequences were used inside the CDA apparatus at 70% RH. Using the procedure reported in **section 3.2.4** of the paper, water was allowed to condense for 2 mins first, followed by dust deposition. This process is called Soiling After Condensation (SAC). In the second sequence, dust was deposited on the surface first, followed by 2 mins of condensation, as reported in **section 3.2.5**. This process is called Soiling Before Condensation (SBC).

The soiling rate for Bare glass samples using the SAC and SBC methods are the same within experimental error. Soiling rates of $4.1 \pm 1.3\%$ and $3.9 \pm 1.7\%$ per dust application were observed for the SAC and SBC methods, respectively as shown in Fig. 3.17a. Similarly, the soiling rates on the Hydrophobic-1 coated glass samples were very similar. Soiling rates of $1.9 \pm 0.7\%$

and $2.1 \pm 0.9\%$ per dust application were observed for the SAC and SBC methods respectively as shown in Figure 3.17b. Thus in both cases, the soiling rates did not depend on the dust deposition and condensation sequence. The dust herding mechanism operates equally effectively, regardless of dust-dew sequence. The hydrophobic coating exhibits significant anti-soiling properties as the overall soiling rate on Hydrophobic-2 coated glass is approximately half the rate observed on Bare glass.

Fig. 3.18. No-Touch Cleaning after Dry Soiling



Percent Transmittance at 550nm as a function of dust application cycle without condensate for bare, uncoated, solar glass (black open circles) and SH coated glass (contact angle of 148° - blue filled triangle).

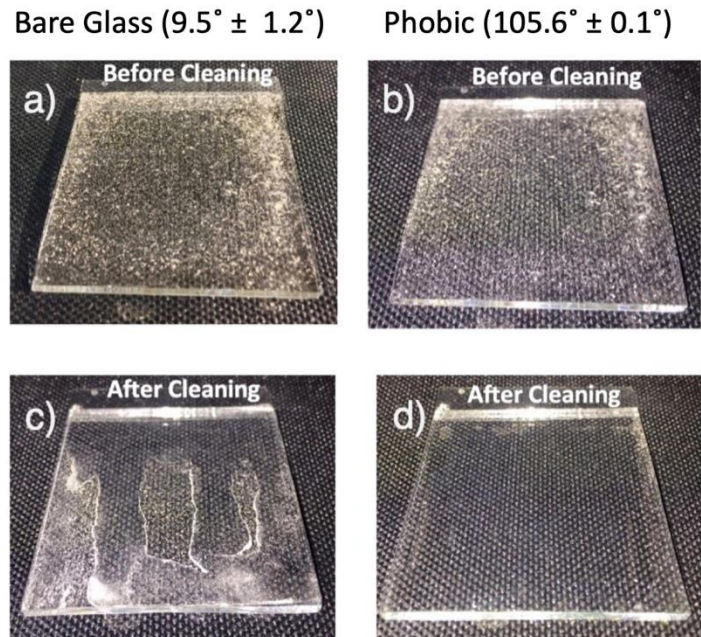
As a control experiment, surfaces were *not* exposed to a condensing environment (i.e. no dew) during dust deposition. Bare glass and SH coated surfaces, in the absence of condensed water, exhibited essentially the same soiling rates of $6.0 \pm 0.1\%$ for Bare glass and $6.2 \pm 0.1\%$ for SH surfaces per dust application cycle using the CDA apparatus as shown in Supplementary Fig. 3.18. These similar soiling rates contrast sharply with the reduced soiling rates observed on Phobic or SH coated surfaces in the presence of condensate (compare with Fig 3.5a). Thus, these results demonstrate that condensed water (i.e. dew) is required for the “dust herding” mechanism to operate as no reduction in soiling rate was observed on SH surfaces relative to bare glass in the absence of condensate.

The SH coating does, however, greatly improve the ease with which surfaces can be cleaned with water. The no-touch cleaning method restored 99.6% of the original $\%t$ of the SH surface after application of 3 mL of water whereas only ~50% of the losses from dust deposition

were restored on Bare glass as shown in Fig. 3.18. The bare glass cleaning process also provides evidence supporting the effect of condensate on the acceleration of cementation mechanisms. The partial restoration of $\% \tau$ observed on bare glass in Fig. 3.18, although relatively meager compared to the SH coated surface, is significantly better than on Bare glass surfaces where dust was deposited on a surface coated with condensed water (compare with Fig. 3.5a in the main text).

Fig. 3.19. Photographs of Bare Glass and Hydrophobic Surfaces after soiling (before controlled cleaning) and after controlled cleaning

The effect of coating contact angle on no-touch cleaning efficiency is shown in Fig. 3.19.



Photographs of a bare glass and a Hydrophobic-1 surface after: (a,b) 5 dew-dust-dry cycles; and (c, d) after no-touch cleaning with 3.0 mL of water.

Bare glass is not effectively cleaned because water preferentially wets the glass surface, forming channels in the deposited dust. In contrast, the Hydrophobic-1 coated glass is cleaned completely. The hydrophobic properties of the surface repel water and allow water drops to slide off in a straight line in the direction of gravity (downslope). Essentially no water is retained on the surface. The dust, which is primarily composed of metal oxides, is preferentially attracted to the water and is removed from the surface.

Table 3.5. Contact Angle Hysteresis and Sliding Angles of the Test Substrates

Sample Abbreviation	Surface Designation	Contact Angle (CA)	Sliding Angle	Advancing CA	Receding CA	CA H*
Bare	Bare Glass	9.5° ± 1.2°	NA	NA	NA	NA
Philic	Hydrophilic - 1	62.8° ± 0.1°	>90°	60.0° ± 1.8°	44.2° ± 0.3°	15.9°
	Hydrophilic - 2	51.2 ° ± 0.2°	36.8° ± 2.6°	51.2 ° ± 0.2°	41.9 ° ± 2.9°	9.3°
Phobic	Hydrophobic - 1	105.6° ± 0.1°	37.0° ± 1.9°	119.3° ± 0.7°	94.4° ± 1.1°	24.9°
	Hydrophobic - 2	87.3° ± 0.1°	73.7° ± 2.2°	97.3° ± 3.7°	75.9° ± 9.4°	21.4°
SH	Superhydrophobic -1	148.7° ± 0.3°	28.9° ± 0.7°	157.3° ± 1.4°	115.9° ± 1.6°	41.4°

* CAH = Contact Angle Hysteresis

Chapter 4. Hydrophobic-Hydrophilic Surfaces Exhibiting Dropwise Condensation for Anti-Soiling Applications

I. Nayshevsky, Q. Xu, and A. M. Lyons, “Hydrophobic-Hydrophilic Surfaces Exhibiting Dropwise Condensation for Anti-Soiling Applications,” *IEEE J. Photovoltaics*, vol. 9, no. 1, pp. 302–307, 2019

4.1 Introduction

Soiling of solar cover glass is a significant challenge that increases the levelized cost of electricity (LCOE) of solar PV energy through loss of electrical output and/or increased operation and maintenance costs. Hydrophobic coatings can reduce the cost of cleaning, but an external source of cleaning water is still required. Dew, however, can be harnessed to create a self-cleaning glass surface. To efficiently use condensation (i.e. natural dew) to create a self-cleaning glass surface, we fabricated a hybrid hydrophobic–hydrophilic coating, with an array of isolated hydrophilic circular rings. Water roll-off collection rates were measured in a simulated dew environment. The effect of hydrophilic ring geometry (location, arrangement, diameter, distance, and count) were studied to determine the optimal cleaning efficiency. The hybrid surface increased water collection rates by 95% over an uncoated (bare) glass surface and 51% compared to uniformly coated hydrophobic low-iron glass. Soiling of solar cover glass is reported as one of the major sources of PV efficiency loss. [12] The annual soiling loss averaged over one year is assumed to be 5% in NREL’s current and long-term levelized cost of electricity (LCOE) input assumptions for the SunShot 2030 targets of 3-5 ¢/kWh. [76] In regions with heavy soiling, the annual soiling loss can be as high as 50%. [77]

In light rain and morning dew conditions, water evaporates before it can roll off the surface; this process accelerates the formation of chemical and physical bonds between dust and glass. [19]

These reactions increase the magnitude and duration of efficiency losses and require mechanical force or the use of detergents to remove the soil from the surface of the glass. [78] Dew has been associated with accelerated dust accumulation in both Arizona [79], [80] as well as the EMEA region [13], [58], [78]. Work has been reported to reduce soiling losses by modifying glass surfaces with either hydrophobic or hydrophilic coatings [13], [81].

Our group has shown that a hydrophobic coating on glass (water contact angle (WCA) of $\geq 90^\circ$ and a contact angle hysteresis (CAH) $< 40^\circ$) reduces soiling rates compared to bare glass surfaces in artificial dew conditions. [82] Optical losses due to dust deposition were reduced by 45% compared to dust-coated bare glass. A dust herding mechanism was identified to account for this anti-soiling property. On bare glass, filmwise condensation was observed where water condenses to form a continuous layer of water, uniformly covering the glass surface. Upon evaporation, dust is spread and redeposited over the entire surface. In contrast, on the hydrophobic coated surface, water condenses in a dropwise manner. As the droplets grow, they imbibe dust on the surface. During evaporation, the droplets shrink laterally, which concentrates the dust into the centers of each former water drop, resulting in improved light transmission performance.

To completely clean hydrophobic coated glass in natural dew conditions, these dust-containing droplets need to grow to a critical size so that they can slide off the surface before drying out. Recently we demonstrated that a hybrid superhydrophobic-hydrophilic surface can accelerate the growth and roll-off of water droplets on hydrophilic needles. [71] The water collection rate was quadrupled compared to a uniform hydrophilic surface and doubled compared to hydrophobic or superhydrophobic surfaces.

In this study, we describe the fabrication of hydrophilic patterns on hydrophobic coated solar cover glass, with a purpose of increasing dew collection efficiency, and ultimately reducing soiling

rates. The effect of hydrophilic ring geometry including array conformation, number of rows of features, and feature diameter, on water condensation rates under artificial dew conditions is presented.

4.2 Methods

4.2.1 Sample Fabrication

Low-iron soda-lime glass, 3 mm thick, was cut to size (58 mm x 58 mm), washed and dried. A thin hydrophobic fluoropolymer coating was applied onto glass using a chemical vapor deposition technique. Briefly, a clean glass sample was placed orthogonal to, and 5 cm above, a piece of fluorinated ethylene propylene (FEP) measuring 5 cm x 5 cm x 0.5 cm. The chamber was sealed and heated at 320°C (60°C above the melt temperature) for 1 hour. Thermal decomposition species from FEP deposited and bonded to the glass, resulting in a robust hydrophobic surface that can withstand condensation conditions. The WCA of the surface after coating on the tin side is $97^\circ \pm 6^\circ$ with a CAH value of $46^\circ \pm 12^\circ$. Hydrophilic rings were formed using a mechanical drill secured

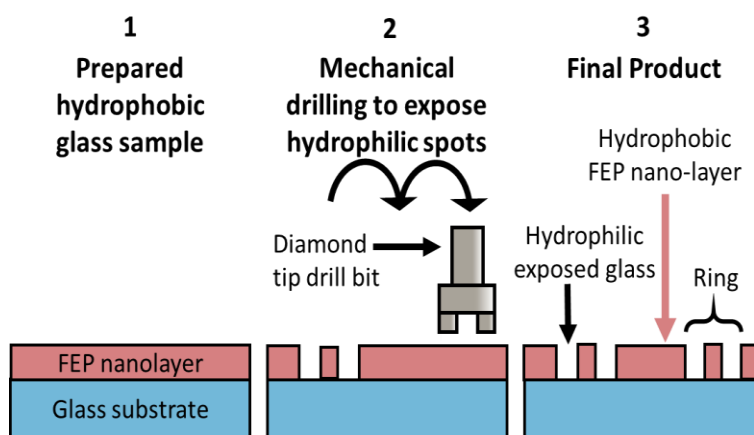


Fig. 4.1. Schematic of hybrid hydrophobic-hydrophilic surface preparation. The process utilizes mechanical drilling to produce hydrophilic features of defined parameters on a hydrophobic surface.

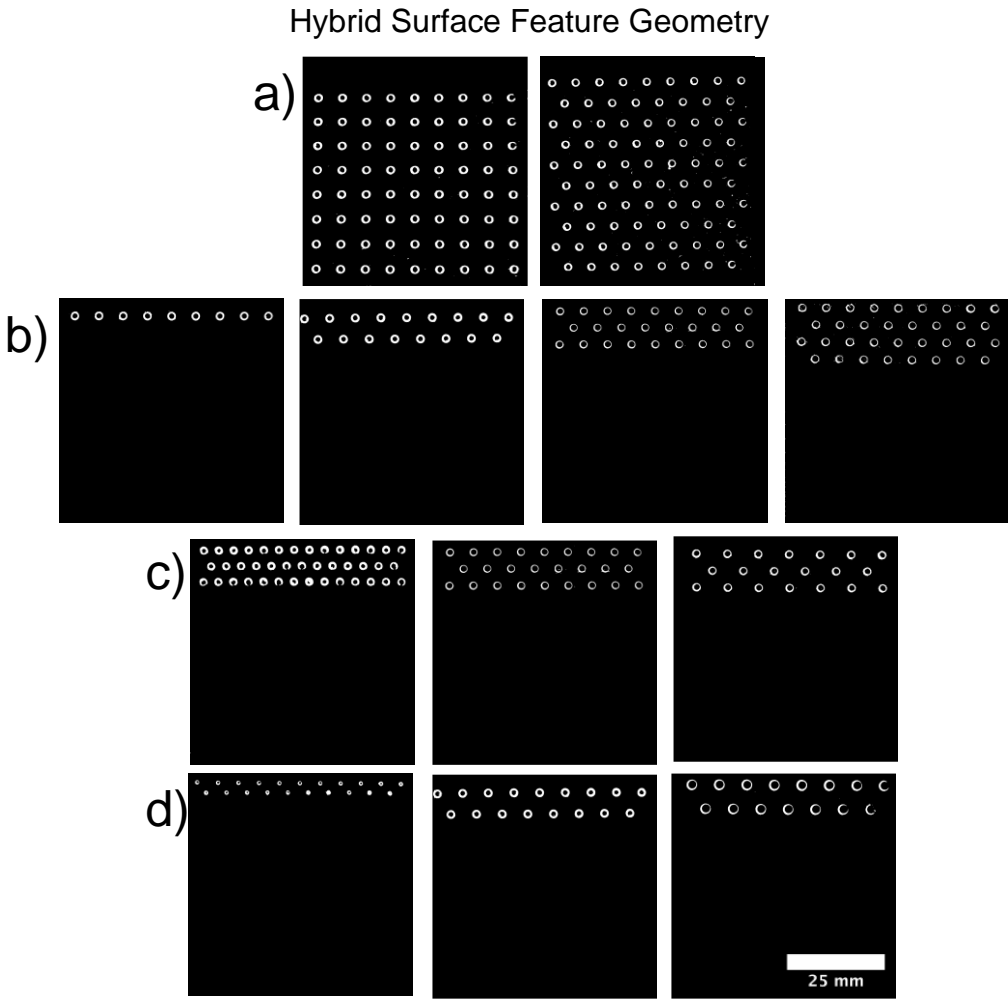


Fig. 4.2. Top-down photographs (computer enhanced) of coated glass surfaces showing: a) geometric arrangement (square vs. staggered), 2 mm o.d., 4 mm distance between features; b) number of rows (1, 2, 3, 4, and 10), 2 mm o.d., 4 mm distance between features; c) distances between hydrophilic rings (2mm, 4mm, 6mm), 2 mm o.d., 3 rows; and d) diameters of hydrophilic rings (1.0mm, 2.0mm, 3.2mm), 4 mm distance between features, 2 rows.

to a Jenome JR2200N robot. Hollow cylindrical diamond drill-bits, 1 mm, 2 mm, and 3.2 mm in diameter were used to cut through the coating and 200 μm into the glass to create hydrophilic rings in a programmed array (Figs. 4.1 & 4.2). Program variables evaluated include: geometric (packing) arrangement (Fig 4.2a), number of rows of hydrophilic features (Fig. 4.2b), edge-to-edge distance between hydrophilic features (Fig. 4.2c), and dimeter of hydrophilic features (Fig. 4.2d). After

drilling, the samples were rinsed with deionized water to remove contaminants resulting from the drilling process. The size of hydrophilic features was determined from optical images.

4.2.2 Condensation Chamber

The condensation experiments were conducted in a Delrin/Acrylic chamber, specifically built for these experiments (Fig. 4.3.). Hybrid-coated glass samples were mounted onto an aluminum plate measuring: 5.0 cm x 5.0 cm x 0.75 cm thick. A digital thermometer integrated circuit within a 6.0 mm o.d. stainless steel sheath (digital thermometer IC) (Maxim Integrated DS18B20) was mounted inside the aluminum heat-spreader. This heat-spreader was mounted onto a 60W Peltier thermoelectric cooler (TEC) (Laqiya TEC1-12706). An aluminum heatsink along with a CPU fan were mounted under the TEC to remove heat from the hot side of the TEC. The heatsink/fan, TEC, and aluminum heat-spreader were secured to the Delrin back-plate with springs. Thermal grease was used in all interfaces to enhance thermal conductivity (Wakefield Solutions, Inc, Type 126

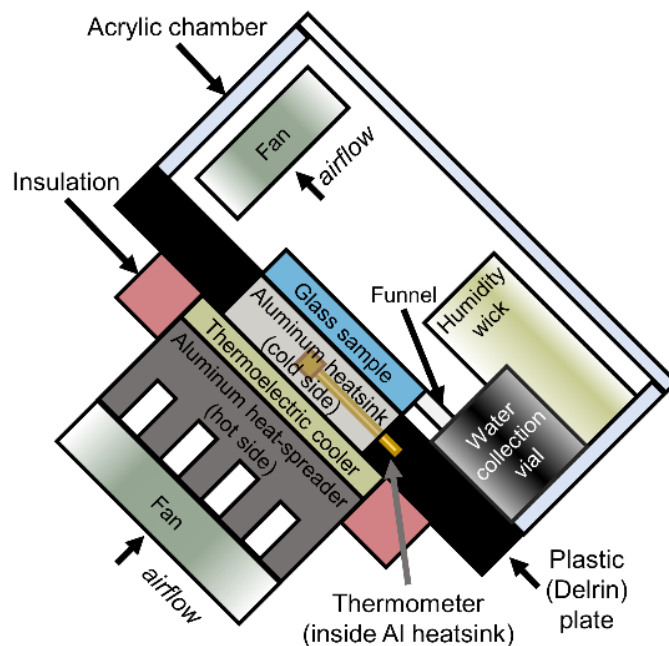


Fig. 4.3. Cross-sectional schematic of the condensation chamber including the thermoelectric cooler system, water collection scheme and humidification system (not to scale).

Non-Silicone Thermal Joint Compound). The temperature of the TEC was controlled via a digital thermometer IC located in the heat-spreader, and a 10A 12VDC relay (Songle SRD-05VDC-SL-C) connected to a Raspberry Pi 3 microcontroller, using a python script.

The entire substrate-TEC assembly was mounted into the base of the environmental chamber, which was constructed from a 25.4 cm x 25.4 cm x 0.25 cm Delrin plate, with a machined opening of 5.0 cm x 5.0 cm in the center. The Delrin plate was mounted at a 45° angle. An acrylic enclosure (LWH: 18 cm x 18 cm x 10 cm) with a silicone gasket was used to isolate the system. The atmosphere inside the enclosure was saturated with water vapor using a wick cut from a Honeywell HC22P Humidifier Pad, which was partially immersed in a beaker of deionized water. A low velocity fan (Thermaltake Mobile Fan II) was mounted to the top of the chamber

The relative humidity was measured with a dry bulb/wet bulb method using two digital thermometer IC's, housed in 6 mm diameter stainless steel sheaths, which were connected to the microcontroller. Water condensate was collected with a home-made superhydrophobic water collection channel and a 50 mL 3D printed plastic beaker, tared before use.

4.2.3. Experimental Methods

Water contact angle measurements were obtained using a râme-hart 250-F1 goniometer with a 5 μ L drop of water. Images of the surface were recorded with a Nikon Coolpix P2 camera at 1-minute time increments; the resolution of images was 2048 x 1536 pixels. Condensation experiments were conducted by first placing the glass sample onto the aluminum heat-spreader. A thin film of water between glass and aluminum was used as the interface material since this eliminates the potential for surface contamination. The acrylic lid to the chamber was secured and the temperature of the aluminum heat-spreader was reduced to 10°C. The TEC cooled the heat-spreader to 10°C within 10 minutes. The temperature of the air inside the chamber was maintained

at 23.0°C ($\pm 0.9^\circ\text{C}$) without additional controls. The relative humidity inside the chamber increased to 89.9% ($\pm 1.4\%$) within 6 minutes after the chamber was closed. Condensation on the samples was monitored for 10-20 hours. Water that condensed and slid-off the surface via gravity was collected and the mass measured at the end of the experiment.

Images of the condensation process were analyzed to determine the diameter and location of the water drop that initiated the water slide-off event. The analysis was conducted via a computer vision algorithm written in python 3 and utilizing OpenCV (Open Computer Vision Library) for image processing.

4.3 Results

4.3.1 Bare Glass vs. Hydrophobic Glass

As expected, film-wise condensation was observed on the hydrophilic bare glass samples while dropwise condensation was observed on the hydrophobic samples. On bare glass, micron-size droplets that formed initially, merged into a continuous film within the first 20 minutes. This continuous liquid film was maintained for the duration of the experiment. Bare clean glass exhibits a water collection rate of $4.7 \pm 1.8 \cdot 10^{-3} \text{ mg/mm}^2 \text{ min}$, which corresponds to 11.2 mL of water over a typical 12.2 hour experiment.

In contrast, the hydrophobic coated glass sample exhibits a condensation rate of $6.7 \pm 0.6 \cdot 10^{-3} \text{ mg/mm}^2 \text{ min}$, which is an increase of 42% over bare glass. Droplets nucleate and grow on the hydrophobic surface as shown in Fig. 4.4a. After 20 minutes, the droplets grow to an average diameter of $\sim 1.5 \text{ mm}$. Over time, the droplets continue to grow and merge through an Ostwald ripening process, resulting in a smaller number of droplets with larger diameters ($2.2 \pm 0.6 \text{ mm}$). As drop coalescence proceeds, larger droplets grow until they reach a critical size ($3.9 \pm 0.2 \text{ mm}$). At that point the gravitational forces are sufficient to overcome the wetting forces along the solid-liquid-vapor triple contact line (TCL) and the droplet slides off the surface, imbibing droplets along

its downward, linear path as shown in the third panel of Fig. 4.4a. This leaves a swath of surface free of droplets, allowing the nucleation and growth process to restart. The last panel of Fig. 4.4a shows a surface that has been swept clear of most of the original droplets after 70 minutes, with new droplets at various stages of growth.

4.3.2 Water Collection Rates on Hybrid Hydrophobic-Hydrophilic Surfaces

Condensation on a hybrid surface proceeds by a combination of the hydrophilic and hydrophobic mechanisms described in the previous section. Nucleation of water droplets occurs on both regions, but as shown in the second panel of Fig. 4.4b, the liquid droplets initially grow more rapidly on the hydrophilic rings. As the experiment progresses, larger droplets form in these locations as seen in the third panel of Fig. 4.4b. The shape of these droplets is a distorted teardrop because of the strong pinning forces along the hydrophilic TCL that counter the gravitational attraction of the mass of water. Some large droplets have merged and become pinned to two

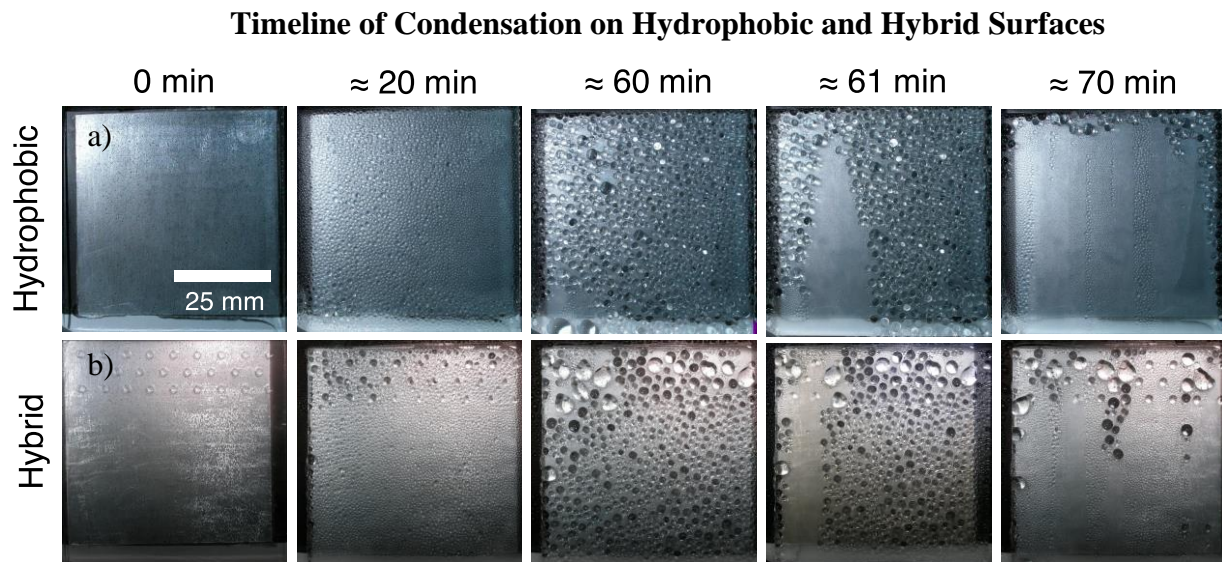


Fig. 4.4. Timeline of condensation on hydrophobic(control) and hybrid hydrophobic-hydrophilic surface. The hybrid surface contains 3 rows of 2 mm diameter hydrophilic features, which are spaced at 4mm distance (edge-to-edge). Visual analysis shows increased condensation and greater water drop diameters on hydrophilic rings when compared to hydrophobic (control) sample.

hydrophilic rings, further increasing the TCL that must be overcome before sliding. After 70 minutes, most large droplets have rolled-off the surface and a new cycle of nucleation and growth has progressed as seen in the last panel of Fig. 4.4b.

In the following sections, the effect of hydrophilic ring array geometry, number of rows of features, pitch of features and diameter of rings is discussed in detail.

4.3.3 Water Collection: Staggered vs. Square Arrays of Hydrophilic Rings

Staggered arrays of the drilled hydrophilic rings were compared to square arrays using samples with rows of features covering the full surface of the glass substrate as shown in Figure 4.2a. The ring o.d. is 2mm, with 4 mm of space between adjacent ring perimeters. As shown in Table 4.1, the water collection rates are $7.9 \pm 0.8 \cdot 10^{-3}$ mg/mm² min, $7.8 \pm 0.2 \cdot 10^{-3}$ mg/mm² min and $6.7 \pm 0.6 \cdot 10^{-3}$ mg/mm² min for staggered arrays, square arrays and the hydrophobic control, respectively. The water collection rates of hybrid surfaces with staggered and square arrays are similar to each other, but ~17 % higher than the hydrophobic control. This result demonstrates that hydrophilic ring arrays can increase the water collection rates, and the difference between different array conformations is not significant. A staggered arrangement of hydrophilic features was used to evaluate the effect of other parameters in all further experiments in this paper. (Table 4.1)

Table 4.1 Effect Of Surface Chemistry And Structure On Condensation Water Collection

Sample [Type (feature diameter- distance between features- count of rows)]	Number of Trials [n]	Water Contact Angle [°]	Number of Hydrophilic Rings [n]	Number of rows [n]	Hydrophilic Ring Diameter [mm]	Distance Between Hydrophilic Rings [mm]	Critical Drop Diameter [mm]	Water Collection Rate [mg/mm ² min] · 10 ⁻³
Hydrophobic (Control)	6	96±5	-	-	-	-	3.9±0.2	6.7±0.6
Bare Glass (Control)	7	<10	-	-	-	-	-	4.7±1.8
Hybrid (2mm-4mm-1row)	3	95±4	9	1	-	-	-	6.6±1.3
Hybrid (2mm-4mm-2rows)	5	98±3	17	2	-	-	4.6±1.2	8.6±0.7
Hybrid (2mm-4mm-3rows)	6	97±5	26	3	1.9±0.2	-	-	9.1±0.6
Hybrid (2mm-4mm-4rows)	3	97±3	34	4	-	-	-	8.7±0.3
Hybrid (2mm-4mm-10rows)	3	96±4	85	10	4.0±0.5	-	-	7.8±0.2
Hybrid (1mm-4mm-2rows)	3	97±3	21	2	1.1±0.1	-	4.4±0.8	7.2±1.1
Hybrid (3mm-4mm-2rows)	3	97±2	15	2	3.2±0.1	-	5.1±0.5	8.0±0.5
Hybrid (2mm-2mm-3rows)	3	95±5	41	3	-	2.0±0.4	-	9.2±1.4
Hybrid (2mm-6mm-3rows)	3	98±4	20	-	1.9±0.2	6.0±0.5	-	8.7±0.2
Hybrid (2mm-4mm-8rows) - square	3	97±5	64	8	4.0±0.5	-	-	7.9±0.8

4.3.4 Water Collection: Number of Rows of Hydrophilic Features

Although coverage of the full surface could increase the number of slide-off events, a larger number of hydrophilic features could also be disadvantageous because a larger number of growing droplets would locally decrease water concentration in the vapor near the glass surface under nature/artificial dew conditions. Observations of condensation on hydrophobic surfaces (Fig. 4.4a) showed that drops rolling-off from the uphill portion of the surface carry away droplets along its downslope path, decreasing the impact of down-slope rows. Thus, the effect of the number of rows of hydrophilic rings was systematically evaluated by starting from the top of the glass sample.

Water collection rate as a function of number of rows of hydrophilic features is shown in Figure 4.5a. For this evaluation, all hydrophilic rings have a diameter of 2mm with an edge-to-edge separation distance of 4 mm. Average and standard deviation values from at least 3 trials is plotted.

A maximum water collection rate was observed for the sample with 3 rows of hydrophilic regions ($9.1 \pm 0.6 \cdot 10^{-3}$ mg/mm² min) (Fig. 4.4a). This value is 36% greater than a hydrophobic surface without hydrophilic rings and more than twice the value on hydrophilic (bare) glass. Increasing the number of rows further resulted in a gradual decrease in water collection rates.

4.3.5 Water Collection: Distance Between Features

The effect of edge to edge spacing on water collection rates was measured for spacing values of 2, 4 and 6 mm with the hydrophilic ring diameter fixed at 2 mm. Almost the same high water collection rate was maintained for hybrid surfaces with 2 mm and 4 mm feature spacing between hydrophilic rings, and a small decrease (~5%) was observed when the spacing feature was

increased to 6 mm (Table 4.1). This may be due to a trade-off between local water vapor concentration and number of hydrophilic nucleation sites.

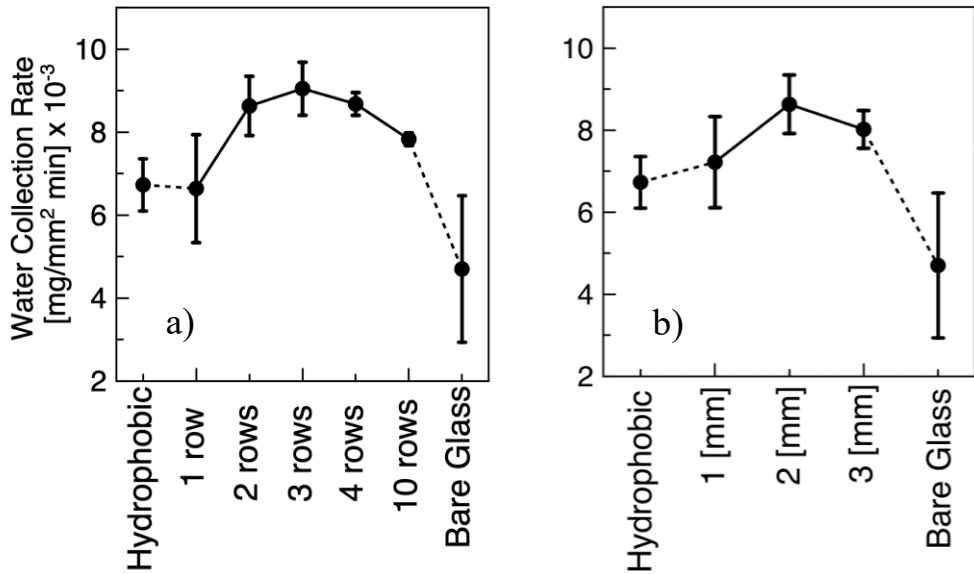


Fig. 4.5. Water collection rates as function of a) number of rows of 2.0 mm diameter hydrophilic ring features and b) diameter of two rows of hydrophilic features. All features spaced 4.0 mm apart.

4.3.6 Water Collection: Feature Diameter

The dependence of water collection rates on the diameter of the hydrophilic rings is shown in Fig. 5b. The distance between features was held at 4 mm, with two rows of features for all samples. A maximum rate was observed for 2 mm diameter hydrophilic rings ($8.6 \pm 0.7 \cdot 10^{-3}$ mg/mm² min); both smaller (1 mm) and larger (3 mm) ring diameters reduced water collection rates by 19% and 8% respectively.

The decreased rate for the 3 mm diameter feature could be due to the longer triple contact line, requiring a larger droplet mass before roll-off. However, the water collection rate for the surface with 1 mm diameter feature dropped even more and was very close to hydrophobic surface without

hydrophilic regions. This result indicates that the hydrophilic features must be above a certain size to accelerate the water collection rate. Further experiments to explore the effect of hydrophilic shape and size are underway.

4.3.7 Roll-off location and critical droplet diameter

Visual and qualitative observations have shown that hydrophilic features serve as efficient droplet nucleation and growth locations on the hybrid samples (Fig. 4.4) and increase water collection rates (Table 4.1). To quantify the impact of hydrophilic rings on the condensation process and the water collection rate, data from the camera images was analyzed to determine both the diameter and location of droplets that initiated roll-off events.

Figure 4.6a shows the results for the hydrophobic control surface. The median critical droplet roll-off diameter was found to be 3.9 ± 0.2 mm. This value was independent of slide-off location; droplets that rolled-off from the top of the glass sample were within 0.1 mm of those that rolled-off from the bottom of the sample. Droplet diameters remained constant over the duration of the experiment. Figure 4.6a also shows that droplets roll-off primarily from the top third of the substrate.

In contrast, the hydrophilic rings of the hybrid surface affect both the diameter and the location of the critical droplet volume. As shown in Figure 4.6b and Table 4.2, the droplets that form on the hydrophilic rings are 4.6 mm in diameter. This value represents an 18% increase,

Table 4.2 Water Drop Diameter At Roll-Off

Location	Hydrophobic [mm]	Hybrid [mm]
Entire sample	3.9 ± 0.2	4.4 ± 1.1
Top of sample (<15mm)	3.9 ± 0.2	4.6 ± 1.2
Bottom of sample (>15mm)	3.8 ± 0.2	3.4 ± 0.3

corresponding to 64% greater mass, than droplets formed on the control hydrophobic surface. The size of the droplets remains constant throughout the 15 mm region that contains hydrophilic rings. Below this location, the critical droplet diameter decreases abruptly to 3.4 mm, which is 13% smaller than the critical drop size on the control surface.

Not only do the hydrophilic rings increase drop diameter, but they also cause the critical droplet roll-off events to initiate from the top of the sample. Forty percent of roll-off events are observed within the top 2.5 mm of the surface, whereas only 17% of drops roll-off from this location on the control hydrophobic surface.

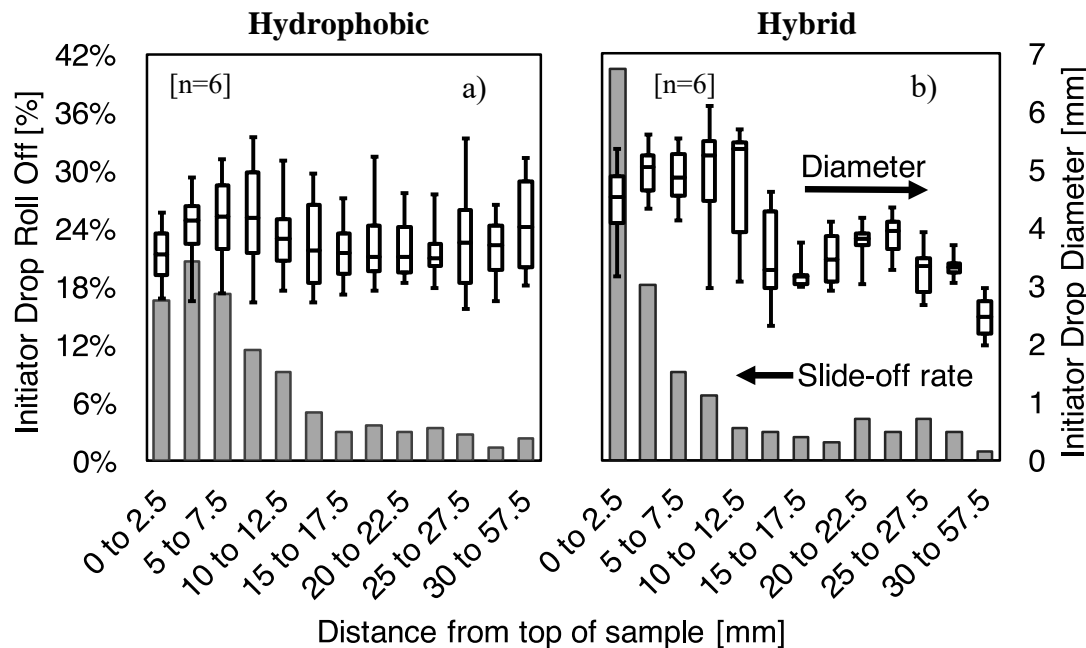


Fig. 4.6. Computational analysis of water drop diameter (right hand axis) and location of the drop initiating the roll-off event (left hand axis) for a) Hydrophobic Control and b) Hybrid Surface with 3 rows of 2 mm diameter rings spaced 4 mm apart.

4.4 Discussion

To increase condensation rates, hydrophilic regions were intentionally created on hydrophobic coated surfaces. Hydrophilic regions enhance condensation rates for several reasons. Nucleation

of liquid water occurs more rapidly on a hydrophilic surface compared to a hydrophobic one. The enhancement ratio is significant and can exceed 1×10^{49} [71], [83]. Once a liquid water droplet nucleates, it will grow rapidly because the condensation rate on a hydrophilic surface, such as liquid water, is much greater than on a hydrophobic surface. Most importantly, larger liquid water droplets will grow at a faster rate than smaller diameter droplets because the vapor pressure of a droplet is an inverse function of droplet radius. Smaller droplets have a higher vapor pressure than larger droplets [84]. Thus, larger water drops grow at the expense of the smaller ones. This mechanism leads to Ostwald ripening as shown in Fig. 4.4.

For a droplet to roll-off the substrate, gravitational attraction must overcome the forces at the TCL that pin the droplet to the surface. These TCL forces are greater on hydrophilic surfaces and scale with increasing TCL length. Thus, larger hydrophilic features require more massive droplets before roll-off can occur. The optimal number and size of the hydrophilic features are thus a trade-off between condensation rates and TCL forces. Larger hydrophilic regions will nucleate liquid water rapidly; exhibit the lowest vapor pressures and fastest growth rates; and generate larger diameter droplets that would clean a larger swath of surface. However, the TCL line will be longer for these larger diameters, requiring a greater mass before roll-off could occur. The experimental results presented in this paper show that a hydrophilic ring diameter of 2 mm is optimal, maximizing water collection rates .

A larger number of growing droplets could reduce the concentration of water molecules in the vapor phase near the surface of the glass. This diffusion limit could, in-turn, reduce overall condensation rates, favoring fewer rather than a larger number/density of nucleation sites. Our experimental results indicate that three rows of 2 mm diameter features is optimal, which further

contributes to higher water collection rates. Other geometrical variables, such as spacing between features and packing geometry were not observed to significantly affect water collection rates.

Two other factors could also influence water collection rates: CAH of the hydrophobic coating and tilt angle of the glass. The chemistry and morphology of the hydrophobic coating can be tuned to reduce the CAH and thus the critical angle for droplets to slide-off the surface as described by the Furmidge equation modified by Extrand [28]. For any given coating, increasing tilt angle will decrease the critical drop diameter [83]. We have recently developed a new method for forming fluoropolymer coatings on glass [39] that exhibit a CAH of $<15^\circ$. Lower CAH coatings would reduce the tilt angle of the glass required for droplets to slide-off the surface as well as decrease the critical droplet size. Such new materials thus hold the promise of extending the range of geographical locations where hybrid coatings can exploit dew to achieve self-cleaning properties to most latitudes. The properties of such new coatings are currently under investigation.

4.5 Conclusions

Creating surfaces with arrays of hydrophilic features on a hydrophobic coating demonstrate higher water collection rates compared to uncoated (bare) glass or uniformly hydrophobic coatings. Preferential nucleation of liquid water on hydrophilic regions, and the high mobility of droplets on hydrophobic regions combine to increase water collection rates by a factor of 2 compared to uncoated glass. The hydrophilic rings were shown to increase not only the overall water collection efficiency but also led to an increased diameter of the droplets rolling off the surface and caused these roll-off events to preferentially occur along the top surface of the sample. These effects are expected to increase the efficacy of self-cleaning from dew.

Although drilling, proved useful for this study, it is obviously not the preferred method for creating hydrophilic patterns on glass due to the cost, scattering of light, and potential for initiating cracks. More feasible methods for creating hydrophilic patterns have recently been developed in our lab; these methods will be used in our subsequent work where anti-soiling properties of hybrid surfaces will be quantified. Future work will also evaluate scaling these effects on larger glass panels.

Chapter 5. Self-Cleaning Hybrid Hydrophobic-Hydrophilic Surfaces: Durability and Effect of Artificial Soilant Particle Type

I. Nayshevsky, Q. Xu, J. M. Newkirk, D. Furhang, D. C. Miller, and A. M. Lyons, “Self-Cleaning Hybrid Hydrophobic–Hydrophilic Surfaces: Durability and Effect of Artificial Soilant Particle Type,” *IEEE J. Photovoltaics*, vol. In Print, pp. 1–8, 2019.

5.1 Introduction

Dew accelerates soiling rates and increases dust adhesion. To use dew for self-cleaning, a fluorinated ethylene propylene (FEP) coating was applied to suppress reactions between dust and glass as well as facilitate dew to condense as mobile droplets. An array of rectangular hydrophilic channels in the coating increases condensation rates and droplet slide-off diameters. The durability of the coating was evaluated by artificial UV weathering. Four different types of soilants were used in artificial soiling tests to assess the effect of soilant type and surface properties on soiling rates and self-cleaning efficacy under simulated dew conditions. Soil deposition and self-cleaning mechanisms are be reported.

Soiling of photovoltaic (PV) cover glass is known to reduce the electrical output by 4-7 % in North America and Europe [12], [17], [45], [50]–[54] and up to 70 % in other locations [12], [17], [53], [55]–[57]. Natural condensation, or dew, has been shown to accelerate soiling rates [12], [15], [17]–[19], [53] and facilitate the adhesion of particulate matter on solar cover glass [12], [18], [19]. Because of the strong interactions between glass and water, dew will spread out, forming a liquid film on the glass. Soiling rates depend on environmental conditions as well as through surface interaction mechanisms, the chemical properties of the glass surface, as well as the chemical composition of the dust itself. Soluble compounds within the contaminant particles can chemically react with the liquid and glass interfaces causing crystallization and/or cementation reactions to occur as the dew evaporates glass [12], [18], [19] . As a result, such particles can

become more strongly adhered to the surface [20]. In addition, surface reactions will affect the cleaning processes required to remove the soil. Strongly bound soil will require mechanical brushing with water [12], [55] to restore performance whereas weakly bound dust can be easily removed with water alone. Thus, there is a need for coatings that can impart both anti-soiling as well as self-cleaning properties to solar cover glass.

Anti-soiling properties increase the amount of energy that a PV panel can produce in a given environment, by reducing the optical losses resulting from soilant absorption and scattering. Self-cleaning properties decrease mechanical cleaning frequency/duration and so reduce operation and maintenance (O&M) costs by using naturally occurring dew or precipitation to wash away particulates without using mechanical brushing.

Our group has shown that a hydrophobic coating on glass (water contact angle (CA) of $\geq 90^\circ$) reduces soiling rates compared to uncoated surfaces in the presence of condensed water [82]. Optical losses due to ISO 12103 A2 Arizona Test Dust deposition were reduced by 45 % on hydrophobic coatings compared to uncoated surfaces. The lower soiling rate results from a dust herding mechanism, where highly mobile liquid water droplets sweep dust particles into concentrated piles as the droplet's solid-liquid-vapor triple contact line (TCL) contracts during evaporation. We have also shown that water collection from simulated dew can be increased by more than 36 % by incorporating an array of hydrophilic features on the hydrophobic coating [9].

In this paper we examine the effect of surface coating and soil composition on soiling rates as well as cleaning efficacy using an enhanced, rectangular shape for the peripheral hydrophilic features. Hybrid hydrophobic-hydrophilic surface coatings were fabricated to optimize water collection rates under simulated dew conditions. Four types of soilants with different chemical properties (Arizona Test Dust, Aramco Test Dust, calcium carbonate and Portland cement) were

studied to determine the effect of soilant solubility and reactivity on soiling rates. In addition, self-cleaning studies were conducted under simulated dew conditions to quantify the ability of dew to clean dust, as a function of dust composition. Coating durability was evaluated using artificial UV weathering tests.

5.2 Methods

5.2.1 Material Fabrication

Three types of surfaces were studied: clean bare glass (Bare Glass), which is hydrophilic; glass with a hydrophobic polymer coating (Phobic); and glass with a hybrid hydrophobic-hydrophilic coating (Hybrid). Low-iron Diamant (Saint-Gobain S.A.) glass substrates, 3 mm thick and cut to 50 mm x 57 mm, were used for all experiments. Substrates were cleaned by washing with an Alconox-water solution (Alconox Inc.), rinsed with DI water and dried with compressed air before use.

Hydrophobic coated glass substrates were prepared by applying a $<1\text{ }\mu\text{m}$ thick, fluorinated ethylene propylene (FEP) coating onto the cleaned glass using a lamination-peeling process [39]. Teflon® FEP film (American Durafilm) was laminated to the glass substrate at $\geq 275\text{ }^{\circ}\text{C}$ for ≥ 5 minutes and allowed to cool below the melt point of the resin ($260\text{ }^{\circ}\text{C}$). Excess polymer was peeled from the surface leaving a nanometer-thick coating of FEP strongly adhered to the glass.

Hybrid hydrophobic-hydrophilic (Hybrid) surfaces, shown schematically in Fig. 5.1, were prepared by creating hydrophilic channels in a hydrophobic coated glass substrate, previously prepared as described in the preceding paragraph. The hydrophilic channels were created by selectively abrading away the hydrophobic coating, revealing the underlying hydrophilic glass substrate. Pumice powder (~5 % by weight) dispersed in water, was rubbed against the coating using a plastic rod (0.5 mm diameter) guided by rectangular openings in a 3-D printed stencil. The stencil was 3-D printed using polylactic acid (PLA) filament. The width and spacing between the

rectangular hydrophilic channels were systematically varied in order to optimize water collection efficiency. Rectangular hydrophilic channels were found to exhibit 78 % greater condensation cleaning rates than hydrophilic rings [9], [41]. Optimal dimensions of the channels were determined to be 0.6 mm x 20 mm on 1.7 mm pitch based on a parametric study [41]. A single row of 23 channels, each measuring 20 ± 0.3 mm tall (Fig 5.1a), 0.6 ± 0.1 mm wide and spaced 1.1 ± 0.1 mm apart (Fig 5.1b) was found to be optimal and positioned along the top edge of the Hybrid substrates.

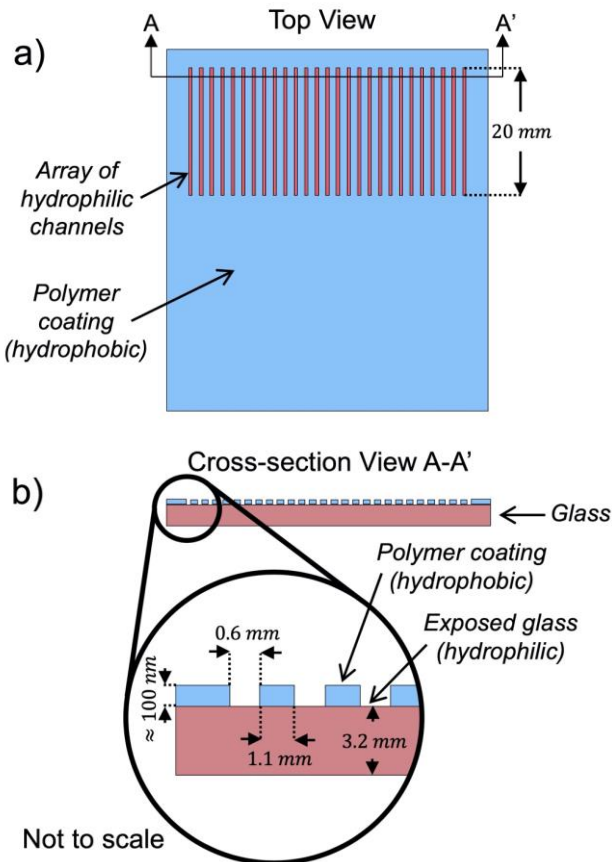


Fig. 5.1. Drawing of a hybrid surface showing a) top and b) cross-sectional views. The dimensioned schematic shows the hydrophobic polymer coating on a glass substrate with exposed glass hydrophilic channel array.

5.2.2 Experimental Methods

Dust was applied to the glass substrates using an accelerated soiling apparatus [82] shown schematically in Fig. 5.2. The apparatus was designed to replicate dust deposition conditions in the Arizona desert [45]; water was allowed to condense on the surface, mimicking natural dew, immediately before airborne dust deposition. After dust deposition, samples were baked before beginning the next deposition cycle. All samples were exposed to three dew-deposition-bake cycles.

A 20 mg sample of test dust was used per cycle. The test dusts used included: Standard Arizona Test Dust (A2 Fine Grade ISO 12103-1, PTI Inc.), Aramco Test Dust (PTI Inc.), calcium carbonate (particle diameter <50 µm, Sigma Aldrich) and Portland cement (PTI Inc.). Humidity inside the chamber was stabilized (70 %RH) and samples were cooled to 10 °C for 2 minutes, using a Peltier device, to induce condensation on the surface. Dust was injected upwards into the dust tunnel by applying a pulse of dry compressed air (20 psi, 30 secs). The overhead fan (3 m/s), dispersed the

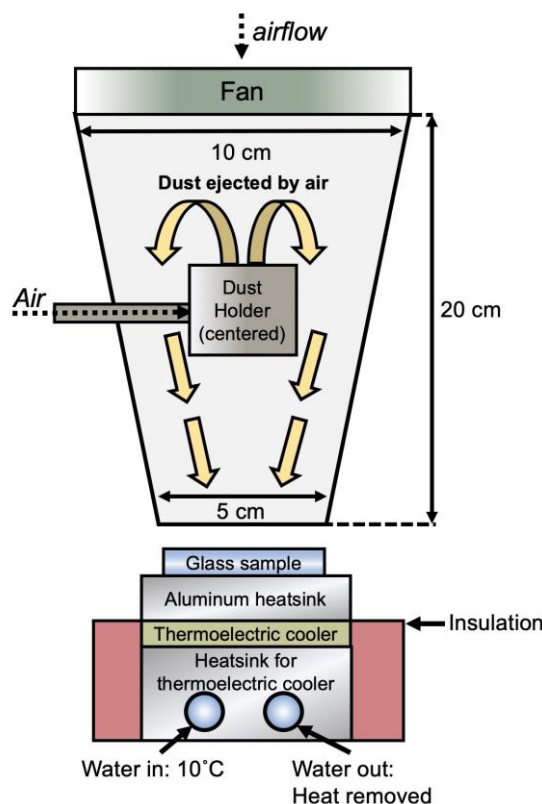


Fig. 5.2. Schematic of artificial soiling chamber.

dust so that it covered the underlying glass. Lastly, the same thermoelectric Peltier device was used to heat the samples to 50 °C for 10 min to facilitate dew evaporation and enable cementation and/or recrystallization of minerals. The time between the deposition cycles was 10-15 minutes (the time required to obtain microscopy images and optical transmittance measurements).

A separate artificial dew chamber, shown schematically in Fig. 5.3, with samples positioned at one of the 3 tilt angles: 25°, 45° and 85° was used to study self-cleaning. Relative humidity in the chamber was maintained at ~90 % by evaporation from a saturated wick at room temperature. Samples were cooled to 10 °C, below the dew point of ~16 °C. Condensation rates and patterns were analyzed via a high definition camera controlled by a computer vision enabled Python programming language algorithm [67]. Condensation time for each set of samples (1x Bare Glass, 2x Phobic and 1x Hybrid coupon per experiment) was determined by the amount of time required for water droplets to slide off from a complete row of hydrophilic channels on the Hybrid surface.

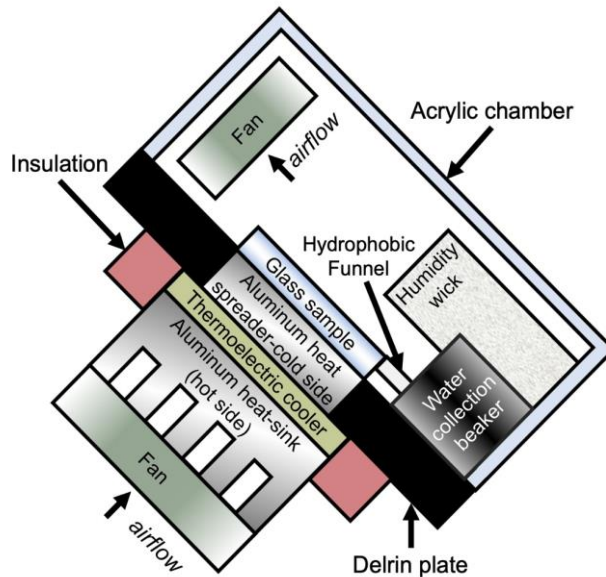


Fig. 5.3. Schematic of artificial dew cleaning chamber.

5.2.3 Analytical Methods and Automation Controls.

For anti-soiling and self-cleaning experiments, soiling was quantified by direct optical transmittance ($\% \tau$) at a wavelength (λ) of 550 nm. Transmittance was recorded using a Lambda 650 UV-VIS spectrophotometer (PerkinElmer Inc.). Three separate 0.6 cm^2 ($0.4 \text{ cm} \times 1.5 \text{ cm}$) areas were measured on each sample, the average of the three results is reported. A single wavelength direct transmittance measurement was used, as opposed to the representative solar-weighted transmittance as per IEC 62788-1-4 [49], [62] for rapid quantification of optical performance.

Several considerations should be remembered regarding assessment at a single optical wavelength. It is well-known that particles scatter shorter wavelengths of light more efficiently than longer wavelengths [85]. This is especially true since most of the soil particles that are found on solar modules are less than 16 microns in diameter [48]. Using field data, Qasem showed [65] that wavelengths below 570 nm are the most sensitive to soiling. The disproportionate impact of soil particulates on shorter wavelengths (<600 nm) was also recently reported by Tanesab [66]. However, there is a lower limit to the optimal wavelength that can be used. Due to the lesser energy present at $\lambda < 400 \text{ nm}$ in the global terrestrial solar spectrum AM1.5 [86] and the spectral response of most semiconductors used for PV, wavelengths above 500 nm are of greatest relevance to characterize PV module soiling. Micheli et al. recently correlated soiling losses to transmittance measurements comparing results from a single wavelength to different spectral ranges [63]. The correlation between singlet wavelength hemispherical transmittance measurements at 550 nm and the Soiling Ratio (as defined by IEC 61724-1)[64] was greater than 98 % for all PV material absorbers. They concluded that soiling can be estimated by using the transmittance at a single wavelength with high accuracy. Moreover, a single wavelength measurement is more economical,

and direct transmittance is more sensitive to soiling and more widely available than hemispherical transmittance measurements. This is especially true when analyzing a large number of samples with redundant measurements. As a result of these considerations, a wavelength of 550 nm was used for direct transmittance measurements for all soiling and cleaning experiments.

Surface coverage of dust and soiling trends were observed via digital optical microscopy (Nikon SMZ 1500 using INFINITY2-1C camera). Water contact angles (CA) were measured using a model 250-F1 contact angle goniometer (ramé-hart Instrument Co.) Ten measurements per coupon were automatically performed using 5 μL droplets of DI.

Indoor accelerated weathering tests were conducted using a Ci5000 Xenon Weather-ometer test chamber (Atlas Material Testing Technology LLC) following the IEC TS 62788-7-2 A3 method [87], i.e., irradiance of $0.8 \text{ W}\cdot\text{m}^{-2}\cdot\text{nm}^{-1}$ at 340 nm, chamber temperature of 65 °C, black panel temperature of 90 °C, and chamber relative humidity of 20 %. Solar grade Acrylite 0Z023 GT poly(methyl methacrylate) sheet (“Acrylic”, Evonik Industries AG), 3.2 mm thick, was used as a reference material. Direct optical transmittance of the accelerated weathering test samples were measured from 200 nm to 2500 nm using a Cary 5000 dual-beam ultraviolet-visible-near infrared (UV-VIS-NIR) spectrophotometer (Agilent Technologies Inc.) Contact angle values during Weather-ometer testing were measured with a “100–25–A” goniometer (ramé-hart Instrument Co.) Ten measurements were automatically performed using 4 μL of deionized water at three different locations within the same coupon, providing an average result for 30 measurements.

5.3 Results

5.3.1 Optical and Wetting Properties

As prepared, the Bare Glass samples (12 replicates) exhibit a direct transmittance at 550 nm ($\%t$) of $91.8 \pm 0.1 \%$ and are hydrophilic (CA = $9.1 \pm 1.5^\circ$). In contrast, the Phobic (24 replicates) and Hybrid (8 replicates) samples are more transparent because the fluoropolymer coating imparts

anti- reflectivity ($\% \tau = 93.6 \pm 0.6\%$ and $94.0 \pm 0.2\%$ respectively). These coated surfaces are hydrophobic, with contact angle values of $119 \pm 2^\circ$.

5.3.2 Artificial Weathering

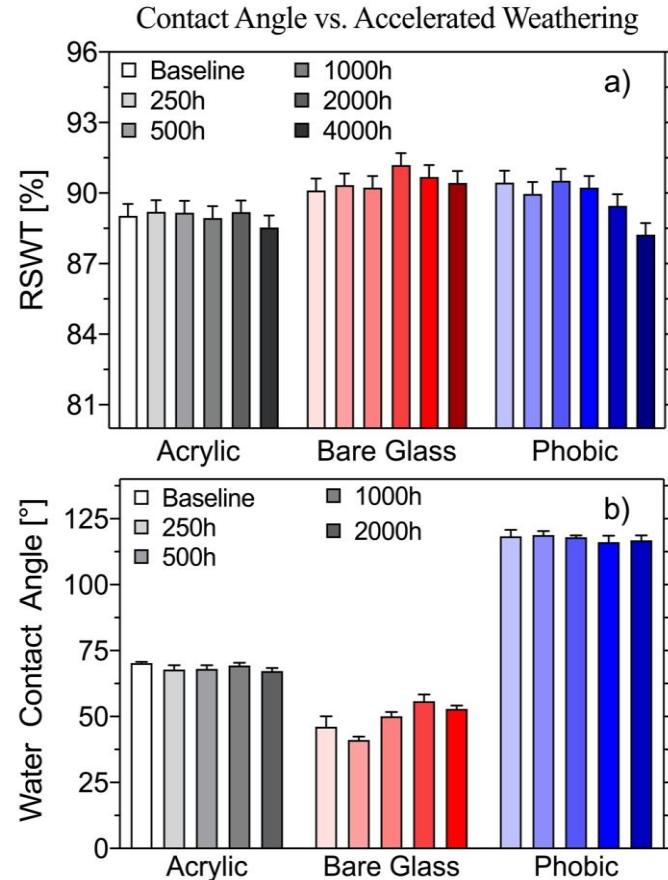


Fig. 5.4. Properties of control and coated Phobic substrates subjected to 2000 h of accelerated indoor weathering: a) change in solar weighted direct transmittance; b) change in CA.

The optical and surface properties of the Phobic glass are stable when exposed to artificial weathering. As shown in Fig. 5.4a, the direct representative solar weighted transmittance (RSWT) evaluated from 300 nm – 1250 nm [49], [62] remains stable after $7.2 \text{ MJ} \cdot \text{m}^{-2}$ (2000 h) of cumulative radiant exposure. Moreover, the surface energy of the Phobic coating remains

unchanged as the water CA remained above 117° (Fig. 5.4b). These results indicate that the surface chemistry of the fluoropolymer coating remains intact through the weathering shown in Fig. 5.4.

5.3.3 Anti-Soiling Properties

The performance loss from soiling depends strongly on the chemistry of both the glass surface coating as, well as the type of soilant. The total change in % τ after three dew-dust-bake cycles for each dust type and surface coating is shown in Fig. 5.5. Soiling loss was observed to be higher on Bare Glass than on Phobic or Hybrid glass surfaces for all soil types. Combining data for all soil types, the average decrease in % τ at $\lambda = 550$ nm on Bare Glass is $4.1 \pm 0.3\%$ ($1.5 \pm 0.3\%$ per dust application), whereas on Phobic and Hybrid surfaces the overall change was $2.3 \pm 0.3\%$ and $2.4 \pm 0.2\%$, respectively. Phobic and Hybrid surfaces exhibit anti-soiling behavior compared to Bare Glass for all four types of soilants tested; these hydrophobic coatings outperform Bare Glass by

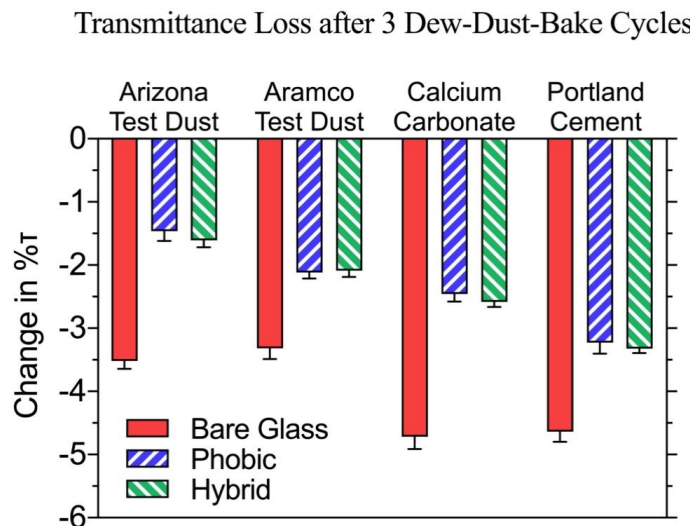


Fig. 5.5. Change in % τ at 550 nm as a function of soilant type and surface coating for Bare Glass, Phobic and Hybrid coatings after three dew-dust-bake soil deposition cycles; averaged over $n = 3$ soiling trials.

$41.7 \pm 6.8\%$. Hybrid and Phobic samples exhibit the same soiling deposition as expected, because the hydrophobic surface coatings are prepared using the same method.

Table 5.1 Soilant Type, Composition, Solubility, and Change in Optical Performance

Soilant	Relevant Chemical Compound	Solubility in water	Soiling on Bare Glass, $\Delta\%_{\tau}$	Soiling on Phobic + Hybrid, $\Delta\%_{\tau}$
AZ Dust	Silicates	Negligible	$-3.5 \pm 0.1\%$	$-1.5 \pm 0.1\%$
Aramco	10% NaCl	360 g/L	$-3.3 \pm 0.2\%$	$-2.1 \pm 0.1\%$
Calcite	CaCO_3	0.047 g/L	$-4.7 \pm 0.2\%$	$-2.5 \pm 0.1\%$
Cement	CaO	Negligible	$-4.6 \pm 0.2\%$	$-3.3 \pm 0.1\%$

Reactive compounds

Soiling on all surface types are lower for soils that do not react with water (Arizona Test Dust) and/or contain NaCl (Aramco Test Dust), which is highly soluble in water. In contrast, calcium carbonate (CaCO_3) and Portland cement, which can react with water [88], [89], soil at higher rates than the silicate-based soils (Table 5.1). CaCO_3 is soluble in water at pH 5.7 (the pH of water saturated with atmospheric CO_2). Upon dissolution, calcium carbonate reacts with water to form CO_2 and Ca(OH)_2 , the latter can further react with glass. The CaO in cement reacts exothermically with water also forming Ca(OH)_2 . The greater soiling losses for the two water-reactive compounds are observed on all surface types but are most apparent on Bare Glass, as shown in Fig 5.5. Of the four soils studied, Portland cement results in the greatest soiling losses.

Anti-soiling effectiveness can also be compared qualitatively by visual comparison of Bare Glass, Phobic and Hybrid surfaces after 3 dew-dust-bake cycles (Fig. 5.6). The amount of soil deposited on Bare Glass (Fig. 5.6a) is qualitatively seen to be greater compared to Phobic and

Hybrid surfaces (Fig. 5.6b, 5.6c) supporting the spectroscopic results. Phobic and Hybrid surfaces soil to a lesser degree, due to the “dust herding” mechanism previously reported [82].

5.3.4 Self-Cleaning Properties

Self-cleaning of the artificial soil was observed in the condensation chamber where liquid water condenses from the vapor phase (90 % RH at 25 °C) into liquid on the glass surfaces cooled to 10 °C, simulating natural dew. The percent of the original optical transmittance (% τ) restored after cleaning in the condensation chamber for all samples studied, including the four soil types and three tilt angles, are presented in Fig. 5.7. For Bare Glass samples, water condenses in a film-wise manner. Dust particles become suspended within the liquid water film and are redistributed during drying, resulting in additional scattering of light. The % τ decreases from between 0.1 % and 3.5 % (average 1.8 ± 1.7 %) after condensation, averaged over all soil types. The relatively large variance of % τ values measured on Bare Glass after condensation cleaning (Fig. 5.7) is caused by the heterogeneous redistribution of soil on the surface. Regions where water slides off the surface are relatively clean (Fig. 5.6d), but because much of the liquid water condensed on the surface does not slide off, large dust spots form on most Bare Glass samples during the drying step as shown in Fig. 5.8. This leaves randomly arrayed cleaned and soiled regions that are comparable in size to the light beam emitted by the spectrophotometer (0.4 cm x 1.5 cm).

In contrast, on Phobic and Hybrid surfaces, water droplets nucleate, grow and slide-off, thereby carrying away soil particles, resulting in increased % τ values. Therefore, Phobic and Hybrid surfaces are cleaned efficiently by condensation; % τ increases by 1.3 ± 1.1 % and 1.6 ± 1.1 %

respectively after \sim 1 hour, recovering to 98.7 ± 0.3 % and 99.2 ± 0.1 % of the original $\% \tau$ (Fig. 5.7), averaged over all soil types and tilt angles.

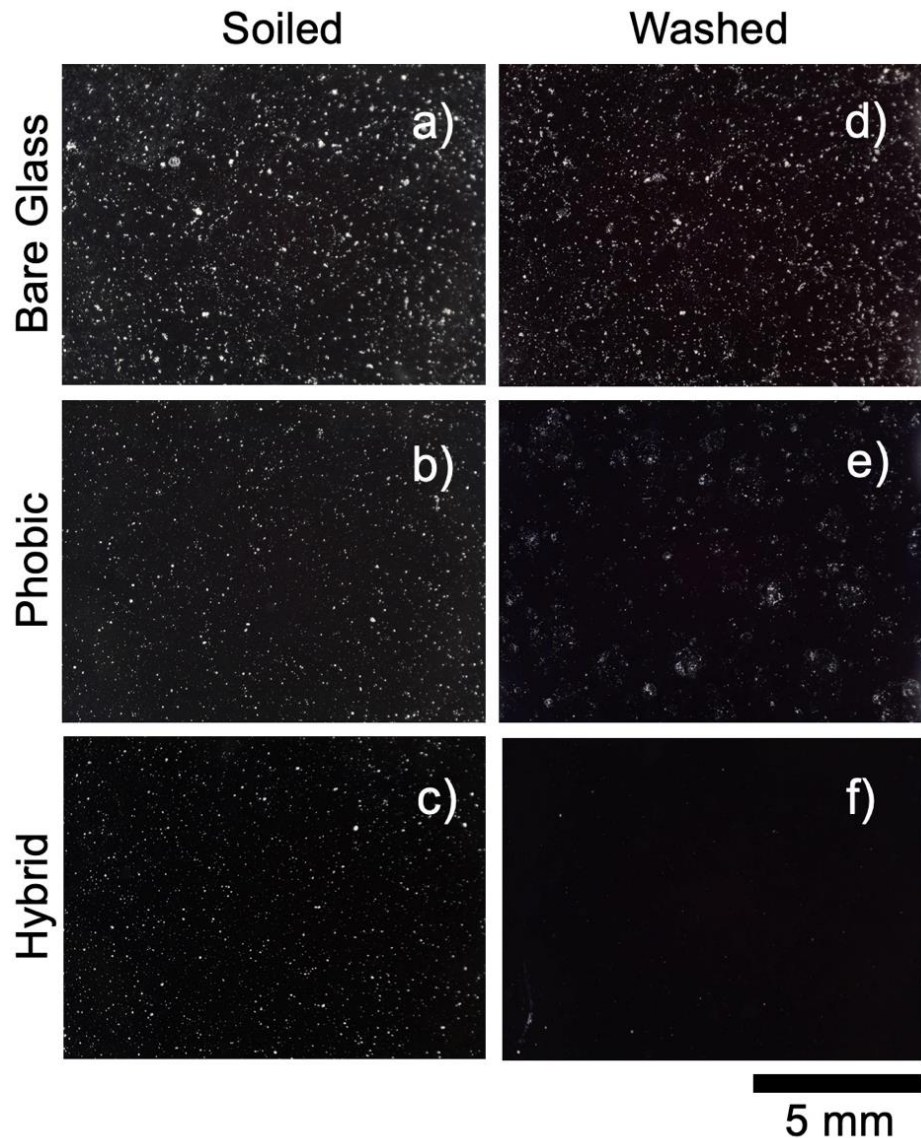


Fig. 5.6. Optical microscopy images of Bare Glass, Phobic and Hybrid surfaces after 3 dew-dust-bake cycles (a, b, c, respectively) and after simulated dew cleaning at 45° tilt angle (d, e, f, respectively), soiled with Portland cement test dust.

Restoration of Original Optical Transmittance for Test Surfaces Soiled with Various Soilants

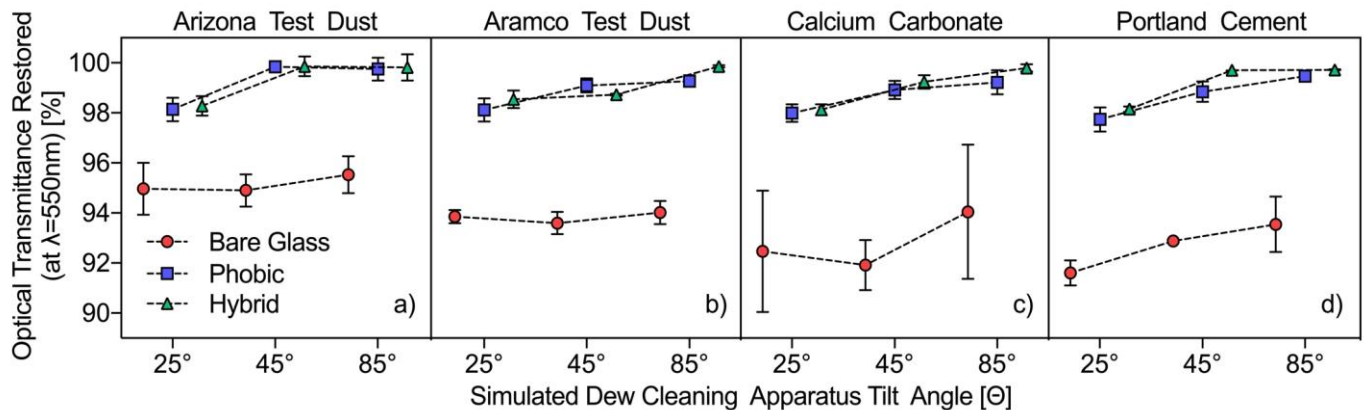


Fig. 5.7. Restoration of original % τ as a function of simulated dew cleaning tilt angle on Bare Glass, hydrophobic (Phobic) and Hybrid coatings after three dew-deposit-bake soil deposition cycles; utilizing a) Arizona Test Dust, b) Aramco Test Dust, c) Calcium Carbonate, and d) Portland Cement.

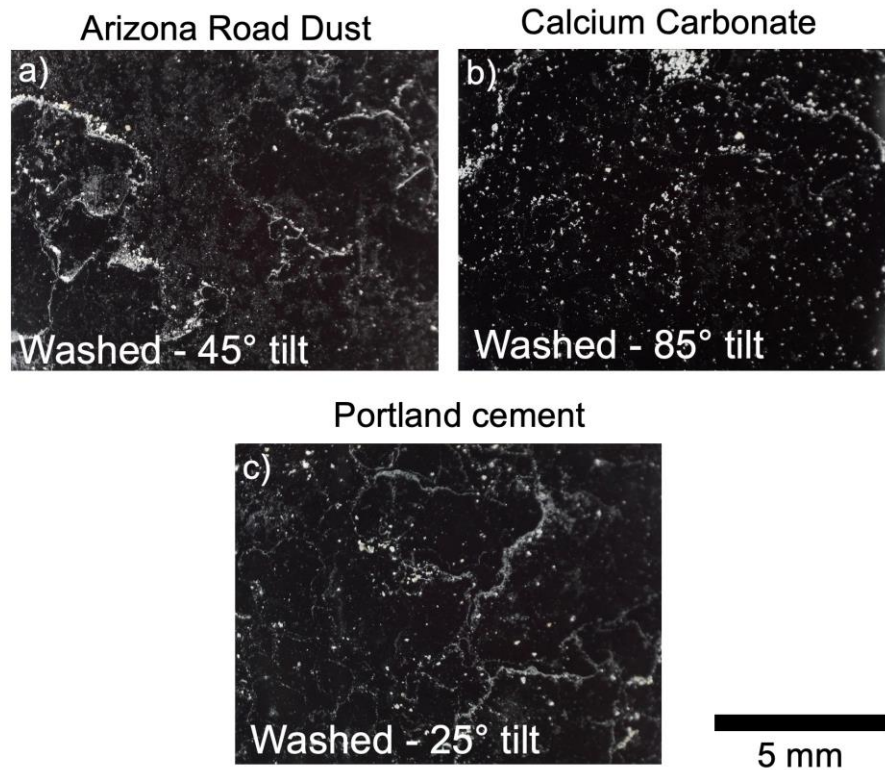


Fig. 5.8. Optical microscopy images of Bare Glass, soiled with a) Arizona Test Dust, b) Calcium Carbonate and c) Portland cement followed by condensation cleaning step at 45°, 85°, and 25° tilt angles respectively. The images show heterogeneous redistribution of soil after condensation cleaning on the surface of the glass.

The angle of substrates positioned within the condensation chamber affects the efficiency with which artificial dew can clean the surfaces. Substrates at higher tilt angles are cleaned more effectively for all types of coatings as well as all soil types, as shown in Fig. 5.7. The largest improvement (1.2 % τ) is seen between a tilt angle of 25° and 45°. A smaller but still significant improvement is observed upon increasing the tilt angle to 85°.

Overall, Hybrid surfaces are cleaned more effectively than Phobic surfaces, which are lacking hydrophilic channels. On the Hybrid surfaces, liquid water droplets are preferentially nucleated on the hydrophilic channels located along the top (up-slope) portion of the glass. The liquid water accumulates at the bottom of the channel until it reaches a critical mass then slides off the surface as shown in Fig. 5.9.

At any given tilt angle, droplets grow to a larger diameter on Hybrid surfaces than on Phobic surfaces before sliding off the surface. For example, at 45°, the diameter of drops sliding off from a soiled Phobic surface measure 2.8 ± 0.8 mm, compared to 3.4 ± 1.0 mm on Hybrid surface. Because of the larger diameter, drops on a Hybrid surfaces clean away dust from a larger swath of the surface.

The difference in drop diameter measured at 25° tilt angle was more pronounced than at a 45° tilt angle with 3.0 ± 1.2 mm on Phobic surfaces and 5.5 ± 1.3 mm on Hybrid surfaces. The larger drop diameter on Hybrid surfaces is attributed to the strong water-glass interactions leading to water drop pinning on the hydrophilic regions of the hybrid surfaces. The lower tilt angle results in a smaller gravitational force component, thus increasing the water drop mass required to overcome the pinning forces at the glass-water-vapor triple contact line. In contrast, the drop diameters at an 85° tilt angle are 2.5 ± 0.5 mm on Phobic surface and 3.0 ± 0.5 mm on Hybrid

surfaces. Optimization of the size of the hydrophilic features may improve performance at each tilt angle.

Hybrid surfaces result in improved cleaning effectiveness in a second important way, less time is required for a full row of liquid water drops to slide off from a complete row of hydrophilic channels on the Hybrid surface than a Phobic surface. Drops roll off 6.5 minutes faster from a Hybrid surface than from a Phobic surface (both at 45° tilt angle) for reactive soilants (CaCO_3 and Portland cement). This enables a Hybrid glass surface to be cleaned faster, thus using the limited naturally occurring dew more efficiently.

Visual comparison of surfaces cleaned with simulated dew confirm the spectrophotometer measurements and show that Phobic and Hybrid surfaces (Figs. 5.6e, 5.6f) were more effectively cleaned whereas the Bare Glass surface (Fig. 5.6d) was cleaned to a lesser degree. Portland cement is absent on the Hybrid surface in these images after condensation cleaning.

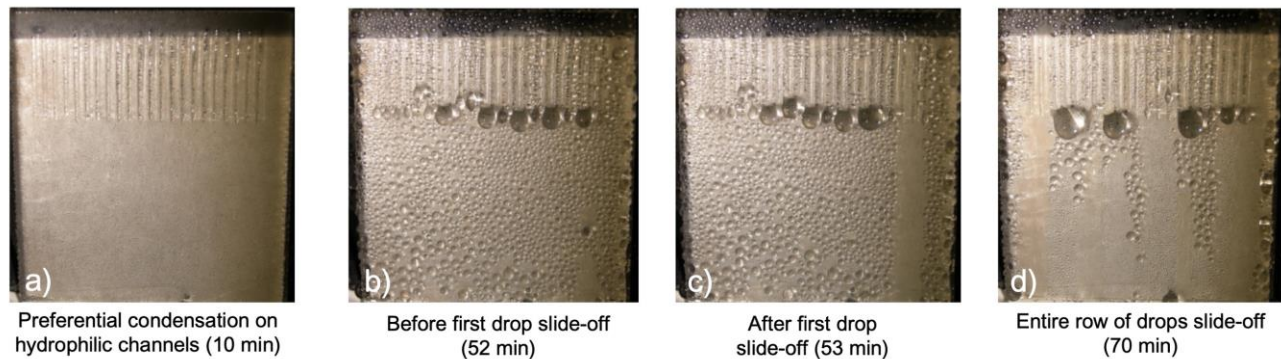


Fig. 5.9. Optical photographs of water condensing on a soiled Hybrid surface in the condensation chamber at 45° tilt angle and using Arizona Test Dust, a) water preferentially nucleates and grows on hydrophilic channels, b) liquid water drops accumulate at base of channels, c) initial drop slides off down the hydrophobic coated glass after reaching critical size (53 min); d) entire row of drops have slid off surface with new drops forming (70 mins).

5.4 Conclusion

Hybrid surfaces comprised of a hydrophobic coating and hydrophilic channels positioned along the top (up-slope) edge of the glass provide both anti-soiling properties as well as self-cleaning behavior when placed in a condensing (simulated dew) environment. The anti-soiling properties are due primarily to the high water droplet mobility and chemical inertness of the fluoropolymer coating, which exhibits good durability, maintains high transparency (>90 % RSWT) and droplet mobility (CA >117°) after 2000 hours of accelerated weathering time. The chemically unreactive surface deters cementation and promotes a previously observed “dust herding” mechanism [82], [90] which concentrates dust into small, discrete piles. This minimizes the reduction in % τ after dew-dust-bake soiling cycles. Hybrid and Phobic surfaces exhibit the same anti-soiling properties; both reduce soiling by ~46 % compared to Bare Glass. Soils that can chemically react with water, such as calcium carbonate and Portland cement, were observed to soil at a faster rate on all surface types than silicate-based soils (Arizona Test Dust and Aramco Test Dust). The greater soiling accumulation with reactive soils are more pronounced on Bare Glass substrates than hydrophobic surfaces.

Hybrid and Phobic surfaces that have been artificially soiled exhibit self-cleaning behavior in the condensation chamber. The % τ at 550 nm of Hybrid and Phobic surfaces is restored to 99.2 % and 98.7 %, of their original transmittance values, respectively. In contrast, Bare Glass surfaces are not cleaned during artificial condensation. The % τ of the artificially soiled Bare Glass surfaces exhibit no significant change after the same time (~60 minutes) in the condensation chamber for all soil types. The low surface energy fluoropolymer coating prevents cementation reactions with the various soilants, facilitating the ability of liquid water droplets to carry soil away from the surfaces. On Bare Glass, stronger interactions between soil and glass, as well as water and glass,

makes soil removal more difficult without the assistance of contact cleaning (risking abrasion). Hydrophilic channels increase cleaning efficacy because liquid water nucleates and grows more rapidly on a hydrophilic surface than a hydrophobic surface. As a result, droplets slide-off the channels approximately 10 % more rapidly than on a uniform hydrophobic surface. Moreover, the drops sliding off a Hybrid surface are larger in diameter than a Phobic surface, thereby cleaning a wider swath. The rectangular channel shape enables water to condense more efficiently as compared to the circular ring structures reported previously [82]. Higher tilt angles increase self-cleaning effectiveness for both Hybrid and Phobic surfaces.

Fabrication of full-size solar PV panels with hybrid coatings would be relatively straightforward to implement. A hydrophobic coating would be applied to the entire exterior-facing surface of the solar cover glass. Hydrophilic channels would be defined along the perimeter of the glass using the clearance and creepage regions to avoid the potential of these channels from adversely affecting light transmittance to the underlying semiconductors. Limiting the location of hydrophilic channels to this region would also enable the use of hydrophilic TiO₂ channels without affecting the reflection or absorption of light. Channels located only along the perimeter are anticipated to be sufficient for self-cleaning of full-sized modules because of the high mobility of water droplets on the hydrophobic coating. Once a single drop is released from a hydrophilic channel, the drop can slide down the entire length of the glass surface, cleaning a swath at least as wide as the drop along the entire length, or width, of the panel. Field experiments on glass substrates to validate these laboratory soiling and condensation test results are presently underway. Fabrication of functioning silicon modules is planned so that Soiling Ratio can be measured and the ability of droplets to traverse the entire panel can be validated.

Chapter 6. Approximating Partial Wetting Regions on Rough Hydrophobic Surfaces Using Atomic Force Microscopy Derived Topography

6.1 Introduction

The structural integrity of modern solar cells is strongly dependent on the protective glass covering that encapsulates it and serves as a barrier against environmental particulates and oxidative compounds. Despite advances in solar energy technology, there is a persistent problem with the efficiency of electrical output. The soiling of panels occurs via the deposition of particulate contaminants on the surface of solar protective glass covers and can reduce the electrical output by an average of 4% to 7% [12], [17], [45], [50]–[54]. It can be reduced by as much as 70% in locations prone to air-laden dust and depends upon the local environment [12], [17], [53], [55]–[57]. Natural condensation, or dew, has been shown to accelerate soiling rates [12], [15], [17]–[19], [53] and facilitate the adhesion of particulate matter on solar cover glass [12], [18], [19]. To reduce soiling rates and cleaning costs, transparent anti-soiling coatings have been developed that are primarily classified as either hydrophobic [4]–[11] or hydrophilic [11]–[14]. Hydrophilic coatings rely on water to fully wet the glass and then carry away dust particles as water is wicked downslope to the bottom of the panel. Hydrophobic coatings are composed of a chemically inert, low-surface-energy material to prevent chemical reactions between the soil and glass surface. Our group has shown that a hydrophobic coating on glass (water contact angle (CA) of $\geq 90^\circ$) reduces soiling rates compared with uncoated surfaces in the presence of condensed water [8]. One study analyzed the anti-soiling properties as a function of contact angle (CA) [82], in which a set of rough hydrophobic coatings was prepared on low-iron glass substrates. The coatings contained fluorinated ethylene propylene (FEP), which has an inherent CA of $\sim 120^\circ$ [91], and were prepared with CAs ranging from 149° to 51° . Anti-soiling effects were observed on

hydrophobic surfaces, but a discrepancy in the theoretical CA was also observed in which some surfaces showed CAs lower than the inherent CA of the polymer used to fabricate the surface coating. This discrepancy can be explained by partial wetting of the surface in which the hydrophobic coating is interrupted to expose the underlying hydrophilic glass. This, in turn, can create surfaces with CAs lower than the inherent CA of the polymer comprising the surface coating. AFM analysis of the surfaces showed that CA variations were correlated with the surface roughness. Thus, understanding the effect of roughness on the CA as a function of partial wetting is an important step in further developing and refining surface coating lamination processes. In this study, a computer simulation was developed to assess partial wetting on rough fluoropolymer surfaces using roughness data obtained from AFM topography data and Delaunay triangulation. The initial results are reported, and additional work is in progress.

An anomaly in the wetting properties of fluoropolymer-coated surfaces was discovered upon evaluating their water sliding angles (roll-off angle) as a function of contact angle

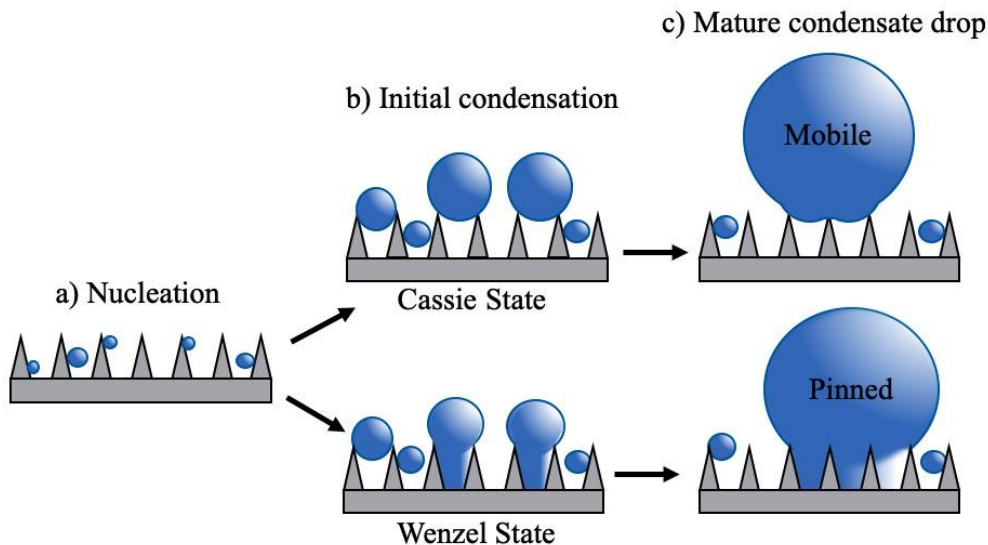


Fig. 6.1 Schematic illustration of surface wetting on a rough surface and a transition to the Wenzel and Cassie states.

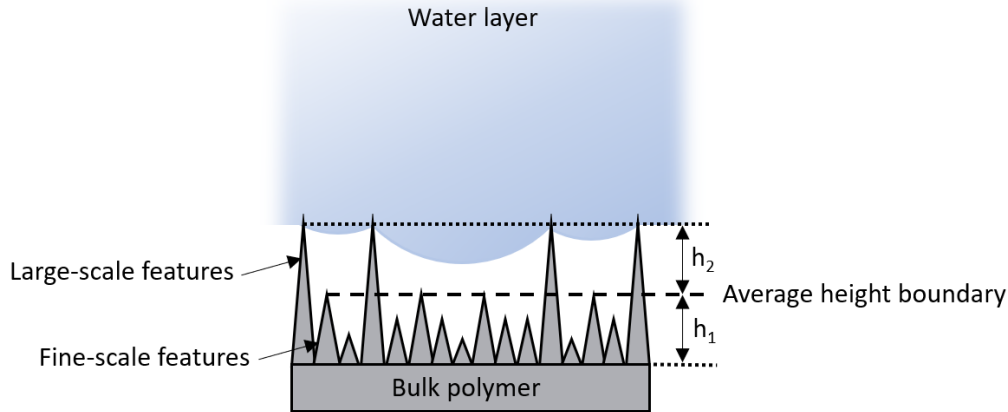


Fig. 6.2. Schematic illustration of a water drop residing on rough surface in the Cassie state. The water drop is supported on the peaks of the large-scale features, where h_1 is the height from the bulk polymer layer to the average feature height boundary and h_2 is the height from the average feature height to the top of the large-scale features.

(hydrophobicity). All hydrophobic surfaces used in the study [82] showed a sliding angle that was higher than expected, indicating the presence of partial wetting, which was likely facilitated by the presence of hydrophilic regions below the fibrous structure of the textured fluoropolymer nanocoating. The hydrophilic spots allowed a transition from the Cassie state to the Wenzel state (Fig. 6.1) when water reached the surface. Due to the surface tension of water, the aspect ratio of the nanocoating's fibers is limited, which would not allow the water meniscus to penetrate the surface, thus keeping it suspended on the tops of the fibrous features (Fig. 6.2). In this study, we identify the geometric parameters of a textured surface (pitch, the distance between surface features, and height of surface features) and used them to simulate surface wetting, via modeling how the water meniscus resides on these features and how deep the meniscus penetrates to the open, hydrophilic regions of glass. The working hypothesis is that if the water meniscus dips below the boundary line that marks the mean height of surface features, water in that specific location

will transition from the Cassie state to the Wenzel state and wet the surface. This will cause the water droplet to become pinned to the surface and increase the sliding angle for such surfaces.

6.2 Methods

A set of rough, low-surface-energy surfaces were selected as representative surfaces that exhibited partial wetting properties. The roughness topography data was obtained from AFM images that were obtained on a Bruker Multimode 8 AFM operating in ScanAssist mode, with a scan rate of 0.125 Hz, peak force set point of 100 pN, feedback gain of 35, and an image resolution of 512 x 512 pixels. The obtained images were corrected with Gwyddion 2.9 software to remove horizontal line defects and normalize the elevation.

The AFM image processing began with correcting horizontal strokes (5 iteration), then aligning the rows using the median method. Then the image level data was corrected by mean plane subtraction and the minimum elevation value was set to 0 nm. The images were cropped as necessary to eliminate any of the edge effect artifacts.

All computational analytical methods were conducted by using python script that is available upon request. The computational analysis first identified large-scale features, which were features with a height above the mean height of all features. Large-scale features are visually described as tall amorphous features, while small-scale features are described as thin fibrous features. Then, the analysis proceeded by isolating large-scale features and masking small-scale features, resulting in the image shown in Figure 6.3b. This was done by marking the grains by thresholding using Gwyddion at average elevation determined by the python script. The AFM image minimum elevation was then again set to 0 nm. At this step the roughness parameters can also be calculated.

The boundaries of the large-scale features were then traced, and their maximum elevation was identified (Fig. 6.3b). Delaunay triangulation was then implemented to find the nearest-neighbor large-scale features (Fig. 6.3c). A calculation was then performed that fit a disc to the maximum elevation of the features and the distance between the features. The calculation was simultaneously run on two neighboring features (a line between the vertices of the Delaunay plot) and took into account the height between the tops of the large-scale features and the boundary at the 50% line (h_1), the height between the bottoms of the valleys in the surface and the boundary at the 50% line

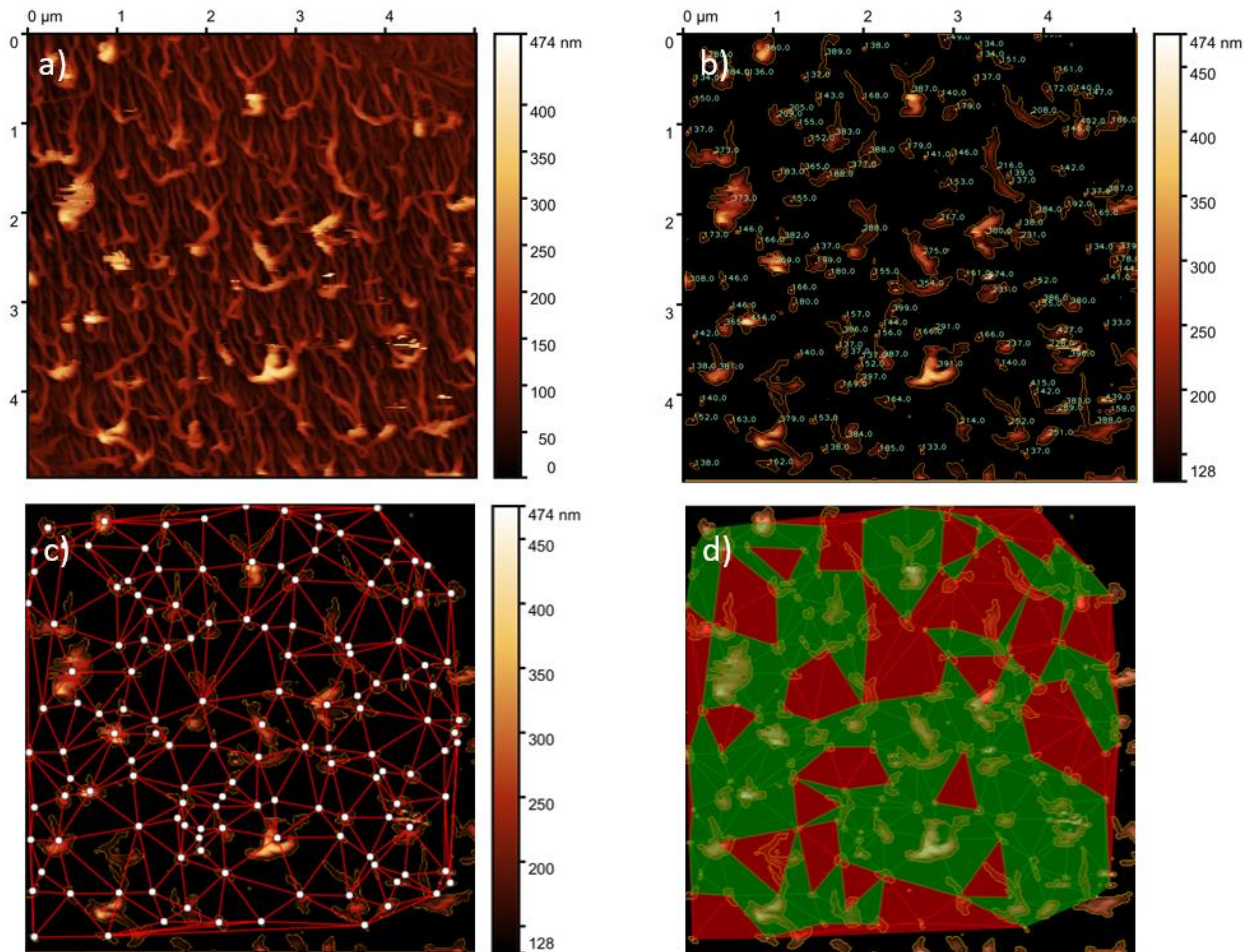


Fig. 6.3. Steps used during AFM image processing, leading to the calculation of the Delaunay plot, where (a) is the original AFM image, (b) shows isolated large-scale features with outlined borders and heights (nm) overlaid on top, (c) shows Delaunay triangulation plot of the large-scale features overlaid on top of the AFM image of isolated large-scale features, and (d) shown the resulting surface binary probability wetting map of the surface, where green area indicate low probability of wetting and red areas indicate high probability of wetting.

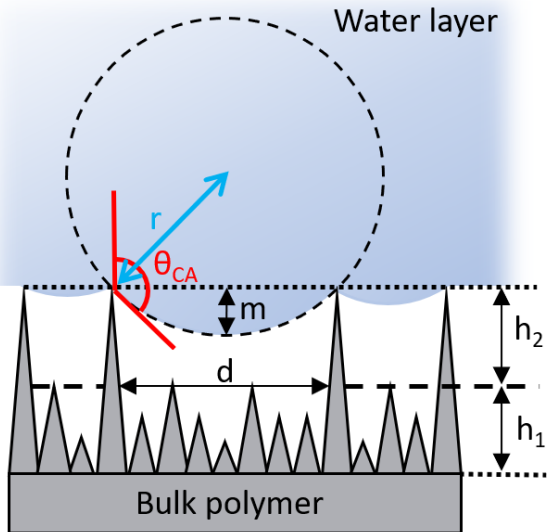


Fig. 6.4. Schematic illustration of a water drop residing on the peaks of large-scale features, in which the meniscus distance is approximated by a disc fitted to the peaks of large-scale features, and the distance between the features. Where r is the radius of the approximated disk fitting the water layer meniscus, m is the distance between the top of the large-scale features and the bottom of the water layer meniscus, d is the distance between the two adjacent large-scale features measured as the mean height boundary, and θ_{CA} is the inherent water contact angle of the polymer used for fabrication of the surface coating.

(h_2), and the distance between the feature boundaries (d). A contact angle of 108.5° (θ) for pure bulk FEP was used to fit the disk. The model was capable of analyzing the binary wetting probability of rough surfaces made from compounds that have a bulk contact angle above 90° (i.e., hydrophobic compounds only). The resulting calculation determined the Sagitta of the circle with a transverse line used as the line traced between the peaks of the two features (m) (Fig. 6.4). The Sagitta was used to approximate the meniscus of a water drop suspended on a rough surface with a given aspect ratio of the surface features. The calculation integrated through all vertices in the Delaunay plot, thus allowing the calculation of the distance between the water drop's meniscus and the mean height line. The result of the calculation was a wetting map (Fig. 6.3d) which predicted the % area which had a probability of being wetted by the water layer above it.

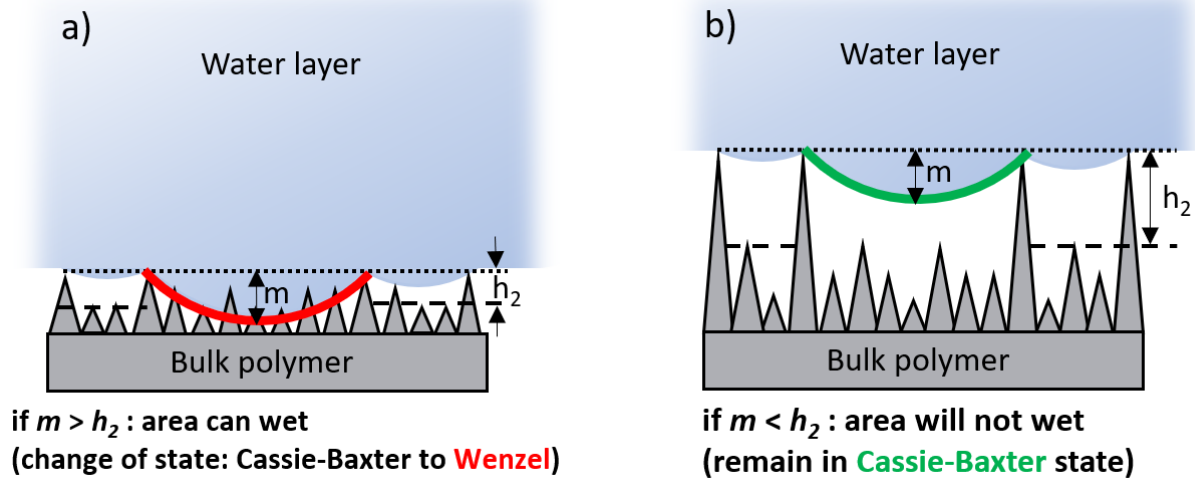


Fig. 6.5. Schematic illustrating the approximated water drop meniscus on a surface that was computed to have a high binary probability of being wetted, and a low binary probability of being wetted (transition to the Wenzel state).

If the surface roughness of the polymer coated surface is relatively low, accompanied by large-scale hydrophobic features that are short, the probability of the partially exposed glass surface to get wetted increases. This occurs due to the meniscus of the water layer extending down below the boundary of the average height of surface features, thus the higher probability of that meniscus to reach the bottom of the partially exposed surface and wetting of the underlying surface (Fig. 6.5 a). If the surface roughness of the polymer coated surface is high, and is accompanied by large-scale hydrophobic features that are tall, the meniscus will remain suspended on the tips of the large scale features, and be restrained from extending below the boundary of the average height of surface features. This would therefore lead to low probability of the underlying exposed glass surface being wetted by the water layer above.

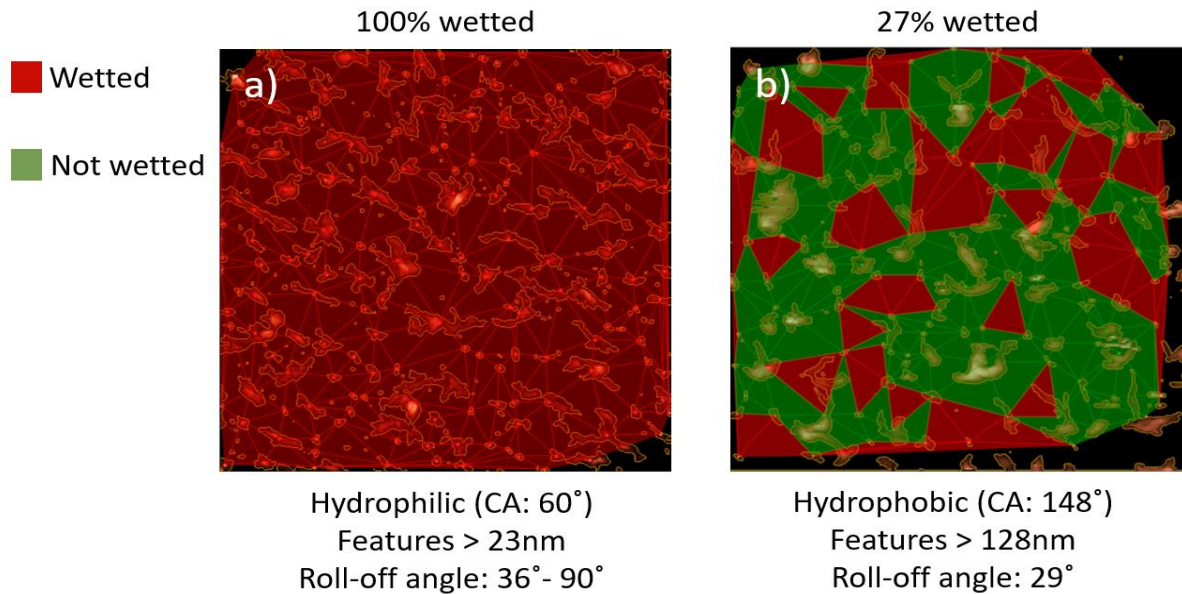


Fig. 6.6. Calculated binary wetting probability maps of the hydrophobic and hydrophilic surfaces.

6.3 Results and Discussion

The experimental results have provided binary wetting maps of the surfaces, outlining the areas of the surface which have a low probability of being wetted (Not Wetted, Green) and those with a high probability of being wetted (Wetted, Red). The computer prediction indicates that the hydrophilic surface with a contact angle of 60° possessed features that would allow the water meniscus to extend down below the boundary located at the 50% line (the line of the mean height of all surface features) over the entire surface. A hydrophobic surface with a contact angle of 148° would allow the meniscus to dip that low in only 27% of its observed area (Fig. 6.6).

When examining the surface geometry of both surfaces, the diameter of the large-scale features, pitch, and distance between the boundaries of the large features were comparable (Fig. 6.7.) The diameter of the features was 171 ± 102 nm for the hydrophilic surface and 154 ± 114 nm for the hydrophobic surface. The pitch of the features was 482 ± 211 nm for the hydrophilic surface and 474 ± 202 nm for the hydrophobic surface. The resulting distance between the features was calculated separately for each set of vertices in the Delaunay plot and was averaged to 446 ± 209

nm for the hydrophilic surface and 423 ± 196 nm for the hydrophobic surface. The resulting meniscus length (m), being dependent on the distance between feature boundaries (d) and the FEP contact angle ($108.5^\circ, \theta$), were also comparable and fell within each other's standard deviation: 179 ± 89 nm for the hydrophilic surface and 166 ± 88 nm for the hydrophobic surface.

The variable factor determining the aspect ratio of the surface features is the height. The hydrophilic sample possessed a height h_2 of 23 nm, while the hydrophobic surface possessed a height h_2 of 128 nm. The proof of concept for the resulting model shows that it is capable of approximating the possibility of wetting (transition from the Cassie to Wenzel state) on rough surfaces with a hydrophobic polymer.

6.4 Conclusion

Probability of local surface wetting on rough hydrophobic surfaces, with partially exposed underlying hydrophilic substrate, has been computationally approximated via mapping of water layer meniscus on surface topology. The topology of the rough hydrophobic surface was obtained via AFM and the computational process has been automated using a python script. This methodology provides a binary wetting probability map, which identifies area with high and low probability of surface wetting based on the extent of the water layer meniscus down in the valleys between the surface features. Calculation of the binary wetting probability on the partially exposed rough hydrophobic surfaces, allows us to tailor the surface structure with specific CA and CAH values. Further work may allow for 3D mapping of the water layer meniscus and may account for mass of the water layer, which will provide for a more representative model of the surface wetting properties.

Chapter 7. Stable Jumping Dropwise Condensation under Large Subcooling Conditions

7.1 Introduction

The spontaneous jumping of microscale water droplets on some superhydrophobic surfaces was first reported by Boreyko and Chen in 2009 [92]. Self-propelled dropwise condensate on superhydrophobic and holds promise for imparting anti-fogging [93], defrosting/anti-icing [94]–[98] and self-cleaning [99]–[102] properties to surfaces without the need for external forces such as gravity. This new mode of dropwise condensation can also improve the heat transfer efficiency from 30% to more than an order of magnitude [103]–[110], and thus holds great potential for energy intensive applications such as heating, ventilation, and air conditioning (HVAC) systems[111], water distillation[112], air water harvesting[113], steam power generation[114] and thermal management of electronic devices[115], [116]. Both experimental work and simulations [117]–[133] have been conducted to define the mechanisms of droplet nucleation, growth and jumping on nanotextured superhydrophobic surfaces with and without the presence of non-condensable gases. A surface comprised of closely packed nanofeatures covered by low surface energy materials is necessary so that condensed liquid droplets can remain suspended and mobile over the nanofeatures. When two or more such droplets coalescence, the release of excess surface energy propels the droplets out of the plane of the surface, which results in jumping dropwise condensation. In addition to jumping, other mechanisms for droplet displacement after coalescence may also occur including: sweeping (merged droplets move along the surface); and flooding (merged droplets wet into the nano/microstructures and are pinned to the surface), depending on the details of the surface

nanostructures and the subcooling temperature (ΔT , defined as the difference between the surface temperature and the dew point of the vapor). Flooding is especially disadvantageous as it decreases the mobility of water droplets and/or irreversibly damages the surface nanofeatures and thus the wetting properties.

The main difficulty in obtaining jumping condensation at high ΔT values is the rapid increase in the nucleation rate with increasing ΔT . Only when the density of nucleation sites on the surface is greater than the nucleation density required to accommodate the water vapor flux is plastron wetting (i.e. flooding) suppressed and the probability of jumping increased. The relationship between the nucleation rate J and nucleation radius r_c is governed by (**Equation 7.1**): [83]

$$J = J_o \exp(-\Delta G/kT) = J_o \exp[-\pi \sigma_{lv} r_c^2 (2 - 3\cos\theta + \cos^3\theta)/3kT]$$

where J_o is the kinetic constant, ΔG is the free energy barrier, k is Boltzmann's constant, T is the condensation temperature, θ is the intrinsic contact angle (CA), and σ_{lv} is the liquid-gas surface tension. The relationship between the nucleation radius r_c and ΔT can be defined by (**Equation 7.2**)[134]:

$$r_c = \frac{2T_v \sigma_{lv}}{H_{fg} \rho_l \Delta T}$$

where T_v is the vapor temperature, h_{fg} is the latent heat, and ρ_l is the liquid density. For a given solid surface, the critical diameter of a nucleated droplet, r_c , is proportional to $1/\Delta T$, and the nucleation rate J is proportional to $\exp(r_c^2)$.

Previously reported surfaces exhibit droplet jumping within narrow temperature ranges for limited periods of time, and durability has not yet been demonstrated. Here, we describe a novel

hot lamination-peeling technique to fabricate durable fluorinated ethylene propylene (FEP) polymer coatings composed of dense nanofibril networks on aluminum. By adjusting the processing parameters, excellent superhydrophobicity with water contact angles approaching 180° and slide-off angles approaching 0° were achieved. Jumping dropwise condensation on the surface was maintained at large subcooling values ($\Delta T > 70$ K) at atmospheric pressure. Due to the inherent chemical stability of FEP, the fabricated surfaces exhibited excellent durability, and superhydrophobicity and jumping condensation were maintained for over 1000 h of condensation at a ΔT of 50 K after 1000 h of salt fog testing at 35 °C and atmospheric pressure. This nanofabrication method is cost-effective and environmentally friendly because it uses no lithography or templates, employs no solvents or harsh chemicals, and can be used to coat large areas.

7.2 Methods

7.2.1 Surface Fabrication

The surfaces utilized in the experiments were fabricated on aluminum surfaces using a peeling lamination method described in Section 2.1.1. In all samples, FEP was laminated onto a cleaned aluminum substrate at 304 °C, followed by cooling before peeling away the bulk FEP layer. The effect of bonding site density on the surface morphology was evaluated using smooth and rough aluminum substrates. The effects of the fabrication method on the crystallinity of the laminated polymer has been previously evaluated by controlling the cooling rate and peeling conditions under both equilibrium and non-equilibrium conditions. Equilibrium conditions were defined as polymer-substrate interface being at the same temperature, while non-equilibrium conditions were defined as when polymer and substrate were at two different temperatures (Table 7.1).

Table 7.1. Surface fabrication conditions

Surface #	Aluminum	FEP nanofibril fabrication conditions				Polymer Status
		Lamination	Cooling	Peeling		
S ₁₈	Smooth	-	-	-	-	-
S ₁₁	Rough	-	-	-	-	-
S ₁₄₂	Smooth	304 °C, 150 psi	25 °C water, 10 min	25 °C, air	Equilibrium	
S ₁₅₀	Smooth	304 °C, 150 psi	25 °C water, 10 min	175 °C, oven	Equilibrium	
S ₁₄₇	Smooth	304 °C, 150 psi	25 °C air, 1 h	175 °C, oven	Equilibrium	
S ₁₅₅	Smooth	304 °C, 150 psi	25 °C aluminum plate 30 sec	25 °C, air	Non-Equilibrium	
S ₁₈₀	Smooth	304 °C, 150 psi	175 °C oven, 1 min	175 °C, oven	Non-Equilibrium	
S ₁₇₀	Rough	304 °C, 150 psi	175 °C oven, 1 min	175 °C, oven	Non-Equilibrium	
S ₁₇₉	Rough	304 °C, 150 psi	25 °C aluminum plate, 30 sec	25 °C, air	Non-Equilibrium	

7.2.2 Surface Characterization

As reported by Xu et al., the contact angle (CA) and sliding angle (SA) of surfaces were measured with a contact angle goniometer (250-F1, Rame-Hart Instrument Co.) using a 3 µL droplet, and a larger droplet when 3 µL could not be transferred to the surfaces due to superhydrophobicity.

The micro- and nanostructures of fabricated surfaces were studied by field emission scanning electron microscopy (FESEM, Amary) under 5 kV. For SEM imaging, samples of FEP-coated aluminum were sputter-coated with 2 nm of platinum for top-down views and 5 nm for cross-sectional views; aluminum substrates were not sputter coated. The samples for cross-sections were prepared using a manual stainless steel shear.

Atomic force microscopy (AFM, Bruker MultiMode 8) was used to measure the surface roughness, the diameter distribution of nanofibrils, and the Young's modulus of single fibrils. The spring constant of the AFM cantilever was 0.4 N/m, the AFM tip radius was 5 nm, and the scan rate range was 0.5 - 2 Hz.

The tensile strength of surface nano-fibrils was evaluated with AFM, and AFM images were obtained utilizing the ScanAsyst-Air probe in the PeakForce Tapping and ScanAsyst modes. The images obtained were 512 x 512 pixels with a view area of 1 μm x 1 μm. The elastic modulus of the fluoropolymer fiber was obtained using the Peak Force Quantitative Nanomechanical Property Mapping (QNM) mode. The deflection sensitivity and spring constant of the ScanAsyst-Air probe were calculated to be 0.2155 N/m and 53.77 nm/V, respectively. A standard crystalline Ti surface (Bruker, RS-12M) was used to calculate the tip diameter: 10.05 nm. The scan area for modulus calculations was 128 x 128 pixels with a view area of 1 μm x 1 μm. The modulus was calculated by applying a Hertzian modulus fit model with a threshold crossing adhesion algorithm to the retract force curves.

7.2.3 Condensation Chamber

In order to observe the coalescence-induced drop jumping effect on the superhydrophobic nano-coatings on aluminum surfaces, a condensation chamber was constructed (Fig. 7.1). An aluminum chamber with a glass window and an inside water reservoir was used as the water condensation chamber. Thermocouples (described in the next section) were installed inside the chamber to detect the dry-bulb and wet-bulb temperatures 3 mm from the sample surface. The sample surface temperature was measured by a precision fine wire thermocouple with a tip diameter of 250 μm. The thermocouple was affixed to the sample surface by a screw-set. The gas pressure

inside the chamber was equalized to atmospheric pressure using a needle vent. Samples were mounted onto an aluminum sample stage with a size of 25 mm x 32 mm using screws connected to a chiller (Thermo Scientific, RTE740). A thin layer of thermally-conductive silicone grease was applied between the sample and the chiller stage to ensure good thermal conductivity. The area of the chiller surface with no attached sample was covered by a half-inch thick sheet of silicone rubber to minimize the effects of environmental temperature on the chiller temperature. Two heater cartridges were built into the aluminum chamber to heat the water reservoir as well as the internal surfaces of the chamber including the glass window to prevent undesired condensation inside the chamber.

Chamber humidity was calculated via the dry-bulb and wet-bulb method. The dry-bulb and wet-bulb temperatures were obtained via K-type thermocouples (Omega, KMQSS-062G-6, 1.6 mm OD) connected to an Omegaette HH303 thermometer. The thermocouples were positioned ~3 mm from the test surface and were vertically spaced 10 mm apart. The wet-bulb thermocouple was wrapped in a cotton cloth wick with the end of the wick submerged in an isolated aluminum water

reservoir measuring 3 mm x 10 mm x 4 mm (LWH). A second wick was used to keep this reservoir filled by bridging to the main water reservoir.

7.2.4 Experimental Conditions

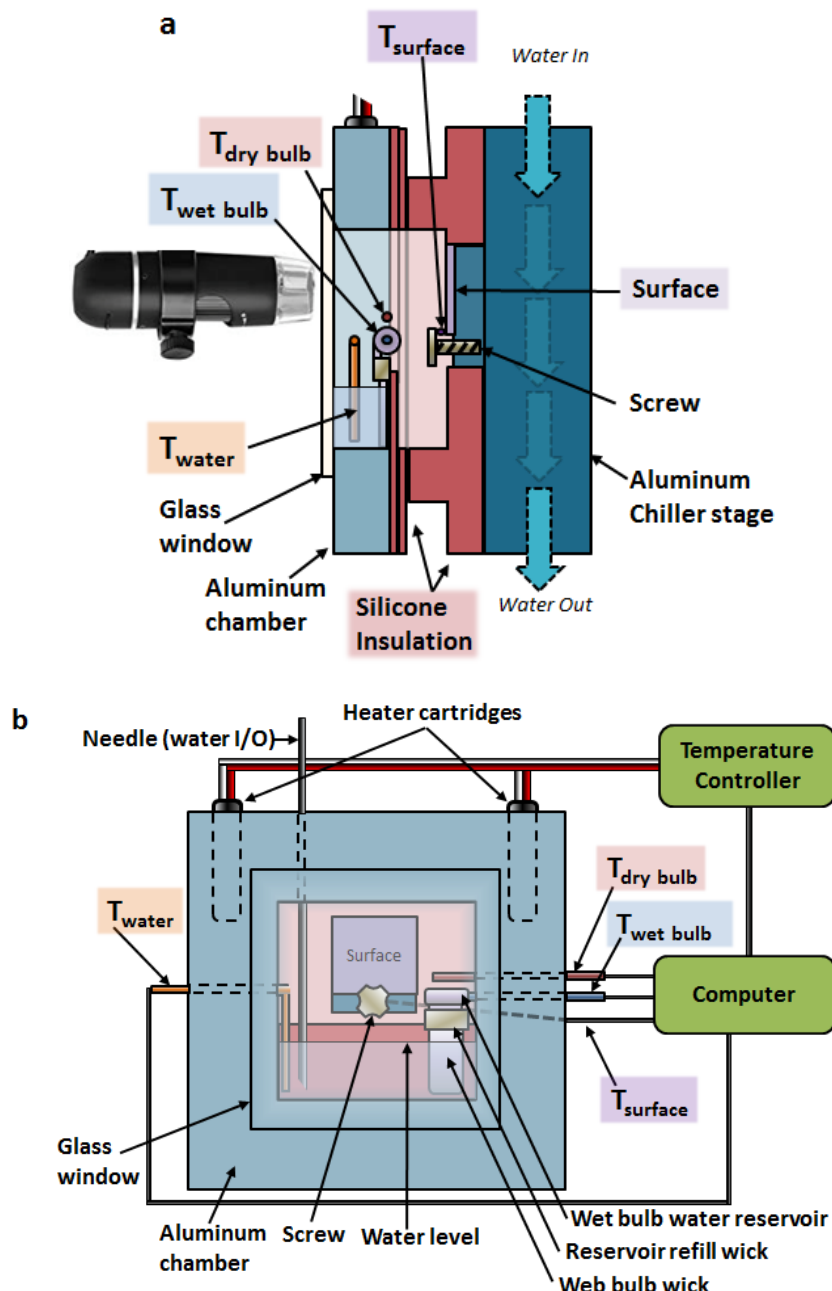


Fig. 7.1. The sketch of condensation chamber and chiller stage set-up.

The water condensation behavior on fabricated superhydrophobic surfaces was studied under a wide range of subcooling temperatures from 1 K to 75 K. To obtain this wide range of ΔT values, a chamber was built (Table 7.2, Addendum) that enabled the heating of the water source and the cooling of the sample surface separately inside the chamber. Small ΔT values were obtained by cooling the surface of the samples to specific temperatures with a chiller (Thermo Scientific, RTE740) while the water source was maintained at ambient temperature. Large ΔT values were obtained by setting the chiller stage to 0 °C and increasing the temperature of the water source. The chamber was maintained at atmospheric pressure using a 22-gauge needle to vent the chamber interior to the atmosphere. The relative humidity of the chamber was measured by a wet-dry bulb located 3 mm from the sample surface. Coated aluminum samples were mounted vertically onto the sample stage (25 mm x 32 mm) by screws. A stainless-steel sheathed thermocouple (250 µm o.d., Type K, OMEGA Engineering) was secured to the top surface with a screw to monitor the surface temperature of samples. The measured ΔT as a function of chiller temperature and heater temperature for each surface is shown in Table S1. Videos of condensation were recorded using a digital microscope (Jiusion-1000x) at 30 frames per second after the ΔT had stabilized for 20 minutes. The same setup was used for long-term stability testing.

The dry-bulb and wet-bulb temperatures were periodically recorded throughout the experiment. The chamber temperature was measured directly from the dry-bulb temperature, and the relative humidity was obtained using the psychrometric hygrometry method based on the following equation [92] (**Equation 7.3**):

$$RH = \frac{e_w - A * P * \Delta T}{e_d} * 100\%$$

where RH is the relative humidity, e_w is the saturation vapor pressure at a given wet-bulb temperature, e_d is the saturation vapor pressure at the dry-bulb temperature, A is the measured humidity coefficient (e_w and e_d can be calculated from the Buck formula,² A can be calculated by an empirical formula²), P is the mean atmospheric pressure, and ΔT is the difference between the dry-bulb and the wet-bulb temperatures.

7.2.5 Video and Image Processing

The diameters of droplets in images were measured using ImageJ (ver. 1.51m9) software. The drop-jumping events on the surfaces were counted using a script written in Python 3.6 utilizing OpenCV (Open Computer Vision) library and Pandas library.

Videos were visually analyzed to locate frames where jumps occurred. These frames were then saved with a known resolution and area length, and the drop diameters were then calculated in ImageJ using a minimum drop size cutoff of 30 μm . Drop diameters of drops that did not jump were calculated by segmenting the video into a length that was roughly 1/9th of the original and then locating drop diameters within that region. This was also performed using ImageJ. The drop volumes were calculated using the formula (**Equation 7.4**):

$$\frac{\pi}{3} * r^3 * ((2 + \cos x) * (1 - \cos x)^2)$$

where x is the contact angle, and r is the radius of the water droplet.

7.3 Results and Discussion

The performance of the superhydrophobic surfaces was characterized by evaluating the rate of sweeping and jumping events, using computer vision-assisted observations of experimental videos. Jumping events were characterized by coalescing drops being propelled away from the surface (Fig 7.2 a), while sweeping events were characterized by coalescing water drops sliding

along the surface and merging with drops present in its path (Fig. 7.2 b). Condensation of the three surfaces with highest superhydrophobicity (S_{170} , S_{179} , and S_{180}) were tested in water vapor saturated air at atmospheric pressure using a customized chamber shown in Section 7.2.3. Images of liquid water condensed on the three surfaces as a function of increasing ΔT are shown in Fig. 7.3.

The drop diameters at the time of event occurrence were quantified and presented in Fig. 7.4a, while the ratio of jumping events to the total coalescence events was quantified and presented in Fig. 7.4b.

At small values of ΔT , e.g., < 5 K, small droplets (< 50 μm diameter) predominated, and the average diameter and size distribution increased gradually with increasing ΔT (Fig 7.3 and Fig 7.4 a). When $\Delta T = 5$ K, the average droplet diameters of all samples were similar: 45 μm for S_{170} and 30 μm for S_{179} and S_{180} . As ΔT increased, the average droplet diameter on S_{170} increased to 115 μm before flooding occurred. Surfaces S_{179} and S_{180} sustained the jumping of larger droplets (200 – 250 μm) before transitioning to the flooding state. Still images of the surfaces during the experiments showing comparative drop sizes are shown in Fig. 7.3.

The critical ΔT , ΔT_{crit} defined as the maximum ΔT when the jumping rate went to zero, was measured to be 24 K, 69 K, and 73 K, for S_{170} , S_{179} , and S_{180} , respectively. As ΔT approached ΔT_{crit} , a few large droplets (diameter of 1300 μm) appeared on all three surfaces. During condensation experiments, droplets grew and coalesced, and after coalescence, the droplets either remained stationary, moved horizontally along the surface (i.e. sweeping), or departed from the surface (i.e. jumping).

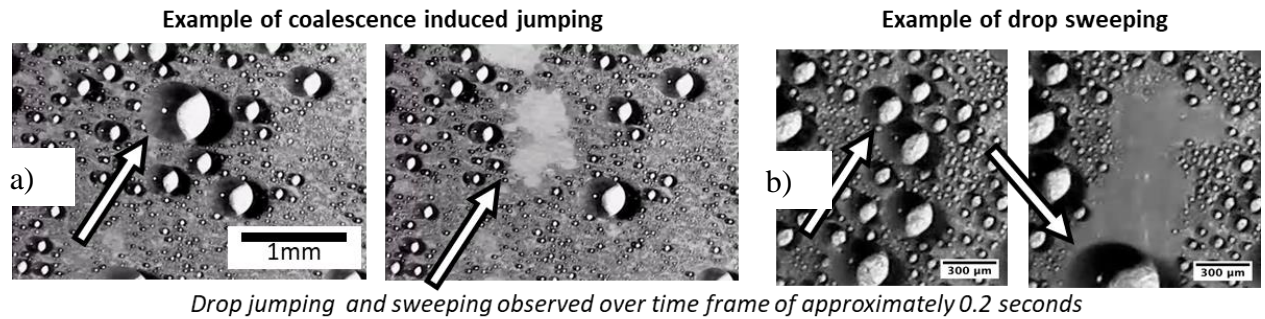


Fig. 7.2. Still frames from experimental video showing examples of jumping (a) and sweeping (b) events.

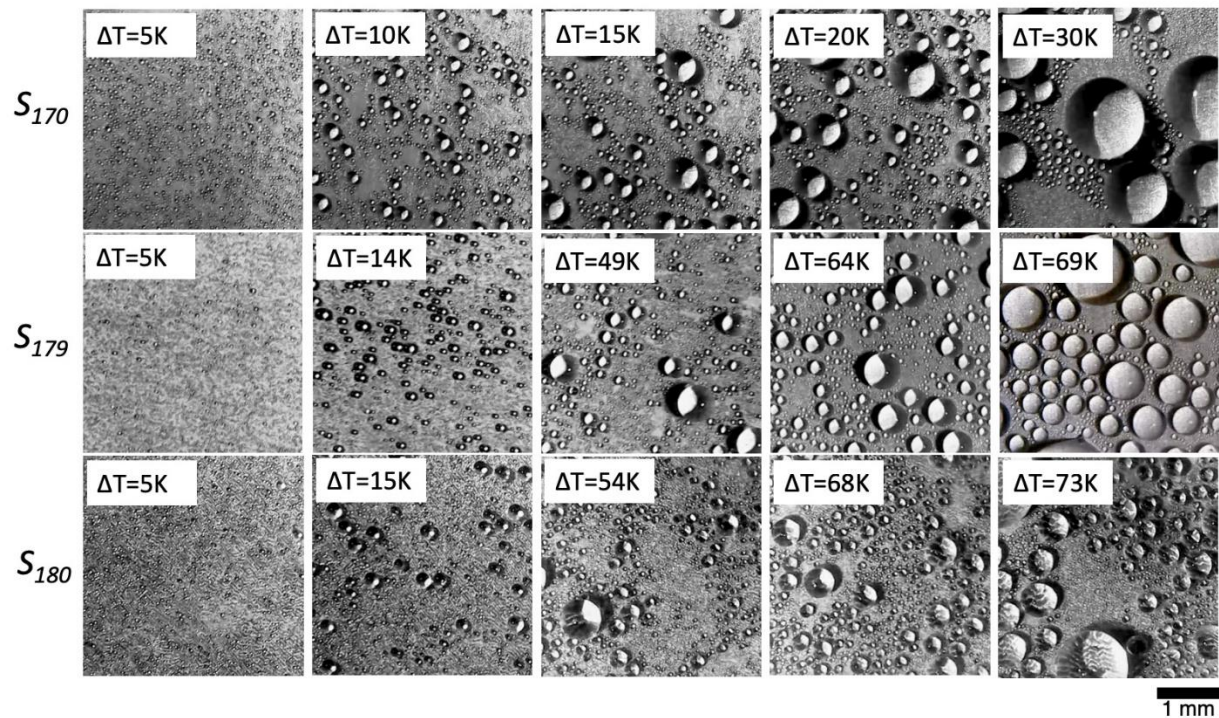


Fig. 7.3. Optical images showing the jumping dropwise condensation performance of surface R₁₇₀, R₁₇₉, and SM₁₈₀ at different ΔT after 15-20 min of condensation.

The percentage of coalescence events resulting in droplet jumping (Fig. 7.4 b) was determined for the three surfaces based on 2-min videos recorded at different ΔT . The jumping percentage was defined as the total number of jumping events divided by the total number of coalescence events. As shown in Fig. 7.4 b, the droplet jumping rate on S_{170} was much lower than either S_{179} or S_{180} at

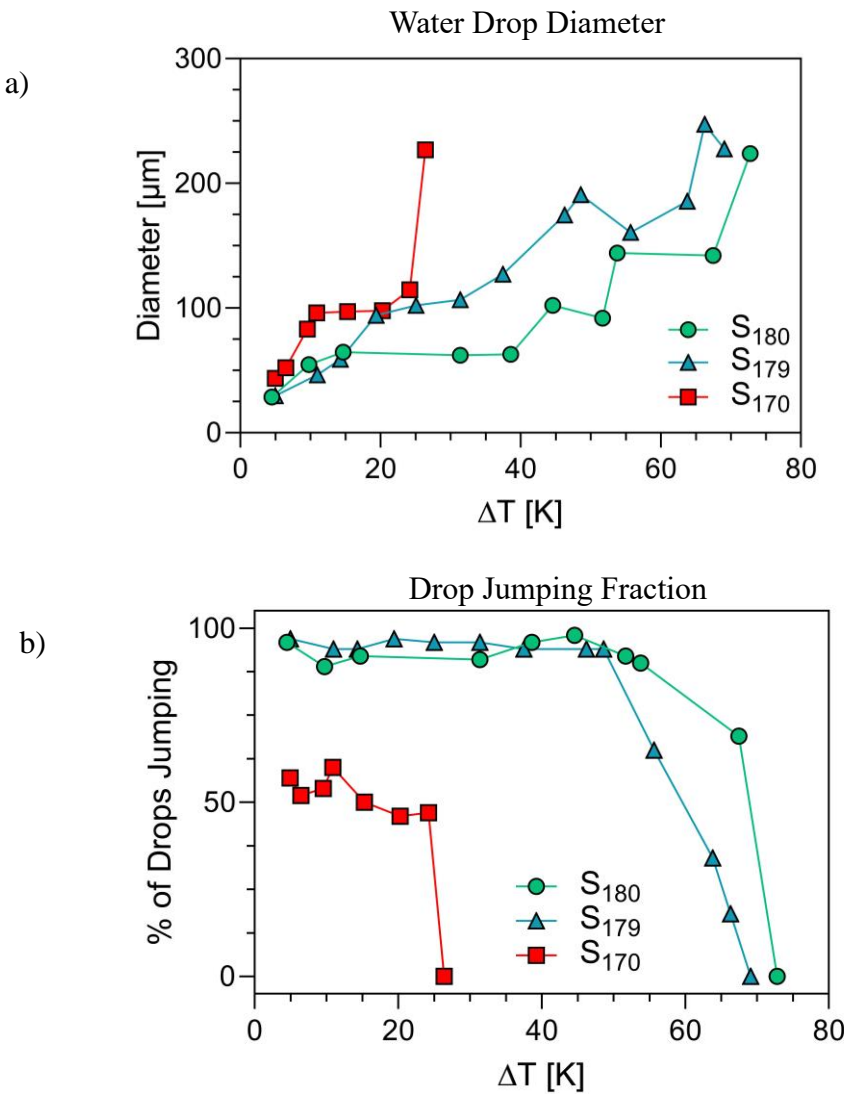


Fig. 7.4. (a) The average diameter of the condensed water droplets. **(b)** The percentage of coalescence events resulting in droplet jumping over 2 min for R_{170} , R_{179} , and SM_{180} at different ΔT after 20 min of condensation. The total number of jumping events over 2 minutes for R_{170} , R_{179} , and SM_{180} at different ΔT . The imaging area was 4.8 mm x 3.6 mm..

all values of ΔT . The jumping rate increased dramatically on both S₁₇₉ and S₁₈₀ with increasing ΔT and reached a maximum at $\Delta T = 55\text{K}$. The high jumping rate freed a large fraction of the surface S₁₇₉ for the nucleation and growth of condensed liquid drops. Above this subcooling value, the jumping rate decreased, and the sweeping rate increased with further increases in ΔT until the surface was completely flooded.

S₁₇₀ exhibited moderate jumping with a percentage of 45-60% up to a ΔT of 24 K, above which a transition to sweeping and flooding occurred. In contrast, S₁₇₉ and S₁₈₀ exhibited significantly higher jumping percentages (>90 %) up to a ΔT of 49 K. The jumping rates decreased from 90% to 50% at ΔT values of 60 K and 70 K for S₁₇₉ and S₁₈₀, respectively. At greater ΔT values, larger droplets were formed that exhibited a slower jumping rate than smaller droplets.

In all samples, the jumping rate increased with increasing ΔT up to a maximum, then gradually decreased to zero as ΔT approached ΔT_{crit} as shown in Fig. 7.4 b. The highest jumping rates were measured to be 183, 3445, 2396 min⁻¹ cm⁻² at ΔT values of 7 K, 30 K, and 40 K for S₁₇₀, S₁₇₉, and S₁₈₀, respectively. These values represent the lower limits of jumping rates because droplets smaller than 25 μm could not be resolved by our optics. As the jumping rate increased, both the water condensation rate and heat flux are expected to increase. At peak ΔT values, the jumping rate on S₁₇₉ was about 19 times higher than S₁₇₀ and 1.4 times higher than S₁₈₀, indicating that S₁₇₉ maintained the highest heat flux. Comparing the results of S₁₇₀ and S₁₇₉ shows that the ΔT_{crit} , the jumping percentage, and the peak jumping rate were significantly improved by the dense FEP nanofibril arrays. Comparing S₁₇₉ and S₁₈₀ shows that micro/nano hierarchical structures can increase ΔT_{crit} by as much as 5 K, although it reduces the peak jumping rate by 30%.

A long-term and continuous condensation experiment was conducted to verify the reliability of surface S₁₇₉. It has been also observed that significant droplets jumping occurred at the same time.

A jumping percentage >90% was maintained after 1000 hr of condensation at ΔT of 50 K based on statistical calculations, demonstrating the excellent durability of S₁₇₉ for jumping dropwise condensation at large ΔT .

Analysis of a single nanofiber modulus was conducted via peak force mapping AFM. AFM samples were prepared by cutting the fluoropolymer-coated aluminum surfaces to 10 mm x 10 mm. In order to prevent measuring the flexural force of the fiber instead of the desired elastic modulus of the polymer that the fiber was composed of, the surface topography was modified to allow the fibers to lay flat on the surface, instead of standing straight up. The change in the geometric orientation of the fibers was conducted by applying a force of 1816 kg/cm² for approximately 1 s normal to the substrate. The force was sufficient to permanently bend the fibers down but low enough to not permanently deform them, as the literature reported Young's modulus of FEP is 450 MPa (4589 kg/cm²).

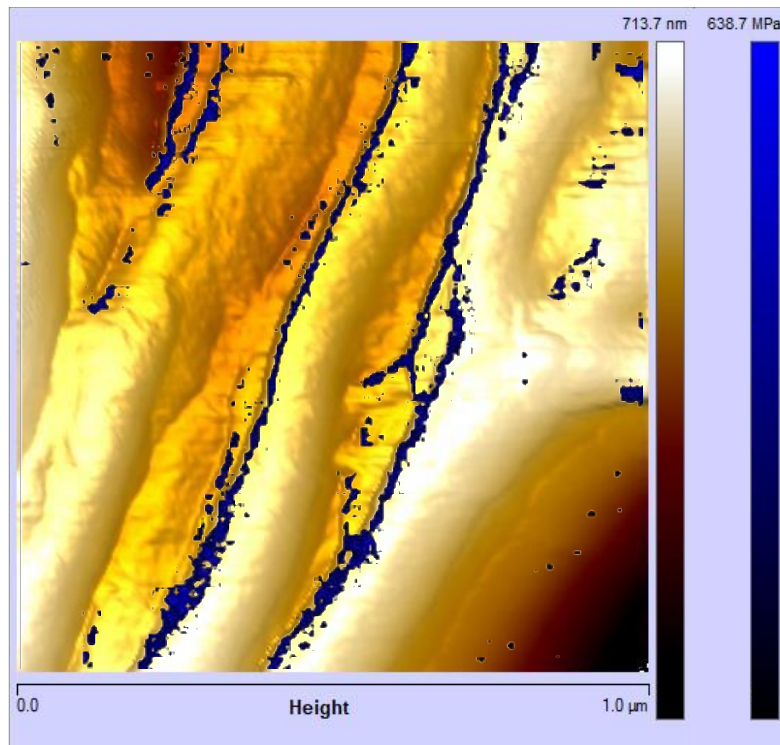


Fig. 7.5 AFM image of surface nano-fibrils used to measure the Young's modulus. Areas used to calculate Young's modulus are overlaid in blue.

The RMS roughness of the sample containing fluoropolymer fibers was calculated 1.9 to be 84.8 nm using NanoScope. The topography of the fibers residing on the substrate are shown in black-orange in Figure 7.5, with the elastic modulus overlaid in blue.

The Elastic (Young's) modulus of a standard PDMS sample (PDMS-SOFT-2-12M, Bruker) with a known elastic modulus was used to test the methodological and quantitative procedures. The elastic modulus of the standard PDMS sample was reported by Bruker to be 3.5 MPa. The elastic modulus of the sample was experimentally determined to be 4 MPa (± 1.9 MPa) by measuring a 128 x 128 pixel area of the sample. The elastic (Young's) modulus of the fluorinated ethylene propylene fiber was then measured by scanning a 128 x 128 pixel area of the surface. The average Young's Modulus was determined to be 503 MPa, with a maximum of 639 MPa.

7.4 Conclusion

In summary, extremely superhydrophobic coatings with FEP nanofibril structures were fabricated on aluminum substrates using a novel, low cost, scalable peeling technology. The nanostructure morphology including: nanofibril density, diameter, aspect ratio, and orientation are determined by controlling the cooling/peeling conditions and the aluminum substrate roughness. The coating composed of dense and uniform nanofibril arrays and network structures on rough aluminum substrates enable a large critical ΔT as high as 69 K for jumping dropwise condensation. The critical ΔT was further increased to 73 K on a smooth aluminum surface coated with a composite of micro-ridges and arrays of nanofibril. The superhydrophobic coatings formed on both smooth and rough aluminum substrates showed excellent durability both in a salt fog testing for 1000 h as well as in condensation testing at a ΔT of 50 K for 1000 h. Such a robust coating

exhibiting stable jumping dropwise condensation could find applications for high flux heat exchanging.

7.5 Addendum

Table 7.2. Experimental environmental parameters and the calculated subcooling temperature for superhydrophobic surfaces exhibiting drop jumping properties

Sample	T _{chiller} [°C]	T _{water} [°C]	T _{dry-bulb} [°C]	T _{wet-bulb} [°C]	T _{surface} [°C]	e _d	e _w	RH [%]	Dew Point [°C]	ΔT [K]
S ₁₇₀	15	20	22.4	21	15.4	27	25	88	20	5
	10	20	21.5	19	10.7	26	22	79	18	6
	5	20	19.4	17	6	23	19	79	16	10
	0	25	17.6	17	1.5	20	19	94	17	15
	0	35	28	24	2.1	38	30	72	22	20
	0	40	32.3	28	2.4	48	38	72	27	24
	0	45	36.1	31	3.2	60	45	69	30	26
S ₁₇₉	15	20	22.6	21	15.6	27	25	87	20	5
	5	20	20	18	6	23	21	82	17	11
	0	20	18.6	17	1.7	21	19	85	16	14
	0	30	24.6	22	1.6	31	26	80	21	19
	0	40	32.3	28	2.1	48	38	72	27	25
	0	50	41.3	36	3.4	79	59	70	35	31
	0	60	51.5	44	5.2	133	91	64	43	38
	0	85	73.6	60	10.8	367	200	52	60	49
	3	91	77.6	65	9.3	434	252	56	65	56
	0	90	78	73.6	10	441	367	82	74	64
	0	95	82	66.2	12	520	266	49	66	66
	0	100	87	69.3	13	635	305	46	69	69
S ₁₈₀	15	20	22	21	15.4	26	25	91	21	5
	5	20	19.8	18	6.6	23	21	84	17	10
	0	25	20.7	18	1.4	24	21	77	16	15
	0	50	41.6	35	2.5	80	56	64	34	31
	0	60	51.1	43	3.2	131	87	62	42	39
	0	70	62.2	51	4.7	222	130	55	50	45
	0	85	74.6	60	5.9	383	200	50	60	54
	0	90	80.9	75	7.1	497	389	77	75	68
	0	95	83.9	82	8.9	561	520	92	82	73

Chapter 8. Characterizing the Chemical Bonding of a Fluoropolymer Coating on Soda-Lime Glass via XPS Depth Profiling of the Polymer-Glass Interface

8.1 Introduction

The electrical output of solar PV panels is reduced by two main factors: the reflection of light at the air-glass interface and the scattering of light due to soiling. Reflections occur because of abrupt changes in the refractive index (RI) between air ($n = 1$) and glass ($n = 1.52$) [135], which results in the reflection of $\sim 4\%$ of light at normal incidence, with greater percentages observed at steeper angles. Anti-reflective coatings (ARCs) have been developed in which a thin layer of a transparent material with an intermediate refractive index is applied to solar cover glass, thereby reducing reflections by 50-80% [136], [137]. Although ARCs are currently applied to $\sim 80\%$ of solar PV modules, they do not improve soiling, which can reduce electrical output by as much as 50%, depending upon the local environment [12], [17], [45], [50]–[54]. In order to mediate losses in PV efficiency due to surface reflections and soiling, ARC coatings must also possess anti-soiling properties. Such coatings must also have a low RI that can be easily manipulated to create a refractive index gradient to improve ARC properties, be mechanically and chemically stable in humid, dry, and high-UV environments, and be chemically inert to prevent the adhesion of contaminants to the surface.

Fluoropolymer materials meet all the above criteria. Although fluoropolymers have been widely utilized to produce hydrophobic coatings [138], [139] and AR/anti-soiling coatings [82], [140], the adhesion mechanism between the coating and glass have not been reported. In this paper, the bonding mechanism of fluoropolymer coatings fabricated on PV-grade soda-lime glass was examined via X-ray photoelectron spectroscopy (XPS) depth profiling using C₆₀ ion sputter etching [141], [142]. The atomic ratios of the soda-lime glass constituents (Si, O, Na, Ca) were

analyzed, along with the diffusion of fluorine ions. Mobile species – fluorine and sodium – were observed to diffuse in and out of the glass SiO_x matrix, respectively, and the diffusion gradients, F ion penetration depth, and Na ion depletion layer are reported. The depletion of Na ion is believed to increase the porosity of the glass surface which allows the fluoropolymer to interpenetrate the glass surface, facilitating bonding between the polymer coating and the glass surface. Additionally, this effect produces a refractive index gradient within the top layers of the glass surface, further increasing the AR properties. High-resolution XPS identified the intensity and shifts of Si, O, Na, and F peaks in order to identify the bonding chemistry between the molecules constituting the polymer coating and soda-lime glass [143]–[147].

8.1.1 ARC and Anti-Soiling Coatings

The two primary types of anti-reflective and anti-soiling coatings are hydrophobic [4]–[11] and hydrophilic coatings [11]–[14]. Hydrophilic coatings rely on water to fully wet the glass to carry away dust particles as water is wicked to the bottom of the panel. Because hydrophilic glass is readily contaminated by adsorbed chemicals (e.g., proteins, salts, surfactants) it can become progressively less hydrophilic (i.e. more hydrophobic) over time, losing its ability to wick water. Hydrophobic coatings are composed of a chemically-inert, low surface energy material that prevents chemical reactions from occurring between soil and the glass surface. Moreover, dew does not wet a hydrophobic surface to form a liquid film, and condensation will instead form discrete droplets with relatively high contact angles (CAs). The difference between the advancing and receding CA (CA hysteresis or CAH) can be decreased using the proper nanostructure, allowing droplets to slide off low-energy surfaces at low tilt angles [28]. Several hydrophobic, anti-reflective, and anti-soiling coatings have been developed, including Enki CleanARC® [11],

[29], [30], DSM's anti-soiling coating [31], [32], and 3M's anti-soiling liquid coating [33]. Fluoropolymers are hydrophobic and chemically inert and have shown promise for use in anti-reflective and anti-soiling coatings. Fluorinated ethylene propylene (FEP) has been utilized to create nanotextured surface coatings on soda-lime glass [39]. The low refractive index and nanotexture derived refractive index gradient of the coating render it anti-reflective, while the inertness of the FEP and surface roughness of the coating are responsible for its anti-soiling properties [82].

8.1.2 Soda-Lime Glass Surface De-alkalization

Ion exchange has been used to modify the refraction of glass surfaces [148]. It involves the use of electrodes or the substitution of alkali ions present in glasses with other cations [149], [150]. Other glass de-alkalization techniques have also been studied [151]. Fluorine doping of glass can reduce the rate of glass corrosion [152] and can be accomplished using chemical vapor deposition (CVD) [153]–[155] and HF exposure [156].

The fabrication of fluoropolymer coatings on soda-lime glass involves a heat treatment in order to bring the temperature of the polymer above its melting point (T_m) for easy mechanical manipulation. The addition of heat during production facilitates polymer decomposition, which releases fluoride ions that easily migrate into the glass matrix. The small size of fluoride ions (1.19 Å) allows them to penetrate the Si-O matrix [157], oxidize silicon and displace oxygen and sodium [158], thereby reducing the structural integrity of the matrix, creating porosity. The top porous layer of glass can then be interpenetrated by the partially decomposed polymer chains, facilitating the bonding of the polymer to the glass substrate. This interpenetration of polymer and the newly-

created fluoride salts in the top glass layer create a refractive index gradient within the glass substrate, giving the glass anti-reflective properties.

8.2 Methods

8.2.1 Sample Fabrication

Fluorinated ethylene propylene (FEP) was used to create a nanotextured coating on top of the substrates. The polymer (Teflon® FEP film, purchased from American Durafilm) was first coated on a glass substrate and then placed in a platen laminator and heated to $T > T_m$, 304 °C ($T_m = 260$ °C) [40]. The polymer was heated above its melting point in order to increase the contact area between the polymer and substrate and to allow the melt to wet the substrate surface. Platens were then pressed with an applied pressure of 10 kPa to form a bonding interface between the polymer and glass. Afterward, the substrate with the attached bulk polymer was annealed at 175 °C for 20 minutes, and the polymer was slowly cooled to $T_g > T > T_m$ ($T_g = 80$ °C) [40]. After the temperature reached the set-point, the bulk polymer was peeled to reveal the nano-textured fluoropolymer layer on the substrate surface [39].

Fluoropolymer peeling occurs via cohesive failure at the interface of polymer adhered to the glass substrate and polymer cohesively bonded to itself at this interface [52]. Cohesive failure of the bulk polymer occurs at polymer temperatures between its T_g and T_m due to tensile force at the polymer-substrate interface [159], [160]. As the bulk polymer is peeled from the substrate surface, the non-uniform cohesive forces within the polymer create uneven breaking between within the bulk polymer, thus creating fibers as the polymer is peeled apart. The fibers ultimately break, creating a nanotextured surface with an underlying nano-layer of bulk polymer that is strongly bonded to the glass substrate.

8.2.2 X-ray Photoelectron Spectroscopy

X-ray photoelectron spectroscopy (XPS) of the test substrates was conducted using a Physical Electronics VersaProbe II XPS using a monochromatic Al K α ($h\nu$: 1486.6 eV) X-ray source. The X-ray beam diameter was set to 200 μm , while the power source was set to 50 W and 15 kV. To reproducibly obtain XPS depth profiles of the bulk polymer, polymer-interface, and bulk-glass interface, a C60 (fullerene) gun was used to remove layers (of the surface coating or substrate) to expose underlying surface for XPS analysis. The depth profiles were used to determine the relative concentrations of C, F, O, Si, Na, and Ca as a function of depth and obtain low-resolution spectra to simply evaluate peak locations and intensities. Additionally, the high-resolution XPS spectra of the layers corresponding to bulk polymer, the polymer-glass interface, and bulk glass were obtained at the surface of the same sample. Surface charge neutralization was performed before prior to data acquisition using low-energy electrons. XPS spectra were obtained using various pass energies appropriate for the particular element (29.35 eV – 46.95 eV) to maximize the electron counts during data acquisition.

Low-resolution spectra were collected in a B.E. range appropriate for each element [161] using a single pass per scan with a resolution of 0.5 eV. Prior to data acquisition, C60 was pre-heated to 400 °C with a beam acceleration of 20 kV and the C60 beam impacted an area of 2 mm x 5 mm. A depth profile data acquisition cycle was composed of C60 sputter etching for a set amount of time, followed by obtaining the photoelectron intensity and binding energy of each element.

Depth profile on bare (uncoated) glass was obtained using two different types of etch cycles, short and long. A short etch time was used to precisely observe atomic concentration changes within the thin top layer of the substrate, and a long etch time to characterize the stable bulk-glass phase. Bare (uncoated) glass depth profile thus consisted of: 2.5 min of etching followed by XPS

data acquisition for a total of 6 cycles, afterwards, 5 min etching followed by XPS data acquisition another 6 cycles. Depth profile on the polymer-coated glass by the short etch cycle was set to 0.1 min of etching followed by XPS data acquisition for a total of 30 cycles, whereas the long etch time used 1.0 min of etching followed by XPS data acquisition per for 7 cycles. The end of the polymer-glass interface was experimentally determined by observing when the fluorine content within the substrate was exhausted, and the stable bulk-glass phase was presumed to follow the polymer-glass interface. Only after the fluorine was exhausted were seven additional data-acquisition cycles conducted to confirm the end of the polymer-glass interface by observing the stable bulk-glass phase. The total etch depth resulted in a 110-nm depth for the uncoated glass control and a 22-nm depth for the polymer-coated samples.

High-resolution XPS spectra of the polymer-coated samples were obtained at four different etch depths in different locations of the same sample. The area of the sample observed using high-resolution XPS was located \approx 5 mm away from the area observed during XPS depth profiling. The etch time required for each depth was determined by studying the previously-obtained depth profiles to determine the depth range where the fluorine and carbon content (constituents of FEP) began to decrease and where the Na, Si, and O content (soda-lime glass) began to increase. From this data, it was estimated that 1.5 - 2.5 minutes of C60 etching were required to reach the polymer-glass interface.

High-resolution XPS spectra were collected in a B.E. range appropriate for each element [161] using three passes per scan with a resolution of 0.1 eV. The spectra were averaged to obtain one high-resolution dataset. The high-resolution XPS analysis was designed to acquire one dataset within the bulk polymer and three datasets within the center on the polymer-glass interface. The etch times between dataset acquisitions were 0.1, 1.4, 0.4, and 0.4 minutes for a total etch time of

2.3 minutes and a total calculated etch depth of 4.5 nm. Initial 0.1-minute etch cycles were used prior to the acquisition of the first dataset to decontaminate the surface.

XPS spectra analysis and peak fitting were conducted using MultiPak Version 9.6.0.15 (Ulvac-Phi, Inc.), and “Shirley” background subtraction was applied to all spectra [162]. Atomic concentrations were calculated by applying relative sensitivity factors [163] to the obtained XPS spectra. All XPS spectra were fit using Gaussian-Lorentzian spectral line shapes, and all B.E are reported relative to C1s at 284.5 eV [161]

8.3 Results and Discussion

8.3.1 Determining Location of the Polymer-Glass Interface

Prior to evaluating the depth profile of the polymer-glass interface, the location of the interface had to be determined to allow the C60 etch time to be converted to distance. The etch rate of the C60 gun on SiO₂ was calibrated using a Si wafer with a 100-nm SiO₂ layer on Si (100), in which the C60 gun was fired at six-minute intervals. This was followed by measuring the atomic concentrations of Si and O in the SiO₂ layer, which were determined to be 37% and 63%, respectively. The 100-nm oxide layer was depleted after 42 minutes of C60 etching, which corresponded to an etch rate of 2.38 nm/min.

Afterward, the location of the glass-polymer interface was determined by analyzing the O/Si ratio. A SiO₂ layer was deemed to be present when the ratio of O/Si stabilized, which occurred after 0.4 min of C60 etch time in the polymer-coated sample (Fig. 8.1a). Once the locations of the polymer-glass interface and the C60 etch rate in SiO₂ were determined, the depth profile was converted from the time domain to the distance domain, with the interface beginning at 0 nm (Fig. 8.1b). The etch rate of the fibrous polymer could not be accurately determined due to its rough

filamentous structure as opposed to the smooth SiO₂ surface which was etched uniformly. It was previously determined that the polymer layer was \approx 50 nm thick and required a C60 etch time of approximately 125 nm/min.

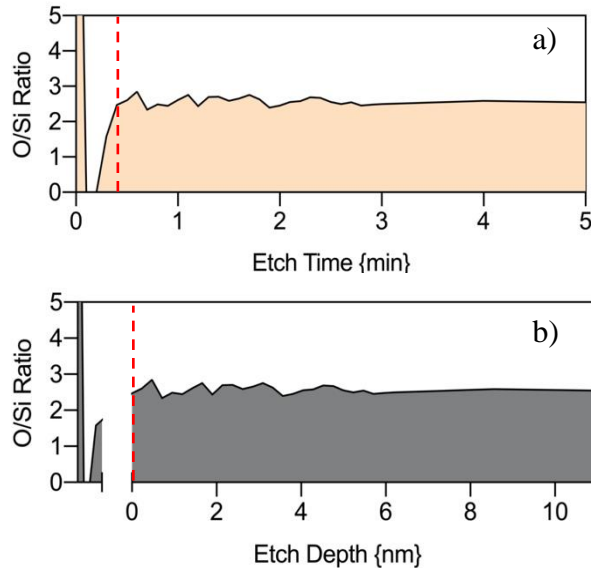


Fig. 8.1 Determination of the polymer-glass interface location via XPS depth profiling of the ratio of the atomic concentration ratio of oxygen to silicon (O/Si). The O/Si ratio was determined by the depth profile C60 gun etch time (a) and was then converted to distance (b), according to the experimentally-determined SiO₂ etch rate.

8.3.2 Depth Profiling

The depth profiles were obtained for the polymer-coated glass as well as bare (uncoated) glass (Fig. 8.2). The initial C60 etching cycle removed surface contaminants as shown by the high atomic concentration of carbon (C 1s). The underlying soda-lime glass contained atomic concentrations of Si, O, Na, and Ca in a ratio of Si_{1.00}O_{2.24}Na_{0.42}Ca_{0.11}, consistent with values reported in the literature [142], [154], [164], [165] in which the sodium content of soda-lime glass was reported to be 10%.

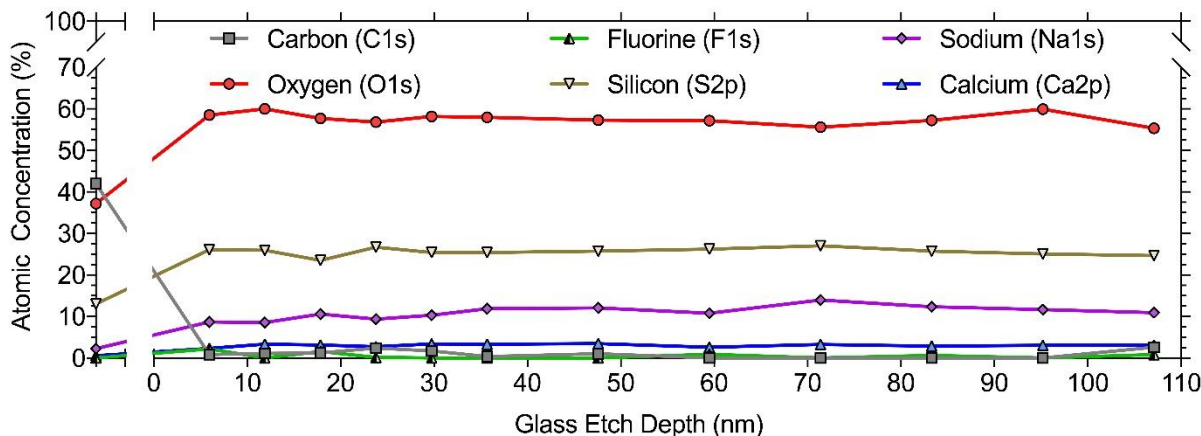


Fig. 8.2 XPS depth profiles of bare (uncoated) glass at etch depths up to 107 nm.

The depth profile analysis of the FEP polymer-coated sample (Fig. 8.3) showed three discrete layers of the polymer-substrate system: a bulk polymer layer, an interface layer, and a bulk glass layer. The bulk polymer layer, labeled the “FEP layer” in Fig. 8.3, was characterized by stable fluorine (atomic concentration = $66.0 \pm 1.4\%$) and carbon contents (atomic concentration = $30.8 \pm 1.4\%$), which are similar to their respective atomic ratio observed in the FEP polymer (2:1). The small deviation from the ideal 2:1 ratio in the XPS spectra is due to the presence of terminal CF_3 groups, the amounts of which vary depending on the polymer’s source and manufacturer. Advancing into the polymer-glass interface layer (Figure 8.3), the atomic concentrations of the constituent atoms changed rapidly. The fluorine atomic concentration decreased from $66.0 \pm 1.4\%$ to $1.7 \pm 0.9\%$, indicating that the fluorine content may have been severely depleted and that some trace fluorine may have penetrated the bulk glass layer. The atomic concentration of carbon decreased from $30.8 \pm 1.4\%$ to 0%, while the oxygen and silicon concentrations increased from 0 % to $59.8 \pm 0.7\%$ and $23.6 \pm 0.4\%$, respectively. In contrast, the sodium atomic concentration increased from 4.3% at the beginning of the polymer-glass interface to a maximum of 18.6% at a depth of 1.9 nm, and then smoothly decreasing and afterward were seen to be stable at $10 \pm 0.6\%$.

at depths past 11 nm. The complete atomic ratio of the bulk glass at an etch depth greater than 11 nm was $\text{Si}_{1.00}\text{O}_{2.53}\text{Na}_{0.42}\text{Ca}_{0.17}\text{F}_{0.1}$, with an Si, O, and Na ratio similar to bare (uncoated) glass.

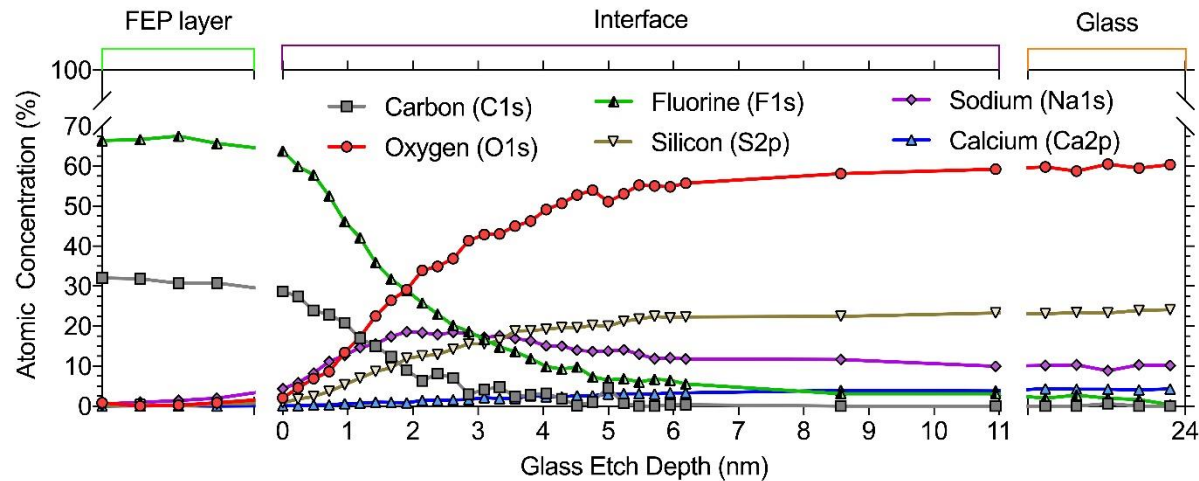


Fig. 8.3 Depth profile of polymer-coated glass, with layers designated as FEP layer, polymer-glass interface and a glass layer that remained un-modified during the polymer treatment.

8.3.3 C 1s Spectra Analysis

To complement the depth profiles, a separate experiment was performed using the same polymer-coated glass samples, where high-resolution spectra were obtained for C, O, Na, F, and Si within the bulk polymer layer and at various depths within the polymer-glass interface. High-resolution C 1s spectra (Fig 8.4) were used to identify the initial chemical state of carbon within the bulk polymer (Fig. 8.4a) by acquiring spectra after 0.1 minutes of C60 etching. C60 etching was performed for 0.1 minutes to remove any contaminants from the polymer layer surface.

The low-resolution C 1s spectra obtained from the bulk polymer layer as part of the depth profile were deconvoluted to reveal multiple C 1s peaks at 293.9 eV, 291.9 eV, and 289.9 eV, which corresponded to carbon-fluorine bonds of $(\text{C})\text{F}_3$, $(\text{C})\text{F}_2$, and $(\text{C})\text{F}$, substitutions respectively [166]–[171]. The high-resolution C 1s spectra of the bulk polymer layer corroborated these findings and

showed that the carbon content decayed rapidly within the polymer-glass interface layer (Fig. 4 b-c), with additional C 1s peaks present at 288.6 and 285.7 eV. Due to the rapid decrease in the number of C 1s peaks at the interface, only the high-resolution spectra obtained at discrete sampling depths were used to characterize the carbon bonding. The spectra were fit with an average FWHM of 2.3 ± 0.3 eV, and the deconvoluted spectra were all $>90\%$ Gaussian-Lorentzian fit and had an average Pearson's (chi-squared) χ^2 value of 1.6 [172], [173].

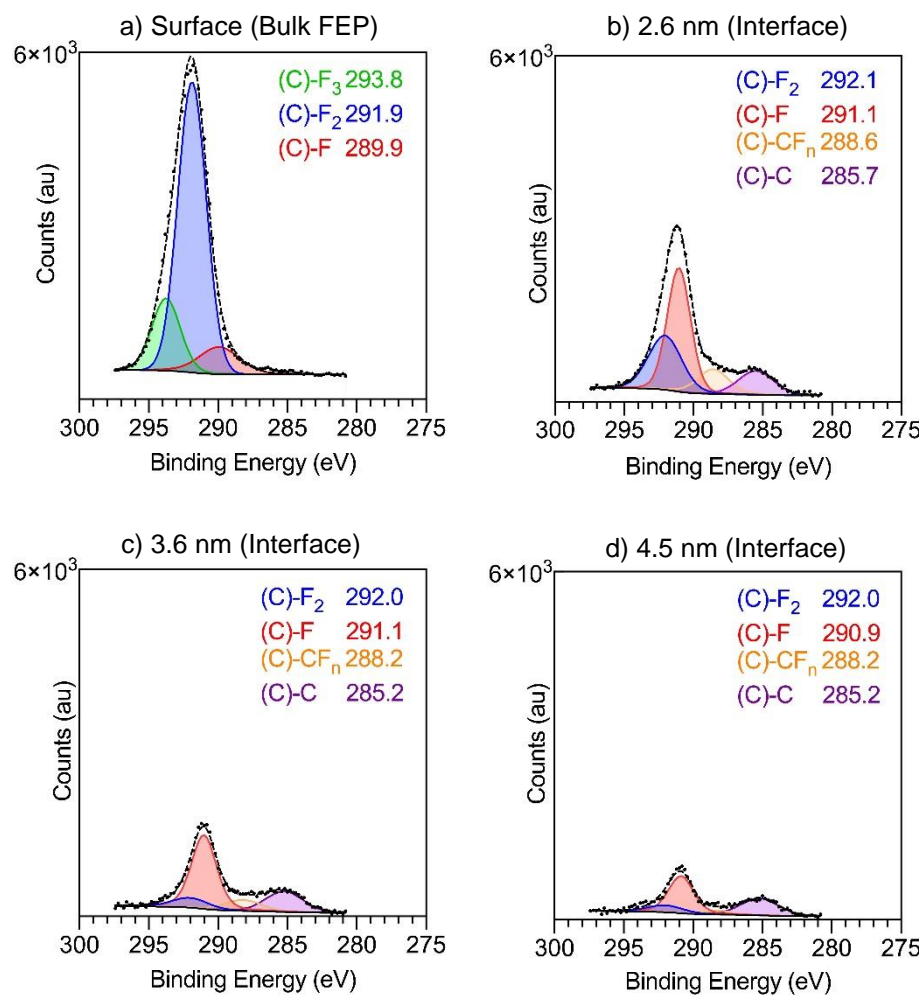


Fig. 8.4 High-resolution XPS C 1s spectra at depth intervals: surface (a), 2.6 nm of interface (b), 3.6 nm of interface (c), and 4.5 nm of interface (d); spectra show changes to the carbon chemistry based on B.E. peak shift, as well as the decomposition of carbon based on peak intensity with depth.

The C 1s spectra of the polymer-glass interface indicated that, at a depth of 2.6 nm, the carbon peak attributed to the (C)F₃ bond disappeared, giving rise to peaks at lower values of B.E., at 288.6 eV and 285.7 eV, which correspond to (C)-CF_n and (C)-C bonds, respectively (Fig. 8.4b). At a depth of 4.5 nm, no B.E. shifts were observed in the peak positions in the fitted C 1s spectra, signifying no significant chemical changes occurred in the carbon bonding throughout the interface layer. The change in the C 1s spectra observed at the interface layer compared with the spectra observed in bulk polymer layer suggested that the decomposition products of the bulk polymer penetrated the interface. As described in Figure 8.3, the interface layer was dominated by SiO₂ with an O/Si atomic ratio corresponding to that of glass, which indicated that the decay products of polymer penetrated and intercalated with the SiO₂ matrix. Analyzing the subsequent high-resolution spectra indicates that the carbon content within the interface layer decayed rapidly (Fig. 8.4 b-d).

8.3.4 O 1s Spectra Analysis

Analysis of the XPS spectra obtained in the B.E. range of 525-545 eV revealed three spectral contributions, one from sodium and two from O 1s: the Na Auger peak (Na KLL), bridging oxygen peak (BO), and non-bridging oxygen peak (NBO). The non-bridging oxygen peak (Si-O-) appeared at 530.9 eV (Fig. 8.5, blue), while the bridging oxygen peak (Si-O-Si) appeared at 532.4 eV (Fig. 8.5, red) [147]. The peak at 537.6 eV was identified at the Na KLL peak. The low-resolution spectra obtained as a part of the depth profile showed a >90% Gaussian-Lorentzian fit, with average FWHM values of 2.3 and 2.5 eV for O 1s and sodium, respectively. The average Pearson's χ^2 test result was 3.39. The high-resolution spectra were obtained at depths of 2.6, 3.6,

and 4.5 nm and were fitted with average FWHM values of 2.2 and 2.7 eV for O 1s and sodium, respectively. High-resolution O 1s spectra could not be obtained in the bulk polymer layer because no oxygen was detected within it, and the average Pearson's χ^2 test result was 4.6.

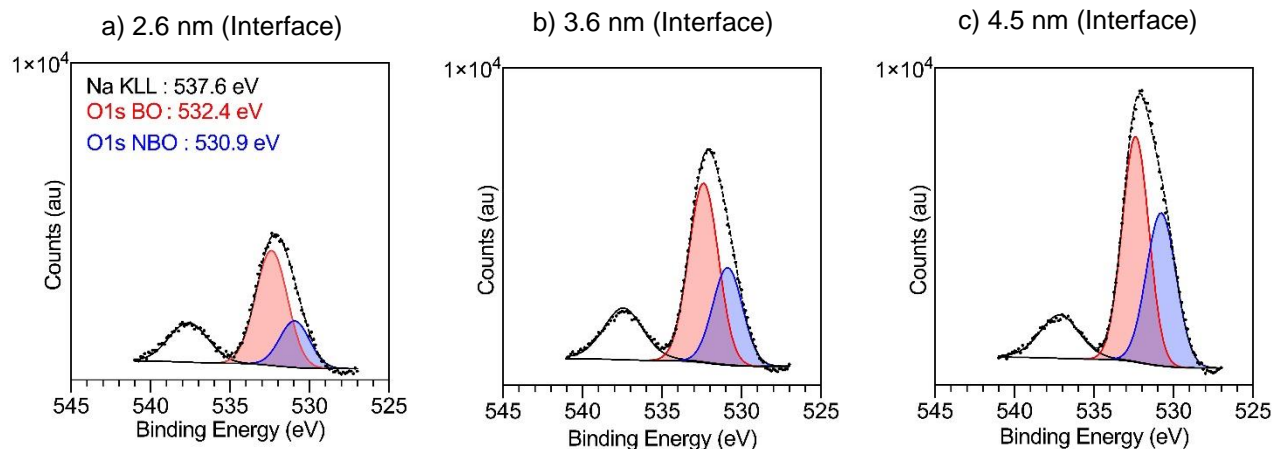


Fig. 8.5 High-resolution XPS spectra of oxygen atom at depth intervals of: 2.6 nm of interface (a), 3.6 nm of interface (b), and 4.5 nm of interface (c); the spectra show evolution of bridging and non-bridging oxygen bonds in the interface layer.

In an important study of the soda-lime glass structure, Warren et. al. [157] determined that glass is not constructed from a collection of discrete silicon dioxide, disodium oxide, and calcium oxide molecules. Instead, it is composed of a matrix of silicon bound to up to four oxygen atoms, with sodium present in the matrix as a network modifier. The Si-O bond distance is 1.62 Å, with some oxygen atoms serving as bridging oxygens between the silicon atoms, while other terminal oxygen atoms are bound to single silicon atoms. The terminal – or non-bridging oxygens (NBO) – help balance the positive charges of the sodium cation, which is thus coordinated to up to six oxygen anions with bond distances of 2.35 Å.

Evaluating the relative peak intensities at each depth showed that the ratio of the peaks of non-bridging to bridging oxygen (NBO/BO) increased with depth (Fig. 8.5 a-c). It is also evident that the overall intensity of the O 1s peaks increased with depth, suggesting that there are fewer silicon atoms near the bulk polymer layer than the bulk glass layer and that the glass may be partially porous at the polymer-glass interface.

8.3.5 F 1s and Na 1s Spectra Analysis

F 1s analysis was conducted by evaluating the depth profile spectra as well as high-resolution spectra obtained at discrete depths within the sample, from the bulk polymer, and within the polymer-glass interface at depths of 2.6, 3.6, and 4.5 nm (Fig. 8.6). The spectra obtained within the bulk polymer layer revealed an F 1s peak at 689.2 eV, while the spectra obtained within the polymer-glass interface revealed two F 1s peaks at 689.2 eV and 684.8 eV. The broad F 1s peak at 689.2 eV could be further deconvoluted into two peaks at 689.2 eV and 688.1 eV.

The low-resolution spectra obtained as a part of the depth profile were fit with FWHM values of 2.9, 2.5, and 3.1 eV for peaks located at 689.2, 684.8, and 684.9 eV, respectively. All maintained a >90% Gaussian-Lorentzian fit, with an average Pearson's χ^2 test value of 5.6. The high-resolution spectra of the bulk polymer layer at discrete depths of 2.6, 3.6, and 4.5 nm had FWHM values of 1.8, 2.1, and 2.8 eV for peaks at 689.2, 684.8, and 684.9 eV, respectively. All peaks had a 100% Gaussian-Lorentzian fit with an average Pearson's χ^2 test value of 3.7.

Correlating the intensity of the F 1s peaks to the depth profile of the F 1s atomic concentration showed that the fluorine content decreased in the polymer-glass interface region at an etch depth of 0 nm - 11 nm. The high-resolution F 1s XPS spectra of the bulk polymer region contained a single peak at 689.2 eV, which corresponded to the covalent F-C bonds in the FEP [161], [171],

[174]–[180]. The fluorine peak observed within the interface had a clearly-defined shoulder at 684.8 eV that corresponded to an ionic fluorine bond [161], [176], [178], [179], [181]. Ionic bonds between fluorine and alkali metals such as Na and Ca are expected to form during the fluorination of soda-lime glass due to fluorine’s high electron affinity and high ionization potential. Fitting the F 1s spectra while preserving the peak positions in the bulk FEP spectra (689.2 ± 0.1 eV) showed that the covalent F peak evolved into two peaks, with a second peak appearing at 688.1 ± 0.1 eV.

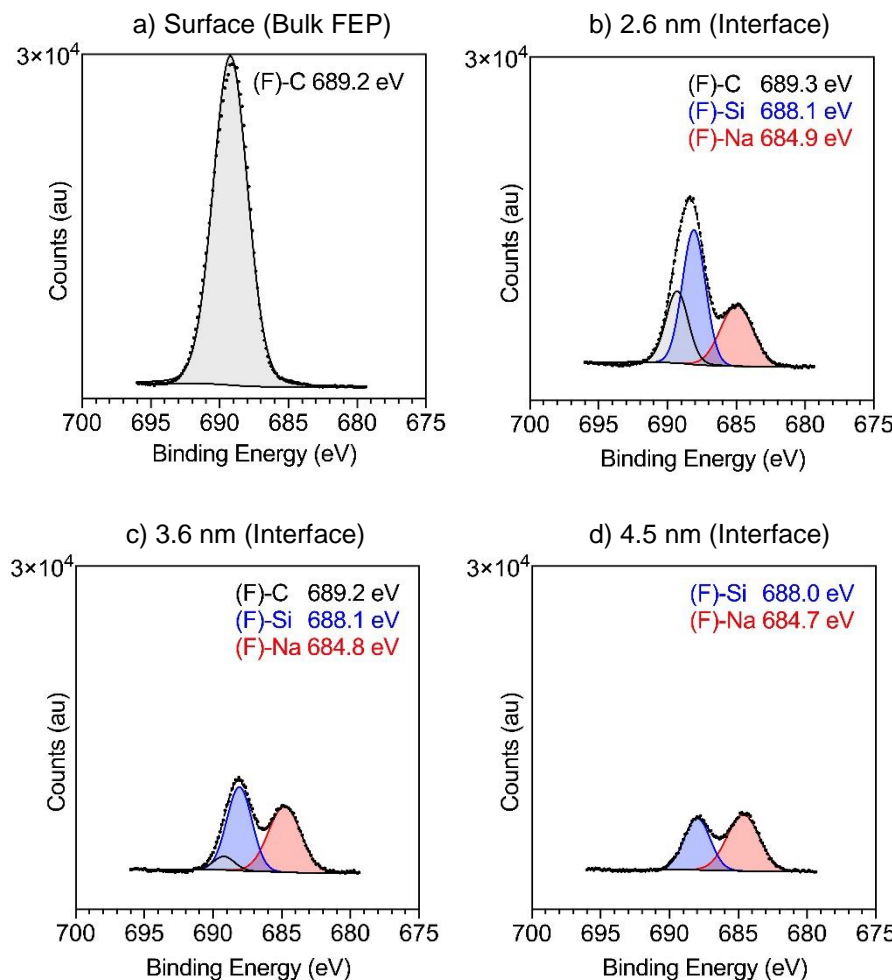


Fig. 8.6 High-resolution F 1s XPS spectra at the following depth intervals: the surface (a), 2.6 nm into the interface (b), 3.6 nm into the interface (c), and 4.5 nm into the interface (d); the spectra indicate changes in the fluorine chemistry due to the presence and intensity of deconvoluted peaks corresponding to (F)-C and (F)-Si covalent bonds and (F)-Na ionic bonds.

According to the literature and the atomic composition of soda-lime glass, the covalent peak at the lower B.E. was attributed to a fluorine-silicon covalent bond [158], [182].

8.3.6 Fluorine-Sodium Bonding Chemistry

Evaluating the ionic F bonds and sodium content in the interface showed the presence of equal amounts of sodium fluoride and sodium oxides. The average atomic concentration of Ca in the interface region was quite small ($1.8 \pm 1.0\%$) compared to the average atomic concentration of Na ($14.3 \pm 3.7\%$), and a maximum Na atomic concentration of 18.7% which was observed at a depth of 1.9 nm. Thus formation of calcium salts would be far less prevalent than formation of sodium salts. Analyzing the state of chemical bonding of sodium was then completed through the F 1s peak evaluation. It is evident that the atomic concentration of fluorine was between 20% and 50% at a depth of 2.6 nm (Fig. 8.6 and 8.3, respectively), thus the atomic concentration of deconvoluted ionic fluorine peak was 6% - 10%. From this it can be inferred that 6-10% of the sodium was bound to fluorine in the form of sodium fluoride (NaF), and the remaining 10% was bound to oxygen, either as the modified SiO₂ lattice of the soda-lime glass or as crystalline Na₂O.

8.3.7 Si 2p Spectra Analysis

The Si 2p spectra were obtained to confirm the presence of fluorine-silicon bonds in the polymer-glass interface layer. Although the Si 2p peak is usually fitted as a doublet, it can also be represented as a single peak to better observe shifts [183], [184]. The single peak obtained from the XPS depth profile was fitted with a FWHM of 3.4 eV – 2.8 eV. All maintained a >95%

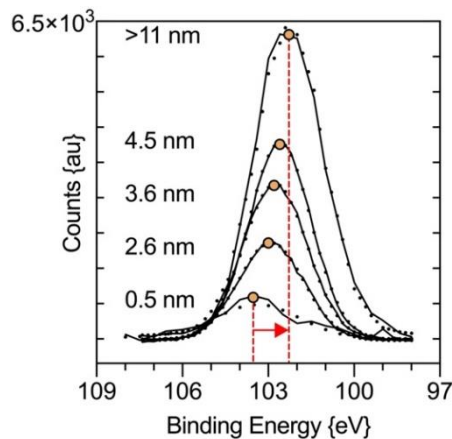


Fig. 8.7 High-resolution Si 2p spectra obtained of the bulk glass layer and at various polymer-interface layer depths. The plot shows a Si 2p chemical shift from 102.4 eV to 103.5 eV, signifying a change in chemical bonding.

Gaussian-Lorentzian fit with an average Pearson's χ^2 test of 2.1. The spectra obtained within the bulk polymer layer at discrete depths of 2.6, 3.6, and 4.5 nm and within the bulk glass were fitted with a FWHM value of 2.8. All had a $> 95\%$ Gaussian-Lorentzian fit, with an average Pearson's χ^2 test value of 3.5.

The depth profile of uncoated soda-lime glass showed a Si 2p peak located at 102.5 eV, which corresponded to silicon in soda-lime glass [147]. The depth profile of the polymer-coated glass within the bulk glass region of the sample also contained a Si 2p peak at 102.4 eV at depths > 18 nm, indicating that the Si bonding of the glass was similar to that of uncoated glass in this region. This finding corroborated the depth profile of polymer-coated glass (Fig. 8.3), which showed that the fluorine content decreased to undetectable levels and no longer modified the Si-O bonds within the glass matrix. The Si 2p spectra of the polymer-glass interface showed the Si 2p peak was located at 103.4 eV (Fig. 8.7) and shifted to a lower binding energy of 102.4 eV as the depth increased.

8.3.8 Polymer-Glass Bonding Interface

The depth profile analysis of the polymer-glass interface layer of FEP-coated glass indicated that the interpenetration of the polymer into the top layers of the soda-lime glass facilitated the formation of bonds between the polymer coating and the soda-lime glass substrate. Interpenetration of the polymer was possible due to the formation of a porous layer within the top 9 nm of the glass substrate due to the de-fluorination of the fluoropolymer. The depth profile of the polymer-coated surface indicated that the polymer degraded into fluorocarbon species, as observed by the locations and areas of peaks in the C 1s and F 1s spectra. This indicates that the relative fluorocarbon content rapidly evolved from (C)-F to (C)-F₃ and suggests decomposition of the polymer chain due to the high temperatures and pressure exerted on the polymer during coating formation. During polymer application process, the temperature of the polymer exceeded the T_m , while the pressure exceeded 10 kPa. Defluorination of the fluoropolymer, as indicated by the evolution of the ionic F 1s peak therefore contributed to the increase of the NaF and Si-F content.

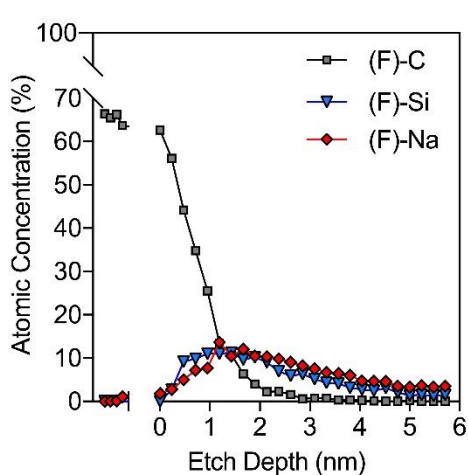


Fig. 8.8 XPS depth profile of the atomic ratio of covalent F bonds (F-C and F-Si) to ionic F bonds (F-Na).

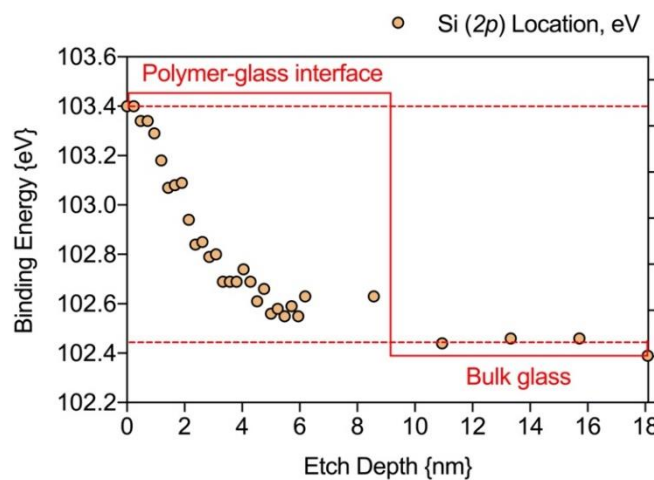


Fig. 8.9 Si 2p peak location derived from the depth profile (eV), plotted as a function of the SiO₂ etch depth within the interface. The peak shifts from 103.4 to 102.4 eV (dashed red line) with increasing etch depth.

The formation of Si-F bonds was confirmed by analyzing the XPS signals of F, C, and Si. The F 1s signal shows the evolution of covalent fluorine (Fig. 8.6), which contained a peak at 689.3 eV (Fig. 8.6a, gray). The bulk polymer layer was observed to have degraded with increasing etch depth (Fig 8.6b-d, gray). Meanwhile, a second covalent fluorine peak at 688.1 eV (Fig 8.6b, blue) first emerged at a depth of 2.6 nm and dominated the covalent part of the fluorine peak at a depth of 3.6 nm. At 4.5 nm, the covalent peak at 689.3 eV completely disappeared (Fig 8.6c-d, gray), while the peak at 688.1 eV remained visible (Fig 8.6d, blue). The ionic fluorine peak contribution (Fig 8.6b-d, red) emerged at a depth of 2.6 nm and remained nearly constant throughout the polymer-glass interface. The low-resolution F 1s spectra obtained from the depth profile corroborated the analysis of the covalent fluorine peaks within the polymer-glass interface (Fig. 8.8). The peak locations were fixed to the B.E. observed in the high-resolution spectra, and the depth profile spectra were fitted and plotted as a function of depth. The covalent and ionic fluorine peak contributions seemed to continue to a depth of \approx 7 nm. Overlaying the C 1s and F 1s depth profiles showed that the carbon content near the polymer-glass interface was completely depleted at a depth of 3 nm, indicating that F-C bonds did not contribute to the covalent fluorine peak past a depth of 4 nm. Thus, the covalent fluorine peak was attributed to (F)-C (Fig. 8.8, black square) and (F)-Si (Fig. 8.8, blue triangle). Covalent peaks were attributed by allocating part of the peak area to the (F)-C bond and then quantitatively applying weights to the peak area with the relative atomic concentrations of carbon and silicon. The reattributed covalent fluorine peak in Fig. 8.8 corresponded with the atomic concentrations of C and Si observed at various etch depths and more accurately represented the covalent fluorine bonds at those depths.

Correlating the depth profile of fluorine atomic concentration to that of carbon within the polymer-glass interface layer revealed that the atomic concentrations of covalent fluorine and carbon decreased. Overlapping the silicon and oxygen atomic concentrations indicated that the fluorocarbon polymer penetrated the top 3 - 4 nm of the glass SiO_2 matrix due to the increased porosity of the matrix, which occurred during the de-alkalization of the soda-lime glass [151]. The presence of fluorocarbon within the polymer-glass interface indicated the interpenetration of polymer and glass.

The Si 2p peak shifted from 103.4 eV to 102.4 eV (Fig. 8.7), suggesting a possible change in the chemical bonding within the silica-oxygen matrix, from Si-F to sodic glass Si-O bonding. The Si 2p peak location was analyzed as a function of depth (Fig 8.9) and gradually shifted from 103.5 eV to 102.6 eV from an etch depth of 0 nm to 9 nm, respectively. This indicates a gradual change in the silicon atom bonding and reached equilibrium at 102.4 eV. The shift in the Si 2p peak towards a higher B.E. indicated an increased density of the Si valence electrons due to a higher sodium content [147]. The shift in the Si 2p peak indicated that fluorine ions penetrated to a depth

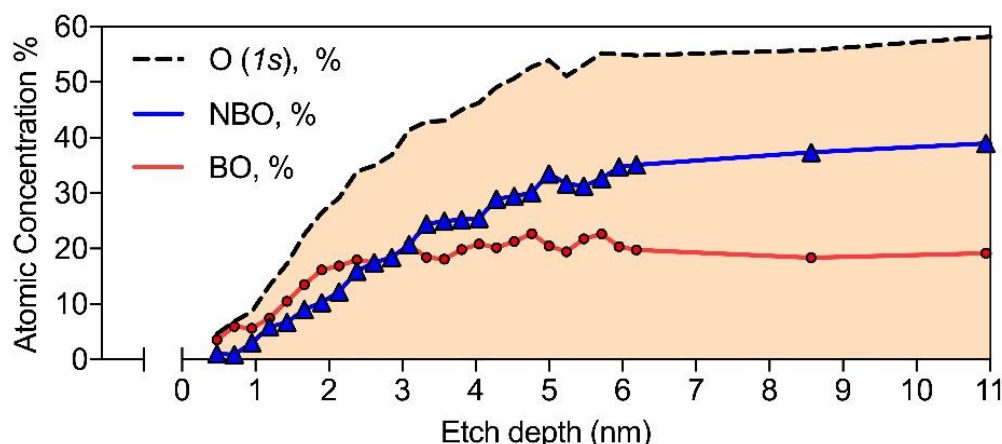


Fig. 8.10 O 1s depth profile spectra (dotted line), non-bridging oxygen (blue triangles), and bridging oxygen (red circles), taken within the polymer-glass interface.

of 9 nm. Thus, the fluorine-silicon boundary within the polymer-glass interface was 0 nm to 9 nm. As Fig. 8.9 indicates, the majority of Si-F bonds were located from 0 nm – 3 nm.

In order to better understand the evolution of non-bridging and bridging oxygen, the low-resolution oxygen spectra from the depth profile were deconvoluted into their NBO and BO constituents and plotted as a function of SiO_2 depth (Fig. 8.10). The results indicated that the ratio of bridging to non-bridging oxygen was greater at shallow interface layer depths (0 nm – 3 nm) and that the amount of bridging oxygen surpassed the amount of non-bridging oxygen at greater depths. The ratio of non-bridging to bridging oxygen in the bulk glass was calculated to be 7:3, which was consistent with the ratio obtained from the O 1s spectra of the uncoated glass. Fluorination of the soda-lime glass caused fluorine to replace the (O)-N [156] and decreased the amount of non-bridging oxygen. The amount of bridging oxygen remained constant, making it appear that the ratio of bridging to non-bridging oxygen increased, explaining the disproportionate amount of non-bridging oxygen at shallow interface layer depths.

The presence of F-Si bonds was supported by the F 1s and Si 2p peak analyses, which clearly indicated the oxygenation of silicon within the glass matrix, which compromised the structural integrity of the glass surface. The high temperature and pressure environment present during the coating lamination has partially degraded and defluorinated the fluoropolymer chains, providing the fluorine ions necessary for silica deoxygenation and simultaneously shortening the polymer chains, allowing them to interpenetrate the top of the glass surface. When the polymer coating was cooled, the interpenetrating polymer chains contracted, strongly binding the polymer coating to the glass surface.

8.4 Conclusion

In order to determine the bonding mechanism of anti-soiling and anti-reflective fluoropolymer nano-coatings on PV grade soda-lime cover glass, XPS depth profile and high resolution XPS analysis have been conducted and evaluated.

The XPS depth profile of polymer-coated glass substrates has determined that the bonding interface between the polymer layer and the glass substrate constitutes primarily of partially decomposed FEP fluoropolymer that has interpenetrated the top 6-10 nm of porous glass matrix. The porosity of the glass matrix has been attributed to de-alkalization of the top layer of SiO_x glass matrix, where the sodium oxide, present at the non-bridging oxygen, has been replaced with fluorine, forming a SiF bond. The SiF bond formation has been confirmed via high resolution F 1s and Si 2p XPS. F 1s XPS has shown a development of additional covalent F peak, while the Si 2p XPS has shown the drift of the peak location to higher B.E. values within the polymer-glass interface region. Migration of Na within the interface region, and de-oxygenation of Si-O matrix have both corroborated the evidence.

Chapter 9. Conclusion

Anti-reflective, anti-soiling, and self-cleaning coatings are of interest for use with photovoltaic (PV) cover glass due to their potential ability to increase the amount of light transmitted through the glass and also improve the efficiency by decreasing the number of contaminants bound to the glass surface (soiling). Fluoropolymer nanocoatings with a rough fibrous texture can provide glass surfaces with anti-reflective properties due to the polymer's low refractive index and the refractive index gradient created by the rough surface morphology. Thus, a fluoropolymer (fluorinated ethylene propylene) coating was fabricated on PV-grade soda-lime glass, and its anti-reflective properties increased the direct light transmittance through glass by up to 3% (from 91.5 to 94.5%). A minimal amount of fluoropolymer was required for the coatings (100 – 1000 nm thick), making the coatings economically viable for further development (Chapter 2).

Dew is known to exacerbate soiling via the cementation of dust on glass surfaces (Chapter 1). Thus, laboratory soiling apparatuses were designed and constructed to simulate soiling in various environmental conditions, both with and without simulated dew on the glass surface (Chapters 2, 3). The anti-reflective and anti-soiling properties of the coating were investigated, and a novel anti-soiling, “dust herding” mechanism was observed on fluoropolymer-coated hydrophobic surfaces (Chapter 3). This mechanism allowed the surface to remain clean when soiled in the presence of dew because of the mobile contact line of dewdrops on the hydrophobic surface. As the dewdrops evaporated, the dust was contained to a localized point on the glass surface, which freed the surrounding area from dust.

Furthermore, hybrid hydrophobic-hydrophilic fluoropolymer coatings with rough nanotextures were designed to harness natural dew and utilize it as a water source for self-cleaning. Hybrid hydrophobic-hydrophilic surfaces were created in order to exploit the seemingly detrimental effect

of dew on PV cover glass for self-cleaning. A simulated dew condensation chamber was constructed to evaluate the self-cleaning properties of the coatings under various environmental conditions and tilt angles (Chapters 2, 4). Initial experiments quantified the water collection rate of the hybrid surfaces to determine how to optimize the surfaces for self-cleaning applications (Chapter 4). The hybrid surfaces were optimized to efficiently harness dew, minimizing the time required to clean the surface with condensed dew and maximizing the cleaning effect provided by each dewdrop (Chapter 2, 5).

In order to optimize the data acquisition methods of the simulated dew experiments, a water drop detection algorithm was written using the OpenCV computer vision library in order to identify the location, size, and time of the dewdrop slide-off events on the glass surface and to calculate the path cleaned by the sliding dewdrops (Chapter 2, 4). The algorithm permitted the analysis of long (up to 48 hours) dew collection and dew cleaning experiments via automated analysis of video footage of the test surface acquired during experiments (Chapters 2, 4).

Hybrid hydrophobic-hydrophilic fluoropolymer coatings were further investigated to observe the self-cleaning properties of the coating soiled with various test dust (soilants). Laboratory-grade test dusts were utilized to simulate soiling in various conditions with chemically reactive and unreactive test dust. The self-cleaning effect was studied at various tilt angles to simulate various geographic locations. It was determined that the anti-soiling effect of the coating decreased the direct transmittance loss, while the hybrid surface promoted surface cleaning under simulated dew conditions.

The wetting properties of the fluoropolymer-coated surface were studied by simulations in order to understand the effects of partial wetting on the surfaces (Chapter 6). The computer simulations utilized atomic force microscopy (AFM) image data of the rough fluoropolymer surfaces in order

to map the dewdrop meniscus on the surface *in silico* using Delaunay triangulation of the peaks of the rough fluoropolymer surface. The *in silico* simulation results were compared with *in situ* goniometric experiment results, and the water contact angle hysteresis results corroborated those of the simulation. These experiments have laid the foundation for using computer simulations to predict the wetting behavior of various rough hydrophobic surfaces.

Additionally, stable coalescence induced condensate drop jumping was observed on the rough superhydrophobic fluoropolymer coatings produced on aluminum substrates (Chapter 7). A condensation chamber was constructed, that was able to reproduce large ΔT temperatures in presence of non-condensable gas (air). The experiments have evaluated the dependency of the coalescence induced jumping effect on the surface structure: morphology and roughness.

To conclude the study of the fluoropolymer coatings on PV-grade soda-lime glass, the bonding between the polymer coating and the glass surface was studied. X-ray photoelectron spectroscopy (XPS) depth profiles of fluoropolymer-coated and uncoated surfaces were obtained (Chapter 8). XPS depth profiles permitted the examination of the chemical bonding of various atomic species present in soda-lime glass: C, Si, O, F, and Na. The results showed that the defluorination of the polymer led to desalination and deoxygenation of the top 9 nm of the glass substrate, which compromised the integrity of the glass SiO_2 matrix, rendering it porous. The partially decomposed fluoropolymer then penetrated the porous top layer of the glass surface, intercalating the glass and forming an interfacial bonding layer.

Deoxygenation and the formation of SiF were confirmed using high-resolution XPS, as well as the relationship between bridging and non-bridging oxygen. The formation of NaF was confirmed, which, along with the compromised silica glass matrix, increased the anti-reflective properties of

the glass by extending the refractive index gradient into the polymer-glass interface within the glass matrix.

Fluoropolymer soda-lime glass coatings have demonstrated their potential for use as anti-reflective, anti-soiling, and self-cleaning applications for PV glass. The studies reported in this thesis advance the PV glass coating field by providing valuable information for the further development of durable and affordable anti-reflective, anti-soiling, and self-cleaning surface coatings.

Bibliography

- [1] J. A. Dobrowolski, “Ch. 42 Optical Properties of Films and Coatings,” in *Handbook of Optics*, 1995, pp. 42.19-42.34.
- [2] J. A. Dobrowolski, D. Poitras, P. Ma, H. Vakil, and M. Acree, “Toward perfect antireflection coatings: numerical investigation,” *Appl. Opt.*, vol. 41, no. 16, p. 3075, 2002.
- [3] H. A. Macleod, *Thin Film Optical Filters, 3rd Edition*. 2001.
- [4] Q. Shang and Y. Zhou, “Fabrication of transparent superhydrophobic porous silica coating for self-cleaning and anti-fogging,” *Ceram. Int.*, vol. 42, no. 7, pp. 8706–8712, 2016.
- [5] D. Kumar *et al.*, “Development of durable self-cleaning coatings using organic-inorganic hybrid sol-gel method,” *Appl. Surf. Sci.*, vol. 344, pp. 205–212, 2015.
- [6] Z. Zhang, B. Ge, X. Men, and Y. Li, “Colloids and Surfaces A : Physicochemical and Engineering Aspects Mechanically durable , superhydrophobic coatings prepared by dual-layer method for anti-corrosion and self-cleaning,” vol. 490, pp. 182–188, 2016.
- [7] X. Meng, Y. Wang, H. Wang, J. Zhong, and R. Chen, “Preparation of hydrophobic and abrasion-resistant silica antireflective coatings by using a cationic surfactant to regulate surface morphologies,” *Sol. Energy*, vol. 101, pp. 283–290, 2014.
- [8] I. Nayshevsky, Q. Xu, G. Barahman, and A. M. Lyons, “Anti-reflective and anti-soiling properties of KleanBoost™, a superhydrophobic nano-textured coating for solar glass,” *2017 IEEE 44th Photovolt. Spec. Conf.*, pp. 2285–2290, 2017.
- [9] I. Nayshevsky, Q. Xu, and A. M. Lyons, “Hydrophobic-Hydrophilic Surfaces Exhibiting Dropwise Condensation for Anti-Soiling Applications,” *IEEE J. Photovoltaics*, vol. 9, no. 1, pp. 302–307, 2019.
- [10] Y. Liu, Q. F. Xu, and A. M. Lyons, “Durable, optically transparent, superhydrophobic polymer films,” *Appl. Surf. Sci.*, vol. 470, no. September 2018, pp. 187–195, 2019.
- [11] M. Gostein *et al.*, “Soiling Measurement Station to Evaluate Anti-Soiling Properties of PV Module Coatings,” *2016 IEEE 43rd Photovolt. Spec. Conf.*, pp. 3129–3131, 2016.
- [12] T. Sarver, A. Al-Qaraghuli, and L. L. Kazmerski, “A comprehensive review of the impact of dust on the use of solar energy: History, investigations, results, literature, and mitigation approaches,” *Renew. Sustain. Energy Rev.*, vol. 22, pp. 698–733, 2013.
- [13] M. A. Bahattab *et al.*, “Anti-soiling surfaces for PV applications prepared by sol-gel processing: Comparison of laboratory testing and outdoor exposure,” *Sol. Energy Mater. Sol. Cells*, vol. 157, pp. 422–428, 2016.
- [14] S. L. Moffitt, R. A. Fleming, C. S. Thompson, M. F. Toney, and L. T. Schelhas, “Fundamental Characterization of Anti-Soiling Coatings for PV Glass : Application of Small-Angle X-ray Scattering,” pp. 3436–3438, 2018.
- [15] K. Ilse, B. Figgis, M. Z. Khan, V. Naumann, and C. Hagendorf, “Dew as a Detrimental Influencing Factor for Soiling of PV Modules,” *IEEE J. Photovoltaics*, pp. 1–8, 2018.
- [16] R. J. Isaifan, D. Johnson, L. Ackermann, B. Figgis, and M. Ayoub, “Evaluation of the adhesion forces between dust particles and photovoltaic module surfaces,” *Solar Energy Materials and Solar Cells*, vol. 191, pp. 413–421, 2019.
- [17] K. K. Ilse, B. W. Figgis, V. Naumann, C. Hagendorf, and J. Bagdahn, “Fundamentals of soiling processes on photovoltaic modules,” *Renew. Sustain. Energy Rev.*, vol. 98, no. September, pp. 239–254, 2018.

- [18] K. Ilse, M. Werner, V. Naumann, B. W. Figgis, C. Hagendorf, and J. Bagdahn, “Microstructural analysis of the cementation process during soiling on glass surfaces in arid and semi-arid climates,” *Phys. Status Solidi - Rapid Res. Lett.*, vol. 10, no. 7, pp. 525–529, 2016.
- [19] L. L. Kazmerski *et al.*, “Fundamental Studies of Adhesion of Dust to PV Module Surfaces: Chemical and Physical Relationships at the Microscale,” *IEEE J. Photovoltaics*, vol. 6, no. 3, pp. 719–729, 2016.
- [20] H. R. Moutinho *et al.*, “Adhesion mechanisms on solar glass: Effects of relative humidity, surface roughness, and particle shape and size,” *Sol. Energy Mater. Sol. Cells*, vol. 172, no. July, pp. 145–153, 2017.
- [21] L. L. Kazmerski, M. Al Jardan, Y. Al Jnoobi, Y. Al Shaya, and J. J. John, “Ashes to ashes, dust to dust: Averting a potential showstopper for solar photovoltaics,” *2014 IEEE 40th Photovolt. Spec. Conf. PVSC 2014*, pp. 187–192, 2014.
- [22] J. Huang, J. Zhang, and L. Wang, “Review of vapor condensation heat and mass transfer in the presence of non-condensable gas,” *Appl. Therm. Eng.*, vol. 89, pp. 469–484, 2015.
- [23] R. J. Isaifan *et al.*, “Improved Self-cleaning Properties of an Efficient and Easy to Scale up TiO₂ Thin Films Prepared by Adsorptive Self-Assembly,” *Sci. Rep.*, vol. 7, no. 1, pp. 1–9, 2017.
- [24] R. J. Isaifan, D. Johnson, S. Mansour, A. Samara, W. Suwaileh, and K. Kakosimos, “Theoretical and Experimental Characterization of Efficient Anti-Dust Coatings under Desert Conditions,” *J. Thin Film. Res.*, vol. 2, no. 1, pp. 25–29, 2018.
- [25] K. Nakata and A. Fujishima, “TiO₂ photocatalysis: Design and applications,” *J. Photochem. Photobiol. C Photochem. Rev.*, vol. 13, no. 3, pp. 169–189, 2012.
- [26] R. Wang and K. Hashimoto, “Light-induced amphiphilic surfaces,” *Nat. Sci. Corresp.*, vol. 388, pp. 431–332, 1997.
- [27] B. Xi *et al.*, “TiO₂ thin films prepared via adsorptive self-assembly for self-cleaning applications,” *ACS Appl. Mater. Interfaces*, vol. 4, no. 2, pp. 1093–1102, 2012.
- [28] C. Extrand and A. Gent, “Retention of Liquid Drops by Solid Surfaces,” *J. Colloid Interface Sci.*, vol. 138, no. 2, pp. 431–442, 1990.
- [29] B. Brophy *et al.*, “Highly Durable Anti-Reflective Anti-Soiling Coating for PV Module Glass,” *PVMRW 2015*, p. 95131, 2015.
- [30] V. Nair and B. Brophy, “Anti-Reflective and Anti-Soiling Coatings with Self-Cleaning Properties,” US 9,461,185 B2, 2016.
- [31] D. Goossens, “Wind tunnel protocol to study the effects of anti-soiling and anti-reflective coatings on deposition, removal, and accumulation of dust on photovoltaic surfaces and consequences for optical transmittance,” *Sol. Energy*, vol. 163, no. September 2017, pp. 131–139, 2018.
- [32] K. Ilse, J. Li, N. Voicu, V. Naumann, and C. Hagendorf, “Laboratory soiling test for evaluation of anti-soiling coating performance,” in *SNEC (2018) International Energy Storage and Mobile New Energy Exhibition and Conference; Session 8: PV Module Quality Assurance*, 2018.
- [33] 3M, “Anti-Soiling (AS) Liquid 600: For Glass Surfaces in Solar Energy Generation Systems,” vol. 2013, no. Dec., pp. 6–7, 2013.
- [34] F. D. Petke and B. R. Ray, “Temperature dependence of contact angles of liquids on polymeric solids,” *J. Colloid Interface Sci.*, vol. 31, no. 2, p. 216, 1969.
- [35] R. J. Good, M. Islam, R. E. Baier, and A. E. Meyer, “The effect of surface hydrogen

- bonding (acid-base interaction) on the hydrophobicity and hydrophilicity of copolymers: Variation of contact angles and cell adhesion and growth with composition," *J. Dispers. Sci. Technol.*, vol. 12, no. 6–7, pp. 1163–1173, 1998.
- [36] W. J. Hamilton III, J. R. Henschel, and M. S. Seely, "Fog collection by Namib Desert beetles," *S. Afr. J. Sci.*, vol. 99, p. 181, 2002.
- [37] E. Alizadeh-Birjandi, A. Alshehri, and H. P. Kavehpour, "Condensation on Surfaces With Biphasic Topography: Experiment and Modeling," *Front. Mech. Eng.*, vol. 5, no. June, pp. 1–8, 2019.
- [38] L. Fisher, R. Gamble, and J. Middlehurst, "The Kelvin equation and capillary condensation," *Nature*, vol. 290, no. April, pp. 575–576, 1981.
- [39] A. M. Lyons and Q. Xu, "Center-side method of producing superhydrophobic surface," US 9,987,818 B2, 2018.
- [40] 3M, "Dyneon™ Fluorothermoplastic." p. 5, 2009.
- [41] Q. Xu, I. Nayshevsky, D. Furhang, J. Newkirk, D. Miller, and A. M. Lyons, "A Hybrid Hydrophobic-Hydrophilic Coating with Anti-Reflective and Anti-Soiling Properties," in *Proceedings of the NREL PV Reliability Workshop*, 2019.
- [42] DIN, "Nationales Vorwort," 2009.
- [43] P. D. Burton and B. H. King, "Artificial soiling of photovoltaic module surfaces using traceable soil components," *Conf. Rec. IEEE Photovolt. Spec. Conf.*, pp. 1542–1545, 2013.
- [44] E. Klimm, T. Kaltenbach, D. Philipp, M. Masche, K. Weiss, and M. Koehl, "Soiling and Abrasion Testing of Surfaces for Solar Energy Systems Adapted to Extreme Climatic Conditions," *Pvsec 31*, no. September, pp. 1–3, 2015.
- [45] W. Herrmann, M. Schweiger, G. Tamizhmani, B. Shisler, and C. Kamalaksha, "Soiling and self-cleaning of PV modules under the weather conditions of two locations in Arizona and South-East India," *2015 IEEE 42nd Photovolt. Spec. Conf. PVSC 2015*, pp. 1–5, 2015.
- [46] K. Ilse, B. Figgis, M. Z. Khan, V. Naumann, and C. Hagendorf, "Dew as a Detrimental Influencing Factor for Soiling of PV Modules," *IEEE J. Photovoltaics*, vol. PP, no. 1, pp. 1–8, 2018.
- [47] E. Afik, "Robust and highly performant ring detection algorithm for 3d particle tracking using 2d microscope imaging," *Sci. Rep.*, vol. 5, no. January, pp. 1–9, 2015.
- [48] I. Nayshevsky, Q. Xu, and A. Lyons, "Literature Survey of Dust Particle Dimensions on Soiled Solar Panel Modules," in *2018 International PV Soiling Workshop*, 2018.
- [49] *Measurement procedures for materials used in photovoltaic modules - Part 1-4: Encapsulants - Measurement of optical transmittance and calculation of the solar-weighted photon transmittance, yellowness index, and UV cut-off wavelength*. IEC 62788-4-1, International Electrotechnical Commission, [Online] Available: <https://webstore.iec.ch/publication/25942>, 2016.
- [50] J. Cano, "Photovoltaic Modules: Effect of Tilt Angle on Soiling," M.S. Dissertation, Arizona State University, 2011.
- [51] J. R. Caron and B. Littmann, "Direct monitoring of energy lost due to soiling on first solar modules in California," *IEEE J. Photovoltaics*, vol. 3, no. 1, pp. 336–340, 2013.
- [52] F. A. Mejia and J. Kleissl, "Soiling losses for solar photovoltaic systems in California," *Sol. Energy*, vol. 95, pp. 357–363, 2013.
- [53] A. Sayyah, M. N. Horenstein, and M. K. Mazumder, "Energy yield loss caused by dust

- deposition on photovoltaic panels,” *Sol. Energy*, vol. 107, pp. 576–604, 2014.
- [54] W. Herrmann, “Time evolution of PV soiling loss at test locations in different climates,” in *Workshop „Soiling effect on PV modules“*, 2016.
- [55] S. Ghazi, A. Sayigh, and K. Ip, “Dust effect on flat surfaces - A review paper,” *Renew. Sustain. Energy Rev.*, vol. 33, pp. 742–751, 2014.
- [56] A. H. Hassan, U. A. Rahoma, H. K. Elminir, and A. M. Fathy, “Effect of airborne dust concentration on the performance of PV modules,” *J. Astron. Soc. Egypt*, vol. 13, no. 1, pp. 24–38, 2005.
- [57] A. Sayyah, M. N. Horenstein, and M. K. Mazumder, “Mitigation of soiling losses in concentrating solar collectors,” *Conf. Rec. IEEE Photovolt. Spec. Conf.*, no. c, pp. 480–485, 2013.
- [58] R. K. Jones *et al.*, “Optimized Cleaning Cost and Schedule Based on Observed Soiling Conditions for Photovoltaic Plants in Central Saudi Arabia,” *IEEE J. Photovoltaics*, vol. 6, no. 3, pp. 730–738, 2016.
- [59] M. K. Mazumder, R. Sharma, A. S. Biris, J. Zhang, C. Calle, and M. Zahn, “Self-Cleaning Transparent Dust Shields for Protecting Solar Panels and Other Devices,” *Part. Sci. Technol.*, vol. 25, no. 1, pp. 5–20, Jan. 2007.
- [60] R. Fu, D. J. Feldman, and R. M. Margolis, “U.S. Solar Photovoltaic System Cost Benchmark: Q1 2018,” Golden, CO: National Renewable Energy Laboratory, 2018.
- [61] A. M. Lyons and Q. Xu, “Center-side method of producing superhydrophobic surface,” CN 106103076B, 2018.
- [62] D. C. Miller *et al.*, “Examination of an Optical Transmittance Test for Photovoltaic Encapsulation Materials: Preprint NREL/CP-5200-60029,” *SPIE Optics & Photonics*, 2013. [Online]. Available: http://nrel-primo.hosted.exlibrisgroup.com/Pubs:PUBS:NREL_PUBS14c54c0f-e8d4-e411-b769-d89d67132a6d.
- [63] L. Micheli *et al.*, “Correlating photovoltaic soiling losses to waveband and single-value transmittance measurements,” *Energy*, vol. 180, pp. 376–386, 2019.
- [64] *Photovoltaic system performance - Part 1: Monitoring*. IEC 61724-1:2017, International Electrochemical Commission, [Online] Available: <https://webstore.iec.ch/publication/33622>, 2017.
- [65] H. Qasem, T. R. Betts, H. Müllejans, H. AlBusairi, and R. Gottschalg, “Dust-induced shading on photovoltaic modules,” *Prog. Photovoltaics Res. Appl.*, vol. 22, pp. 218–226, 2014.
- [66] J. Tanesab, D. Parlevliet, J. Whale, and T. Urmee, “The effect of dust with different morphologies on the performance degradation of photovoltaic modules,” *Sustain. Energy Technol. Assessments*, vol. 31, pp. 347–354, 2019.
- [67] I. Nayshevsky, “pyCondrop: Surface self-cleaning analytics.” GitHub Repository: <https://github.com/illyanayshevsky/pyCondrop.git>, New York, NY, 2019.
- [68] L. Gao and T. J. McCarthy, “Wetting 101°,” *Langmuir*, vol. 25, no. 24, pp. 14105–14115, 2009.
- [69] D. Quéré, “Non-sticking drops,” *Reports Prog. Phys.*, vol. 68, no. 11, pp. 2495–2532, 2005.
- [70] B. Figgis, A. Ennaoui, B. Guo, W. Javed, and E. Chen, “Outdoor soiling microscope for measuring particle deposition and resuspension,” *Sol. Energy*, vol. 137, pp. 158–164, 2016.

- [71] B. Mondal, M. Mac Giolla Eain, Q. F. Xu, V. M. Egan, J. Punch, and A. M. Lyons, “Design and Fabrication of a Hybrid Superhydrophobic–Hydrophilic Surface That Exhibits Stable Dropwise Condensation,” *ACS Appl. Mater. Interfaces*, vol. 7, no. 42, pp. 23575–23588, 2015.
- [72] F. M. White, *Heat and Mass Transfer*. Addison-Wesley Publishing Co., 1988, pp. 602–604.
- [73] Z. Pan, S. Dash, J. A. Weibel, and S. V. Garimella, “Assessment of water droplet evaporation mechanisms on hydrophobic and superhydrophobic substrates,” *Langmuir*, vol. 29, no. 51, pp. 15831–15841, 2013.
- [74] L. Zhang, A. Pan, R. Cai, and H. Lu, “Indoor experiments of dust deposition reduction on solar cell covering glass by transparent super-hydrophobic coating with different tilt angles,” *Sol. Energy*, vol. 188, no. July, pp. 1146–1155, 2019.
- [75] I. Nayshevsky, Q. Xu, J. M. Newkirk, D. Furhang, D. C. Miller, and A. M. Lyons, “Self-Cleaning Hybrid Hydrophobic–Hydrophilic Surfaces: Durability and Effect of Artificial Soilant Particle Type,” *IEEE J. Photovoltaics*, vol. In Print, pp. 1–8, 2019.
- [76] M. Woodhouse *et al.*, “On the Path to SunShot: The Role of Advancements in Solar Photovoltaic Efficiency, Reliability, and Costs,” *Natl. Renew. Energy Lab.*, no. May, p. 44, 2016.
- [77] H. Qasem, “Modelling dust for optimization, long term analysis,” *Soiling Eff. PV Modul. Work.*, 2016.
- [78] T. Sarver, A. Al-Qaraghuli, and L. L. Kazmerski, “A comprehensive review of the impact of dust on the use of solar energy: History, investigations, results, literature, and mitigation approaches,” *Renew. Sustain. Energy Rev.*, vol. 22, pp. 698–733, 2013.
- [79] M. Schweiger and W. Herrmann, “Electrical stability of PV modules in different climates,” *2017 IEEE 44th Photovolt. Spec. Conf. PVSC 2017*, vol. 0049, no. 0, pp. 1–3, 2018.
- [80] L. Simpson, M. Muller, M. Deceglie, D. Miller, and H. Moutinho, “The Modeling of the Effects of Soiling , Its Mechanisms , and the Corresponding Abrasion PV Module Reliability Workshop,” 2016.
- [81] L. L. Kazmerski *et al.*, “Fundamental Studies of Adhesion of Dust to PV Module Surfaces : Chemical and Physical Relationships at the Microscale Fundamental Studies of Adhesion of Dust to PV Module Surfaces : Chemical and Physical Relationships at the Microscale,” no. February, pp. 1–11, 2016.
- [82] I. Nayshevsky, Q. Xu, G. Barahman, and A. M. Lyons, “Fluoropolymer Coatings for Solar Cover Glass : Anti-Soiling Mechanisms in the Presence of Dew,” *Sol. Energy Mater. Sol. Cells*, vol. In Press, 2019.
- [83] K. K. Varanasi, M. Hsu, N. Bhate, W. Yang, and T. Deng, “Spatial control in the heterogeneous nucleation of water,” *Appl. Phys. Lett.*, vol. 95, no. 9, pp. 2007–2010, 2009.
- [84] L. Skinner and J. Samples, “The Kelvin equation—a review,” *J. Aerosol Sci.*, vol. 3, no. 3, pp. 199–210, 1972.
- [85] D. J. Lockwood, *Rayleigh and Mie Scattering*. Springer, New York, NY, 2016.
- [86] *Photovoltaic devices - Part 3: Measurement principles for terrestrial photovoltaic (PV) solar devices with reference spectral irradiance data*. IEC 60904-3, International Electrochemical Commission, [Online] Available: <https://webstore.iec.ch/publication/61084>, 2008.

- [87] *Measurement procedures for materials used in photovoltaic modules - Part 7-2: Environmental exposures - Accelerated weathering tests of polymeric materials*. IEC TS 62788-7-2, International Electrochemical Commission, [Online] Available: <https://webstore.iec.ch/publication/33675>, 2017.
- [88] M.-A. Simard and C. Jolicoeur, “Chemical admixture-cement interactions: Phenomenology and physico-chemical concepts,” *Cem. Concr. Compos.*, vol. 20, no. 2–3, pp. 87–101, 1998.
- [89] F. Wolfgang Tegethoff, Ed., *Calcium Carbonate: From the Cretaceous Period into the 21st Century*. Birkhäuser Basel, 2001.
- [90] K. K. Ilse *et al.*, “Comparing indoor and outdoor soiling experiments for different glass coatings and microstructural analysis of particle caking processes,” *IEEE J. Photovoltaics*, vol. 8, no. 1, pp. 203–209, 2018.
- [91] S. Lee, J. S. Park, and T. R. Lee, “The wettability of fluoropolymer surfaces: Influence of surface dipoles,” *Langmuir*, vol. 24, no. 9, pp. 4817–4826, 2008.
- [92] J. B. Boreyko and C. H. Chen, “Self-propelled dropwise condensate on superhydrophobic surfaces,” *Phys. Rev. Lett.*, vol. 103, no. 18, pp. 2–5, 2009.
- [93] T. Mouterde *et al.*, “Antifogging abilities of model nanotextures,” *Nat. Mater.*, vol. 16, no. 6, pp. 658–663, 2017.
- [94] J. B. Boreyko and C. P. Collier, “Delayed frost growth on jumping-drop superhydrophobic surfaces,” *ACS Nano*, vol. 7, no. 2, pp. 1618–1627, 2013.
- [95] Q. Hao, Y. Pang, Y. Zhao, J. Zhang, J. Feng, and S. Yao, “Mechanism of delayed frost growth on superhydrophobic surfaces with jumping condensates: More than interdrop freezing,” *Langmuir*, vol. 30, no. 51, pp. 15416–15422, 2014.
- [96] “2013-Zhang-Anti-icing surfaces based on enhanced self-propelled jumping of condensed water microdroplets.pdf.” .
- [97] X. Chen *et al.*, “Activating the microscale edge effect in a hierarchical surface for frosting suppression and defrosting promotion,” *Sci. Rep.*, vol. 3, pp. 1–8, 2013.
- [98] T. M. Schutzius, S. Jung, T. Maitra, G. Graeber, M. Köhme, and D. Poulikakos, “Spontaneous droplet trampolining on rigid superhydrophobic surfaces,” *Nature*, vol. 527, no. 7576, pp. 82–85, 2015.
- [99] K. M. Wisdom, J. A. Watson, X. Qu, F. Liu, G. S. Watson, and C. H. Chen, “Self-cleaning of superhydrophobic surfaces by self-propelled jumping condensate,” *Proc. Natl. Acad. Sci. U. S. A.*, vol. 110, no. 20, pp. 7992–7997, 2013.
- [100] G. S. Watson, M. Gellender, and J. A. Watson, “Self-propulsion of dew drops on lotus leaves: a potential mechanism for self-cleaning,” *Biofouling*, vol. 30, pp. 427–434, 2014.
- [101] G. S. Watson, L. Schwarzkopf, B. W. Cribb, S. Myhra, M. Gellender, and J. A. Watson, “Removal mechanisms of dew via self-propulsion off the gecko skin,” *J. R. Soc. Interface*, vol. 12, p. 20141396, 2015.
- [102] R. L. Chavez, F. Liu, J. J. Feng, and C. H. Chen, “Capillary-inertial colloidal catapults upon drop coalescence,” *Appl. Phys. Lett.*, vol. 109, p. 011601, 2016.
- [103] N. Miljkovic *et al.*, “Jumping-droplet-enhanced condensation on scalable superhydrophobic nanostructured surfaces,” *Nano Lett.*, vol. 13, pp. 179–187, 2013.
- [104] Y. Zhao, Y. Luo, J. Zhu, J. Li, and X. Gao, “Copper-Based Ultrathin Nickel Nanocone Films with High-Efficiency Dropwise Condensation Heat Transfer Performance,” *ACS Appl. Mater. Interfaces*, vol. 7, no. 22, pp. 11719–11723, 2015.
- [105] M. C. Lu, C. C. Lin, C. W. Lo, C. W. Huang, and C. C. Wang, “Superhydrophobic Si

- nanowires for enhanced condensation heat transfer," *Int. J. Heat Mass Transf.*, vol. 111, pp. 614–623, 2017.
- [106] R. Wen *et al.*, "Hydrophobic copper nanowires for enhancing condensation heat transfer," *Nano Energy*, vol. 33, pp. 177–183, 2017.
- [107] C. Dietz, K. Rykaczewski, A. G. Fedorov, and Y. Joshi, "Visualization of droplet departure on a superhydrophobic surface and implications to heat transfer enhancement during dropwise condensation," *Appl. Phys. Lett.*, vol. 97, p. 033104, 2010.
- [108] J. Zhu, Y. Luo, J. Tian, J. Li, and X. Gao, "Clustered ribbed-nanoneedle structured copper surfaces with high-efficiency dropwise condensation heat transfer performance," *ACS Appl. Mater. Interfaces*, vol. 7, pp. 10660–10665, 2015.
- [109] M. Qu, J. Liu, and J. He, "Fabrication of copper-based ZnO nanopencil arrays with high-efficiency dropwise condensation heat transfer performance," *RCS Adv.*, vol. 6, pp. 59405–59409, 2016.
- [110] R. Wang *et al.*, "Bio-inspired superhydrophobic closely packed aligned nanoneedle architectures for enhancing condensation heat transfer," *Adv. Funct. Mater.*, vol. 28, p. 1800634, 2018.
- [111] S. Wang, X. Yu, C. Liang, and Y. Zhang, "Enhanced condensation heat transfer in air-conditioner heat exchanger using superhydrophobic foils," *Appl. Therm. Eng.*, vol. 137, pp. 758–766, 2018.
- [112] D. E. M. Warsinger, J. Swaminathan, L. A. Maswadeh, and L. J. H. V., "Superhydrophobic condenser surfaces for air gap membrane distillation," *J. Memb. Sci.*, vol. 492, pp. 578–687, 2015.
- [113] H. G. Andrews, E. A. Eccles, W. C. E. Schofield, and J. P. S. Badyal, "Three-dimensional hierarchical structures for fog harvesting," *Langmuir*, vol. 27, pp. 3798–3802, 2011.
- [114] R. Xiao, N. Miljkovic, R. Enright, and E. N. Wang, "Immersion condensation on oil-infused heterogeneous surfaces for enhanced heat transfer," *Sci. Rep.*, vol. 3, p. 1988, 2013.
- [115] K. F. Wiedenheft *et al.*, "Hotspot cooling with jumping-drop vapor chambers," *Appl. Phys. Lett.*, vol. 110, p. 141601, 2017.
- [116] J. B. Boreyko and C. H. Chen, "Vapor chambers with jumping-drop liquid return from superhydrophobic condensers," *Int. J. Heat Mass Transf.*, vol. 61, pp. 409–418, 2013.
- [117] X. Chen *et al.*, "Nanograssed micropyramidal architectures for continuous dropwise condensation," *Adv. Funct. Mater.*, vol. 21, pp. 4617–4623, 2011.
- [118] K. Rykaczewski and J. H. J. Scott, "Methodology for imaging nano-to-microscale water condensation dynamics on complex nanostructures," *ACS Nano*, vol. 5, pp. 5962–5968, 2011.
- [119] E. Ölçeroğlu, C. Y. Hsieh, M. M. Rahman, K. K. S. Lau, and M. McCarthy, "Full-field dynamic characterization of superhydrophobic condensation on biotemplated nanostructured surfaces," *Langmuir*, vol. 30, pp. 7556–7566, 2014.
- [120] R. Enright, N. Miljkovic, A. Obeidi, C. V. Thompson, and E. N. Wang, "Condensation on superhydrophobic surfaces: the role of local energy barriers and structure length scale," *Langmuir*, vol. 28, pp. 14424–14432, 2012.
- [121] T. Q. Liu, W. Sun, X. Y. Sun, and H. R. Ai, "Mechanism study of condensed drops jumping on super-hydrophobic surfaces," *Colloids Surfaces A Physicochem. Eng. Asp.*, vol. 414, pp. 366–374, 2012.
- [122] B. Peng, S. Wang, Z. Lan, W. Xu, R. Wen, and X. Ma, "Analysis of droplet jumping

- condensation with lattice boltzmann simulation of droplet coalescence,” *Appl. Phys. Lett.*, vol. 102, p. 151601, 2013.
- [123] R. Enright, N. Miljkovic, J. Sprittles, K. Nolan, R. Mitchell, and E. N. Wang, “How coalescing droplets jump,” *ACS Nano*, vol. 8, pp. 10352–10362, 2014.
- [124] K. Zhang, F. Liu, A. J. Williams, X. Qu, J. J. Feng, and C. H. Chen, “Self-propelled droplet removal from hydrophobic fiber-based coalescers,” *Phys. Rev. Lett.*, vol. 115, p. 074502, 2015.
- [125] M. K. Kim *et al.*, “Enhanced jumping-droplet departure,” *Langmuir*, vol. 31, pp. 13452–13466, 2015.
- [126] M. He *et al.*, “Hierarchically structured porous aluminum surfaces for high-efficient removal of condensed water,” *Soft Matter*, vol. 8, pp. 6680–6683, 2012.
- [127] N. Miljkovic, R. Enright, and E. N. Wang, “Effect of droplet morphology on growth dynamics and heat transfer during condensation on superhydrophobic nanostructured surfaces.,” *ACS Nano*, vol. 6, pp. 1776–1785, 2012.
- [128] G. Q. Li, M. H. Alhosani, S. Yuan, H. Liu, A. A. Ghaferi, and T. J. Zhang, “Microscopic droplet formation and energy transport analysis of condensation on scalable superhydrophobic nanostructured copper oxide surfaces,” *Langmuir*, vol. 30, pp. 14498–14511, 2014.
- [129] C. Lv, P. Hao, X. Zhang, and F. He, “Dewetting transitions of dropwise condensation on nanotexture-enhanced superhydrophobic surfaces,” *ACS Nano*, vol. 9, pp. 12311–12319, 2015.
- [130] C. S. Sharma, J. Combe, M. Giger, T. Emmerich, and D. Poulikakos, “Growth rates and spontaneous navigation of condensate droplets through randomly structured textures,” *ACS Nano*, vol. 11, pp. 1673–1682, 2017.
- [131] M. D. Mulroe, B. R. Srijanto, S. F. Ahmadi, C. P. Collier, and J. B. Boreyko, “Tuning superhydrophobic nanostructures to enhance Jumping-Droplet condensation,” *ACS Nano*, vol. 11, pp. 8499–8510, 2017.
- [132] Y. Nam, H. Kim, and S. Shin, “Energy and hydrodynamic analyses of coalescence-induced jumping droplets,” *Appl. Phys. Lett.*, vol. 103, p. 161601, 2013.
- [133] K. Rykaczewski, “Microdroplet growth mechanism during water condensation on superhydrophobic surfaces,” *Langmuir*, vol. 28, pp. 7720–7729, 2012.
- [134] X. Liu and P. Cheng, “Dropwise condensation theory revisited: Part I. Droplet nucleation radius,” *Int. J. Heat Mass Transf.*, vol. 83, pp. 833–841, 2015.
- [135] S. Chattopadhyay, Y. F. Huang, Y. J. Jen, A. Ganguly, K. H. Chen, and L. C. Chen, “Anti-reflecting and photonic nanostructures,” *Mater. Sci. Eng. R Reports*, vol. 69, no. 1–3, pp. 1–35, 2010.
- [136] Electric Power Research Institute (EPRI), “Assessing anti-reflective and anti-soiling coatings for photovoltaic modules,” no. September, p. 14, 2016.
- [137] H. K. Raut, V. A. Ganesh, A. S. Nair, and S. Ramakrishna, “Anti-reflective coatings: A critical, in-depth review,” *Energy Environ. Sci.*, vol. 4, no. 10, pp. 3779–3804, 2011.
- [138] J. Gardiner, “Fluoropolymers: Origin, Production, and Industrial and Commercial Applications,” *Aust. J. Chem.*, vol. 68, no. 1, pp. 13–22, 2015.
- [139] H. Teng, “Overview of the Development of the Fluoropolymer Industry,” *Appl. Sci.*, vol. 2, no. 4, pp. 496–512, 2012.
- [140] J. Li, W. Yu, D. Zheng, X. Zhao, C. H. Choi, and G. Sun, “Hot embossing for whole Teflon superhydrophobic surfaces,” *Coatings*, vol. 8, no. 7, pp. 1–13, 2018.

- [141] T. Nobuta and T. Ogawa, “Applied Surface Science Improvement of depth resolution in XPS analysis of fluorinated layer using C60 ion sputtering,” *Appl. Surf. Sci.*, vol. 256, pp. 1560–1565, 2009.
- [142] Y. Yamamoto, “Precise XPS depth analysis of soda-lime-silica glass surface after various treatments,” *Surf. Interface Anal.*, vol. 44, no. 8, pp. 931–933, 2012.
- [143] J. Lou, H. He, N. J. Podraza, L. Qian, C. G. Pantano, and S. H. Kim, “Thermal Poling of Soda-Lime Silica Glass with Nonblocking Electrodes — Part 1: Effects of Sodium Ion Migration and Water Ingress on Glass Surface Structure,” *J. Ceram. Soc.*, vol. 99, no. 4, pp. 1221–1230, 2016.
- [144] N. Janke, O. Grassme, and R. Weibmann, “Alkali ion migration control from flat glass substrates.” .
- [145] F. Geotti-Bianchini, D. R. Luca, G. Gagliardi, M. Guglielmi, and C. G. Pantano, “New interpretation of the IR reflectance spectra of SiO₂-rich films on soda-lime glass,” *Glas. Ber.*, vol. 64, no. 8, pp. 205–217, 1991.
- [146] G. Scarinci, V. Gottardi, G. P. Gambaretto, and D. Rosa Festa, “Effects of treatment with fluorinating agents on the composition of surface structure of soda-lime glasses,” *J. Non. Cryst. Solids*, vol. 34, no. 1979, pp. 371–380, 2017.
- [147] H. W. Nesbitt *et al.*, “Bridging, non-bridging and free (O₂⁻) oxygen in Na₂O-SiO₂glasses: An X-ray Photoelectron Spectroscopic (XPS) and Nuclear Magnetic Resonance (NMR) study,” *J. Non. Cryst. Solids*, vol. 357, no. 1, pp. 170–180, 2011.
- [148] R. Rogoziński, *Producing the Gradient Changes in Glass Refraction by the Ion Exchange Method — Selected Aspects, Ion Exchange - Studies and Applications*. .
- [149] H. Y. Xia, C. X. Teng, X. W. Zhao, and J. Zheng, “Refractive index profiles of copper ion exchange glass planar waveguides,” *Chinese Phys. Lett.*, vol. 29, no. 8, 2012.
- [150] S. Karlsson, *Modification of Float Glass Surfaces by Ion Exchange*. 2012.
- [151] H. A. Schaeffer, M. Stengel, and J. Mecha, “Dealkalization of Glass Surfaces Utilizing HCl Gas,” *J. Non. Cryst. Solids*, vol. 80, pp. 400–404, 1986.
- [152] J. P. Poole and H. C. Snyder, “Corrosion Retarding Fluorine Treatment of Glass Surfaces,” 3,314,772, 1967.
- [153] J. W. Fleming and D. L. Wood, “Refractive index dispersion and related properties in fluorine doped silica,” *Appl. Opt.*, vol. 22, no. 19, pp. 3102–3104, 1983.
- [154] C. R. Hense, J. Mecha, and H. A. Schaeffer, “Treatment of soda-lime-silica glass surfaces with fluorine-containing gases,” *Glas. Ber.*, vol. 5, pp. 127–134, 1990.
- [155] M. C. Paul, R. Sen, R. E. Youngman, and A. Dhar, “Fluorine incorporation in silica glass by the MCVD process: Study of fluorine incorporation zone , evaluation of optical properties and structure of the glass,” *J. Non. Cryst. Solids*, vol. 354, pp. 5408–5420, 2008.
- [156] M. Tanaka *et al.*, “Fluorine Treatments of Soda-Lime Silicate Glass Surfaces,” *Commun. Am. Ceram. Soc.*, no. August, pp. 123–124, 1983.
- [157] B. E. Warren and J. Biscoe, “FOURIERANALYSIS OF X-RAY PATTERNS OF SODA-SILICA GLASS,” *J. Am. Ceram. Soc.*, vol. 21, no. 7, pp. 259–265, 1938.
- [158] S. R. Kasi, M. Liehr, and S. Cohen, “Chemistry of fluorine in oxidation of silicon,” *Appl. Phys. Lett.*, vol. 58, no. 25, pp. 2975–2977, 1991.
- [159] J. A. Williams and J. J. Kauzlarich, “Mandrel Peeling of a Flexible Laminate With a Pressure-Sensitive Adhesive : Comparison of Experiment with Numerical Analysis,” pp. 439–448, 2011.

- [160] S. Meyer, “Adhesion - Considerations, Testing and Interpretation,” *Proc. NREL PV Modul. Reliab. Work.*, 2015.
- [161] J. F. Moulder, W. F. Stickle, P. E. Sobol, and K. D. Bomben, *Handbook of X-Ray Photoelectron Spectroscopy*. 1992.
- [162] D. A. Shirley, “High-resolution x-ray photoemission spectrum of the valence bands of gold,” *Phys. Rev. B*, vol. 5, no. 12, pp. 4709–4714, 1972.
- [163] C. D. Wagner, “SENSITIVITY FACTORS FOR XPS ANALYSIS OF SURFACE ATOMS,” *J. Electron Spectros. Relat. Phenomena*, vol. 32, pp. 99–102, 1983.
- [164] M. Hasanuzzaman, A. Rafferty, M. Sajja, and A.-G. Olabi, “Properties of Glass Materials,” *Mater. Sci. Mater. Eng.*, vol. Reference, p. 9, 2016.
- [165] H. G. Pfaender, “Glass , the material,” in *Schott Guide to Glass*, 1996, pp. 23–24.
- [166] Q. Gao, Y. Chen, Y. Wei, X. Wang, and Y. Luo, “Heparin-grafted poly(tetrafluoroethylene-co-hexafluoropropylene) film with highly effective blood compatibility via an esterification reaction,” *Surf. Coatings Technol.*, vol. 228, no. SUPPL.1, pp. 126–130, 2013.
- [167] C. D. Li, D. Z. Yang, and S. Y. He, “Effects of proton exposure on aluminized Teflon FEP film degradation,” *Nucl. Instruments Methods Phys. Res. Sect. B Beam Interact. with Mater. Atoms*, vol. 234, no. 3, pp. 249–255, 2005.
- [168] X. Zhong, J. Sun, F. Wang, and Y. Sun, “XPS study of radiation crosslinked copolymer of tetrafluoroethylene with hexafluoropropylene,” *J. Appl. Polym. Sci.*, vol. 44, no. 4, pp. 639–642, 1992.
- [169] B. Parekh, S. Zheng, A. Entenberg, T. Debies, and G. A. Takacs, “Surface modification of poly(tetrafluoroethylene-co-hexafluoropropylene) with vacuum UV radiation from rotating helium dc arc plasmas,” *J. Adhes. Sci. Technol.*, vol. 21, no. 10, pp. 983–998, 2007.
- [170] Z. J. Yu, E. T. Kang, and K. G. Neoh, “Amidoximation of the acrylonitrile polymer grafted on poly(Tetrafluoroethylene-co-hexafluoropropylene) films and its relevance to the electroless plating of copper,” *Langmuir*, vol. 18, no. 26, pp. 10221–10230, 2002.
- [171] B. Kim *et al.*, “Mechanisms and Characterization of the Pulsed Electron-Induced Grafting of Styrene onto Poly(tetrafluoroethylene-co-hexafluoropropylene) to Prepare a Polymer Electrolyte Membrane,” *Radiat. Res.*, vol. 190, no. 3, p. 309, 2018.
- [172] W. H. Press, S. A. Teukolsky, W. T. Vetterling, and B. P. Flannery, *Numerical Recipes - The Art of Scientific Computing*. 2007.
- [173] R. D. Evans, “Ch. 27 - Statistical Tests for Goodness of Fit,” in *The Atomic Nucleus*, 1955, pp. 775–783.
- [174] C. Girardeaux and J.-J. Pireaux, “Analysis of Poly(tetrafluoroethylene) (PTFE) by XPS,” *Surf. Sci. Spectra*, vol. 4, no. 2, pp. 138–141, 1996.
- [175] K. N. Jung, J. I. Lee, J. H. Jung, K. H. Shin, and J. W. Lee, “A quasi-solid-state rechargeable lithium-oxygen battery based on a gel polymer electrolyte with an ionic liquid,” *Chem. Commun.*, vol. 50, no. 41, pp. 5458–5461, 2014.
- [176] L. Bodenes, A. Darwiche, L. Monconduit, and H. Martinez, “The Solid Electrolyte Interphase a key parameter of the high performance of Sb in sodium-ion batteries: Comparative X-ray Photoelectron Spectroscopy study of Sb/Na-ion and Sb/Li-ion batteries,” *J. Power Sources*, vol. 273, no. October, pp. 14–24, 2015.
- [177] N. Sanada, A. Yamamoto, R. Oiwa, and Y. Ohashi, “Extremely low sputtering degradation of polytetrafluoroethylene by C60ion beam applied in XPS analysis,” *Surf.*

Interface Anal., vol. 36, no. 3, pp. 280–282, 2004.

- [178] W. Liu, H. Li, J. Y. Xie, and Z. W. Fu, “Rechargeable room-temperature CF_x-sodium battery,” *ACS Appl. Mater. Interfaces*, vol. 6, no. 4, pp. 2209–2212, 2014.
- [179] S. Tasker, R. D. Chambers, and J. P. S. Badyal, “Surface defluorination of PTFE by sodium atoms,” *J. Phys. Chem.*, vol. 98, no. 47, pp. 12442–12446, 1994.
- [180] K. Okano *et al.*, “Induction of Cell-Cell Connections by Using *in situ* Laser Lithography on a Perfluoroalkyl-Coated Cultivation Platform,” *ChemBioChem*, vol. 12, no. 5, pp. 795–801, 2011.
- [181] F. Liu *et al.*, “Preparation of high-purity V₂C MXene and electrochemical properties as lithium batteries,” *J. Electrochem. Soc.*, vol. 164, no. 4, pp. A709–A713, 2017.
- [182] J. Pereira *et al.*, “*In situ* x-ray photoelectron spectroscopy analysis of SiO_xF_y passivation layer obtained in a SF₆/ O₂cryoetching process,” *Appl. Phys. Lett.*, vol. 94, no. 7, pp. 1–4, 2009.
- [183] P. Orazaio, T. Alberto, and M. Giovanni, “XPS Investigation of the Effects Induced by the Silanization on Real Glass Surfaces,” *J. Non. Cryst. Solids*, vol. 68, pp. 219–230, 1984.
- [184] A. Sharma, H. Jain, and A. C. Miller, “Surface modification of a silicate glass during XPS experiments,” *Surf. Interface Anal.*, vol. 31, no. 5, pp. 369–374, 2001.

Bibliography Addendum 1 (Chapter 2.6)

- [1] A. S. Al-Ammri, A. Ghazi and F. Mustafa, "Dust effects on the performance of PV street light in Baghdad city," 2013 International Renewable and Sustainable Energy Conference (IRSEC), Ouarzazate, 18-22. 2013
- [2] Ahmad Y. Al-hasan & Adel A. Ghoneim "A new correlation between photovoltaic panel's efficiency and amount of sand dust accumulated on their surface", International Journal of Sustainable Energy, 24:4, 187-197, 2005
- [3] Appels, R. et al., "Effect of soiling on photovoltaic modules", Solar Energy, 96, 283–291, 2013
- [4] B. S. Yilbas, G. Hassan, H. Ali, and N. Al-Aqeeli, “Environmental dust effects on aluminum surfaces in humid air ambient,” Scientific Reports, vol. 7, p. 45999, May 2017.
- [5] Bergin, M.H., et al, "Large Reductions in Solar Energy Production Due to Dust and Particulate Air Pollution", Environmental Science Technoogy. Letters, 4, 339–344, 2017
- [6] Bernd Weber et al., "Performance Reduction of PV Systems by Dust Deposition", Energy Procedia, 57, 99 – 108, 2014
- [7] Biryukov SA. "An experimental study of the dry deposition mechanism for airborne dust", Journal of Aerosol Science, 29, 129–3, 1998
- [8] Biryukov SA. Degradation of optical properties of solar collectors due to the ambient dust deposition as a function of particle size. Journal of Aerosol, Science 1996;27:S37–8.
- [9] Boddupalli, N., et al., "Dealing with dust – Some challenges and solutions for enabling solar energy in desert regions", Solar Energy, 150, 166–176, 2017
- [10] Brahim Aïssa, Rima J. Isaifan, Vinod E. Madhavan & Amir A. Abdallah, "Structural and physical properties of the dust particles in Qatar and their influence on the PV panel performance", Scientific Reports, Vol 6, Article number: 31467, 2016
- [11] Brem GF, Woyski MS, Ryan JS. "Investigation of soiling of candidate mirrors for solar power installations", McDonnell aeronautics company subcontract report. MDAC Rpt.

G8131, 1980

- [12] Chen, E., et al., "Measurement of dust sweeping force for cleaning solar panels", *Solar Energy Materials and Solar Cells*, 179, 247–253, 2018
- [13] Christopher Sansom, Heather Almond, Peter King, Essam Endaya, and Sofiane Bouaichaoui, "Airborne sand and dust soiling of solar collecting mirrors", *AIP Conference Proceedings* 1850, 130011, 2017
- [15] D. Goossens and Z. Y. Offer, "Comparisons of day-time and night-time dust accumulation in a desert region," *Journal of Arid Environments*, vol. 31, no. 3, pp. 253–281, 1995.
- [16] F. H. Haynie, "Size Distribution of Particles That May Contribute to Soiling of Material Surfaces," *Journal of the Air Pollution Control Association*, vol. 35, no. 5, pp. 552–554, 1985.
- [17] Fraga, M.M., et al "Analysis of the soiling effect on the performance of photovoltaic modules on a soccer stadium in Minas Gerais", Brazil, *Solar Energy* 163, 387–397, 2018
- [18] Gandhi Amarnadh et al., "Investigation of the Effects of Dust Accumulation, and Performance for Mono and Poly Crystalline Silica Modules", *International Journal of Renewable Energy Research*, Vol.4, No.3, 2014
- [19] Ghazi, S, Ip, K. "The effect of weather conditions on the efficiency of PV panels in the southeast of UK", *Renewable Energy*, 69, 50-59, 2014
- [20] Guan, Z., et al, "Dust characterization for solar collector deposition and cleaning in a concentrating solar thermal power plant," *Proceedings of International Conference on Heat Exchanger Fouling and Cleaning*, http://heatexchanger-fouling.com/papers/papers2015/40_Guan_F.pdf
- [21] Guo, B., Javed, W., "Efficiency of Electrodynamic Dust Shield at Dust Loading Levels Relevant to Solar Energy Applications", *IEEE Journal of Photovoltaics*, Vol. 8, No. 1, Jan 2018
- [22] H.A. Kazem, M.T. Chaichan, "Experimental analysis of the effect of dust's physical properties on photovoltaic modules in Northern Oman", *Solar Energy*, 139, 68–80, 2016
- [23] H.R. Moutinho et al., "Adhesion mechanisms on solar glass: Effects of relative humidity, surface roughness, and particle shape and size", *Solar Energy Materials and Solar Cells*, 172,145–153, 2017
- [24] Hegazy, A.A., "Effect of dust accumulation on solar transmittance through glass covers of plate-type collectors", *Renewable Energy*, 22, 525–540, 2001
- [25] Jiang, Y., et al, "Analyzing wind cleaning process on the accumulated dust on solar photovoltaic (PV) modules on flat surfaces", *Solar Energy*, 159, 1031–1036, 2018
- [26] Kaldellis, J., Fragos, P., Kapsali, M., 2011. Systematic experimental study of the pollution deposition impact on the energy yield of photovoltaic installations. *Renew. Energy* 36, 2717–2724.
- [27] Karmouch R, Hor HE "Solar Cells Performance Reduction under the Effect of Dust in Jazan Region", *Journal of Fundamental Renewable Energy Applications*, 7: 228, 2017
- [28] Kawamotoa,H, G, Bing, "Improvement of an electrostatic cleaning system for removal of dust from solar panels", *Journal of Electrostatics*. 91, 28–33, 2018
- [29] Klugmann-Radziemska, E., "Degradation of electrical performance of a crystalline photovoltaic module due to dust deposition in northern Poland", *Renewable Energy*, 78, 418-426, 2015
- [30] L. L. Kazmerski et al., "Fundamental studies of the adhesion of dust to PV module chemical and physical relationships at the microscale," *2015 IEEE 42nd Photovoltaic*

- Specialist Conference (PVSC), New Orleans, LA, 2015, pp. 1-7. 2015
- [31] M. Saidan et al., "Experimental study on the effect of dust deposition on solar photovoltaic panels in desert environment", Renewable Energy, 92, 2016
- [32] McTanish, G.H., "Dust deposition and particle size in Mali, West Africa" Catena, 29, 307-322, 1997
- [33] Mehmood, U., et al. "Characterization of dust collected from PV modules in the area of Dhahran, Kingdom of Saudi Arabia, and its impact on protective transparent covers for photovoltaic applications", Solar Energy, 141, 203–209, 2017
- [34] Menoufi, K., et al., "Dust accumulation on photovoltaic panels: a case study at the East Bank of the Nile (Beni-Suef, Egypt)", Energy Procedia, 128, 24–31, 2017
- [35] Mohamed and Hasan, "Effect of Dust Accumulation on Performance of Photovoltaic Solar Modules in Sahara Environment", Journal of Basic and Applied Scientific Research, 2(11)11030-11036, 2012
- [36] Morris VL. "Cleaning agents and techniques for concentrating solar collectors", Solar Energy Materials, 3, 35–55, 1980
- [37] Olivares, D., et al, "Characterization of soiling on PV modules in the Atacama Desert", Energy Procedia, 124, 547–553, 2017
- [38] Pennetta, S., et al, "A Case Study on Parameters Influencing DustAccumulation on CSP Reflectors," Journal of Energy and Power Engineering 10, 73-81, 2016
- [39] R. Appels, B. Muthirayan, A. Beerten, R. Paesen, J. Driesen, and J. Poortmans, "The effect of dust deposition on photovoltaic modules," 2012 38th IEEE Photovoltaic Specialists Conference, 2012.
- [40] R. E. Cabanillas, and H. Munguía, "Dust accumulation effect on efficiency of Si photovoltaic modules", Journal of Renewable and Sustainable Energy, 3, 043114, 2011
- [41] Roth EP, Anaya AJ. "Effect of natural soiling and cleaning on the size distribution of particles deposited on glass mirrors". Journal of Solar Energy Engineering, 102, 248–56, 1980
- [42] Roth EP, Pettit RB. "Effect of soiling on solar mirrors and techniques used to maintain high reflectivity", Chapter 6 in Solar Materials Science. TJ810.S667, 199–227, 1980
- [43] Solend, T.A., "Cleaning Schedule based on Soiling Effects on Photovoltaics in Kalkbult, South Africa", 2017 (Master's Thesis)
https://brage.bibsys.no/xmlui/bitstream/handle/11250/2468083/Master_final.pdf?sequence=1
- [44] Syed A.M. Said, Husam M. Walwil, "Fundamental studies on dust fouling effects on PV module performance", Solar Energy, 107, 328–337, 2014
- [45] Sylva, Jason, "Characterization of Dust on Solar Devices in Southern Nevada" (2017). UNLV Theses, Dissertations, Professional Papers, and Capstones. 3042,
<https://digitalscholarship.unlv.edu/thesesdissertations/3042>
- [46] T. Sarver, A. Al-Qaraghuli, and L. L. Kazmerski, "A comprehensive review of the impact of dust on the use of solar energy: History, investigations, results, literature, and mitigation approaches," Renewable and Sustainable Energy Reviews, vol. 22, pp. 698–733, 2013.
- [47] T. Sarver, A. Al-Qaraghuli, and L. L. Kazmerski, "A comprehensive review of the impact of dust on the use of solar energy: History, investigations, results, literature, and mitigation approaches," Renewable and Sustainable Energy Reviews, vol. 22, pp. 698–733, 2013.

- [48] Tanesab, J., et al, "Seasonal effect of dust on the degradation of PV modules performance deployed in different climate areas", *Renewable Energy*, 111, 105-115, 2017
- [49] Tanesab, J., et al, "The contribution of dust to performance degradation of PV modules in a temperate climate zone", *Solar Energy*, 120, 147–157, 2015
- [50] Urrejola, E., "Effect of soiling and sunlight exposure on the performance ratio of photovoltaic technologies in Santiago, Chile, E. Urrejola et al.", *Energy Conversion and Management*, 114, 338–347, 2016
- [51] W. Javed et al., "Characterization of dust accumulated on photovoltaic panels in Doha, Qatar", *Solar Energy*, 142, 123–135, 2017
- [52] W. Javed, B. Guo, Y. Wubulikasimu and B. W. Figgis, "Photovoltaic performance degradation due to soiling and characterization of the accumulated dust," 2016 IEEE International Conference on Power and Renewable Energy (ICPRE), Shanghai, 2016, 580–584, 2016
- [53] Y. Guan et al., "In-situ investigation of the effect of dust deposition on the performance of polycrystalline silicon photovoltaic module", *Renewable Energy*, 101, 2017
- [54] Yilbas, B.S., et al., "Effect of environmental dust particles on laser textured yttria-stabilized zirconia surface in humid air ambient," *Optics and Laser Technology*, 101, 388–396, 2018
- [55] Yilbas, B.S., et al, "Influence of dust and mud on the optical, chemical, and mechanical properties of a pv protective glass", *Scietific Reports*, 5: 15833, 2015
- [56] Yilbas, B.S., et al., "Water Droplet Dynamics on a Hydrophobic Surface in Relation to the Self-Cleaning of Environmental Dust", *Scientific Reports*, Volume 8, Article number: 2984, 2018
- [57] Yilbas, Bekir Sami., Haider Ali, Naseer Al-Aqeeli, Mazen M. Khaled, Syed Said, Numan Abu-Dheir, Necar Merah, Kamal Youcef-Toumi, and Kripa K. Varanasi.
"Characterization of Environmental Dust in the Dammam Area and Mud After-Effects on Bisphenol-A Polycarbonate Sheets." *Scientific Reports*, 6, 24308, 2016
- [58] Zarei, T., "Optical and thermal modeling of a tilted photovoltaic module with sand particles settled on its front surface", *Energy*, 95, 51-66, 2015